VNIVERSITAT DE VALÈNCIA

(ICMOL)

"Multifunctional hybrid nanocomposites based on carbon nanotubes and chemically modified graphene"

Memoria de Tesis Doctoral presentada por

Concha Bosch Navarro

Dirigida por

Prof. Eugenio Coronado Miralles y Dr. Carlos Martí Gastaldo

Para optar al Grado de doctor en Nanociencia y Nanotecnología

Valencia, Junio 2013

Eugenio Coronado Miralles, Catedrático de Química Inorgánica de la Universidad de Valencia y D. Carlos Martí Gastaldo, Investigador Post-doctoral en la Universidad de Liverpool

CERTIFICAN:

Que el trabajo que presenta D. Concha Bosch Navarro en esta memoria, con el título: "Multifunctional hybrid nanocomposites based on carbon nanotubes and chemically modified graphene" ha sido realizado bajo nuestra dirección en el Instituto de Ciencia Molecular.

Y para que así conste, a efectos de su presentación para optar al Grado de doctor en Nanociencia y Nanotecnología, expedimos el presente documento

D. Eugenio Coronado Miralles D. Carlos Martí Gastaldo

En Valencia, 20 abril 2013

A mis padres y a "mi puti"
por estos 29 años

Agradecimientos

Agradecimientos

Desde que empecé esta aventura unos cuantos años atrás muchas son las personas que de manera más o menos directa han contribuido a que esto haya podido llegar a buen puerto. Muchos ni si quiera serán conscientes y es por ello por lo que me gustaría empezar con unas breves palabras de agradecimiento.

En primer lugar me gustaría agradecerle a Eugenio todo lo que ha hecho por mí. He de reconocer que no siempre ha sido fácil, pero con los años uno aprende a entenderle y a lidiar con sus bromas. Gracias por darme la oportunidad de trabajar y por darme la libertad y la confianza necesaria con la que creo haber crecido como investigador. Espero poder seguir trabajando contigo, y contando con tu apoyo en el futuro.

Esta Tesis es tan mía como de Carlos. Carlos no ha sido un simple codirector de Tesis, ha sido ante todo un AMIGO. Empezamos en esto juntos unos 5 años atrás, y desde hace aproximadamente 3 años hemos continuado este proyecto desde la distancia. Gracias por esas conversaciones por Skype, por esa pasión por la ciencia, por esa disposición a ayudar, por tu sinceridad, por tu apoyo… Sólo espero seguir hablando contigo por Skype de vez en cuando, y disfrutar de una cervecita a tu lado siempre que sea posible. Con suerte en unos años volveremos a ser vecinos, y con suerte podremos seguir trabajando juntos por muchos años. Ya de paso, agradecerle a Lola su paciencia infinita.

Julia y Efrén. Sin duda alguna, lo que más pena me da de acabar la Tesis es pensar que pronto ya no estaremos juntos todos los días. Habéis sido la alegría de cada día, me habéis enseñado tantas cosas y me he reído tanto!!!!. No me puedo imaginar lo que habría sido esto sin vosotros, pero seguro que yo habría sido mucho menos feliz. Ya sabéis que en mi tenéis una amiga para toda la vida, prometo cantaros siempre que lo necesitéis, bailar, hacer excursiones, torrás, ver unos cortos…. Gracias por todo lo que hemos vivido y todo lo que nos queda por vivir. Dentro de poco nos tocará hacer las tarjetas desde la distancia, pero se harán. Y por si acaso, en estas líneas me comprometo ya a correr la San Silvestre de Rocafort con vosotros las próximas 20 Navidades.

Agradecimientos

Quería agradecérselo especialmente a Sergio. Empecé trabajando mano a mano con él en el mundo de los TTFs. La vida del orgánico es muy dura y poco a poco me lo fui dejando. En cualquier caso, aprendí mucho trabajando contigo. Gracias por lo que me enseñaste, y gracias por estar siempre dispuesto ayudarme.

Nora!!, nunca olvidaré cuando aún trabajabas con nosotros. Sin duda fue un placer, y sin duda eres una amiga.

Mención especial para el gran José, el hombre para todo. Tú eres un colega, así que ya sabes que en el futuro tenemos unas cuantas cervezas pendientes. María, alegra esa cara que tú también puedes acompañarnos siempre que quedemos ;)

Gracias a Helena porque hasta que llegó ella no era capaz de medir nada. Gracias por tu entusiasmo y tu dedicación. Chema y Gloria, sé que puedo ser muy pesada, así que gracias por ayudarme en todo lo que he necesitado.

También quiero agradecérselo a todas aquellas personas con las que he colaborado y que han hecho que mi trabajo haya sido un poco más fácil.

Al resto de la familia del ICMol: Ángel,"Pini", Juampi, Yan Duan, Estela, Marian, Paco, Eva, Alejandra, Sonsoles, Patricia, Victor, Mauri, Marian, Guille, Alex Gaita, los ya no cajales, … Gracias, porque todos en mayor o menor medida habéis contribuido a que hoy esté aquí.

La Tesis es un periodo de tu vida. Soy consciente que la gente que no ha vivido una Tesis de cerca no sabe muy bien lo que supone, pero hay momentos, sobre todo a medida que se acerca el final, que crece la negatividad de una manera indescriptible. En esos momentos uno necesita desconectar si es posible, y que le aguanten sus "malos humos" cuando de vez en cuando llegan. En este sentido tengo muchísimos amigos a los que agradecerles muchas cosas:

- Vero, Pili, Isa y "los Jorges", ya son muchos años y qué decir tiene que vosotros sois uno de esos pilares sólidos que hacen que nada se tambalee. Gracias por todos estos 10-23 años que nos conocemos, por esas ricas meriendas, por las incontables risas y los innumerables momentos que hemos vivido.
- A Carmina, mi casi hermana, porque con ella aprendí a imaginar cosas inimaginables que me han ayudado a avanzar en mi camino siempre con

una sonrisa y un toque de locura. Además, a Yara, Cris y Mª José, por esas tardes de tenis, por esas risas tontas, y por todos los momentos divertidos. Me cuesta mucho recordar un "fiestote" sin vosotras. Sois guays!!!. ;) , y espero poder disfrutar de parte de vuestro tiempo durante muchos años más.

- Gracias a las "perras". Ya son muchos años, pero sobre todo este último periodo ha sido especialmente intenso. Gracias por ayudarme a desconectar, por las incontables tardes, por los fines de semana, los viajes en furgococche, las noches de folclóricas… gracias por todo. Ya sabéis que mi casa es vuestra casa, y que siempre estoy dispuesta para quedar un ratete. No sé cómo lo hacéis, pero nunca me canso de vosotras ;)

Si alguien se merece un hueco especial en estas líneas son mis padres. Uno llega a donde llega tras muchos años de vivencias. Yo tengo la inmensa suerte de haber nacido en la mejor familia del mundo, con los mejores padres del mundo. No siempre he sido fácil (tengo mucho carácter) pero vosotros habéis sabido llevarme muy bien. Sin duda alguna, en ese sentido me siento la persona más afortunada del mundo. Además, tengo la suerte de contar con el hermano más maravilloso y más divertido del mundo, "mi puti". Claramente el mérito es de nuestros padres, pero la suerte es nuestra. En este punto no quiero olvidarme de Nuria porque aunque llegará más tarde a la familia, ya forma parte importante de ella. Os quiero, y a vosotros os dedico esta Tesis.

Por último y no por ello menos importante a Juan, "mi monito". Siempre he sido muy feliz, pero desde que llegaste tú lo soy todavía más. No me quiero imaginar lo que habría sido de estos últimos años sin ti. Gracias por aguantar mis manías, sólo espero poderlas compartir contigo muchos años más.

Agradecimientos

Table of Contents

List of Abbreviations **21**

Summary **25**

Preface: An Historical Overview **27**

Introduction to Carbon Nanotubes **29**

1.1. Types of CNTs. 30

1.2. Synthesis of CNTs. 32

a) Arc Discharge. 33

b) Laser Ablation. 34

c) Chemical Vapor Deposition (CVD). 35

1.3. Purification of CNTs. 36

1.4. Functionalization of CNTs. 37

a) Non-Covalent functionalization. 37

b) Covalent functionalization. 39

c) Endohedral functionalization of CNTs. 42

1.5. Properties and applications 44

1.6. References. 45

Introduction to Graphene **49**

2.1. Classification and Properties of Graphene. 50

a) Graphene (G). 50

b) Graphite Oxide (GO) and reduced Graphite Oxide (rGO). 51

c) Graphene Nanoribbons (GNRs). 52

2.2. Synthesis of Graphene. 52

Liquid phase exfoliation of graphite. 53

Reduction of GO. 54

2.3. Functionalization of Graphene and applications. 55

Non-Covalent functionalization. 55

Covalent functionalization. 57

2.4. Graphene-based hybrid materials. 58

2.5. References 60

Carbon Nanotubes based hybrid materials' 63

3.1. Electrostatic Anchoring of Mn_4 Single-Molecule Magnets on Chemically Modified Multi-walled Carbon Nanotubes 64

3.1.1. Introduction 64

3.1.2. Results and Discussion 65

3.1.2.1. Synthesis 65

3.1.2.2. Anchoring of Mn4 Molecules. 67

3.1.2.3. Electron Microscopy and EDS analysis. 70

3.1.2.4. X-Ray Photoelectron Spectroscopy (XPS) 74

3.1.2.5. Magnetic measurements. 76

3.1.3. Conclusions 78

3.1.4. Experimental 79

3.1.4.1. General synthesis remarks. 79

3.1.4.2. Synthesis procedure. 80

Synthesis of $[Mn_4(OAc)_2(pdmH)_6](ClO_4)_2$ (pdmH = deprotonated pyridine-2,6-dimethanol; $C_5H_4NO_2$). 80

Route 1. 81

Route 2. 82

3.1.4.3. Physical characterization. 83

3.2. Polyoxometalate - Single-Walled Carbon Nanotube Hybrids by Supramolecular Grafting. 85

3.2.1. Introduction 85

3.2.2. Results and Discussion 86

3.2.2.1. Synthesis of the hybrid 86
3.2.2.2. Anchoring of POM molecules 87
3.2.2.3. X-Ray Photoelectron Spectroscopy 88
3.2.2.4. Electron Microscopy and EDS analysis 89
3.2.3. Conclusions 91
3.2.5. Experimental 91
3.2.5.1. General synthesis remarks 91
3.2.5.2. Synthesis procedure 91
Synthesis of ({(TBA)$_6$(P$_2$W$_{17}$O$_{61}$}{O(Si-Ph-ethylpyrene))$_2$} = POM(pyr) 91
Synthesis of SWNT@POM(pyr) 93
3.2.5.3. Physical characterization 93

3.3. References 95

Chemical Synthesis of Graphene 99

4.1. Influence of the pH on the Synthesis of reduced Graphene Oxide under Hydrothermal Conditions 100

4.1.1. Introduction 100
4.1.2. Results and Discussion 101
4.1.2.1. Synthesis 101
4.1.2.2. Thermogravimetric Analysis 102
4.1.2.3. Infra-red Spectroscopy (FT-IR) 103
4.1.2.4. X-Ray Diffraction Powder (XRD) 104
4.1.2.5. High Resolution Electron Microscopy (HR-TEM) 105
4.1.2.6. X-Ray Photoelectron Spectroscopy (XPS) 108
4.1.2.7. Raman Spectroscopy 110
4.1.3. Conclusions 112
4.1.4. Experimental 112
4.1.4.1 General synthesis remarks. 112
4.1.4.2 Synthesis of GO. 112
4.1.4.3. Synthesis of rGO. 113

4.1.4.4. Physical Characterization. 113

4.2. Anthracene as a precursor of Graphite-like materials 115

4.2.1. Introduction 115

4.2.2. Bulk synthesis of graphite from anthracene 117

4.2.2.1 Results and discussion 117

4.2.2.1.1. Synthesis 117

4.2.2.1.2. FT-IR 119

4.2.2.1.3. X-Ray Diffraction powder (XRD) 120

4.2.2.1.4. Thermogravimetric analysis 122

4.2.2.1.5. Raman spectroscopy. 123

4.2.2.1.6. HR-TEM 124

4.2.2.2. Conclusions 126

4.2.2.3. Experimental. 126

4.2.2.3.1. General synthesis remarks 126

4.2.2.3.2. Synthesis of Graphite (G2) 126

4.2.2.3.3. Physical characterization 127

4.2.3. Synthesis of Ultrathin Graphene Nanoforms Induced by the Fusion of anthracene rings inside the channels of MCM-41 128

4.2.3.1. Results and discussion 128

4.2.3.1.1. Synthesis of graphitic nanoforms 128

4.2.3.1.2. X-Ray Diffraction powder (XRD) 130

4.2.3.1.3. Adsorption Experiments 132

4.2.3.1.4. Scanning Electron Microscopy (SEM) 134

4.2.3.1.5. Thermogravimetric Analysis 134

4.2.3.1.6. Raman spectroscopy. 136

4.2.3.2. Etching with HF 137

4.2.3.3. Conclusions 140

4.2.3.4. Experimental 141

4.2.3.4.1. General synthesis remarks 141

4.2.3.4.2. Synthesis of graphene nanoforms (GNFs) 141

4.2.3.4.3. Physical characterization. 142

4.2.4. Synthesis of graphene by confinement of anthracene in between TaS_2 layers. 144

4.2.4.1. Results and discussion 144

4.2.4.1.1. Synthesis of TaS_2@G 144

4.2.4.1.2. X-ray diffraction powder (XRD) 145

4.2.4.1.3. Thermogravimetric analysis (TGA) 146

4.2.4.1.4. Raman Spectroscopy 146

4.2.4.1.5. Morphology Analysis 147

4.2.4.2. Conclusions 149

4.2.4.3. Experimental 150

4.2.4.3.1. General synthesis remarks 150

4.2.4.3.2. Synthesis of TaS_2@G 150

4.2.4.3.3. Physical characterization. 150

4.3. References. 151

..... 155

Chemical Functionalization of Graphene' 155

5.1. Controllable coverage of chemically modified graphene sheets with gold nanoparticles by thermal treatment of graphite oxide with N,N-Dimethylformamide 156

5.1.1. Introduction 156

5.1.2. Results and discussion 157

5.1.2.1. Synthesis 157

5.1.2.2. Evidence on the functionalization with amino groups 157

5.1.2.2.1. FT-IR 157

5.1.2.2.2. Elementary Analysis and Thermogravimetry 158

5.1.2.2.3. Functionalization mechanism 161

5.1.2.3. Anchoring of Gold Nanoparticles 163

5.1.2.3.1. Thermogravimetry 163

5.1.2.3.2. X-Ray Photoelectron Spectroscopy 164
5.1.2.3.3. HR-TEM 167
5.1.3. Conclusions 169
5.1.4. Experimental 169
5.1.4.1. General synthesis remarks 169
5.1.4..2. Synthesis of Au NPs 169
5.1.4.3. Synthesis of GO 170
5.1.4.4. Synthesis of CMG f(T,t) 170
5.1.4.5. Synthesis of CMG f(T,t)@Au 170
5.1.4.6. Physical Characterization 170

5.2 Covalent grafting of organic radicals to graphene. Magnetoresistance properties. 172

5.2.1. Introduction 172
5.2.2. Results and discussion 174
5.2.2.1. Functionalization of graphene with organic radicals 174
5.2.2.1.1. Synthesis 174
5.2.2.1.2. HR-TEM 176
5.2.2.1.3. Thermogravimetric Analysis 177
5.2.2.1.5. Raman spectroscopy 178
5.2.2.1.6. X-Ray Photoelectron Spectroscopy (XPS) 179
5.2.2.1.7. Electron Paramagnetic Resonance (EPR) 181
5.2.2.2. Electrical conductivity and magnetoresistance 182
5.2.3. Conclusions 187
5.2.4. Experimental 188
5.2.4.1. General synthesis remarks 188
5.2.4.2. Synthesis of TEMPO Biradical (1). 188
5.2.4.3. Synthesis of 1-G 189
5.2.4.4. Synthesis 1-G+ 189
5.2.4.5. Synthesis 2-G 189
5.2.4.6. Physical characterizationv 189

5.2. References.....191

Spanish Summary.....**195**

Capítulo 1: Introducción a los nanotubos de carbono.....198

Capítulo 2: Introducción al grafeno.....201

Capítulo 3: Materiales híbridos basados en nanotubos de carbono.....204

Capítulo 4: Síntesis Química de Grafeno.....211

Capítulo 5: Funcionalización Química de Grafeno.....220

ANEX.....**231**

A.1. Transmission Electron Microscopy (TEM).....233

A.2. Infra-red Spectroscopy (FT-IR).....236

A.3. Raman Spectroscopy.....237

A.4. X-ray photoelectron spectroscopy (XPS).....240

Curriculum Vitae.....**243**

Table of Contents

List of Abbreviations

A	Anthracene
AGNRs	Armchair Graphene Nanoribbons
1D	1 Dimension
2D	2 Dimensions
3D	3 Dimensions
A	Absorbance
AFM	Atomic Force Microscopy
BE	Binding Energy
BF-STEM	Bright Field- Scanning Transmission Electron Microscopy
ca.	*Circa* (approximately)
CNT	Carbon Nanotube
CMG	Chemically Modified Graphene
CVD	Chemical Vapor Deposition
DMF	Dimethylformamide
DMSO	Dimethylsulfoxide
DNA	Deoxyribonucleic acid
DTA	Differential Thermal Analysis
DTBP	4,4-ditertbutylbiphenyl
DWNT	Double Walled Nanotube
EDS/EDX/EDAX	Energy Dispersive X-Ray Spectroscopy
et al.	*Et alii* (and the others)
FT-IR	Fourier transformed Infra-Red
G	Graphene
GICs	Graphite Intercalated Compounds
GNFs	Graphene Nanoforms
GNR	Graphene Nanoribbons
GO	Graphite Oxide or Graphene Oxide
HAADF-STEM	High Angle Annular Dark-Scanning Transmission Electron Microscopy

List of Abbreviations

Hdpm	Dipivaloylmethane
HOPG	High Oriented Pyrolitic Graphite
HR-TEM	High Resolution Transmission Electron Microscopy
HT	Hydrothermal
I	Intensity
ITO	Indium Tin Oxide
LbL	Layer by Layer
LCD	Liquid Crystal Display
LPCVD	Low Pressure Chemical Vapor Deposition
MR	Magnetoresistance
MWNT	Multiwalled Carbon Nanotube
Nd-YAG	Neodimium-doped yttrium aluminium garnet
NMP	N-Methyl Pyrrolidone
NP	Nanoparticle
oDCB	Ortho dichlorobencene
PAH	Polyaromatic hydrocarbon
PBI	Perylenebisimide
PdmH	Deprotonated pyridine-2,6-dimethanol
PECVD	Plasma Enhanced Chemical Vapor Deposition
POM	Polyoxometalate
Pyr	Pyrene
QD	Quantum Dot
RBM	Radial Breathing Modes
rGO	reduced Graphite Oxide / reduced Graphene Oxide
SAED	Selected Area Electron Diffraction
SC	Sodium Cholate
SDBS	Sodium Dodecylbenzenesulfonate
SEM	Scanning Electron Microscopy
SMM	Single Molecule Magnet
SQUID	Superconducting Quantum Interference Device
ssDNA	Single Stranded Deoxyribonucleic acid

STEM-XEDS	Scanning Transmission Electron-Microscopy-X-ray Energy Dispersive Spectroscopy
SWNT	Single walled nanotube
TEM	Transmission Electron Microscopy
TG/TGA	Thermogravimetric analysis
UV-vis	Ultra Violet- Visible
vs	*versus*
XPS	X-Ray Photoelectron Spectroscopy
XRD	X-Ray Difraction Powder
ZGNRs	Zigzag graphene nanoribbons

Summary

For a better understanding of this Thesis, we are going to summarize the principal aspects that would be included in the different chapters.

This Thesis deals with the chemistry and development of new hybrid multifunctional systems based on carbon nanotubes (CNTs) and graphene (G). To introduce both types of carbon nanoforms a brief historical overview of these systems has been briefly given at the **Preface**. Next and prior to the presentation of the results, two introductory chapters in which the principal aspects of the synthesis, properties and applications of carbon nanotubes (**chapter 1**) and graphene (**chapter 2)** are given.

The results have been divided in three chapters:

Chapter 3 is related with the development of hybrid materials based on CNTs, and it has been divided in two independent parts. The first part deals with the modification of the walls of the carbon nanotubes (CNTs) to drive their interaction with Mn_4 single molecule magnets (SMMs). The deposition of SMMs along the CNT surface may have implications in molecular magnetism, field in which the organization of magnetic moieties along a conducting wire turns out to be essential. Our approach implies the use of weak electrostatic interactions which contribute to preserve the SMM structure. We will show how the magnetic properties of the attached molecules are significantly affected by the grafting process. In the second part, a hybrid between a photoactive polyoxometalate (POM) and single walled carbon nanotubes (SWNTs) has been developed. In contrast to the first system, in this case the POM has been conveniently modified with pyrene moieties capable to bind to the unmodified walls of the SWNTs. The deposition of photoactive molecules (POM) over CNTs may have important implications in photovoltaics and other electronic devices. Moreover, we will describe the system at the atomic level by the employment of microscopic techniques.

Chapter 4 focuses on the chemical synthesis of graphene (G). This chapter has been divided in two parts. In a first part, G will be obtained from graphite oxide (GO) by a hydrothermal (HT) method. In particular, our work deals with the important role that the pH plays in the reduction of GO under HT conditions. An in-

depth description about the morphologies and characteristic of the prepared material will be given. In a second part, a bottom up approach to synthesize graphite will be described. With this aim, anthracene molecules have been used as starting material. Afterwards, some ideas toward the synthesis of graphitic nanoforms following the previous bottom up approach will be introduced.

Finally, **chapter 5** is devoted to the chemical functionalization of graphene via covalent bonds. In a first part, a general procedure to synthesize chemically modified graphene (CMG) by simple functionalization/reduction of GO under thermal treatment with DMF is described. The as-made CMG will be further decorated with gold nanoparticles (Au NPs). Our approach introduces a degree of control over the coverage of the CMG with Au NPs. We believe that the attained system could be useful for a wide range of applications such as sensing, energy storage, or catalysis. In a second part, a controlled doping of the layers with paramagnetic radicals will be directly synthesized by chemical functionalization of graphite through the Bingel-Hirsch cyclopropanation reaction. Those paramagnetic moieties have shown to influence the magnetoresistance response of the hybrid by the appearance of a low field magnetoresistance effect at low temperatures. This kind of arrangement can have important in sensing applications.

Preface: An Historical Overview

In 1996, Harry Kroto, Robert Curl and Richard Smalley were awarded with the Nobel Prize in chemistry for the discovery of fullerene (C_{60}) **(Figure 1(a))** in the early 1980s.[1] This molecule composed of 60 carbon atoms in a spherical distribution was the first of a series of carbon nanoforms that marked the start of a new era in the context of science 40 years ago. Following this discovery, in 1991 Sumio Iijima published in *Nature* its observations with transmission electron microscopy of some elongated forms of fullerene, which were named as carbon nanotubes (CNTs) (**Figure 1(b)**).[2] As it happened before with C_{60}, CNTs become one of the most investigated systems due to its intriguing physical properties –electronic, mechanical, optical and chemical–, and both, CNT and C_{60}, are still two of the hottest topics of research nowadays.

The last discovery concerning carbon nanoforms was the isolation of single layers of graphene (G) –a one-atom-thick planar sheets of sp^2-bonded C atoms packed in a honeycomb lattice distribution **Figure 1(c)** – in 2004 by Andre Geim and Konstantine Novoselov via the micromechanical exfoliation of graphite,[3] this finding gave rise to the discovery of the undoubtedly most studied system of the last 10 years, and due to its enormous importance, a few years after, in 2010, both of them were awarded with the Nobel Prize in physics by the Royal Swedish Academy of Sciences.

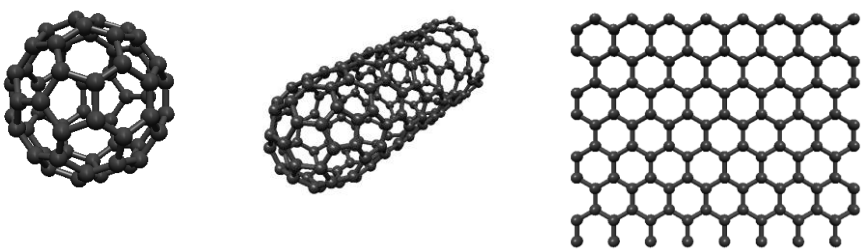

(a) (b) (c)

Figure 1. Molecular model representing a C_{60} fullerene (a), a capped single walled nanotube (b) and a graphene sheet (c).

Although, the work done by Geim and co-workers supposed the boom of G chemistry, it is necessary to mention previous works based on graphite oxide (GO) and graphite intercalation compounds (GICs) to fully give an historical overview about the field.[4] In fact, the first report about GICs can be found in 1840, when Schafhaeutl introduced some small alkali metals in between the layers of graphite.[5] Almost a century later, in 1958, Hummers synthesized for the first time GO by treating graphite in a strong acid medium.[6] Finally, in 1962 Boem *et al.* realized that the reduction of GO with hydrazine lead to a lamellar carbon with small oxygen or hydrogen impurities, that, since the discovery of graphene, it has been known as reduced graphene oxide (rGO), and it has become one of the most widely used methods for the chemical synthesis of G.[7]

---

[1] H.W. Kroto, J.R. Heath, S.C. O'Brien, R.F. Curl, R.E. Smalley, *Nature*, **1985**, *318*, 14.

[2] S. Iijima, *Nature*, **1991**, *354*, 56.

[3] K.S. Novoselov, A.K. Geim, S.V. Morozov, D. Jiang, Y. Zhang, S.V. Dubonos, I.V. Grigorieva, A.A. Firsov, *Science*, **2004**, *306*, 666.

[4] D.R. Dreyer, R.S. Ruoff, C.W. Bielawski, *Angew. Chem. Int. Ed.*, **2010**, *49*, 9336.

[5](a) C. Schafhaeutl, *J. Prakt. Chem.*, **1840**, *21*, 129. (b) C. Schafhaeutl, *Phil. Mag.*, **1840**, *16*, 570.

[6] W.S. Hummers, R.E. Offeman, *J. Am. Chem. Soc.*, **1958**, *80*, 1339.

[7] H.P. Boehm, A. Clauss, G. Fischer, U. Hofmann, *Z. Naturf.*, **1962**, 73.

1 Introduction to Carbon Nanotubes

The discovery of carbon nanotubes (CNTs) represented a hot topic in many fields such as chemistry, physics or materials science due to its remarkable physical properties which includes very high electrical and thermal conductivity, enormous strength, outstanding optical properties, and so on.[1] The huge interest that this tubular material has attracted promoted a rapid growth of the field, and many advances concerning their synthesis, chemical derivatization, solubility and applications can be found day after day in the literature.

1.1. Types of CNTs.

Depending on the number of layers, CNTs can be divided in two types: single walled nanotubes (SWNTs) and multi walled nanotubes (MWNTs). SWNTs are those composed by a unique graphitic layer of around 1 nm of diameter, whereas MWNTs are composed by a superior number of layers disposed in a concentric way, which are separated by a distance of approximately the order of the interlayer distance of graphite (*ca.* 0.34 nm) (**Figure 2**). SWNTs offer quite interesting properties when compared with MWNTs. In particular, they have a tunable band gap that can vary between zero and 2 eV, so they can show even metallic or semiconducting behavior appearing as the most likely candidate for the development of new nanometric electronic devices.[2] Meanwhile, MWNTs are zero-gap metals, although their robustness makes them useful candidates when the functionalization of the walls should be carried out. In fact, the functionalization of SWNTs directly affects their electronic properties as its sp^2 conjugation would appear altered by the introduction of defects. In this direction, it is adequate to consider Double-wall nanotubes (DWNTs) (i.e. those composed by two graphitic layers in a concentric distribution) as a third type of CNT. Their morphology and properties are similar to those of SWNTs but their resistance to chemical treatments is greatly improved because the functionalization would take part just in the outer layer.[3]

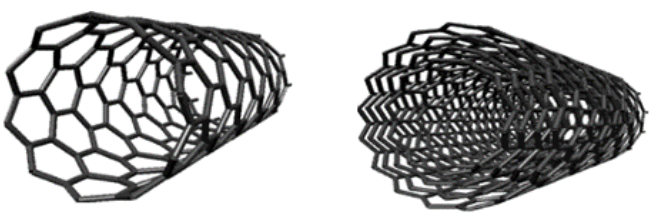

Figure 2. Representation of a SWNT (left) and a MWNT (right).

Another classification that is usually employed for SWNTs depends on how the graphene sheet is folded. Accordingly, the structure of a SWNT is given by the chiral vector, $C_h = na_1 + ma_2$, that connects two cristallographically equivalent sites (A, A') on a graphene sheet (**Figure 3**).[4] In this equation a_1 and a_2 are the unit vectors of the graphene sheet, whereas (n, m) are the integers that define the number of unit vectors along the two directions of the graphene lattice. Once the integers are defined other parameters such as the diameter of the tube or the chiral angle can be determined.[5] According to this definition, three different types of SWNTs can be described. If m = 0 the nanotubes are known as zigzag, on the other hand, it is possible that m has the same value as n appearing the so-called armchair nanotubes. Any other combination of (n, m) factors gives rise to what is known as chiral nanotubes.[4] Some theorical experiments, that has been confirmed afterwards by physical experiments, have demonstrated that when (n – m) is multiple of 3 the nanotubes exhibits a metallic behavior, otherwise they are semiconductors.[6]

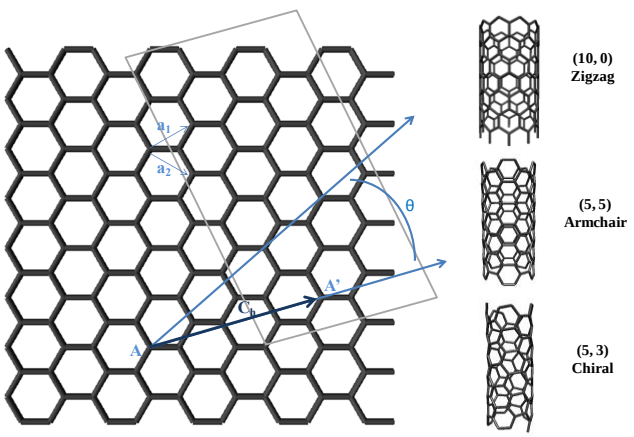

Figure 3. Schematic diagram showing the folding of a graphene sheet to obtain a SWNT.

1.2. Synthesis of CNTs.

The synthesis of CNTs encompasses various methods, and continuously new alternatives are developed. Normally, CNTs are synthesized from precursors (metal catalysts) that serve as seeds for the growing of the tube, needing also high temperatures and sophisticated systems (**Figure 4**).This metal catalysts enable the decomposition of the hydrocarbon (carbon source) to occur at lower temperature than its spontaneous decomposition temperature. The most common metal catalysts employed are Fe, Co, and Ni because of its high solubility with carbon at high temperature, and due the high carbon diffusion rate on them.[7] The generally used methodologies for large scale production of CNTs includes (a) Arc Discharge, (b) Laser ablation, and (c) Chemical Vapor Deposition, although some other procedures can be found in the literature. [8,9]

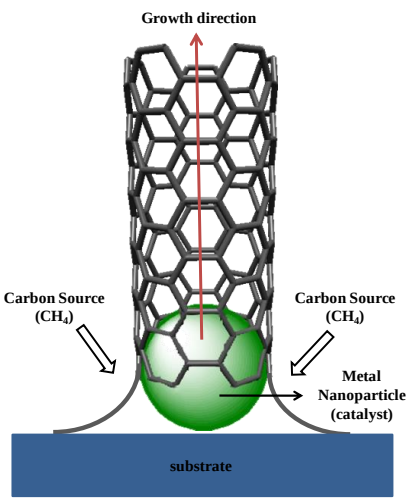

Figure 4. Schematic representation of the growth of a SWNT by the employment of a metal catalyst.

a) Arc Discharge.

The arc discharge method has been used for the production of carbon nanofibers and fullerenes for many years,[10] and it was the method employed by Iijima in 1991 in which CNTs were observed for the first time.[2] The method is based on the arc-vaporization of two graphite rods separated 1 mm from each other by an inert gas at low pressure (**Figure 5**). A high temperature arc discharge is produced between the electrodes by applying a direct current of 50 to 100 A driven by a potential different of 20 V. This procedure reaches the temperature (> 3000 ºC) necessary to vaporize one of the carbon electrodes forming a CNT deposit on the other one.[2] In fact, when the anode is the one that is evaporated, fullerenes can be found in the chamber, and part of the evaporated product is deposited in the cathode in the form of MWNTs.[11] Moreover, employing metallic catalysts (Fe, Co, Ni) in the anode favors the formation of SWNTs.[12] The main drawback of this method is that, although it can be performed in such a way that one of the carbon compounds is favored, the result is always a mixture of SWNTs, MWNTs, metallic catalyst, fullerenes and other carbon nanoforms that should be purified afterwards, what inevitably hampers the process and rises the price of the final product.

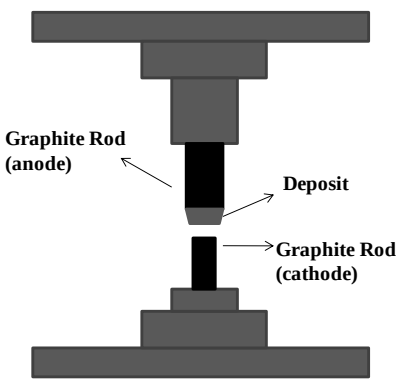

Figure 5. Representation of an arc discharge set-up.

b) Laser Ablation.

Laser ablation is the most advantageous method for the production of SWNTs. Despite it is not suitable for large scale production, it is very useful as the result is high quality SWNTs with high reproducibility and a variety of diameters, which can be obtained by varying some parameters (furnace temperature, catalytic metals and flow rate).[13] It was first developed by Smalley and coworkers in 1996,[14] following similar conditions to those employed for the production of fullerenes in 1992.[15] The technique consists in the vaporization of a graphite target with the help of a laser beam (typically a Nd-YAG or a CO_2 laser) at high temperature (1200ºC). As depicted in **Figure 6** the laser furnace is composed by a furnace, a quartz tube with a window in which the carbon target containing metal catalysts is placed, a laser beam that is focusing to the carbon target and a water-cooled trap. Inside the chamber a flow of inert gas (Ar or He) is applied. The laser induces the vaporization of the carbon target at high temperature, and the vaporized SWNTs are transported by the inert gas to the water-cooled trap where they are finally collected.[17]

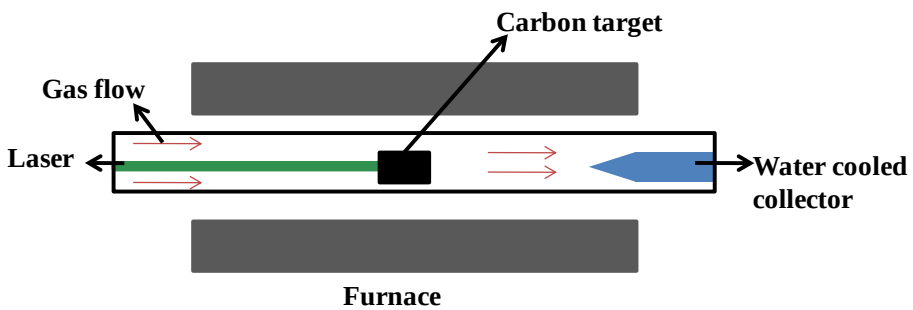

Figure 6. Schematic representation of a laser ablation apparatus.

c) Chemical Vapor Deposition (CVD).

Chemical Vapor deposition is a process in which chemical precursors are transported in the vapor phase to decompose on a heated substrate to form a film. In the case of CNTs, the substrate, normally quartz, is prepared with a layer of catalyst metal nanoparticles (iron, copper, nickel, or a combination of different metals) that would serve as seeds for the CNT growth (**Figure 4**, page 32). Afterwards a carbon-containing gas (acetylene, ethylene, ethanol or methane) is introduced in the reactor chamber. Due to the high temperature inside the reactor those gases decompose and the CNT grows at the sites of the metal nanoparticles.[16] In addition, the size of the metal nanoparticles used as catalysts appears as a crucial factor for the diameter size and nanotube type obtained in the CVD process. In fact, it has been demonstrated that, in general, nanoparticles of few nanometers favors the formation of SWNTs, while, those of greater size (tens of nanometers) results in the formation of MWNTs. In the same direction, the temperature of the reactor chamber also seems to affect the final product as it has been described that low temperatures (600-900 ºC) result in the formation of MWNTs, whereas higher temperatures lead to the formation of SWNTs.[14]

The two main CVD techniques are the Low Pressure CVD (LPCVD; **Figure 7(a)**), and the Plasma Enhanced CVD (PECVD; **Figure 7(b)**). Both of them are based on the CVD principles, but while LPCVD employs very high temperatures (higher than 600 ºC) for the decomposition of the precursors, PECVD can operate at lower temperatures (below 300ºC) due to the extra energy that is supplied by the plasma. The reduced deposition temperature is one of the numerous advantages that PECVD offers against LPCVD. Moreover, the low pressures needed to maintain the plasma promotes greater film uniformity, and the strong electric field employed for the generation of the plasma favors the alignment of the nanotubes so, vertically aligned CNTs can be grown by this method.[17] Meanwhile, LPCVD has the main advantage that, unlike PECVD, CNTs can be deposited on both sides of the substrates hence increasing the productivity with the consequent reduction of costs.

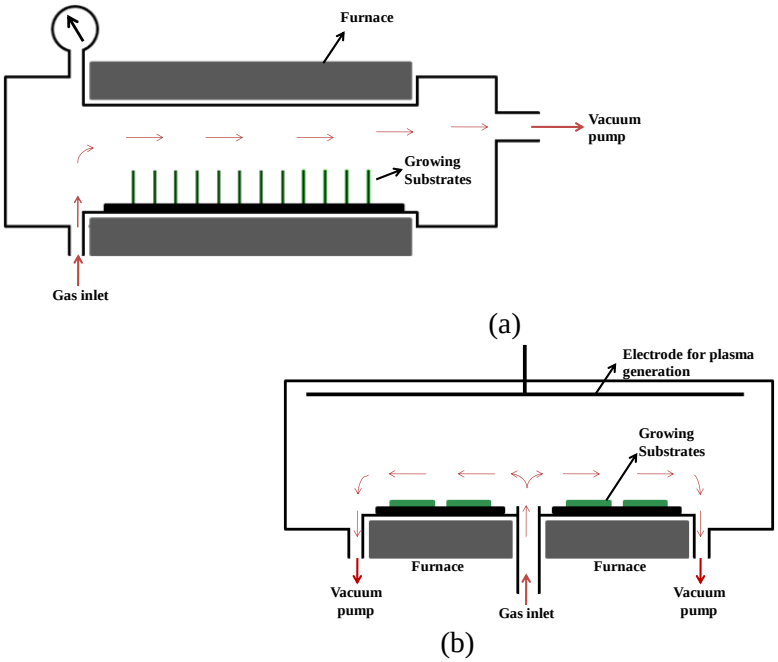

Figure 7. Schematic representation of an LPCVD (a) and a PECVD (b) reactor.

Compared with the arc discharge and the laser ablation techniques, CVD is the most versatile way of synthesizing CNTs. The low temperatures required, its performance carried out at ambient pressure, and the possibility of employing various substrates at once, make of this technique the most suitable for the production of CNTs.

1.3. Purification of CNTs.

The growth mechanism that CNT follows during its production involves the encapsulation of the catalyst inside their cavity (**Figure 4**, page 32), so those metallic catalysts become impurities as they persist once the CNTs are obtained. Moreover, in the final soot, along with the CNTs and the metallic catalysts, some undesired amorphous carbon also coexists, so a purification step is needed in order to get rid of the impurities.

The most common purification method implies the treatment of the carbon soot with acids, typically nitric acid or a mixture HNO_3/H_2SO_4, in order to dissolve the metallic nanoparticles. This acidic treatment partially oxidizes the wall of the

nanotubes introducing some oxygen functionalities on it, and totally oxidizes the amorphous carbon removing it from the final product. [18] Moreover, the length of the tubes is also affected, so shorter tubes are obtained.[19] It is important to control the temperature and the acid concentration of the process as in many cases an over functionalization of the tubes is not desired because it would affect their physical properties. In a non-very oxidative medium the oxidation would take place preferably over the caps of the tubes as due to its curvature the rigid sp^2 carbons placed there are the most reactive sites. This would lead to the dissolution of the metal catalyst without affecting to the physical properties of the CNTs and would leave the end or the CNTs opened.[20]

1.4. Functionalization of CNTs.

The chemical functionalization of CNTs has been one of the most studied topics since the beginning of the carbon nanoforms era as through it some challenges, such as the solubilization of the tubes, could be overcome. Furthermore, the chemical functionalization of the tubes permits the introduction of new features and functionalities on CNTs, thus increasing the *per se* interesting properties and opening the door for their tuning by chemical derivatization.

Taking into account the morphology of the CNTs three possibilities can be considered: (a) The non-covalent functionalization of the CNTs through π-π stacking, (b) the covalent derivatization of their wall, and (c) the endohedral functionalization of the CNT's cavity.

a) Non-Covalent functionalization.

Non-covalent functionalization appears as a very attractive method for the derivatization of CNTs as it offers the possibility of attaching chemical species without affecting the electronic structure of the tubes. The non-covalent interactions are based either on van der Waals forces or π-π stacking. Moreover, it is also possible to introduce some charged moieties along the tubes (doping of the tubes) thus permitting the electrostatic interaction between the tubes and a charged specie of opposite sign.

This kind of functionalization has been widely used towards the solubilization of the nanotubes. In this direction many polymer composites has been obtained. For example, CNTs have been dissolved in aqueous and alcoholic medium by wrapping it with poly(vinylpirrolidine).[21] With the same aim some fluoropolymers such as Nafion or Teflon have been used.[22] Poly(vinyl alcohol) is another interesting polymer for CNT-polymer composites as it increases the stiffness of the tubes upon with its dissolution.[23] In the same direction, CNT-poly(ethylene glycol) composites present an enhanced mechanical resistance due to the hydrogen bond interaction between the oxygen moieties of the polymer chain and the defects of the tube.[24] Those are some examples of a very long family of CNT-polymer composites that can be found in the literature.[25] As it has been just exemplified, in addition to the enhancement of the solubility, nanotube-polymer composites show superior mechanical properties, which make of them outstanding candidates, for example, in aerospace applications where lightweight robust materials are needed. In a related way, it has been described that some proteins, as well as DNA molecules or other kinds of biomolecules can be adsorbed strongly on the wall of the nanotubes what could be employed for creating biosensors, for gene delivery or for many other medical applications.[26]

π-π interactions is another way of chemically modified CNTs as it has been reported that some aromatic systems can interact very strongly with the wall of the nanotubes by π-π stacking. This approach is quite interesting as no alteration of the tubes is done, and it opens the way to the combination of CNTs with a wide range of molecules by modifying some side substituents in order to bind them to the tubes. In this direction pyrene moieties have been commonly employed. For example, Prato *et al.* have described a hybrid SWNT@Fullerene-pyrene (**Figure 8(a)**), by employing this approximation, which may have potential applications in photovoltaics and molecular electronics.[27] Another interesting example of such important association framed in the field of optoelectronic devices was described by Guldi *et al.* which

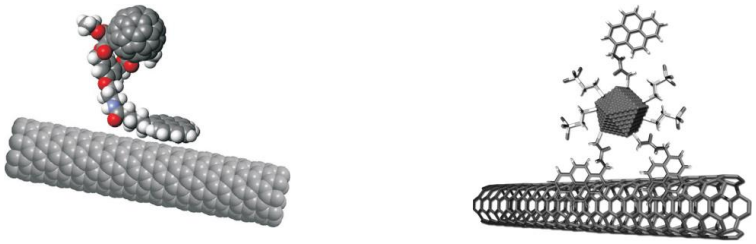

(a) (b)

Figure 8. Representation of the π-π interaction in the hybrid SWNT@Fullerene-pyrene extracted from reference [27] (a), and in the hybrid SWNT@CdTe QD extracted from reference [28] (b).

were able to functionalized CdTe quantum dots (QDs) with a pyrenyl substituent in order to obtain a hybrid with SWNTs (**Figure 8(b)**).[28] This last system showed prospective applications towards the development of donor-acceptor inorganic-organic nanohybrids oriented to solar cells technology. Besides, some SMMs have been anchored to the sidewalls of the nanotubes through this methodology. For example, Ruben and co-workers have been able to bind rare-earth-based SMMs over the nanotubes wall taking advantage of this well-known π-π affinity.[29] In a similar manner, Bogani *et al*. have obtained the hybrid CNT@[$Fe_4L_2(dpm)_6$] SMM (Hdpm = dipivaloylmethane) where the ligand L bears a pyrenyl moiety.[30] These hybrid systems are particularly interesting in molecular spintronics, where the organization of a number of nanomagnets over an electronic nanodevice is vital.

b) Covalent functionalization.

The introduction of covalently linked groups over the wall of CNTs produces a disruption of the sp^2 conjugation of the tubes altering its electronic properties. Those new functionalities can be seen as defects, but although they tend to diminish the conducting properties of the tubes they open many new opportunities toward its dissolution and toward the implementation of new functionalities. The most simple covalent functionalization method comes from the purification procedure, as it has been previously explained, the treatment with strong acids introduces oxygen moieties (carboxylic and hydroxyl groups), which can be further employed as reactive sites either for producing an electrostatic interaction with other charged molecules or to further functionalization of the tubes, for example, by the subsequent creation of amides.[25] Moreover, those oxygenated groups increase the

solubility of CNTs in aqueous media favoring its processability for many applications.

Besides the functionalization in acidic media, many chemical reactions have been reported to be effective for the derivatization of CNTs, and the covalent attachment of different molecules appears as an active field in CNTs chemistry. Upon the large quantity of chemical procedures described, the 1,3-Dipolar Cycloaddition of azomethine ylides (*Prato reaction*) and the treatment of CNTs with aryldiazonium salts are probably the most employed ones. The *Prato reaction* was first described by Prato *et al.* for the functionalization of fullerene and afterwards it has been extended to CNTs.[31] It takes place between an α-aminoacid and an aldehyde with the CNT's wall (**Scheme 1**), thus permitting the introduction of two different functionalities (R_1, R_2), being possible, for example, the employment of one of those tunable positions to introduce an active site while the other one can be used to add a solubilizing moiety. Meanwhile, the functionalization with diazonium salts can be done either by the reaction between a diazonium salt (prepared in a previous step) and a CNT, or by the *in situ* generation of the desired diazonium compound in the presence of isoamyl nitrite (**Scheme 2**).[32] In both cases, the mechanism involves the reduction of the diazonium salt to generate an active radical that is covalently attached to the carbon surface.[33] Unlike *Prato* reaction, this second procedure permits the introduction of a single functionality (R_3), but it is less time consuming and in many cases most accessible as diazonium salts can be obtained easily from amines.[34]

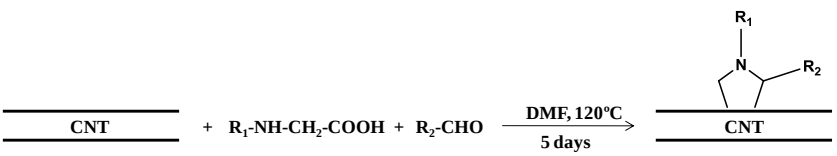

Scheme 1. Synthesis conditions for the Prato reaction.

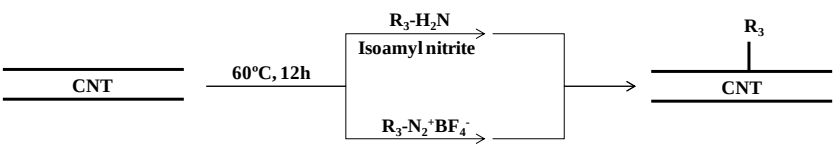

Scheme 2. Synthesis conditions for the diazonium derivatization of CNTs.

Both, Prato reaction and the aryldiazonium derivatization of CNTs have been extensively used, but, among the broad spectrum of substituents that can be introduced via those approaches, the use of acetylene groups is probably the most employed one. This functionality is particularly interesting because it opens the way to further functionalization of the tubes via the use of the well-known *click-chemistry*. The concept "*click-chemistry*" refers to an easy chemistry tailored to bind small molecules together by a simple pathway which involves simple work-up and purification procedures.[35] Normally, in the field of carbon nanoforms the concept of click-chemistry is closely associated to the Huisgen 1,3-dipolar cycloaddition (*Click reaction)* between an azide and an acetylene derivative in the presence of Cu(I) catalyst (**Scheme 3**). The mentioned cycloaddition has been used for example by Campidelli *et al.* to decorate SWNTs with phthalocyanines in order to construct interesting devices oriented to photovoltaics,[36] or by Zheng *et al.* which employed it for the chemical modification of SWNTs with β-cyclodextrin thus creating a useful hybrid oriented to drug delivery.[37] Another interesting approach was carried out by Rao *et al.* who were able to attach covalently gold nanoparticles to the CNT surface, or Gao *et al.* which succeeded in the functionalization with Fe_2O_3 nanoparitcles.[38] The importance of these latter systems arouses from the potential applications of CNTs-metal based nanoparticles hybrid materials in the field of electronics, catalysis and optical or magnetic applications.

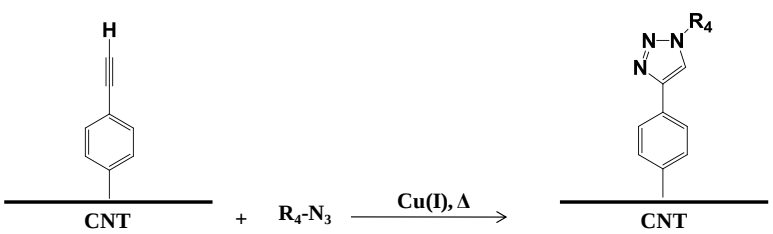

Scheme 3. Schematic representation of the Huisgen 1,3-dipolar cycloaddition (Click reaction) over a CNT.

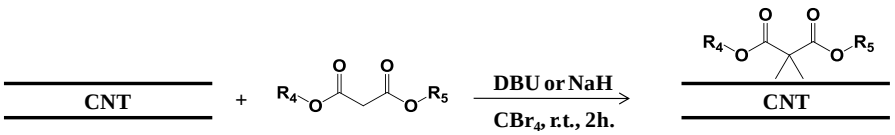

Scheme 4. Bingel reaction conditions for the in situ formation of a bromomalonate derivative.

Finally, the nucleophilic addition of carbenes, or the Bigel-Hirsch cyclopropanation reaction, which takes place between a bromomalonate (that can be generated *in situ*) and the wall of the CNT in the presence of a base (NaH or DBU) (**Scheme 4**), are other interesting examples of the great assortment of covalent reactions that can be followed to chemically functionalize CNTs.[25]

c) Endohedral functionalization of CNTs.

Filling CNTs with foreign elements or compounds can lead to the modification of the properties of both, CNTs and the encapsulated species. For example, leading electrodonor-compounds into the nanotube's channel would increase the carrier density of the CNT thus increasing its conductivity.[39] Besides, the endohedral functionalization of CNTs has also been employed to drive the growing of nanometric 1D chains of many different elements or compounds. This nanometric confinement is of outmost relevance as it would give rise to novel and unexplored physical properties.[40] In this context many examples such as the formation of nanochains of KI, the encapsulation of metal nanoparticles (Ag, Au, Pd, Pt) or the formation of atomic metal nanowires (Mo, Eu, Gd) can be found.[41] In some cases the filled-CNT is considered as a whole new system, while in many others it is just used as a nano-mold for the formation of nanometric 1D-chains and it is removed after the formation of the chains. Another important application comes from the encapsulation of drugs or biomolecules inside CNTs. In those cases, CNTs would act as carriers taking the biomolecules to the specific place where they should arrive or even be delivered, while they would prevent direct contact of the drug with the blood flow. In this direction some toxic metals such as Gd which is used for enhanced contrast in MRI applications, or some platinum anticancer drugs have been introduced by employing CNTs.[42] To end, a very interesting application comes from the encapsulation of Mn_4 SMMs inside the cavity of MWNTs.[43] In this case, the

CNT serve to bind the nanometric magnets with the macroscopic world and the result is a hybrid which possesses the unique electronic properties of CNTs and interesting magnetic characteristics of SMMs.

To successfully fill CNTs, a previous oxidation step to open its caps is required. With this aim, even the treatment with strong acids (HNO_3, H_2SO_4),[18] or the employment of milder conditions such as ozonolysis or the oxidation of the tubes by steam at high temperature, have been employed.[44] Once the caps have been removed, CNTs are disposed to be filled. To afford this latter objective either a gas phase diffusion procedure or a liquid phase capillarity method can be followed. In the first approximation, gas molecules are passed and absorbed inside the carbon nanotubes (CO_2, NO, SF_6).[45] In the second methodology just those compounds with surface tensions between 130-170 mN/m and low melting point would be able to fill the cavity; otherwise, a two-step procedure, in which a low melting point precursor (*i.e.* metal halides) is introduced, would be necessary in order to fruitfully fill the inner cavity of the tube (*molten media method*). Following the *molten media method* many confined systems such as CdS, CdSe, ZnTe, PbS and so on has been obtained (**Figure 9**).[39]

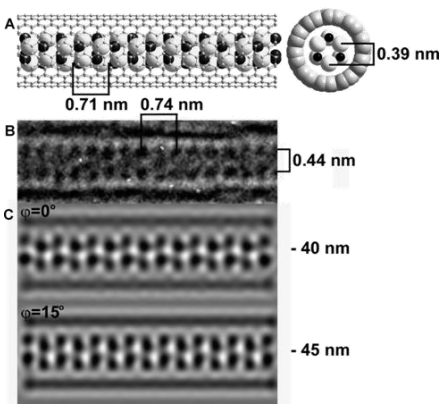

Figure 9. A) structural model of CdS 1D-crystal inside a SWNT channel, B) HR-TEM image of the CdS@SWNT and C) Simulated images for the proposed model. Extracted from reference [39].

1.5. Properties and applications

Many different applications can be imagined taking into account the unique physical properties of CNTs. On one hand, they offer extraordinary electronic properties varying between semiconducting and metallic behavior. In this direction, semiconductor SWNTs would be useful, for example, as field-effect transistors (FET), while metallic CNTs would be useful, for example, for the fabrication of electrodes oriented to electrocatalysis.[46] A very appealing example of a CNT FET device was recently reported by Mallah *et al.*.[47] In this work a binuclear paramagnetic Cu_2 complex was attached to SWNTs through π-π interactions, and they demonstrates that the grafting process leads to a tuning of the CNT-FET device properties due to the charge transfer between the complex and the nanotube.

Moreover, they present a very high mechanical resistance, which makes them suitable for the formation of high resistive fibers for several applications.[1] In addition, their high surface area together with their transparency open the way for the creation of transparent electrodes, which may be an alternative of those based on rare earth metals that have been traditionally employed with the same purpose. In this direction, CNTs have been used for the fabrication of organic solar cells or organic light-emitting diodes.[48] For example Martin *et al.* succeed in synthesizing a hybrid between a tetrathiafulvalene and CNTs,[49] or Guldi *et al.* which synthesize a hybrid SWNT-phtalocyanine.[50] Both systems showed effective electron transfer between the CNT and the attached moiety and offer promising potentiality in photovoltaics.

Finally, when considering their chemical versatility in addition to their unique physical properties, many new prospective systems can be envisioned which would give rise to uncountable different applications such as catalysis,[38] biomedicine,[26,37] solar cells,[27,28,36] and so on.

1.6. References

[1] J.M. Schnorr, T.M. Swanger, *Chem. Mater.*, **2011**, *23*, 646.

[2] H. Dai, *Acc. Chem. Res.*, **2002**, *35*, 1035.

[3] K.E. Moore, B.S. Flavel, A.V. Ellis, J.P. Shapter, *Carbon*, **2011**, *49*, 2639.

[4] J.-C. Charlier, *Acc. Chem. Res.*, **2002**, *35*, 1063.

[5] M. Ouyang, J.L. Huang, C.M. Lieber, *Acc. Chem. Res.*, **2002**, *35*, 1018.

[6] (a) J.W.G. Wildöer, L.C. Venema, A.G. Rinzler, R.E. Smalley, C. Dekker, *Nature*, **1998**, *391*, 59. (b) T.W. Odom, J.-L. Huang, P. Kim, C.M. Lieber, *Nature*, **1998**, *391*, 62.

[7] M. Kumar, Y. Ando, *Journal of nanoscience and nanotechnology*, **2010**, *10*, 3739.

[8] M. Quintana, M. Grzelczak, K. Spyrou, M. Calvaresi, S. Bals, B. Kooi, G. Van Tendeloo, P. Rudolf, F. Zerbetto, M. Prato, *J. Am. Chem. Soc.*, **2012**, *134*, 13310.

[9] C. Bosch-Navarro, E. Coronado, C. Marti-Gastaldo, J.F. Sanchez-Royo, M. Gomez-Gomez, *Nanoscale*, **2012**, *4*, 3977.

[10] W. Krätschmer, L.D. Lamb, K. Fostiropoulos, Huffman, *Nature*, **1990**, *347*, 354.

[11] Y. Saito, M. Inagaki, H. Shinohara, *Chem. Phys. Lett.*, **1992**, *200*, 643.

[12] S. Iijima, T. Ichihashi, *Nature*, **1993**, *363*, 603.

[13] C.D. Scott, S. Arapalli, P. NiKolaev, R.E. Smalley, *Appl. Phys. A*, **2001**, *72*, 573.

[14] A. Thess, R. Lee, P. Nikolaev, H. Dai, P. Petit, J. Robert, C. Xu, Y.H. Lee, S.G. Kim, A.G. Rinzler, D.T. Colbert, G.E. Scuseria, D. Tomalnek, J.E. Fischer, R.E. Smalley, *Science*, **1996**, *273*, 483.

[15] Guo, T., Diener, M.D., Chai, Y., Alford, M.J., Haufler, R.E., McClure, S.M., Ohno, T., Weaver, J.H., Scuseria, G.E., Smalley, R.E., *Science*, 1992, *257*, 1661.

[16] N.M. Rodriguez, A. Chambers, C. Bielawski, R.T.K. Baker, *Langmuir*, **1995**, *11*, 3862.

[17] Z.F. Ren, Z.P. Huang, J.W. Xu, J.H. Wang, P. Bush, M.P. Siegal, P.N. Provencio, , *Science*, **1998**, *282*, 1105.

[18] K.A. Worsley, I. Kalinina, E. Bekyarova, R.C. Haddon, *J. Am. Chem. Soc.*, **2009**, *131*, 18153.

[19] B.K.Price, J.R. Lomeda, J.M. Tour, *Chem. Mater.*, **2009**, *21*, 3917.

[20] M.A. Hamon, J. chen, H. Hu, Y. Chen, M.E. Itkis, A.M. Rao, P.C. Eklund, R.C. Haddon, *Adv. Mater.*, **1999**, *11*, 834.

[21] a) M.J. O'Connell, P. Boul, L.M. Ericson, C. Huffman, Y.H. Wang, E. Haroz, C. Kuper, J.M. Tour, K.D. Ausman, R.E. Smalley, *Chem. Phys. Lett.*, **2001**, *342*, 265. b) J.H. Rouse, *Langmuir*, **2005**, *21*, 1055.

[22] a) B.J. Landi, R.P. Raffaelle, M.J. Heben, J.L. Alleman, W. VanDerveer, T. Gennett,, *Nano Lett.*, **2002**, *2*, 1329. b) J. Wang, M. Musameh, *Anal. Chem.*, **2003**, *75*, 2075.

[23] a) M.S.P. Shaffer, A.H. Windle, *Adv. Mater.*, **1999**, *11*, 937. b) X. Zhang, T. Liu, T.V. Sreekumar, S. Kumar, V.C. Moore, R.H. Hauge, R.E. Smalley, *Nano Lett.*, **2003**, *3*, 1285.

[24] H.W. Goh, S.H. Goh, G.Q. Xu, K.P. Pramoda, W.D. Zhang, *Chem. Phys. Lett.*, **2003**, *379*, 236.

[25] D. Tasis, N. Tagmatarchis, A. Bianco, M. Prato, *Chem. Rev.*, **2006**, *106*, 1105.

[26] a) Z. Guo, P.J. sadler, S.C. Tsang, *Adv. Mater.*, **1998**, *10*, 701. b) B.J. Taft, A.D. Lazareck, G.D. Withey, A. Yin, J.M. Xu, S.O. Kelley, *J. Am. Chem. Soc.*, **2004**, *126*, 12750. c) S.-H. Baek, B. Kim, K.-D. Suh, *Colloids and Surfaces A: Physicochem. Eng. Aspects*, **2008**, *316*, 292.

[27] D.M. Guldi, E. Menna, M. Maggini, M. Marcaccio, S. Paolucci, F. Paolucci, S. Campidelli, M. Prato, G.M. Aminur Rahman, S. Schergna, *Chem. Eur. J.*, **2006**, *12*, 3975.

[28] C. Schulz-Drost, V. Sgobba, C. Gerhards, S. Leubner, R.M. Krick Calderon, A. Ruland, D.M. Guldi, D.M., *Angew. Int. Ed.*, **2010**, *49*, 6425.

[29] S. Hyatskaya, J.R. Galán-Mascarós, L. Bogani, F. Hennrich, M. Kappes, W. Wernsdorfer, M. Ruben, *J. Am. Chem. Soc.*, **2009**, *131*, 15143.

[30] L. Bogani, C. Danieli, E. Biavardi, N. Bendiab, A.-L. Barra, E. Dalcanale, W. Wernsdorfer, A. Cornia, *Angew. Chem. Int. Ed.*, **2009**, *48*, 746.

[31] M. Maggini, G. Scorrano, M. Prato, *J. Am. Chem. Soc.*, **1993**, *115*, 9798.

[32] a) J.L. bahr, J.M. Tour, *Chem. Mater.*, **2001**, *13*, 3823-3824. b) S.M. Chergui, A. Ledebt, F. Mammeri, F. Herbst, B. Carbonnier, H.B. Romdhane, M. Delamar, M.M. Chehimi, *Langmuir*, **2010**, *26*, 16115.

[33] J.L. Bahr, J. Yang, D.V. Kosynkin, M.J. Bronikowski, R.E. Smalley, J.M. Tour, *J. Am. Chem. Soc.*, **2001**, *123*, 6536.

[34] a) M.S. Strano, C.A. Dyke, M.L. Usrey, P.W. Barone, M.J. Allen, H.C. Shan, C. Kittrell, R.H. Hauge, J.M. Tour, R.E: Smalley, *Science*, **2003**, *301*, 1519. b) G. Maas, *Angew. Chem. Int. Ed.*, **2009**, *48*, 8186.

[35] H.C. Kolb, M.G. Finn, K.B. Sharpless, *Angew. Chem. Int. Ed.*, **2001**, *40*, 2004.

[36] S. Campidelli, B. Ballesteros, A. Filoramo, D.D. Díaz, G. de la Torre, T. Torres, G.M. Aminur Rahman, C. Ehli, D. Kiessling, F. Werner, V. Sgobba, D.M. Guldi, C. Cioffi, M. Prato, J.-P. Bourgoin, *J. Am. Chem. Soc.*, **2008**, *130*, 11503.

[37] Z. Guo, L. Liang, J.J. Liang, Y.F. Ma, X.Y. Yang, D.M. Ren, Y.S. Chen, J.Y. Zheng, *J. Nanopart. Res.*, **2008**, *10*, 1077.

[38] a) R. Voggu, P. Suguna, S. Chandrasekaran, C.N.R. Rao, *Chem. Phys. Lett.*, **2007**, *443*, 118. b) H. He., Y. Zhang, C. Gao, J. Wu, *Chem. Comm.*, **2009**, 1655.

[39] A.A. Eliseev, M.V. Chernysheva, N.I. Verbitskii, E.A. Kiseleva, A.V. Lukashin, Y.D. Tretyakov, N.A. Kiselev, R.M. Zhigalina, R.M. Zakalyukin, A.L. Vasiliev, A.V. Krestinin, J.L. Hutchison, B. Freitag, *Chem. Mater.*, **2009**, *21*, 5001.

[40] M. Monthioux, *Carbon*, **2002**, *40*, 1809.

[41] a) J. Sloan, M.C. Novotny, S.R. Bailey, G. Brown, C. Xu, V.C. Williams, S. Friedrichs, E. Flahaut, R.L. Callender, A.P.E. York, K.S., Coleman, M.L.H. Green, R.E. Dunin-Borkowski, R.L. Hutchison, *Chem. Phys. Lett.*, **2000**, 329, 61. b) R. Kitaura, R. Nakanishi, T. Saito, H. Yoshikawa, K. Awaga, H. Shinohara, *Angew. Chem. Int. Ed.*, **2009**, *48*, 8298. c) H. Muramatsu, T. Hayashi, T.A. Kim, D. Shimamoto, M. Endo, M. Terrones, M.S. Dresselhaus, *Nano Lett.*, **2008**, *8*, 237.

[42] V.V: Mody, M.I. Nounou, M. Bikram, *Advanced Drug Delivery Reviews*, **2009**, *61*, 795.

[43] M.C. Gimenez-Lopez, F. Moro, A. La Torre, C.J. Gomez-Garcia, P.D. Brown, J. van Slageren, A.N. Khlobystov, *Nat. Commun.*, **2011**, *2*, 407.

[44] a) T. Hemraj-Benny, T.J. Bandosz, S.W. Stanislaus, *Journal of Colloid and Interface Science*, **2008**, *317*, 375. b) G. Tobias, L. Shao, C.G. Salzmann, Y. Huh, M.L.H. Green, *J. Phys. Chem. B.*, **2006**, *110*, 22318.

[45] C. Matranga, B. Bockrath, *J. Phys. Chem. B.*, **2005**, *109*, 9209.

[46] P. Avouris, *Acc. Chem. Res.*, **2002**, *35*, 1026.

[47] G. Magadur, J.-S. Lauret, G. Charron, F. Bounais, E. Norman, V. Huc, C.-S. Cojocaru, S. Gomez-Coca, E. Ruiz, T. Mallah, *J. Am. Chem. Soc.*, **2012**, *134*, 7896.

[48] a) V. Sadhu, N.A. Nismy, A.A.D.T. Adikaari, S.J. Henley, M. Shkunov, S.R.P. Silva, *Nanotechnology*, **2011**, *22*, 265607. b) D.S. Hecht, L. Hu, G. Irvin, G., *Adv. Mater.*, **2011**, *23*, 1482.

[49] C. Romero-Nieto, R. Garcia, M.A. Herranz, C. Ehli, M. Ruppert, A. Hirsch, D.M. Guldi, N. Martin, *J.Am. Chem. Soc.*, **2012**, *134*, 9183.

[50] J. Bartelmess, C. Ehli, J.-J. Cid, M. Garcia-Iglesias, P. Vazquez, T. Torres, D.M. Guldi, *Chem. Sci.*, **2011**, *4*, 652.

2 Introduction to Graphene

Graphene (G) was the latest carbon nanoform found, and since its discovery it has been considered as the parent of all the rest of graphitic forms (**Figure 10**).[1] CNTs or fullerenes can be built up by folding a G sheet in the correct way, but despite their similarities, their physical properties differ considerably from each other. G has many extraordinary electrical, thermal or mechanical properties such as ballistic electron conductivity, superior thermal conductivity, tunable band gap, high elasticity, and so on.[2] Those unique characteristics have made of G one of the most attractive materials in many research fields.[3] On the other hand, the obvious similarities between G and CNTs have promoted a rapid growth of the field, and many important advances appear continuously since it was first isolated just 10 years ago.

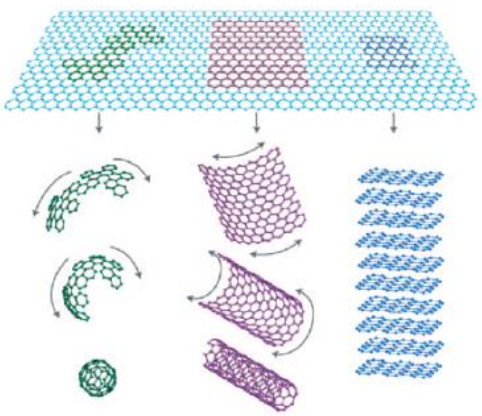

Figure 10. Graphene, the parent of all the graphitic forms. (Reproduced from reference [1])

2.1. Classification and Properties of Graphene.

Although the most general definition of graphene (*i.e.* a single layer of sp^2 hybridized C-C atoms in a hexagonal distribution) does not admit a broader classification of it in subgroups, the common employment of some specific derivatives of G (*i.e.* GO or G nanoribbons) without distinction should be taken into consideration, and it seems appropriate to introduce the main differences that can be found between them.

a) Graphene (G).

Graphene is a two dimensional monolayer of hybridized sp^2 carbon atoms in a honeycomb lattice distribution that possess an unhybridized half-filled *p* orbital perpendicular to the graphene plane which enables electron conductivity parallel to the graphene lattice having a remarkably high electron mobility at room temperature (15000 $cm^2\ V^{-1}\ s^{-1}$).[1] Due to symmetry reasons, G is a semimetal or a zero-gap semiconductor.[4] Undoubtedly, the electronic properties of G have attracted scientific interest for many reasons, although the lack of a band-gap limits its use for sensing or transistor applications as big resistivity changes are needed for these purposes.

Perhaps one of the most promising applications of G comes from its optical transparency, in addition to its conductivity. Traditionally, in electronic devices Indium Tin Oxide (ITO) has been employed as standard electrode due to its transparency (optical transmission around 82-85%) and conductivity, but its high instability and elevated cost claims for the search of new materials capable of replacing it. Meanwhile, G is chemically stable, cheap and easy accessible, and show on enhanced optical transparency (optical transmission around 98%). Thus, it can be a promising substitute of ITO in future electronic devices. In fact, it has just been published the first solar cell made up totally of carbon.[5] In this work, Bao *et al*. have been able to substitute all the expensive metallic components of a conventional solar cell (ITO, silver electrodes) by graphene, carbon nanotubes and fullerenes. Although this "all carbon solar cell" shows a very low efficiency when compared with conventional solar cells, it would pave the way for future photovoltaic devices. Besides, it is possible to find a never-ending quantity of works in which it is

demonstrated that G is adequate for the fabrication of optoelectronic devices.[6] For example, Geim *et al.* have demonstrated the advantages of employing G instead of ITO for transparent electrodes in liquid crystal displays (LCDs).[7] Another interesting example was reported by Müllen *et al*,. who succeed in the fabrication of dye-sensitized solar cells with high transparency and stability.[8]

Another important characteristic of G is its tremendous high strength, which is known to be 200 times higher than that of steel, having a tensile strength of 130 GPa.[9] Moreover, its lightness, flexibility and sustainability turn G as a promising material for future car or airplane development.

Finally, due to the small spin-orbit interaction in graphene, and the absence of spin moments in carbon, G is thought to be an ideal material for spintronics, as it can transport the spin over long distances. Thus, several studies similar to those previously described for CNTs (**Chapter 1**) have been developed with G.[10]

b) Graphite Oxide (GO) and reduced Graphite Oxide (rGO).

GO is one of the most employed precursors for obtaining graphene. It is synthesized directly from graphite by harsh oxidation (Hummers method, see section 2.2., page 54). During the process the sp^2 structure of graphite is disrupted, so GO is an insulator. In order to restore the electronic properties of G it is necessary its subsequent reduction to obtain reduced graphite oxide (rGO). Usually, rGO and G are treated as equals, but, as a total restoration of the structural properties of G upon reduction is never fully accomplished, this equality should be treated carefully, as for example, the presence of some defects would lead to a semiconducting behavior in rGO. Still, rGO possesses some advantages with respect G. For example, it is easier to functionalize or to exfoliate into single layers and it is possible to play with its conducting or optical properties by controlling the degree of reduction. So, despite these differences, GO it is usually employed with the same purposes than G.[14a] Very importantly, unlike G –which possesses a zero band gap– the presence of defects in rGO provokes the appearance of a band gap –which according to theorical calculations can range from a few tenths to 4 eV, depending on the reduction degree– that allows the use of rGO for sensing or transistors applications in which big resistivity changes are needed.[11]

c) Graphene Nanoribbons (GNRs).

GNRs can be defined as the quasi-one-dimensional counterpart of graphene having a few nanometers in width. It is particularly interesting because due to its finite size, their properties can be controlled by its two possible edges geometries, zigzag GNRs (ZGNRs) or armchair GNRs (AGNRs) (**Figure 11**), so, as happened with CNTs, GNRs can be either metallic or semiconducting, allowing it use for sensing or transistors applications were G was not suitable.[12]

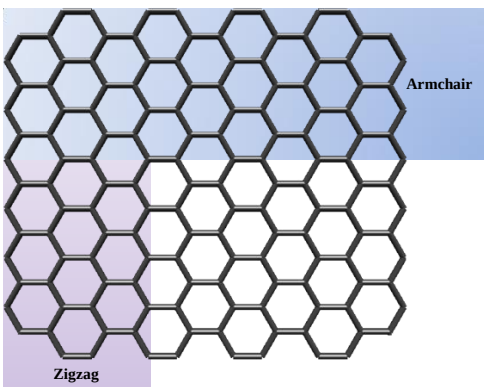

Figure 11. Representation of cutting a graphene sheet to obtain ZGNRs (purple) and AGNRs (blue).

2.2. Synthesis of Graphene.

Since the isolation of graphene in 2004,[3] one of the main focus of interest has been the synthesis of such a novel material. In this vein, both, physical - CVD and the micromechanical exfoliation of graphite-[13] and chemical methods- Liquid phase exfoliation of graphite and reduction of the previously prepared Graphite Oxide (GO)[14] have been reported. Either physical methods or liquid phase exfoliation of graphite lead to high quality G sheets but in a very low yield; Meanwhile the reduction of GO leads to bulk production of G but with poor quality mainly due to the disruption of the sp^2 structure produced by the introduction of defects. Therefore, a scalable method for the production of high-quality G sheets is needed in order to make G suitable for practical purposes.

Notice that many other methodologies such as the unzipping of CNTs,[15] the epitaxial growth on SiC or ruthenium substrates,[16] the organic synthesis of G [17] and some other methods have also been reported.[18, 19] Here we are going to focus in the two chemical methods named before, as they are the most widely used and the ones in which our work would be based on.

Liquid phase exfoliation of graphite.

In 2008 Coleman and coworkers described that some solvents are able to interact with graphite in such a way that the exfoliation into single to few layers can be achieved (**Figure 12**).[14b] As a solution-phase method it is versatile and opens the way to the deposition of G on a variety of substrates that are not accessible from other procedures.[20] As Coleman described, such exfoliation is only possible if the energy cost is very low, so, just those solvents in which the G-solvent interaction matches that of G-G would be able to exfoliate graphite in an effective manner. In this direction, just solvents with surface tensions close to 40 mJ m^{-2} such as NMP (N-Methylpyrrolidone), DMF (N,N-Dimethylformamide) or oDCB (ortho-dichlorobenzene), are suitable for the direct exfoliation of graphite (**Table 1**).[21] However, it is also possible to exfoliate graphite in other solvents with surface tensions far away from those mentioned above by using a solvent exchange method.[21] In this method a well dispersed G in NMP is filtered under vacuum in a first step, and then the resulting solid is subjected to various cycles of dispersion and centrifugation in ethanol, leading finally to a stable G dispersion in this later solvent. This method is very interesting because it allows to use solvents such as ethanol (that has a low boiling point), which are not accessible by direct exfoliation. Unfortunately, the solvent exchange procedure is limited by the low G concentration obtained (below 1 wt%),[22] so a protocol that favors the achievement of greater concentration levels is needed in order to upscale this interesting procedure.

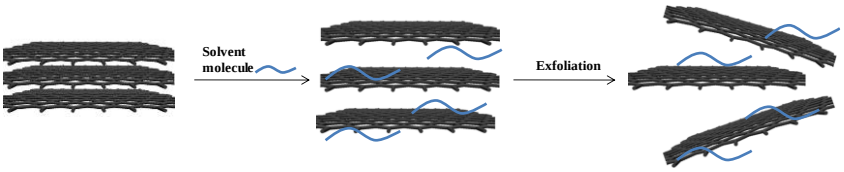

Figure 12. Schematic representation of the liquid phase exfoliation of graphite procedure.

Table 1. Surface tensions and boiling points of some solvents employed in the liquid phase exfoliation of graphite procedure.

Solvent	Surface Tension ($mJ\ m^{-2}$) at 20°C	Boiling Point (°C)
DMF	37.1	153
NMP	40.1	202
ODCB	37	180.5
Ethanol	22.1	78

Reduction of GO

Among the chemical methods, the reduction of the previously synthesized an exfoliated GO is probably the most employed.[23] This method implies, first, an oxidation of graphite with strong acids (H_2SO_4, HNO_3) in order to obtain GO (Hummers method).[24] During this process oxygen moieties (i.e. hydroxyl, epoxy and carboxylic groups) are introduced in the graphite lattice, thus increasing the separation between the sheets and permitting their exfoliation into individual GO platelets. Secondly, GO is reduced in order to restore its electronic properties by recovering the sp^2 structure (**Figure 13**). So far, this reduction step has been accomplished by several strategies, most of which imply the use of hazardous reduction agents (i.e. hydrazine, dimethylhydrazine, L ascorbic acid, Sodium Borohydride, etc.).[25] Still, new reduction methodologies are developed continuously. For example some "green" routes have been described. On one hand, it has been demonstrated that supercritical water can act as a reducing agent for GO under

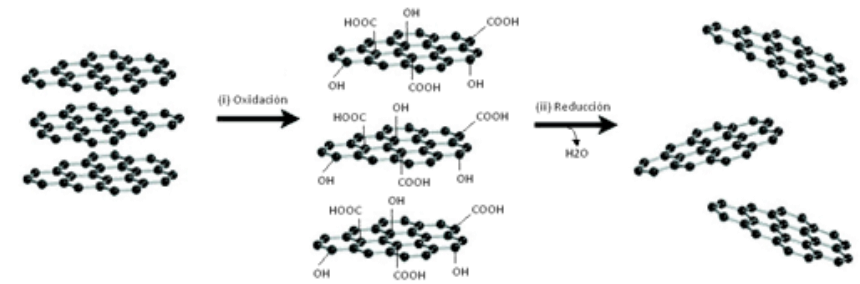

Graphite GO rGO

Figure 13. Schematic representation of the chemical synthesis and reduction of GO.

hydrothermal conditions.[26] On the other hand, it has also been described that the reduction can be driven by applying a pulsed xenon flash directly to the GO sample in what is known as flash reduction.[27] Moreover, it is also possible to reduce GO electrochemically,[28] solvothermally,[29] or thermally.[30]

The main limitation of this method comes from the impossibility to recover completely the sp^2 conjugation. Hence, at the end of the process the remaining defects of G sheets diminish their electronic properties. Still, as it has been pointed out before (see **section 2.1 (b)**, page 50), the obvious differences with respect G do not limit its employment for many important purposes.

2.3. Functionalization of Graphene and applications.

The similarities between CNTs and G have promoted a rapid development of G chemistry by applying the same strategies that were previously studied for CNTs. In the case of G, either covalent functionalization or non-covalent interactions has been explored. Those strategies are useful in order to overcome the great insolubility of G in common organic solvents, as well as to introduce new functionalities that would complement or modify those of G.

Non-Covalent functionalization.

The main limitation of G for real applications is the strong van der Waals and π-π interaction between layers that should be overtaken in order to exfoliate it into

single graphene sheets. In this direction, the non-covalent functionalization is the most attractive option as it is accessible, scalable, reversible, and it does not affect the integrity of the sp^2 structure of graphene. Moreover, through this approximation it is possible to introduce anchoring groups that would provide new functionalities to the final product. As happened with CNTs, many surfactants (Sodium Dodecylbenzenesulfonate, Sodium Cholate, or many other detergents).[31] and polymers have been employed to solubilize G. An interesting alternative would be to take advantage of the π-π interactions. As occurred with CNTs, pyrene moieties appear as a reliable functional group to interact with G, so it has been employed for functionalizing G in a similar context to that explained for CNTs. In this direction, for example, Lee and co-workers succeeded in the solubilization of G (1.5 g mL^{-1}) in aqueous solution by employing an aromatic amphiphile based on a flexible aromatic segment composed by four pyrene units (**Figure 14**).[32]

Based in the same π-π principles, perylene bisimide (PBI) appears as a very attractive derivative to successfully solubilize and functionalize non-covalently G. Those PBIs have been widely studied by Hirsch group, who has found that PBI core constitutes an exceptionally well suited anchor group to match the sp^2 carbon network of G (as well as that of CNTs).[33] Moreover, the PBI can be functionalized with a great assortment of solvophylic moieties that favor the dissolution of G in a

Figure 14. Aromatic amphiphile formed by four pyrene units which have been successfully used to dissolve G in aqueous media (extracted from reference [32]).

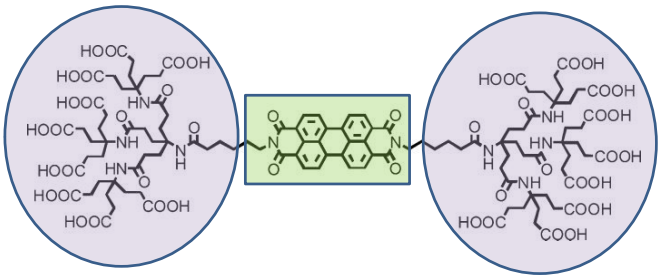

Figure 15. Perylene bisimide employed at reference 34 to solubilize graphene in aqueous medium. The anchor unit in indicated by a green square, while the solvophilic moiety by purple circles.

variety of solvents (**Figure 15**).[34] In fact, the extraordinary surfactant capabilities of PBIs are demonstrated through comparison with the equivalent pyrene derivatives which has shown dispersion efficiency much lower than that offered by the corresponding PBI.[33]

To finish, it is also interesting to point out that single-stranded DNA (ssDNA) molecules which offer many important biomedical applications have shown important skills to disperse graphene in aqueous media through π-π stacking between the carbon sp^2 lattice and the purine and pyrimidine bases of the DNA molecules, reaching concentration levels of the order of 2.5 mg mL^{-1}.[35]

Covalent functionalization.

Along with CNTs, G is also chemically inert for many organic reactions. In fact, due to its planar nature it is even more inert than CNTs, and the most active sites appear at the edges or at the defect sites that can be over the G sheet. Moreover, to succeed in the functionalization process it is necessary to overcome the van der Walls interaction between the layers, so a previous step to exfoliate them is always required. Once exfoliated, the typical organic reactions that have been used to fuctionalize fullerenes or CNTs, such as the Prato reaction, aryldiazonium derivatization, or the Bingel-Hirsch reaction, can be successfully extended to G. For example, Prato *et al.* used the Prato reaction in the functionalization of graphene with amino groups, which were further employed to bind metal nanoparticles.[36] With respect the functionalization with aryldiazonium salts, Tour *et al.* introduced several

side groups through this procedure, which resulted in highly soluble G sheets.[37] Finally, Tagmatarchis *et al.* were able to bind covalently an extended tetrathiafulvalene (TTF) to G following the Bingel-Hirsch reaction.[38]

Another interesting feature of G is its double side functional configuration. In contrast to CNTs, in which the outer wall is the most reactive one, in G both sides are equally reactive. Hence, through convenient functionalization, it can lead to 3D structures for special applications, as might be the formation of porous materials which would have interesting gas-adsorption properties.[39]

Despite all the advances that have been carried out concerning G chemistry, the most challenging issue to achieve a bulk functionalization of G. A useful strategy to reach this goal consists of employing GO as starting material. Still, the principal problem of this method comes from the limited properties of GO. A bulk functionalization of G from graphite has been proposed by. Hirsch and co-workers who followed a reductive treatment with NaK to activate graphite. Those reduced layers were further functionalized by adding an electrofile that readily reacts with the activated sheets functionalizing them with the desired moiety.[40]

2.4. Graphene-based hybrid materials.

Many promising applications of graphene can appear from the formation of hybrid materials, since the exciting properties of G are combined with those offered by other systems giving rise to a hybrid compound whose characteristics may be far beyond from those of the pristine materials.[41] To achieve that goal, covalent and non-covalent functionalization can be employed. Thus, it is possible to imagine two types of G-based hybrid composites. On one hand, those that comes from the decoration or deposition of the exogenous systems over the G sheets, and, on the other hand by those resulting from the intercalation of the exogenous compound to form a sandwich-like structure. Many examples have been reported in both cases. For example, composites of G with a variety of metal nanoparticles that can find their way in catalysis, biosensors and energy storage, have been described,[42] or the decoration of G sheets with fluorescent CdSe quantum dots (QDs), which may have potential applications in bio-imaging and light emitting devices.[43] G has also been combined with $Ni(OH)_2$ nanoplates giving rise to an interesting material oriented to

the creation of electrochemical pseudocapacitors due to its high energy densities, high power densities and long cycle life.[44] It has also been described that the absorption of polyoxometallate (POM) over GO lead to the photoreduction of GO upon with the formation of a hybrid composite with potential applications due to the magnetic, catalytic and optical properties that POM could offer to the system.[45] Concerning the sandwich-like type material, the creation of composites by alternating layers of G and Co-Al layered double hydroxides,[46] or embedding nickel oxide molecules in between the G sheets to obtain a composite suitable for energy storage matters,[47] are two important examples. Of course, a never-ending list of works could be introduced thereon, demonstrating the potential that G-based hybrid materials offer for future technological developments.

2.5. References

[1] A.K. Geim, K.S. Novoselov, *Nat. Mater.*, **2007**, *6*, 183.

[2] a) E. Charles, H. Sykes, *Nat. Chem.* **2009**, *1*, 175. b) G. Eda, M. Chhowalla, *Adv. Mater.* **2010**, *22*, 2392. c) J. Liu; L. Tao, W. Yang, D. Li, C. Boyer, R. Wuhrer, F. Braet, T.P. Davis, *Langmuir*, **2010**, *2*, 10068. d) C.N.R. Rao, K. Biswas, K.S. Subrahmanyam, A. Govindaraj, *J. Mater. Chem.*, **2009**, *19*, 2457.

[3] (a) K.P. Loh, Q. Bao, G. Eda, M. Chhowalla, *Nat. Chem.*, **2010**, *2*, 1015. (b) S. Stankovich, D.A. Dikin, G.H.B. Dommett, K.M. Kohlhaas, E.J. Zimney, E.A. Stach, R.D. Piner, S.D. Nguyen, R.S. Ruoff, *Nature*, **2006**, *442*, 282. (c) D. Wei, Y. Liu, *Adv. Mater.*, **2010**, *22*, 3225.

[4] L. Huang, B. Wu, G. Yu, Y. Liu, *J. Mater. Chem.*, **2010**, *21*, 919.

[5] M.P. Ramuz, M. Vosgueritchian, P. Wei, C. Wang, Y. Gao, Y. Wu, Y. Chen, Z. Bao, *ACS Nano*, **2012**, DOI: 10.1021/nn304410w.

[6] a) Y. Chen, B. Zhang, G. Liu, X. Zhuang, E.-T. Kang, *Chem. Soc. Rev.*, **2012**, *41*, 4688. b) Q. Bao, K.P. Loh, *ACS Nano*, **2012**, *6*, 3677.

[7] P. Blake, P.D. Brimicombe, R.R. Nair, T.J. Booth, D. Jiang, F. Schedin, L.A. Ponomarenko, S.V. Morozov, H.F. Gleeson, E.W. Hill, A.K. Geim, K.S. Novoselov, *Nano Lett.*, **2008**, *8*, 1704.

[8] X. Wang, L. Zhi, K. Müllen, *Nano Lett.*, **2008**, *8*, 323.

[9] C. Lee, X. Wei, J.W. Kysar, J. Hone, *Science*, **2008**, *321*, 385.

[10] a) A. Candini, S. Klyatskaya, M. Ruben, W. Wernsdorfer, M. Affronte, *Nano Lett.*, **2011**, *11*, 2634. b) E. Kan, Z. Li, J. Yang, *Nano*, **2008**, *3*, 433. c) C.N.R. Rao, H.S.S. Ramakrishna Matte, K.S. Subrahmayan, U. Maitra, *Chem. Sci.*, **2012**, *3*, 45.

[11] a) J.-A. Yan, L. Xian, M. Y. Chou, *Phys. Rev. Lett.*, **2009**, *103*, 086802. b) F. Yavari, C. Kritzinger, C. Gaire, L. Song, H. Gullapalli, T. Borca-Tasciuc, P.M. Ajayan, N. Koratkar, *Small*, **2010**, *6*, 2535.

[12] S. Dutta, S. K. Pati, *J. Mater. Chem.*, **2010**, *20*, 8207.

[13] S. Park, R.S. Ruoff, *Nat. Nanotech.*, **2009**, *4*, 217.

[14] a) D.R. Dreyer, S.W. Park, R.S. Ruoff, *Chem. Soc. Rev.*, **2010**, 39, 228. b) Y. Hernandez, V. Nicolosi, M. Lotya, F.M. Blighe, Z. Sun, S. De, I.T. McGovern, B. Holland, M. Byrne, Y.K. Gun'ko, J.J. Boland, P. Niraj, G. Duesberg, S. Krishnamurthy, R. Goodhue, J. Hutchison, V. Scardaci, A.C. Ferrari, J.N. Coleman, *Nat. Nanotech.*, **2008**, 3, 563.

[15] D.V. Kosynkin, A.L. Higginbotham, A. Sinitskii, J.R. Lomeda, A. Dimiev, B.K. Price, J.M. Tour, *Nature*, **2009**, *458*, 872.

[16] a) C. Berger, Z. Song, X. Li, X. Wu, N. Brown, C. Naud, D. Mayou, T. Li, J. Hass, A.N. Marchenkov, E.H. Conrad, P.N. First, W.A. de Heer, *Science*, **2006**, *312*, 1191. b) P.W. Sutter, J.-I. Flege, E.A. Sutter, *Nat. Mater.*, **2008**, *7*, 406.

[17] J. Wu, W. Pisula, K. Müllen, *Chem. Rev.*, **2007**, *107*, 718.

[18] M. Inagaki, Y.A. Kim, M. Endo, *J. Mater. Chem.*, **2011**, *21*, 3280.

[19] Y. Zhu, D.K. James, J.M. Tour, *Adv. Mater.*, **2012**, *24*, 4924.

[20] D. Rangappa, K. Sone, M. Wang, U.K. Gautam, *Chem. Eur. J.*, **2010**, *16*, 6488.

[21] X. Zhang, A.C. Coleman, N. Katsonis, W.R. Browne, B.J. van Wees, B.L. Feringa, *Chem. Commun.*, **2010**,*45*, 7539.

[22] A.B. Bourlino, V. Georgakilas, R. Zboril, T.A. Steriotis, A.K. Stubos, *Small*, **2009**, *5*, 1841.

[23] C.N.R. Rao, A.K. Sood, K.S. Subrahmanyam, A. Govindaraj, *Angew. Chem. Int. Ed.*, **2009**, *48*, 7752.

[24] W.S. Hummers, R.E. Offeman, *J. Am. Chem. Soc.*, **1958**, *80*, 1339.

[25] a) S. Stankovich, D.A. Dikin, R.D. Piner, K.A. Kohlhaas, A. Kleinhammes, Y. Jia, Y. Wu, S.T. Nguyen, R.S. Ruoff, *Carbon*, **2007**, *45*, 1558. b) H.-J. Shin, K.K. Kim, A. Benayad, S.-M. Yoon, H.K. Park, I.-S. Jung, M.H. Jin; H-K. Jeong, J.M. Kim, J.-Y. Choi, Y.H. Lee., *Adv. Funct. Mater.*, **2009**, 19, 1987.

[26] Y. Zhou, Q. Bao, L.A.L. Tang, Y. Zhong, K.P. Loh, *Chem. Mater.*, **2009**, *21*, 2950.

[27] L.J.Core, R. Cruz-Silva, J. Huang., *J. Am. Chem. Soc.*, **2009**, *131*, 11027.

[28] M. Zhou, Y. Wang, Y. Zhai, J. Zhai, W. Ren, F. Wang, S. Dong, *Chem. Eur. J.*, **2009**, *15*, 6116.

[29] V.H. Pham, T.V. Cuong, S.H. Hur, E. Oh, E.J. Kim, W.E. Shin, J.S. Chung, *J. Mater. Chem.*, **2011**, *21*, 3371.

[30] M.J. McAllister, J.-L. Li, D.H. Adamson, H.C. Schniepp, A.A. Abdala, J. Liu, M. Herrera-Alonso, D.L. Milius, *Chem. Mater.*, **2007**, *19*, 4396.

[31] S. Stankovich, D.A. Dikin, G.H.B. Dommett, K.M. Kohlhaas, E.J. Zimney, E.A. Stach, R.D. Piner, S.T. Nguyen, R.S. Ruoff, *Nature*, **2006**, *442*, 282.

[32] D.-W. Lee, T. Kim, M. Lee, *Chem. Commun.*, **2011**, 47, 8259.

[33] C. Backes, F. Hauke, A. Hirsch, *Adv. Mater.*, **2011**, *23*, 2588.

[34] J.M. Englert, J. Röhrl, C.D. Schmidt, R. Graupner, M. Hundhausen, F. Hauke, A. Hirsch, *Adv. Mater.*, **2009**, *21*, 4265.

[35] A.J. Patil, J.L. Vickery, T.B. Scott, S. Mann, *Adv. Mater.*, **2009**, *21*, 3159.

[36] M. Quintana, K. Spyrou, M. Grzelczak, W.R. Browne, P. Rudolf, M. Prato, *ACS Nano*, **2010**, *4*, 3527.

[37] J.R. Lomeda, C.D. Doyle, D.V. Kosynkin, W.-F. Hwang, J.M. Tour, *J. Am. Chem. Soc.*, **2008**, *130*, 16201.

[38] S.P. Economopoulos, G. Rotas, Y. Miyata, H. Shinohara, N. Tagmatarchis, *ACS Nano*, **2010**, *4*, 7499.

[39] a) J.W. Burress, S. Gadipelli, J. Ford, J.M. Simmons, W. Zhou, T. Yildirim, *Angew. Chem. Int. Ed.*, **2010**, *49*, 8902-8904. b) C. Petit, T.J. Bandosz, *Adv. Mater.*, **2009**, *21*, 1.

[40] J.M. Englert, C. Dotzer, G. Yang, M. Schmid, C. Papp, J.M. Gottfried, H.-P. Steinrück, E. Spiecker, F. Hauke, A. Hirsch, *Nat. Chem.*, **2011**, *3*, 279.

[41] X. Huang, X. Qi, F. Boey, H. Zhang, *Chem. Soc. Rev.*, **2012**, *41*, 666.

[42] a) J. Lu, I. Do, L.T. Drzal, R.M. Worden, I. Lee, *ACS Nano*, **2008**, *2*, 1825. b) C. Xu, X. Wang, J. Zhu, *J. Phys. Chem. C*, **2008**, *112*, 19841. c) Y.C. Si, E.T. Samulski, *Chem. Mater.*, **2008**, *20*, 6792. d) B. Wang, X.-L. Wu, C.-Y. Shu, Y.-G. Guo, C.-R. Wang, *J. Mater. Chem.*, **2010**, *20*, 10661.

[43] Y. Wang, H.-B. Yao, X.-H. Wang, S.-H. Yu, *J. Mater. Chem.*, **2011**, *21*, 562.

[44] H. Wang, H.S. Casalongue, Y. Liang, H. Dai, *J. Am. Chem. Soc.*, **2010**,*132*, 7472.

[45] H. Li, S. Pang, X. Feng, K. Müllen, C. Bubeck, *Chem. Commun.*, **2010**, *46*, 6243.

[46] L. Wang, D. Wang, X.Y. Dong, Z.J. Zhang, X.F. Pei, X.J. Chen, B. Chen, J. Jin, *Chem. Commun.*, **2011**, *47*, 3556.

[47] Lv, W., Sun, F., Tang, D.-M., Fang, H.-T., Liu, C., Yang, Q.-H., Cheng, H.-M., *J. Mater. Chem.*, **2011**, *21*, 9014.

3 Carbon Nanotubes based hybrid materials*,†

In this chapter carbon nanotubes have been chosen as main building block for the development of hybrid composites. In a first part, two different routes that enable the electrostatic grafting of cationic Single-Molecule Magnets (SMMs) onto the surface of chemically modified anionic multi-walled carbon nanotubes (MWNTs) will be described. The chemical nature and physical properties of the resulting hybrids are discussed on the basis of a complete battery of experimental techniques, which prove that the chemical nature of the SMM unit remains intact whereas its magnetic response is significantly affected by the grafting process, likely due to surface effects. In the second part, a hybrid composed by single walled nanotubes (SWNT) and a polyoxometalate (POM) will be developed. The POM has been conveniently modified with pyrene units which act as anchoring group between the POM and the SWNTs by the creation of π-π interactions. The hybrid system is deeply studied by the employment of different characterization techniques. Interestingly, by the use of high-resolution transmission microscopy (HR-TEM) we will go down to the atomic level, showing the atomic resolution of the POM linked to the SWNTs.

* C. Bosch-Navarro, E. Coronado, C. Martí-Gastaldo, B. Rodríguez-González, L.M. Liz-Marzán, *Adv. Funct. Mater.* **2012**, *22*, 979-988.

† C. Bosch-Navarro, E. Coronado, C. Martí-Gastaldo, C. Romero-Nieto, D. Guldi, to be submitteed

3.1. Electrostatic Anchoring of Mn_4 Single-Molecule Magnets on Chemically Modified Multi-walled Carbon Nanotubes

3.1.1. Introduction

Single-molecule magnets (SMMs) constitute an active area of interest within the broader field of Molecular Magnetism.[1] These 0D systems are typically formed by magnetic clusters, wherein transition metal ions are connected through oxo-ligands and surrounded by capping organic ligands. More recently, analogous behavior has also been observed in mononuclear complexes based on lanthanide ions.[2] Physical studies have demonstrated that these molecules behave as hard magnets at low temperatures, additionally showing interesting quantum phenomena. In view of these properties, SMMs are attractive candidates for Molecular Spintronics and Quantum Computing.[3] A key step to implement these systems into these exciting application areas is the deposition/grafting of SMMs on suitable substrates, or their connection to electrodes. On the basis of their electronic properties, carbon nanotubes (CNTs) have been proposed as excellent substrates in this context.[4] This scenario takes advantage of the large sensitivity of the electronic properties of CNTs towards any change in their chemical environment and their extremely low spin-orbit and hyperfine couplings, which provide high-spin coherence lengths.[5]

So far, different routes have been exploited to drive the controlled organization of SMMs on CNTs. One of them exploited the robustness of the anionic polyoxometalate $[Fe_4(H_2O)_2(FeW_9O_{34})_2]^{6+}$ to mediate its assembly on purified single-walled nanotubes (SWNTs), producing a hybrid material that retained the magnetic bi-stability of the pristine SMM unit.[6] Other examples benefit from the chemical versatility of these unimolecular magnets, which permit tailoring their organic shells and introducing functional groups that enable grafting on the sidewalls of the CNTs through strong supramolecular π-π interactions. For example, the assembly of a Fe (III) tetranuclear cluster $[Fe_4(L)_2(dpm)_6]$ (H_3L=2-hydroxymethyl-2-(4-(pyren-1-yl)butoxy) methylpropane-1,3-diol; Hdpm=dipivaloylmethane) and a heteroleptic bis(phtalocyaninato) terbium (III) mononuclear complex incorporating a

pyrene group in its periphery have been reported.[7] Nevertheless, before these systems can be successfully implemented into operational CNT-based nanoelectronic devices, several questions remain to be answered, namely: i) How does the grafting affect the magnetic properties of the SMMs, through hybridization or environmental effects; ii) Which are the most suitable chemical interactions (i.e. covalent, supramolecular, electrostatic…) needed to drive the assembly of the molecular magnets without dramatically affecting the electrical conductivity of the CNTs.

In this work, we focused on two chemical routes enabling the electrostatic grafting of positively charged SMMs onto chemically functionalized anionic MWNTs. As molecular nanomagnets we chose the cationic manganese (II, III) tetranuclear complex $[Mn_4(O_2CCH_3)_2(pdmH)_6]^{4+}$ (Mn_4) (pdmH=deprotonated pyridine-2,6-dimethanol)[8] because of its structural robustness and chemical versatility, which has been previously demonstrated through incorporation in several coordination frameworks whilst maintaining its intrinsic magnetic properties.[9]

3.1.2. Results and Discussion

3.1.2.1. Synthesis

So far, different routes have been exploited to attach functional molecules on carbon nanotubes. These have mainly focused on a) the formation of strong covalent bonds between pre-functionalized nanotubes and the molecular moiety of interest, b) the presence of weaker π-π supramolecular interactions between the aromatic sidewalls of the nanotubes and a pre-designed molecule carrying a polyaromatic group, and c) electrostatic interaction between the nanotube and the molecular unit. The two former strategies give rise to weakly coupled hybrids as they force the molecular cluster to reside far from the direct contact with the nanotubes, thus minimizing the electronic interaction between the nanotubes and the molecular unit, while the last one can favor a more direct grafting of the molecular cluster with the MWNT and therefore, a stronger interaction. In this work we have exclusively focused on this latter approach to attach the cationic Mn_4 cluster onto

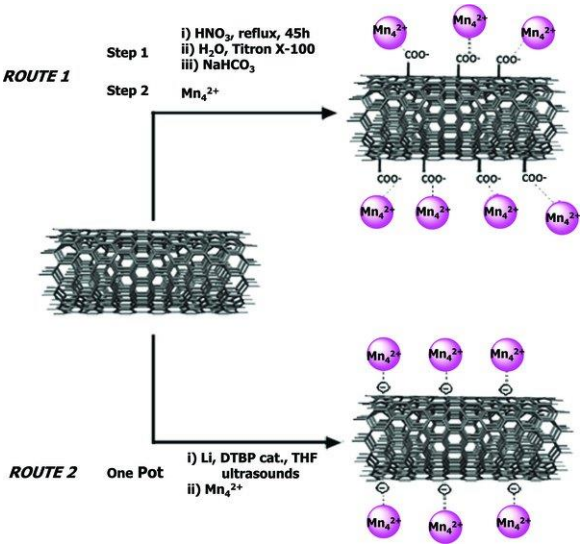

Scheme 5. Chemical routes used to electrostatically graft the positively charged SMM units onto chemically functionalized anionic MWNTs.

negatively charged MWNTs. According to **Scheme 5**, two different synthetic routes were followed in this context: 1) The attachment through a two-step process, which includes the introduction in a first step of carboxylic groups to the outer walls of the MWNTs, which are subsequently deprotonated in basic medium, and their further linkage in a second step to the cationic Mn_4 complex, and 2) The direct attachment via a one-step process by combining the cationic complex with *in situ* generated anionic MWNTs.

The use of two different routes to accomplish a common goal stems from the different electronic effects that can be potentially introduced to the CNTs as a result of their functionalization. At this point it is worth remarking that the electrical conductivity of the resulting Mn_4-MWNTs hybrids is of utmost importance to develop working carbon nanotube-based electronic devices. In this context, the first route will afford poorly conducting hybrids, as the carboxylic groups on the sidewalls of the CNTs are expected to behave as defects that disrupt the original sp^2 carbon electronic structure. On the contrary, the second approach should result in an enhancement of the electrical conductivity of the hybrid in comparison with the pristine MWNT, as it involves n-type doping of the CNTs.

3.1.2.2. Anchoring of Mn4 Molecules.

Route 1. Commercially available MWNTs were refluxed in a concentrated HNO_3 acid medium (further details can be found in the experimental section). According to previous works,[10] this process not only enables the introduction of carboxylic groups at the periphery of the nanotubes but also leads to removal of small traces of metal particles, which are commonly employed as catalysts in the production of CNTs, as well as amorphous carbonaceous forms present in the pristine material. In a first stage, the success of the functionalization was monitored through FT-IR and thermogravimetric analysis. FT-IR shows the appearance of a broad band at 1115 cm^{-1}, which corresponds to the C-O stretching mode (**Figure 16a**).[11] This band is merely residual in the pristine MWNTs, indicating the presence of a bigger amount of carboxylic groups in the post-functionalized material. **Figure 16b** shows the thermal decomposition of these materials under ambient conditions. Whereas the pristine unmodified MWNTs exhibit a single decomposition process around 550 ºC, which can be associated to the oxidation of carbon, the carboxylated material exhibits a more complex behavior with two different mass loss steps. The first, occurring between 300 and 400 ºC and yielding a weight loss of 17 %, can be associated to the coupled decomposition of the carboxylic groups connected to the CNTs and the Triton X100 surfactant molecules present in the medium. The presence of the surfactant was confirmed by Atomic Force Microscopy (AFM) images, collected from casting a dispersion of the MWNT-COOHs onto a High Oriented Pirolytic Graphite (HOPG) surface (**Figure 17**). This complex situation did not allow us to estimate quantitatively the percentage of carboxylic groups present in the sample, thus making necessary the employment of indirect methods (*vide infra*). Upon heating, complete decomposition of the nanotubes was observed around 480 ºC. This temperature is significantly smaller than that recorded for the non-carboxylated material, as expected from the presence of a larger amount of defects in the structure of the CNTs, which decrease their thermal stability.[12]

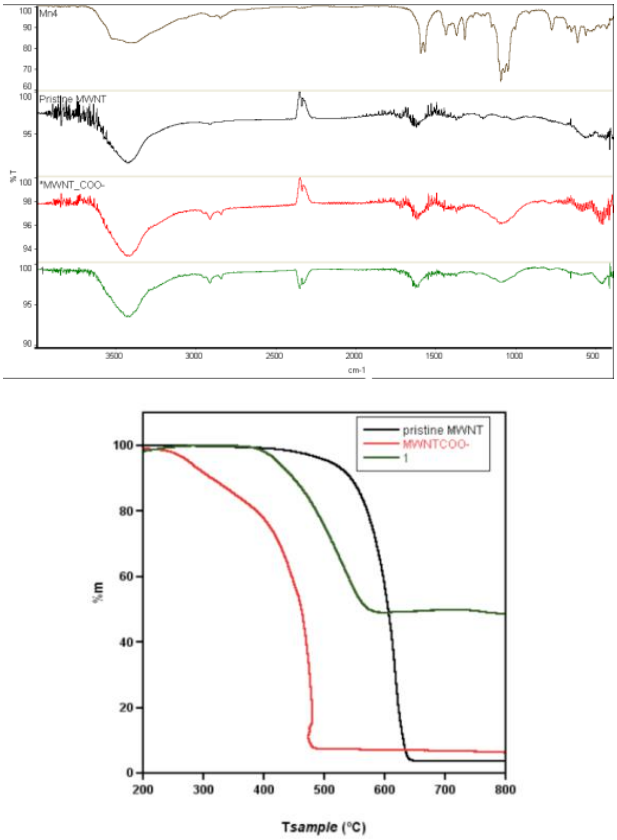

Figure 16. (*Top*) FT-IR spectra of Mn_4 (brown), pristine MWNT (black), MWNT-COO^- (Bottom) and MWNT-Mn 1 (green)

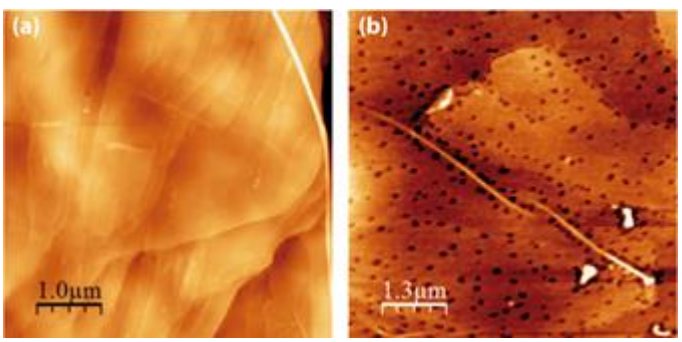

Figure 17. AFM topographic images of: (*left*) Clean HOPG and (*right*) Post-functionalized MWNT-COOHs accompanied by Triton X100 surfactant molecules (black dots).

To determine the total percentage of acidic groups in the MWNT-COOHs, the nanotubes were backwards titrated (see experimental section). Assuming that all the acidic sites in our sample are carboxylic groups and that the sample is just composed of carbon atoms, this experiment yielded a percentage of 1.4 %, in excellent agreement with other values reported in the literature.[13]

Finally, the deprotonated MWNT-COO^-s were suspended in acetonitrile, and the mixture was subjected to sequential ultrasonication cycles to achieve a homogeneous dispersion. Then, the Mn_4 clusters were added under continuous mechanical stirring. The presence of attractive Coulomb forces between the negatively charged walls of the MWNT-COO^- and the cationic $[Mn_4(OAc)_2(pdmH)_6]^{2+}$ units, enables the grafting of the latter to produce the hybrid Mn_4-MWNT (**1**; **Scheme 5**). This grafting was preliminarily confirmed through the thermogravimetric study of **1** (**Figure 16b**), which shows the formation of an oxide above 550 ºC, which represents approximately 50 % of the sample weight, and was mainly composed of manganese, according to the EDS analysis.

Route 2. Commercially available MWNTs were reduced by the addition of lithium and 4,4´-di-tertbutyl-biphenyl (DTBP), acting as a catalyst, to a suspension containing the nanotubes. This strategy permits directly introducing negative charges onto the sidewalls of the CNTs in a single step (further details can be found in the experimental section). The Mn_4 cluster was then carefully added to the mixture and anchored to the negatively charged MWNTs via attractive electrostatic interactions, producing the hybrid Mn_4-MWNT (**2**; **Scheme 5**).

The thermal decomposition of **2** under oxygen suggests the presence of several components in the sample. Mn_4 shows a complex thermogram with a number of decomposition steps. These steps can also be observed in the hybrid. Still, the thermogram for **2** is even more complex, and the remaining mass is larger than that calculated by assuming a pure Mn_4-MWNT composition. This suggests the presence of DTBP, lithium or intermediate species in the final hybrid, in agreement with the FT-IR spectra (**Figure 18a**). Due to this complex situation the Mn_4 content in **2** cannot be disclosed from the TG analysis (**Figure 18b**), and its presence was again confirmed by EDS studies (*vide infra*).

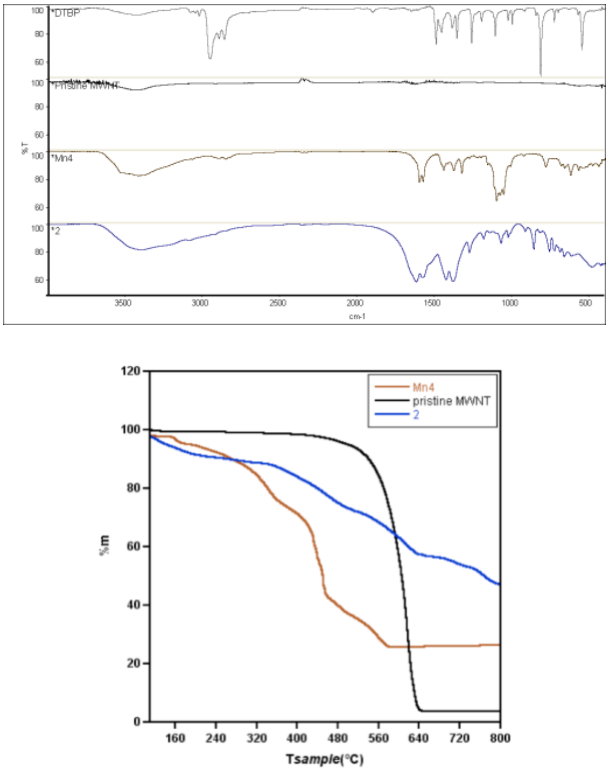

Figure 18. (*Top*) FT-IR spectra of DTBP (grey), pristine MWNT (black), Mn_4 (brown) and Mn-MWNT 2 (blue) (route 2). (*Bottom*) Thermal decomposition under O_2 atmosphere of: - route 2 - Mn_4 cluster (brown), MWNT (black) and Mn4-MWNT 2 (blue).

3.1.2.3. Electron Microscopy and EDS analysis.

High resolution transmission electron microscopy (HR-TEM) images of the purified MWNTs and the Mn_4-MWNTs hybrids **1** and **2** were collected from specimens prepared by dropping freshly prepared dispersions in ethanol on carbon-coated copper grids.

Whilst the commercially supplied MWNTs are generally aggregated in weak-contrast bundles, accompanied by a significant number of dark spots, associated to the remaining particles of the metal catalysts employed in their synthesis, the purified material exhibits a better dispersion of the nanotubes with a smaller number of interlocked junctions and no trace of high-contrast metal impurities (**Figure 19**).

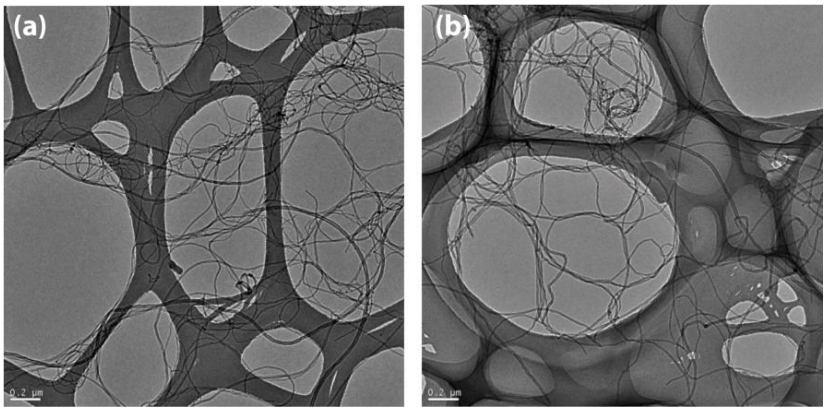

Figure 19. HRTEM images of the MWNTs as received from commercial suppliers (a) and after the acid treatment (b).

Route 1. A close look at the Mn_4-MWNT hybrid **1**, obtained from the addition of Mn_4 molecules to the pre-purified carboxylate-containing nanotubes, reveals important differences with respect to the bare material (**Figure 20a**). At first sight, one can see some low contrast material attached to the surface of the MWNTs, which is likely related to the grafting of the SMMs. **Figure 20b** displays a close up of one of these decorated MWNTs, which evidences low contrast objects attached to the surface of the nanotube with sizes of *ca.* 1-2 nm, in excellent agreement with the dimensions of the molecular cluster. These objects are heterogeneously distributed along the nanotube's sidewall, with separations of 5-10 nm in some cases, while in others they tend to aggregate. Additional information regarding the chemical composition of the grafted objects was provided by X-ray energy dispersive spectroscopy (EDS). Several spectra were collected from different areas across a single decorated MWNT, confirming that manganese was the only metal present and hence can be associated to the objects on the surface of the tube (**Figure 20c**; the copper signal observed can be attributed to the grid used to support the sample). Unfortunately, the manganese signal was too low to permit performing a proper compositional mapping, suggesting that the grafting degree obtained by this procedure is poorer than that accomplished through route 2, in excellent agreement with the results obtained from XPS and magnetic studies (*vide infra*) which also point toward a smaller amount of grafted material in **1**.

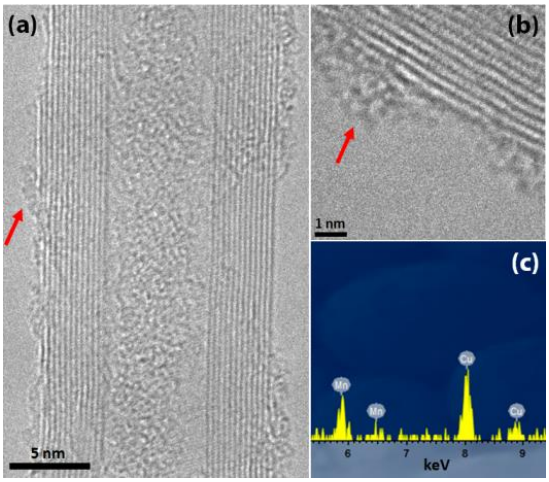

Figure 20. (a,b) HRTEM images of 1 displaying the grafting of the Mn_4 complex (indicated by the arrows) on the surface of pre-functionalized MWNTs. The multi-walled structure of the CNTs is also shown. (c) EDS spectrum acquired from a single decorated MWNTs like the one shown in (a) confirming the presence of Mn -Cu signal can be attributed to the TEM grid-.

These high-resolution images also reveal the regular overlap of several planes (multi-wall) along the nanotubes' sidewalls, confirming that their internal structure is maintained after functionalization and grafting of Mn_4 clusters (**Figure 20a,b)**. This is of utmost importance, since the successful integration of this sort of hybrids into carbon nanotube-based electronic devices is generally limited by the modification of the intrinsic transport properties of the nanotubes through the introduction of non-reversible structural damages.[14]

Route 2. Direct attachment of the Mn_4 clusters to the MWNTs as reduced "*in-situ*", yields a homogeneous grafting of the molecular component. **Figure 21a** shows an almost regular distribution of grafted material on the nanotube's sidewall. This grafting behavior is likely induced by the presence of equally intense repulsive electrostatic interactions between the positively charged clusters in the presence of a homogeneous distribution of negative charges along the nanotube wall. In this case the clusters exhibit strongest contrast due to the larger thickness of the attached material, which in some places almost forms a complete shell over the tube. The grafted material shows a globular arrangement with sizes ranging between 2 and 3 nm, again in good agreement with the size of the grafted molecular component. The Z contrast image confirms that these spheres are composed by high Z material

(**Figure 21b**). The chemical nature of these moieties was corroborated by EDS analysis, confirming that except for Cu, arising from the supporting grid, Mn was the only metal present (**Figure 21c**). This point was additionally confirmed by STEM-XEDS elemental mapping (**Figure 22**), which clearly shows the presence of units containing Mn surrounding the carbon nanotubes, in agreement with the bright spots identified in the Z-contrast HAADF-STEM image **(Figure 21b)**.

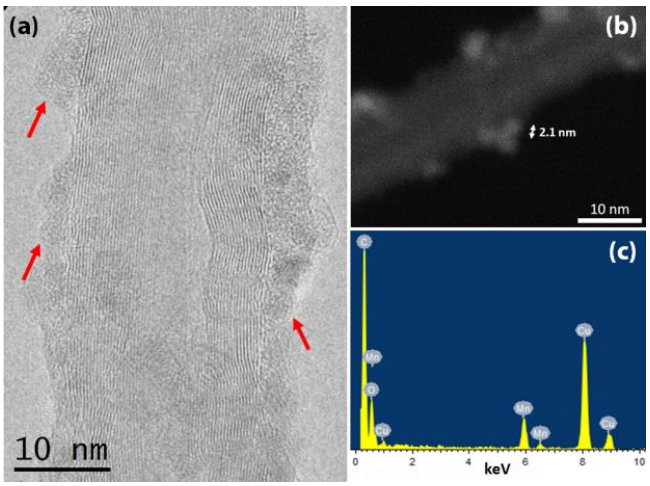

Figure 21. (a) HRTEM images of 2 displaying the grafting of the Mn4 complex (indicated by the arrows) on the negatively charged MWNTs. (b) Z-contrast HAADF-STEM image showing the distribution of the clusters along the nanotubes (brighter spots) and their size (2.1 nm). (c) Local area EDS spectrum confirming the presence of Mn on the MWNTs -again, the Cu signal is attributed to the TEM grid- .

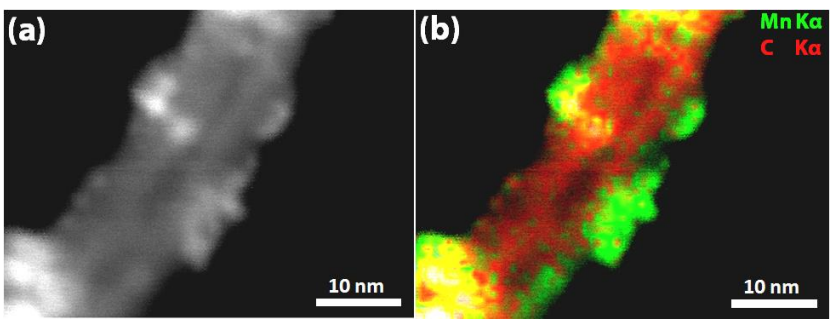

Figure 22. (a) Z contrast HAADF-STEM image of Mn4-MWNTs hybrid 2. (b) STEM-XEDS elemental mapping performed over the area represented in (a) showing an excellent agreement between the Mn distribution and the bright spots grafted to the nanotube.

3.1.2.4. X-Ray Photoelectron Spectroscopy (XPS)

XPS experiments provided evidence for all the elements expected to be present in the grafted MWNTs with binding energies in agreement with the expected bonding states. **Table 2** summarizes the binding energy (BE) values extracted from high-resolution spectra.

Table 2. Chemical bonding binding energies (BE) extracted from high resolution XPS spectra.

Sample	Mn 2p [eV][a]				Mn 3s [eV]		
	$Mn(2p_{3/2})$	$Mn(2p_{1/2})$	Δ_{BE}	$Mn(2p_{3/2})_{sat}$	Mn(3s)'	Mn(3s)''	Δ_{BE}
Mn_4	641.34	653.06	11.72	646.36	83.29	89.26	5.97
1	641.80	653.60	11.80	646.59	84.16	90.18	6.02
2	641.24	653.04	11.80	646.60	83.71	89.79	6.08

[a] Binding energy values referenced to $Si(2p_{3/2})$ (Si-Si) at 99.8 eV on un-sputtered surfaces

According to **Figure 23**, the Mn 2p (*top*) and Mn 3s (*bottom*) signals exhibited by the hybrids are in good agreement with the data collected from a crystalline sample of the Mn_4 complex, providing a strong indication of the grafting success. In every case, the Mn 2p spectra (**Figure 23a**) display two dominant peaks between 641 and 654 eV, which can be assigned to the spin–orbit splitting into the $Mn(2p_{3/2})$ and $Mn(2p_{1/2})$ levels with an energy splitting of ~11.8 eV. Besides, the $Mn(2p_{3/2})$ level is accompanied by a less intense satellite peak at higher binding energies (~5 eV), in excellent agreement with that expected for the presence of Mn^{2+} ions.[15] This satellite contribution can be clearly observed for the Mn_4 blank and **2** whilst its presence is only marginal in **1**, thus suggesting a smaller amount of grafted Mn_4 complexes in the latter. The Mn 3s region (**Figure 23b**) displays an asymmetric doublet which can be ascribed to a multiplet splitting of ~6 eV, in good agreement with the presence of Mn (II). Again, the Mn 3s spectrum of **1** exhibits a weaker and less defined signal than **2**, therefore suggesting a minor grafting degree. Additionally, the presence of Mn_4 in all the samples studied is confirmed by the nearly identical values of $\Delta E = [E(Mn_{2p1/2}) - E(Mn_{2p3/2})] = 11.72$ and 11.80 eV for pristine Mn_4 molecules and the hybrids **1** and **2**, respectively. Besides, the ΔE values

described for other phases of manganese oxides such as MnO (5.5), Mn_2O_3 (10.5), Mn_3O_4 (11.3) or MnO_2 (11.9 eV) permits discarding their formation.[16] It is worthwhile mentioning that MnO_2 exhibits a ΔE value very close to that exhibited by the hybrids. Still, its absence was additionally confirmed on the basis of the magnetic characterization (*vide infra*).

It is worth reminding that, except for Mn (II), which has the maximum number of unpaired d-electrons, and accordingly exhibits the most intense satellite peaks, the identification of other oxidation states on the basis of XPS data has proven to be very difficult due to the small influence of these Mn oxidation states on the BE shifts and the broad nature of the collected peaks. Furthermore, the low concentration of the Mn_4 complex in the studied hybrids makes this task even more difficult due the poor signal/noise ratio.

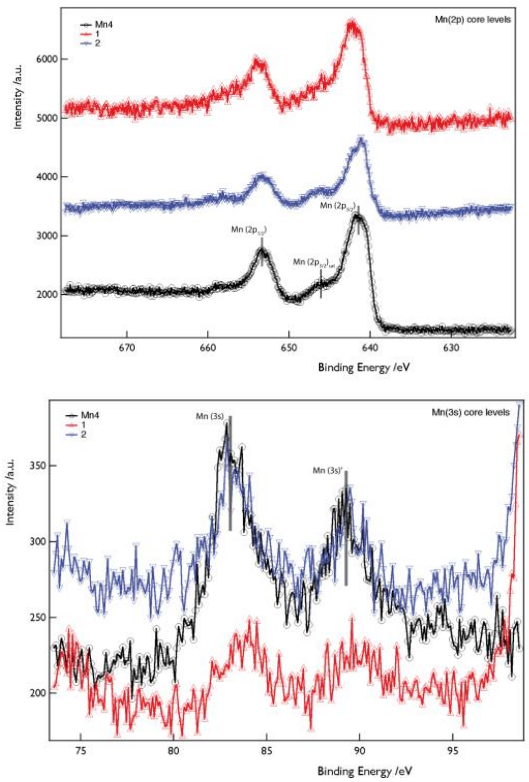

Figure 23. Core-level Mn 2p (*top*) and 3s (*bottom*) XPS spectra of the bulk Mn_4 complex (black circles) and the Mn4-MWNTs hybrids (1; red triangles and 2; blue triangles).

3.1.2.5. Magnetic measurements.

Static magnetic properties of the purified MWNTs and the hybrids containing Mn_4 complexes were examined by studying the isothermal field dependence of their magnetization collected at 2 K (**Figure 24**). Bare purified nanotubes exhibit a ferromagnetic response, due to the presence of traces of metallic nanoparticles, reminiscent of the catalysts employed in their production. This behavior has already been described and reflects the difficulties inherent to the purification of carbon nanotubes.[17] The addition of Mn_4 complexes is clearly accompanied by an increase in the magnetic response of the hybrids with saturation values at 2.17 and 5.43 $emu.g^{-1}$ at 5 T, for **1** and **2**, respectively. The different response exhibited by these two hybrids indicates that a bigger degree of grafting is accomplished through the direct one-step metallization (route 2) in comparison with the two-step carboxylation/deprotonation process (route 1). This was already anticipated by the low intensity Mn signals observed for **1** in the EDS and XPS experiments (*vide supra*). The less pronounced increase of the magnetization of **1** and **2** at low fields with respect to the response exhibited by the bulk Mn_4 cluster seems to indicate that the polynuclear cluster might possess a different electronic structure when grafted to the nanotubes. In fact, previous works have already pointed out the direct relationship between the internal symmetry of the cluster (affected by the nature and number of solvate molecules accompanying the tetranuclear cluster) and its magnetic response.[8]

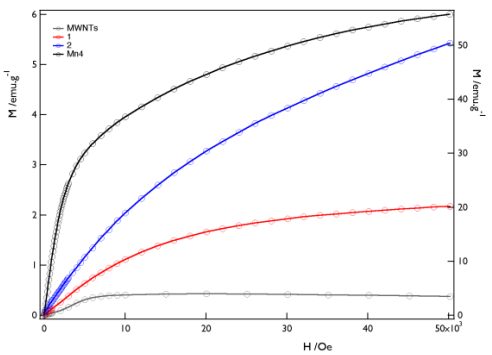

Figure 24. Isothermal field dependence of the magnetization of purified MWNTs (grey), Mn4-MWNTs hybrids 1 (red) and 2 (blue), and non-grafted Mn4 complex (black). Solid lines are only a guide to the eye.

AC dynamic magnetic measurements were carried out under an external applied field of 3.95 G (**Figure 25**). No out-of-phase signal was detected for **1** in the interval of temperatures explored. This is attributed to the small amount of Mn_4 molecules grafted through this route, which gives rise to a weak magnetic signal far below the sensitivity of conventional SQUID magnetometers. On the other hand, **2** exhibits an exponential increase in the in-phase signal (χ') which is accompanied by a positive response in the imaginary component below 5 K. Though the temperature limit does not permit observing the presence of a maximum in the χ'' signal, the position of the susceptibility tails seems to be frequency-dependent as expected for a dynamic relaxation process. These features suggest the presence of a superparamagnetic state, providing additional support to the presence of Mn_4 SMMs in the hybrid material. Still, clear differences between the hybrid **2** and the pristine Mn_4 are observed in the low *T* magnetic behavior. Hence, the blocking temperature for the latter appears at lower temperatures, *ca.* 3.5 K, and exhibits a more clear dependence of the positions of the in-phase and out-of-phase peaks with respect to the frequency. Such a difference may be probably ascribed to small structural changes in the magnetic clusters when anchored to the MWNTs as result of the chemical distortion and loss of symmetry, triggered by their contact with the carbon nanotubes. The presence of contamination traces of manganese oxides that could be responsible for the magnetic response detected at low temperatures can be discarded in view of the data. In fact, Mn_3O_4 exhibits ferrimagnetic behavior below 43 K,[18] MnO behaves as an antiferromagnet with a Néel temperature of approximately 120 K[19] and MnO_2 and Mn_2O_3 exhibit antiferromagnetic ordering below 84 and 90 K, respectively.[20]

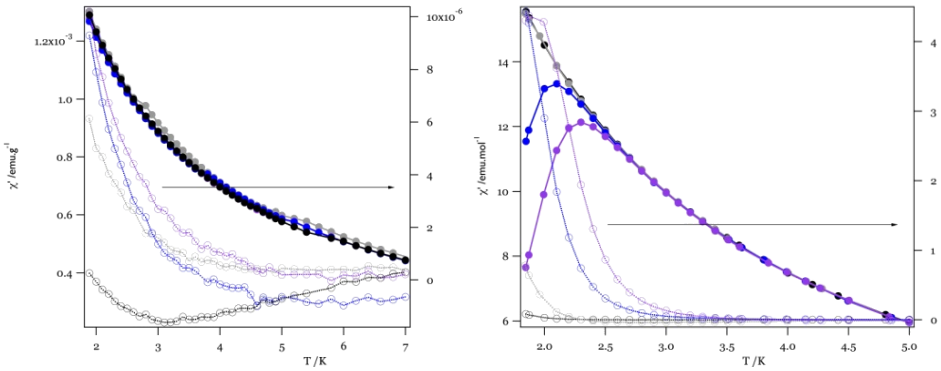

Figure 25. Ac susceptibility of the hybrid 2 (left) and the pristine Mn_4 complex (right) collected in the 1 (black), 10 (grey), 110 (blue) and 333 Hz (purple) range. In-phase susceptibility and out-of-phase signals are represented by filled and empty symbols, respectively. Solid lines are only a guide to the eye.

3.1.3. Conclusions

We have developed a new method to attach magnetic molecules (single molecule magnets) to carbon nanotubes, based on the electrostatic interactions established between the SMM and the CNT. Our approach contrasts with those reported so far, which have mainly focused on the chemical functionalization of the molecular component, while keeping intact the pristine CNTs. However this strategy neglects the important effects that the chemical treatments used for the purification of the CNTs can have on their electronic properties. In fact, these treatments, which are crucial for the removal of the magnetic particles accompanying the carbonaceous material, generally lead to a residual functionalization of the CNTs and the introduction of scattering centers in their structure. On the other hand, these methods lead to hybrids in which the magnetic molecule is far away from the carbon nanotube. For this reason, we have decided to explore an alternative approach which relies on keeping the SMM unit intact and exploring the controlled chemical functionalization of MWNTs, more robust than their single-walled counterparts, by introducing negative charges in their sidewalls through: 1) A two-step process, which includes the introduction of carboxylic groups and their subsequent deprotonation, and 2) A one-step reduction of the CNT in the presence of a metal.

Once negatively charged, the MWNTs can be readily grafted with the cationic SMMs through the presence of attractive Couloumb interactions in solution.

A first indication of the success of our method is provided by HRTEM and EDS, which show the attachment of manganese-containing molecular components whose size and composition are in good agreement with those expected for the Mn_4 clusters. Next, the chemical integrity of these nanometric objects after the grafting process has been confirmed by XPS, which show a good agreement between the spectra of the isolated hybrids and the response exhibited by the bulk Mn_4 complex. Finally, the magnetic response of the grafted molecules has been studied with conventional magnetometry. From the saturation values of the isothermal field dependence of the magnetization we can conclude that route **2** produces a larger degree of grafting than **1**. This is additionally confirmed by HRTEM images, EDS spectroscopy and XPS experiments. Besides, the deviation of the M *vs* H curves and the dynamic ac susceptibility measurements with respect to the behavior exhibited by the bulk Mn_4 cluster, suggests that its magnetic response is significantly affected by the grafting process, via surface effects.

Further work will involve an in-depth study of the electronic transport properties of these hybrids, along with the use of single-walled carbon nanotubes. Additionally, we aim to introduce polyaromatic linkers in the organic shell of the Mn_4 cluster to enable its supramolecular grafting on CNTs, in agreement with the commonly used methodology. The physical characterization of these complementary hybrids should provide further insights on the environmental effects affecting the magnetic properties of this particular SMM when grafted onto nanotubes.

3.1.4. Experimental

3.1.4.1. General synthesis remarks.

MWNTs were purchased from Thomas Swan & Co. LTD (Elicarb MW-PR0940). Reactions requiring inert conditions were conducted under argon atmosphere, employing oven-dried glassware (100°C). Acetonitrile and THF were dried over $CaCl_2$ and sodium, respectively whilst the rest of the reagents were used

as received from commercial suppliers. The samples were filtered employing a vacuum filter funnel of pore size number 3 , and either hydrophobic PFTE membrane filters (Ø 0.45 μm pore) or cellulose nitrate membrane filters (Ø 0.8 μm pore). The ultrasounds were achieved with a Bransonic 5510E-MT operating at 135W.

3.1.4.2. Synthesis procedure.

Synthesis of $[Mn_4(OAc)_2(pdmH)_6](ClO_4)_2$ (pdmH = deprotonated pyridine-2,6-dimethanol; $C_5H_4NO_2$).

The tetranuclear cluster of Mn was synthesized according to the method previously described by Yoo et al.[8] with minor modifications. In a first step, $[Mn_3O(O_2CMe)_6(py)_3](ClO_4)$ (py = pyridine; C_5H_5N) was prepared as described elsewhere[21]. Next, 1g of this complex (1.1 mmol) was dissolved in 75 mL of CH_2Cl_2 to afford a very dark brown solution. 480 mg of $pdmH_2$ (3.4 mmol) were then thoroughly suspended in another 75 mL of dichloromethane and the mixture gradually poured over the first. The slurry was mechanically stirred overnight at room temperature to allow for complete precipitation of the cluster perchlorate salt. Finally, the insoluble fine brownish powder formed was separated from its deep-brown supernatant by filtrating in vacuum and washing with dicholoromethane until clear colourless filtrate was observed. The solid was thoroughly dried *in vacuo* overnight and recovered as ready-to-use ochre flour. Anal. calc. (%) for $C_{46}H_{54}Cl_2Mn_4N_6O_{24}\cdot 2.5H_2O$ (M_W = 1365.6): N, 5.96; C 39.17; H, 4.22. Found (%): N, 5.80; C, 39.00; H, 3.97. FT-IR (cm^{-1}): 3423,4 (m, br), 2913,1 (w), 2650,7 (w), 1604,5 (m, sh), 1578,3 (m, sh), 1462,4 (m, sh), 1445,8 (m, sh), 1387,0 (m, sh), 1330,6 (m, sh), 1237,7 (w, sh), 1205,0 (w, sh), 1161,0 (w, sh), 1103,6 (st, sh), 1070.9 (s, br), 1008,9 (m, sh), 928,1 (w, sh), 790,5 (m, br), 743,2 (w), 690,7 (m, sh), 669,5 (m, sh), 624,4 (m, sh), 574,0 (m), 547,7 (m), 530,8 (m), 478,9 (m), 453,1 (m), 443,9 (m), 434,5 (m) [where: st (strong), m (medium), w (weak); and: broad (br), sharp (sh)].

Route 1.

The indirect attachment of the Mn4 cluster to the nanotubes is accomplished through a two-step process: a) Introduction of carboxylic groups to the MWNTs and their further deprotonation in basic medium and b) Combination of the cationic Mn4 complex with the previously generated anionic nanotubes.

a) Functionalization of MWNTs with carboxylic groups. Typically, 3 g of MWNTs were refluxed for 4.5 hours in 420 mL of HNO_3 2.6 M. Next, the mixture was left to cool at room temperature, the solution was centrifuged and finally the supernatant acid was decanted off. Afterwards, the resulting black solid was sequentially re-suspended in water and centrifuged until the pH of the supernatant solution reached neutrality. Finally, deprotonation of the as-prepared MWNT-COOH was accomplished by re-suspending them in 500 mL of water containing 7 mL of Titron X-100 surfactant, and carefully adding an aqueous solution of sodium hydroxide until pH 10 was achieved. Finally the carbon-based material was filtered off under vacuum over a cellulose nitrate membrane (pore size of 0.8 μm) and thoroughly cleaned with deionized water.

The concentration of carboxylic groups was estimated through acid-base titration [13, 22]. In a typical procedure, 50 mg of MWNT-COOH were suspended in 25 mL of $NaHCO_3$ (aq) and stirred for 48 hours. Afterwards, the deprotonated nanotubes were filtered off over a cellulose nitrate membrane, and washed up with deionized water. Finally, 25 mL of HCl (aq) 0.05 M were added to the filtrated solution and the mixture was boiled during 20 minutes to degas it. The excess of acid was backwards titrated using NaOH (aq) 0.05 M.

*b) Preparation of the Mn4-MWNT hybrid (**1**).* 4 mg of previously deprotonated MWNT-COO^- were suspended in 40 mL of acetonitrile, and subjected to sequential cycles of ultra-sounds for 30 minutes. Next, 10 mg (7 μmol) of $[Mn_4(OAc)_2(pdmH)_6](ClO_4)_2$ were added, and the brownish mixture mechanically stirred at room temperature for 3 days. Finally, the carbon-based black solid was filtered over a PFTE membrane in vacuum, washed thoroughly with acetonitrile and dried under vacuum.

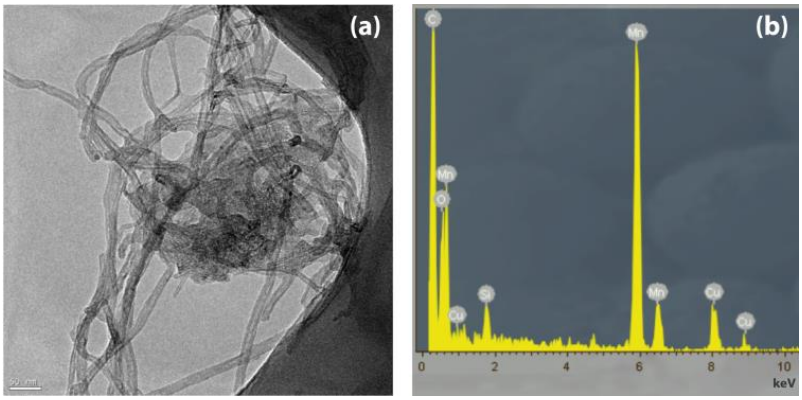

Figure 26. HRTEM image (a) and EDX spectrum (b) collected from a fraction of 1 subjected to a softer cleaning procedure.

Additional experiments were devoted to outline the critical importance that the cleaning protocol used has in determining the nature of the resulting hybrid nanocomposite. In this regard, a little fraction of the hybrid **1** was separated after the Mn_4 loading and subjected to softer cleaning, which did not include continuous cycles of ultrasounds. **Figure 26** displays a more bundled material accompanied by the presence of numerous dark islands, which, on basis of the EDS analysis, turned out to be mainly composed by manganese therefore indicating that the main part of the Mn_4 cluster added was co-precipitated but not directly attached to the carbon material. This heterogeneous distribution is far from the ideal situation, where the molecular component must be exclusively grafted on the MWNTs, and hence important efforts were devoted to remove these contaminant islands via exhaustive cleaning protocols.

Route 2.

Direct attachment of the Mn4 cluster to the nanotubes was accomplished in one step by combining the cationic complex with anionic MWNTs generated *in situ.*

*Preparation of the Mn4-MWNT hybrid (**2**).* According to a previously reported method [23], 7 mg of granular lithium (1 mmol) were added to a flask purged with argon, containing 12 mg of commercial grade MWNT and 26 mg of 4,4-

ditertbutylbiphenyl (DTBP) (0.1 mmol) in 10 mL of THF anhydrous. The mixture was sonicated during 1 hour, to facilitate the lithium dissolution. Once the metal was dissolved, a solution containing 100 mg (70 µmol) of the Mn4 cluster in 5 mL of acetonitrile was added and the mixture subjected to continuous sonication at room temperature overnight. After evaporation of the solvent under reduced pressure, the black solid was thoroughly washed, successively with dichloromethane and acetonitrile, and finally filtrated in vacuum over a PFTE membrane.

3.1.4.3. Physical characterization.

FT-IR spectrum were acquired from a FT-IR Nicolet 5700 spectrometer in the 4000-400cm^{-1} frequency range, using powdered samples diluted in KBr pellets.

Thermogravimetric analysis were carried out with a Mettler Toledo TGA/SDTA 851 apparatus in the 25-800 Cº temperature range under a 30 $mL.mol^{-1}$ air flow and a 10 K min^{-1} scan rate.

Electron spectroscopy for chemical Analysis (ESCA) and X-ray photoelectron spectroscopy (XPS), were performed using a Thermo Scientific K-Alpha ESCA instrument equipped with aluminium Ka1,2 monochromatized radiation at 1486.6 eV X-ray source. The non-conductive nature of the samples made necessary to use an electron flood gun to minimize surface charging. Neutralization of the surface charge was performed by using a low energy flood gun (electrons in the range 0 to 14 eV) and a low Argon ions gun. The XPS measurements were carried out using monochromatic Al-K radiation (h=1486.6 eV). Photoelectrons were collected from a take-off angle of 90° relative to the sample surface. The measurement was done in a Constant Analyser Energy mode (CAE) with a 100 eV pass energy for survey spectra and 20 eV pass energy for high resolution spectra. Charge referencing was done by setting the lower binding energy C 1s photo peak at 285.0 eV C1s hydrocarbon peak.[24]. Surface elemental composition was determined using the standard Scofield photoemission cross sections.

HRTEM images were obtained in a JEOL JEM 2010F high-resolution field emission transmission electron microscope. High angle annular dark field scanning transmission electron microscopy (HAADF-STEM) images shows mass-thickness contrast, corresponding the brighter areas to the presence of heavier elements; these

images were obtained coupling the annular detector to the STEM unit. STEM-XEDS elemental maps show the relative distribution of the elements, and were obtained coupling the STEM unit to the EDS detector. In the images, the red areas correspond to C (C Kα line), and green areas correspond to Mn (Mn Kα line); background was subtracted in the map.

AFM images were taken using an AFM commercial multimode III from Veeco. The MWNT were deposited into a HOPG (High Oriented Pirolytic Graphite) surface, and the measurements were taken using a silica tip (frequency 300KHz, K=40N/m), at room temperature in ambient conditions.

Magnetic measurements were performed using a Quantum Design (SQUID) Magnetometer MPMS-XL-5. The dc data were collected under an external applied field of 1000 G in the 2-300 K temperature range. The susceptibility data were corrected from the diamagnetic contributions of the atomic constituents of the samples as deduced by using Pascal's constant tables and the samples holder. Magnetization studies were performed between -5 and +5 T at a constant temperature of 2 K. The dynamic ac susceptibility data were collected in the 2-14 K range with an applied alternating field of 3.95 G at different frequencies between 1 and 333 Hz.

3.2. Polyoxometalate - Single-Walled Carbon Nanotube Hybrids by Supramolecular Grafting.

3.2.1. Introduction

Polyoxometalates (POM) are polynuclear metal-oxo clusters that possess considerable structural and composition versatility, which enables fine tuning of their electronic properties and of their functionality. So far many different POMs have been synthesized and employed in different areas such as catalysis, spintronics, molecular materials science and molecular magnetism.[25] Their interest arises from their excellent redox character, unique molecular structure, huge electronic versatility and chemical versatility. Due to these unique characteristics and robustness, POMs have been commonly employed for the creation of hybrid organic-inorganic materials and devices that may display advanced functions.[26]

So far, hybrid organic-inorganic systems composed by CNTs and POMs have been developed for different purposes. For example, Chen et al. synthesized a hybrid between CNT and $H_7PMo_{12}O_{42}$ and employed it in the catalysis of methanol electro-oxidation.[27] Besides, Mallah *et al.* succeed in creating two different hybrids based in magnetic POMs, namely $[As_2W_{20}O_{68}Co(H_2O)]^{8-}$ and $[Fe_4(H_2O)_2(FeW_9O_{34})2]^{6+}$,[6] oriented to the development of model spintronic devices. In all these examples, the driving force employed for the anchoring of the POM was simple chemisorption of the POM over the chemically unmodified nanotubes, but to date no work regarding other possible bindings between POMs and CNTs have been developed. Besides, as thoroughly described along the previous chapters, π-π interactions have been widely employed as the driving force for the synthesis of hybrids with CNTs. Importantly, this kind of interactions have been commonly employed in hybrids oriented towards the development of photophysical devices, as they would permit the interaction between both specimens without affecting to the electronic properties of the CNTs. For example, a modified fullerene with pyrene units has been employed to form a hybrid with CNTs, the hybrid showed electronic interaction between the pyrene part of the fullerene with the CNTs.[28] Another example used pyrene-modified quantum dots with similar purposes.[29] Some other examples employed phtalocianines, tethrathiafulvalenes and some other active

molecules, all of them having a highly conjugated π-π core, to develop photophysical properties.[30]

In this work, in collaboration with the group of Professor Anna Proust, we have employed a POM modified with pyrene units ({$(TBA)_6(P_2W_{17}O_{61}$\{O(Si-Ph-ethylpyrene))$_2$\} = POM(pyr)) (**Figure 27**) to obtain a hybrid with SWNTs. Interestingly we have been able to observe for the first time a POM with atomic resolution over CNTs by employing HR-TEM and complementary techniques (HAADF-STEM, BF-STEM). Currently, the photophysical properties are being measured by the group of Professor Dirk Guldi.

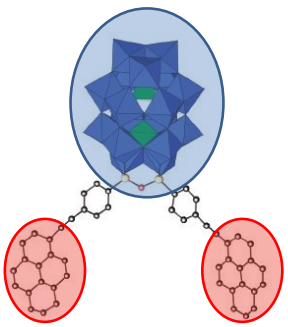

Figure 27. Representation of the POM(pyr) employed for the synthesis of the hybrid. The photophysic core (POM) is marked with a blue circle, while the anchoring moieties (pyrene units) are indicated with a red circle.

3.2.2. Results and Discussion

3.2.2.1. Synthesis of the hybrid

In this case we have chosen the π-π stacking as the driving force to carry out the binding between the SWNT and the polyoxometalate (POM). With this aim, a POM modified with pyrene moieties (POM(pyr)) has been employed. This POM was provided by the group of Professor Anna Proust from Paris and used as-received. [31] It is easily obtained from its iodo-silyl counterpart following a Sonogashira coupling. SWNTs have been chosen because they have been better characterized and they possess characteristic fingerprints in many analytical and

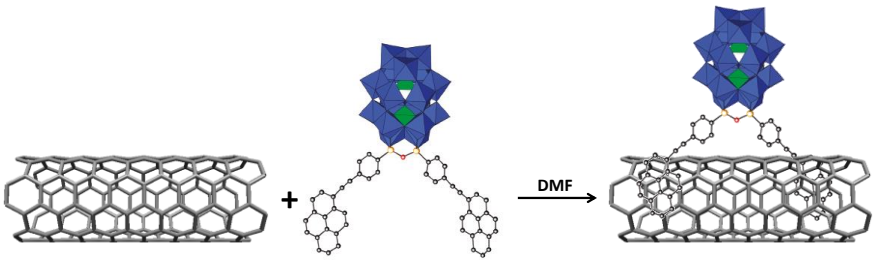

Scheme 6. Chemical route followed for the π-π stacking of POM(pyr) onto unmodified SWNT.

spectroscopic techniques which, upon with its electron transport features, makes them more adequate for charge-transfer proposes. In addition, as no modification of the walls is needed, no alteration of their electronic properties will be produced before and after the grafting process, thus making them suitable for photophysical studies. In fact, a charge transfer between the POM and the SWNT has to be expected that should be detected in the photophysical properties of the hybrid.

The interaction between SWNT and POM(pyr) is done by simply mixing both systems in an adequate solvent (**Scheme 6**). Prior to all the physical characterization, the hybrid is thoroughly washed in order to get rid of the non-attached POM.

3.2.2.2. Anchoring of POM molecules

Thermogravimetric analysis was employed to get information on the POM loading over the SWNT. As it was expected, the thermal decomposition of the hybrid SWNT@POM under ambient conditions shows a very similar behavior to that presented by pristine nanotubes having a main decomposition temperature placed at 550 ºC and 580 ºC respectively (**Figure 28a**). Those temperatures are in good agreement with the maintenance of the graphitic-like structure of the SWNT. In addition, from the remaining mass of the hybrid with respect the pristine CNTs the percentage of functionalization can be estimated to be ca. 10% (one POM(pyr) per 4590 carbon atoms).

Raman spectroscopy was employed to check the integrity of the CNT in the hybrid. As shown in **Figure 28b** the hybrid shows the same spectra as the pristine nanotubes. Both spectra present three main peaks, one centered around 1590 cm^{-1}

that is associated to the G band, the second peak which correspond with the D band appears at 1340 cm^{-1}, and the last one at 2665 cm^{-1} related to the 2D band, which is an overtone of the D band. This pattern is common for all graphitic like forms. The G band can be associated to the E_{2g} vibrational modes being characteristic of highly conjugated sp^2 systems; the D band is activated by the presence of defects and tends to diminish in defect free graphitic materials.[32] Besides, in the case of CNTs the presence of the D band may stem from the chiral angle and the diameter of the tube.[33] Although it is not easy to distinguish between single and multi-walled nanotubes, the clear difference in intensity between the D and G bands,[34] and the sharpness of the G band,[35] along with the observation of the RBM at frequencies as low as 170 cm^{-1}, points out to the presence of SWNT with a low defect content in both cases (pristine SWNT and the hybrid sample).

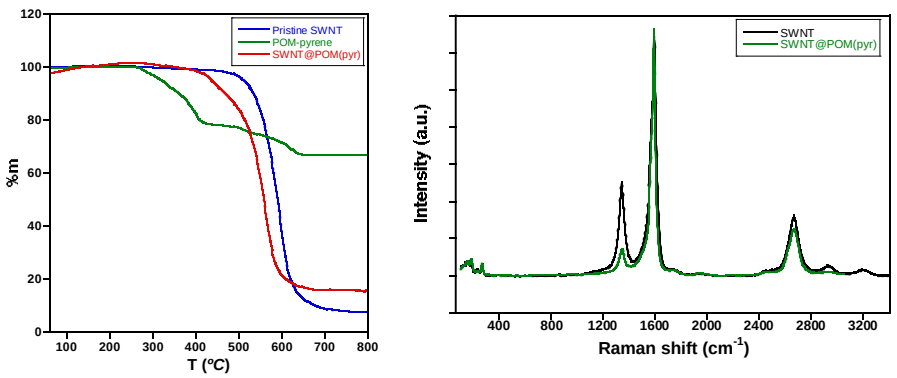

a b

Figure 28. a) Thermogravimetric analysis under ambient conditions of pristine SWNT (blue), POM(pyr) (green) and the hybrid SWNT@POM(pyr). b) µRaman spectra of pristine SWNT (black) and the hybrid SWNT@POM(pyr).

3.2.2.3. X-Ray Photoelectron Spectroscopy

XPS experiments provided evidence for the grafting of POM on the SWNTs with binding energies for the W in agreement with the expected bonding states. **Table 3** summarizes the binding energies (BE) as extracted from high-resolution XPS spectra.

Table 3. Chemical bonding binding energy (BE) extracted from high-resolution XPS spectra

Sample	W4f (BE, eV)	
	W4f7	W4f5
POM	35.43	37.53
SWNT@POM	35.62	37.68

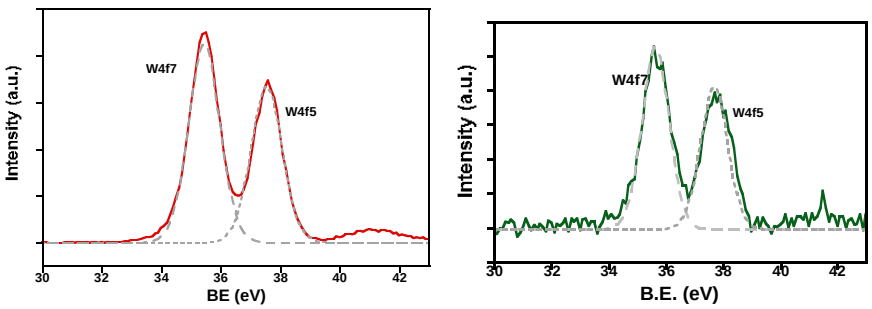

Figure 29. W4f high-resolution XPS spectra of pristine POM (left) and SWNT@POM (right).

According to **Figure 29**, the W4f signal exhibited by the hybrid is in good agreement with the data collected from a crystalline sample of the pristine POM, providing a strong indication of the grafting success. In both cases, the W4f spectra (**Figure 29**) display two dominant peaks between 35 and 38 eV, which can be assigned to the spin–orbit splitting into the W4f7 and W4f5 levels with an energy splitting of ~2.1 eV. This values are in good agreement with the presence of W-O bonds in both samples, and points to the presence of POM in the hybrid sample.

3.2.2.4. Electron Microscopy and EDS analysis

High resolution transmission microscopy (HR-TEM) of the hybrid SWNT@POM shows the presence of bundles which are mainly composed by carbon that comes from the SWNTs, and Si and W which confirms the presence of POM in the sample (**Figure 30**). In addition, BF-STEM and HAADF-STEM were performed in order to identify the place in which the POMs were in the sample. As shown at

Figure 31, in the HAAF-STEM some bright spots were observed decorating the walls of the CNTs. Those bright spots must be assigned to metals, and have a section of 1.4-1.9 nm which can be associated to the POM, thus meaning that the grafting has taken place and that the POM remains intact upon anchoring on the CNTs.

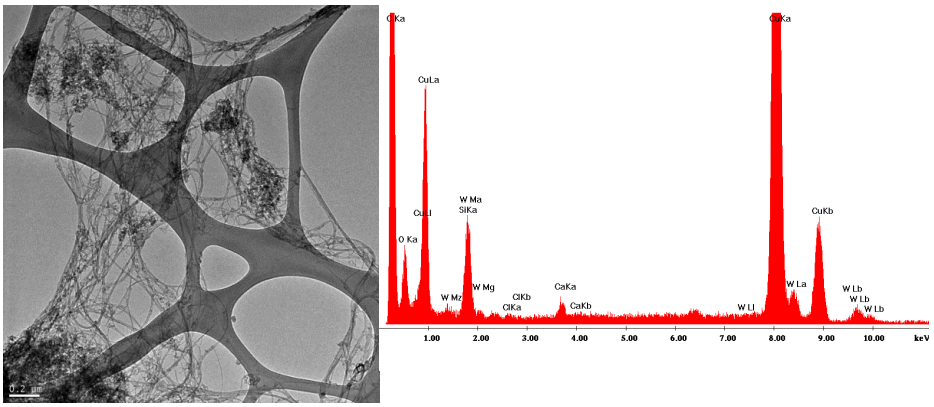

Figure 30. (*left*) HR-TEM image of SWNT@POM. (*right*) Microanalysis performed over the sample SWNT@POM showing the presence of Si and W from the POM molecule. The Copper signal is due to the TEM grid.

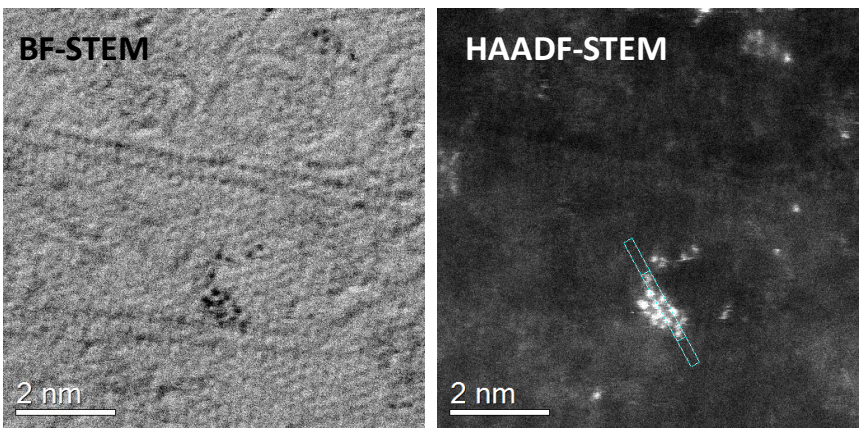

Figure 31. BF-STEM and HAADF-STEM images showing the presence of POMs (bright spots) of 1.4-1.9 nm along the walls of the CNTs.

3.2.3. Conclusions

A hybrid between a POM modified with pyrene substituents and SWNT has been successfully obtained. The interaction between both components has been done taking advantage of the affinity between pyrene units and the walls of the nanotubes. TGA experiments have shown that a 10 % of functionalization has been achieved. In addition, we have confirmed the stability of the SWNT after the grafting process by the use of μ- Raman spectroscopy. Finally, it has been possible to visualize for the first time a POM down to the atomic level by the employment of HR-TEM along with HAADF-STEM and BF-STEM. The dimensions and the microanalysis performed over the isolated POM demonstrate its presence and confirm the binding over the SWNTs.

Future work will involve the study of the photophysical properties of the described hybrid. In fact, they are currently being carried out by the group of Professor Dirk Guldi.

3.2.5. Experimental

3.2.5.1. General synthesis remarks

Single Walled Nanotubes (SWNTs) were purchased from Thomas Swan ¬ Co. LTD. The samples were filtered employing a vacuum filter funnel pore size 3, and nylon membrane filters (ø 0.2 μm pore). The ultrasound conditions were achieved with a Brandson 5510E-MT operating a 135 W.

3.2.5.2. Synthesis procedure

Synthesis of ({(TBA)$_6$(P$_2$W$_{17}$O$_{61}${O(Si-Ph-ethylpyrene))$_2$} = POM(pyr)

The POM(pyr) was synthesized by the group of Anna Proust following the described procedure at reference [31]. In a typical procedure, POM(pyr) is obtained in two steps from *(TBA)$_6$[P$_2$W$_{17}$O$_{62}${O(Si-PhI)$_2$}] (TBA-1D).*

(TBA-1D). K$_{10}$[α$_2$-P$_2$W$_{17}$O$_{61}$] 20 H$_2$O (2 g, 0.407 mmol, 1 equiv) was set insuspension in a 30 mL mixture of acetonitrile/water (2/1). The apparent pH of the

suspension was fixed at 2 by dropwise addition of 1 M hydrochloric acid at 0 ºC. 1-Iodo-4-(triethoxysilyl)benzene (600 mg,1.628 mmol, 4 equiv) was added at -20 ºC. After being stirred for 2 h at this temperature the solution was stirred at room temperature under air atmosphere overnight. TBABr (920 mg, 2.86 mmol, 7 equiv) was then added to precipitate the polyoxometalate as a tetrabutylammonium salt. After partial evaporation of the acetonitrile, the crude solid was recovered by centrifugation. For purification purposes, the compound was dissolved in acetonitrile and ethanol was then added in similar volume to initiate precipitation. After removal of the precipitate by filtration, the filtrate was precipitated by further addition of Et_2O. The obtained solid was finally dissolved in dichloromethane and filtered on a small column of Sephadex LH20, using dichloromethane as eluant. After evaporation of the solvent TBA-1D was obtained as a white powder. Yield: 90%. ^{1}H NMR (CD3CN): δ 7.76 (d, J = 8.1 Hz, 4H), 7.58 (d, J =8.1 Hz, 4H), 3.15 (m, 48H), 1.64 (m, 48H), 1.41 (sextuplet, 7.2 Hz, 48H), 0.99 (t, J = 7.2 Hz, 72H).31P NMR (CD3CN): δ 9.22 and12.19 ppm. MS (ESI): most intense peaks, {aggregates}$^{-x}$m/z (%):{H[1D]}$^{-5}$928.5 (64), calcd 928.1; {TBA[1D]}$^{-5}$976.8 (100), calcd 976.6; {H,TBA[1D]}$^{-4}$1220.4 (4), calcd 1221.2; {TBA2[1D]}$^{-4}$1281.6 (11), calcd 1281.8; IR (KBr, cm^{-1}): ν 2962 (s), 2935 (s),2874 (s), 1570 (m), 1483 (s), 1378 (m), 1151 (m), 1124 (s), 1089 (s),1042 (s), 988 (m), 955 (s), 916 (s), 813 (s), 767 (s), 722 (sh), 598 (m),562 (m), 529 (s), 389 (s), 353 (s), 330 (s). Calcd elemental analysis for $P_2W_{17}O_62Si_2I_2C_{108}H_{224}N_6$ (%): C 21.28, H 3.70, N 1.38. Found: C21.17, H 3.67, N 1.38.

POM(pyr). A mixture of TBA-1D (300 mg, 0.05 mmol, 1 equiv), 1-ethynylpyrene (28 mg, 0.125 mmol, 2.5 equiv), $Pd(PPh_3)_2Cl_2$(0.005mmol, 10 mol %), and CuI (0.0075 mmol, 15 mol %) in 5 mL of driedand freshly distilled DMF was prepared. After careful degassing with argon for 10 min, freshly distilled Et_3N (1 mmol, 20 equiv) was added. The mixture was stirred at 70 ºC for 40 min under microwave irradiation. After cooling to room temperature $TBABr_3$ (24 mg, 0.05 mmol, 1 equiv) and TBABr (20 equiv) in 30 mL of CH_2Cl_2 were added to the mixture under argon. The solution was washed 4 times with water and precipitated with diethyl ether. The obtained solid was finally dissolved in DMSO and

precipitated with EtOH to obtain POM(pyr) as a clear yellow/brown solid. Yield: 94%. ^{1}H NMR (DMSO-d_6): δ 8.69 (d, J = 9.1 Hz, 2H), 8.338.42 (m, 10H), 8.27 (d, J = 9.0 Hz, 2H), 8.23 (d, J = 9.0 Hz, 2H), 8.13 (t, J = 7.7 Hz, 2H), 7.91 (d, J = 8.1 Hz, 4H), 7.80 (d, J = 8.1 Hz, 4H), 3.16 (m, 48H), 1.57 (m, 48H), 1.33 (sextuplet, 7.2 Hz, 48H), 0.93 (t, J = 7.2 Hz, 72H). ^{31}P NMR (DMSO-d_6): δ 9.31 and12.32 ppm. MS (ESI): most intense peaks, {aggregates}$^{-x}$m/z (%):{POM(pyr)}$^{-5}$ 968.2 (80), calcd 968.0; { POM(pyr)}$^{-5}$1016.2 (100), calcd 1015.6; {H, POM(pyr)}$^{-4}$1270.0 (6), calcd 1270.0. IR (KBr, cm^{-1}): ν 2961 (s), 2933 (s), 2873 (s), 2205 (vw), 1600 (w), 1483 (m), 1380 (m), 1150 (w), 1119 (s), 1089 (s), 1041 (s), 1018 (w), 988 (sh), 954 (s), 916 (s), 812 (s), 765 (s), 720 (sh), 688 (w), 581 (w), 528 (m), 391 (m). Calcd elemental analysis for $P_2W_{17}O_{62}$ $Si_2C1_{44}H_{242}N_6$ (%): C 27.48, H 3.88, N 1.34. Found: C 27.24, H 3.75, N 1.34.

Synthesis of SWNT@POM(pyr)

The hybrid was obtained as follows; 6 mg of SWNTs were dispersed in 24 mL of DMF by applying ultrasounds during 30 minutes (Brandsonic 5510). Afterwards, 8mg of POM were added to the above mixture and the slurry stirred during 4 hours. Then, the mixture was left to settle down during one night, and the nanotubes were washed by dispersing them first with DMF and secondly with acetonitrile with the aid of ultrasounds. Finally, SWNT@POM were isolated by filtering through a nylon membrane filter (0.2 μm pore size) and washing them with acetonitrile and with ethanol.

3.2.5.3. Physical characterization

HR-TEM images were obtained using a TECNAI G2 F20 microscope. Field Emission Gun (FEG)200 kV.

Thermogravimetric analysis was carried out with a Mettler Toledo TGA/SDTA 851 apparatus in the 25-800^{o}C temperature range under air aotmosphere and at 10K min^{-1} scan rate.

X-ray photoelectron spectroscopy (XPS) measurements were performed in an ultra-high vacuum system ESCALAB210 (base pressure 1.0x10^{-10} mbar) from

Thermo VG Scientific. Photoelectrons were excited by using the Mg-Kα line (1253.6 eV). All spectra have been referred to the Fermi level.

μ-Raman measurements at room temperature were performed with a dispersive Jobin-Yvon LabRam HR 800 microscope, working with an excitation line of 532 nm. The scattered light was detected with a thermoelectric cooled (-70 ºC) charge coupled device detector (CCD). It also has an Olympus BXFM optic microscope. All the measurements were carried out directly over the sample. In the performed experiments, the power employed over the samples was of the order of 0.3 mW, and the exposition time 60 seconds.

3.3. References

[1] a) R. Sessoli, D. Gatteschi, A. Caneschi, M. A. Novak, *Nature* **1993**, *365*, 141; b) D. Gatteschi, R. Sessoli. *Angew. Chem. Int. Ed.* **2003**, *42*, 268.

[2] a) N.Ishikawa, M. Sugita, T. Ishikawa, S. Koshihara, Y. J. Kaizu, *J. Am. Chem. Soc.* **2003**, *125*, 8694; b) M. A. Aldamen, J. M. Clemente-León, E. Coronado, C. Martí-Gastaldo, A. Gaita-Ariño, *J. Am. Chem. Soc.* **2008**, *130*, 8874.

[3] a) E. Coronado, J. Camarero, *J. Mat. Chem.* **2009**, *19*, 1678; b) M. N. Leuenberger, D. Loss Nature **2001**, *410*, 789.

[4] L. Bogani, W. Wernsdorfer, *Nature Mater*., **2008**, *7*, 179.

[5] a) P. G. Collins, K. Bradley, M. Ishigami, A. Zettl, *Science* **2000**, *287*, 1801; b) S. Sanvito, A. R. Rocha, *J. Comput. Theor. NanoSci.* **2006**, *3*, 624; c) B. L. Allen, P. D. Kichambare, A. Star, *Adv. Mater.* **2007**, *19*, 1439.

[6] a) A. Giusti, G. Charron, S. Mazerat, J.-D. Compain, P. Mialane, A. Dolbecq, E. Rivière, W. Wernsdorfer, R. N. Biboum, B. Keita, L. Nadjo, A. Filoramo, J.-P. Bourgoin, T. Mallah., *Angew. Chem. Int. Ed.* **2009**, *48*, 4949. b) G. Charron, A. Giusti, S. Mazerat, P. Mialane, A. Gloter, F. Miserque, B. Keita, L. Nadjo, A. Filoramo, E. Rivière, W. Wernsdorfer, V. Huc, J.-P. Bourgoin, T. Mallah, *Nanoscale*, **2010**, *2*, 139.

[7] a) L. Bogani, C. Danieli, E. Biavardi, N. Bendiab, A.-L. Barra, E. Dalcanale, W. Wernsdorfer, A. Cornia, *Angew. Chem. Int. Ed.* **2009**, *48*, 746; b) S. Kyatskaya, J. R. Galán-Mascarós, L. Bogani, F. Henrich, M. Kappes, W. Wernsdorfer, M. Ruben, *J. Am. Chem. Soc.* **2009**, *131*, 15143.

[8] J. Yoo, E. K. Brechin, A. Yamaguchi, M. Nakano, J. C. Huffman, A. L. Maniero, L.-C. Brunel, K. Awaga, H. Ishimoto, G. Christou, D. N. Hendrickson, *Inorg. Chem.* **2000**, *39*, 3615.

[9] H. Miyasaka, K. Nakata, K. Sugiura, M. Yamashita, R. Clerac, *Angew. Chem. Ed.* **2004**, *43*, 707.

[10] a) B.K. Price, J. R. Lomeda, J. M. Tour, *Chem. Mater.* **2009**, *21*, 3917; b) B. Smith, K. Wepasnick, K. E. Schrote, H-H. Cho, W. P. Ball, D. H. Fairbrother, *Langmuir* **2009**, *25*, 9767.

[11] H. Peng, L. B. Alemany, J. L. Margrave, V. N. Khabashesku, *J. Am. Chem. Soc.* **2003**, *125*, 15174.

[12] H. Igarashi, H. Murakami, Y. Murakami, S. Maruyama, N. Nakashima, *Chem. Phys. Lett.* **2004**, *392*, 529.

[13] H. Hu, P. Bhowmik, B. Zhao, M. A. Hamon, M. E. Itkis, R. C. Haddon, *Chem. Phys. Lett.* **2001**, *345*, 25.

[14] L. Bogani, W. Wernsdorfer, *Inorg. Chim. Acta* **2008**, *361*, 3807.

[15] M. Fukiwara, T. Matsushita, S. Ikeda *J., Electron Spectrosc. Relat. Phenom.* **1995**, *74*, 201.

[16] V. Dicastro, G. Polzonetti, *J. Electron Spectrosc. Relat. Phenom.* **1989**, *48*, 117.

[17] G. Charron, A. Giuti, S. Mazerat, P. Mialane, A. Gloter, F. Miserque, B. Keita, L. Nadjo, A. Filoramo, E. Rivière, W. Wernsdorfer, V. Huc, J.-P. Bourgoin, T. Mallah, *Nanoscale* **2010**, *2*, 139.

[18] I. S. Jacobs, *J. Phys. Chem. Solids* **1959**, *11*, 1.

[19] G. Srinivisan, M. S. Seehra, *Phys. Rev. B* **1983**, *28*, 6542.

[20] M. Regulski, R. Przenioslo, I. Sosnowska, D. Holwein, R. Schneider, *J. Alloy Compd.* **2004**, *362*, 236.

[21] J. B. Vincent, H.-R. Chang, K. Folting, J. C. Huffman, G. Christou, D. N. Hendrickson, *J. Am. Chem. Soc.* **1987**, *109*, 5703.

[22] S. C. Tsang, Y. K. Chen, P. J. F. Harris, M. L. H. Green, *Nature* **1994**, *372*, 159.

[23] A. García-Gallastegui, I. Obieta, I. Bustero, G. Imbuluzqueta, J. Arbiol, J. I. Miranda, J. M. Aizpurua, *Chem. Mater.* **2008**, *20*, 4433.

[24] D. Briggs, M. P. Seah, *Practical Surface Analysis* Vol. 1, 2 ed., Wiley,**1990**.

[25] a) M. Clemente-Leon, E. Coronado, C. Martí-Gastaldo, F.M. Romero, *Chem. Soc. Rev.*, **2011**, *40*, 473. b) S. Cardona-Serra, J.M. Clemente-Juan, E. Coronado, A. Gaita-Ariño, A. Camon, M. Evangeliste, F. Luis, M.J. Martinez-Perez, J. Sese, *J. Am. Chem. Soc.*, **2012**, *134*, 14982. c) D.-L. Long, E. Burkholder, L. Cronin, *Chem. Soc. Rev.*, **2007**, *36*, 105.

[26] a) J.M. Clemente-Juan, E. Coronado, A. Gaita-Ariño, *Chem. Soc. Rev.*, **2012**, *41*, 7464. b) D.-L. Long, E. Burkholder, L. Cronin, *Chem. Soc. Rev.*, **2007**, *36*, 105. c) A. Proust, R. Thouvenot, P. Gouzerh, *Chem. Commun.*, **2008**, *16*, 1837. d) A. Dolbecq, P. Mialane, B. Keita, L. Nadjo, *J. Mater. Chem.*, **2012**, *47*, 24509

[27] D. Pan, J. Chen, W. Tao, L. Nie, S. Yao, *Langmuir*, **2006**, *22*, 5872.

[28] D.M. Guldi, E. Menna, M. Maggini, M. Marcaccio, D. Paolucci, F. Paolucci, S. Campidelli, M. Prato, G.M. Aminur Rahman, S. Schergna, *Chem. Eur. J.*, **2006**, *12*, 3975.

[29] C. SchulzDrost, V. Sgobba, C. Gerhards, S. Leubner, R.M. Krick Calderon, A. Ruland, D.M. Guldi, *Angew. Chem. Int. Ed.*, **2010**, *49*, 6425.

[30] a) C. Romero-Nieto, R. Garcia, M.A. Herranz, C. Ehli, M. Ruppert, A. Hirsch, D.M. Guldi, N. Martin, *J. Am. Chem. Soc.*, **2012**, *134*, 9183. b) C. Oelsner, C. Schmidt, F. Hauke, M. Prato, A. Hirsch, D.M. Guldi, *J. Am. Chem. Soc.*, **2011**, *133*, 4580. c) U. Hahn, S. Engmann, C. Oelsner, C. Ehli, D.M. Guldi, T. Torres, *J. Am. Chem. Soc.*, **2010**, *132*, 6392.

[31] B. Matt, S. Renaudineau, L.-M. Chamoreau, C. Afonso, G. Izzet, A. Proust, *J. Org. Chem.*, **2011**, *76*, 3107.

[32] C. Bosch-Navarro, E. Coronado, C. Martí-Gastaldo, J.F. Sánchez-Royo, M. Gómez-Gómez, *Nanoscale*, **2012**, *4* (13), 3977-3982

[33] L. Deng, *Raman Spectroscopic Studies of Carbon Nanotube Composite Fibres*, University of Manchester, 2010.

[34] S. Costa, E. Borowiak-Palen, M. Kruszynska, A. Bachmatiuk, R. J. Kalenczuk, *Materials Science-Poland*, **2008**, *26*, 433.

[35] P.H. Tan , C.Y. Hu , F. Li , S. Bai , P.X. Hou , H.M. Cheng, *Carbon*, **2002**, *40*, 1131.

4 Chemical Synthesis of Graphene*†

This chapter covers different strategies that enable the chemical synthesis of graphene. First, we will explore the "top-down" synthesis of graphene by hydrothermal reduction of GO, highlighting the vital role played by the pH in controlling the morphology and quality of the resulting rGO sheets. Next, by following a "bottom-up" approach, we report the synthesis of graphite from the fusion of sublimable polyaromatic molecules like anthracene. Finally, we will illustrate how the confinement of these molecules in mesoporous MCM-41 and layered TaS_2 hosts affects their decomposition, leading to an increase in the cristallinity.

* C. Bosch-Navarro, E. Coronado, C. Martí-Gastaldo, J.F. Sánchez-Royo, M. Gómez-Gómez, *Nanoscale* **2012**, *4*, 3977-3982

† C. Bosch-Navarro, E.Coronado, C. Martí-Gastaldo, Pedro Amorós, to be submitted.

4.1. Influence of the pH on the Synthesis of reduced Graphene Oxide under Hydrothermal Conditions

4.1.1. Introduction

As commented in Chapter 2, since G was first isolated in 2004,[1] its synthesis in high scale and quantitative yields probably stands as one of the main scientific challenges still to be accomplished. This is supported by the vast number of works pursuing this target that are currently being published. So far, graphene can be isolated by using physical[2] or chemical methodologies.[3] The main difference between these two approaches is that while physical methods lead to high quality G sheets in a very low yield, chemical methods lead to the production of bulk quantities of G with poorest electronic conductivity mainly due to the disruption of the sp^2 structure by the introduction of defects.[4] In addition, the variable morphology and size of the G layers obtained with these chemical approaches may also affect its physical or chemical properties.[5] In this context, a better understanding of the key factors influencing the quality and morphology of the obtained G sheets certainly appears as a vital point of study.

Among these chemical methods, we are going to focus on the synthesis of graphene from GO (Hummers method).[6] As it has been already introduced, this method implies the reduction of the previously prepared GO. With this aim, several strategies have been followed, generally implying the use of hazardous reduction agents as hydrazine, dimethylhydrazine or sodium borohydride amongst others.[7,8] In this context, the use of hydrazine is probably the most well-known procedure, although its high toxicity makes worthwhile the exploration of new environmentally friendly methods. Recently, it has been demonstrated that supercritical water may act as a reducing agent for GO under hydrothermal conditions, offering a new and "green" route for the production of graphene.[9] Despite previous works have illustrated the influence of the pH on the reduction step,[9,10] a better understanding of how the morphology and structural properties of rGO are affected by the pH of the reaction medium is still lacking. Moreover, hydrothermal reactions have been successfully used to produce rGO composites by *in-situ* combination with different systems like metal oxide nanoparticles (TiO_2, SnO_2),[11] or layered materials (Ni-Fe

Layered Double Hydroxides, MoS_2).[12] Hence, it represents an appealing approach for the production of graphene-like hybrid composites, further emphasizing the importance of understanding the factors that may affect the final product. Here we provide new insights into this hydrothermal method, by studying in detail the effects that the pH has in the reduction of exfoliated GO to produce rGO. We show how equivalent synthetic conditions lead to the formation of different carbon nanoforms, with variable reduction degrees and morphologies dependent on the pH of the medium, which was fixed to oscillate in the 3–11 interval (**Scheme 7)**.

4.1.2. Results and Discussion

4.1.2.1. Synthesis

First the oxidation of graphite is produced to obtain GO, which can be readily exfoliated in water into single to few layers. Next, this aqueous dispersion is transferred to a Teflon autoclave and reacted under HT conditions to produce rGO sheets. The pH of the reaction medium –which was set to 3, 5, 7, 9 and 11 by adding diluted aqueous solutions of NaOH or HCl prior to the HT treatment– exerts a drastic influence on the morphology of the resulting material with the appearance of variable size (micrometric or sub-micrometric) graphene layers and other graphitic carbon nanoforms like nanoonions, fullerenes and multi-walled nanotubes.

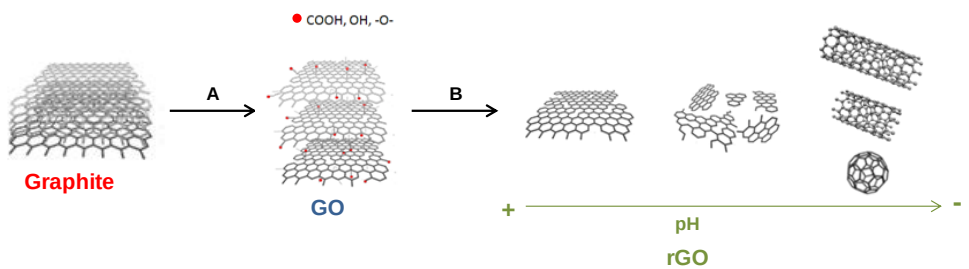

Scheme 7. Representation of the processes occurring during the experiment. (A) Hummers oxidation of graphite: (i) $NaNO_3$, H_2SO_4, K_2MnO_4, 0 °C, (ii) H_2O_2. (B) Hydrothermal reduction at 180°C and different pH values in the 3-11 interval. As a function of the pH, drastic changes in the morphologies and sizes of the obtained carbon forms can be observed.

4.1.2.2. Thermogravimetric Analysis

The presence of functional groups on the sheets has been first analyzed by thermogravimetric (TG) study under Nitrogen atmosphere (**Figure 32**). As expected, GO exhibits the higher functionalization degree. A first loss of weight is observed around 100 ºC, which corresponds to the release of the interstitial water trapped between the GO sheets,[13] and a second step is observed at 260 ºC corresponding to the decomposition of the labile oxygen functional groups (i.e. carboxylic, hydroxyl and epoxy groups) present in the sample. Concerning rGO obtained at different pH values, the shape of the TG curves is very similar for all the pHs, with no remarkable differences between them. As shown the thermal stability is increased for all the reduced samples (*ca.* 550 ºC), suggesting a partial restoration of the graphitic structure –sp^3 to sp^2 rehybridization of carbons.structure– after the hydrothermal treatment. No apparent weigh loss for the pyrolysis of oxygen moieties appears at 260 ºC, even though a 30% weight loss is observed, thus confirming the presence of sp^3 defects that may be associated to oxo groups that has not been reduced, along with other groups such as C-N that appear during the reduction process. This point has been additionally confirmed with XPS measurements (*vide infra*).

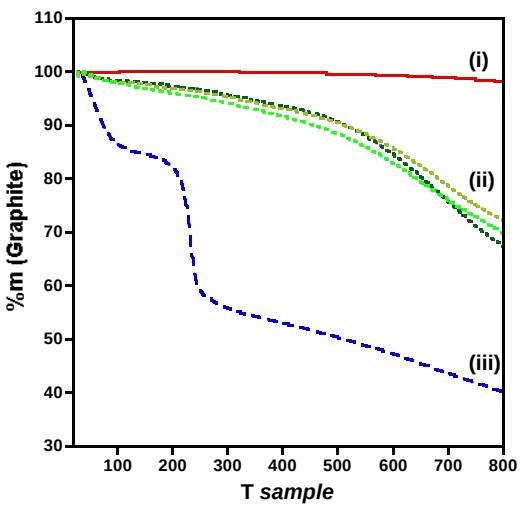

Figure 32. TG performed under N_2 atmosphere of (i) graphite, (ii) rGO at pH3, pH7 and pH11, (iii) GO.

4.1.2.3. Infra-red Spectroscopy (FT-IR)

This technique was used to preliminary assess the effect of the hydrothermal reductive treatment on the studied samples. The FT-IR for the starting GO and the rGO samples obtained at pH values of 3, 7, 9 and 11 are shown in **Figure 33** and **Figure 34**. For GO a first band, which corresponds to intercalated water, is observed at 3417 cm^{-1}. This signal is also present in the reduced samples, although, in the case of GO it is wider due to the contribution of two more peaks placed at around 3610cm^{-1} and 3170 cm^{-1}. These peaks can be associated to hydroxyl and –COOH groups across the GO layers, respectively.[14] Moreover, four more main contributions are observed: a sharp peak centered at 1621 cm^{-1} consistent to in-plane δ (OH_2) modes, another at 1410 cm^{-1} which is associated to in-plane δ (C-OH) bends -both of them disappear upon reduction-, a third one, placed at around 1100 cm^{-1}, which can be assigned to ν (C-O), and finally, a last peak centered at 1720 cm^{-1} which fits with the stretching of the ν (C=O). This latter peak is also observed in the reduced samples, but it appears severely attenuated in good agreement with the smaller content of C=O groups present in the rGO samples reflected by the thermogravimetric studies. On the other hand, two new broad bands appear in the reduced samples, one at around 1550 cm^{-1} associated to the aromatic ν (C=C) stretching, and another one at 1130 cm^{-1} corresponding to the in-plane δ (C=C), thus evidencing the restoration of the sp^2 structure.

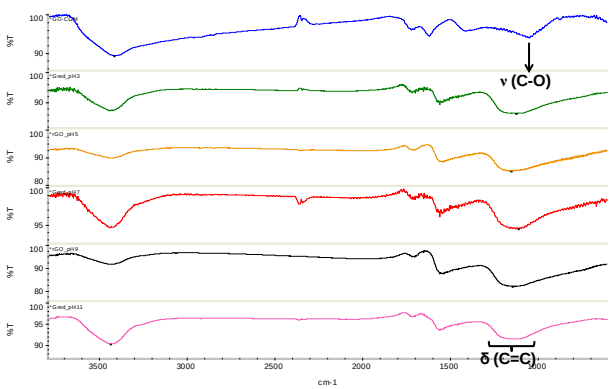

Figure 33. FT-IR spectra of GO (blue) and rGO at pH3 (green), pH5 (orange), pH7 (red), pH9 (black) and pH11 (pink)

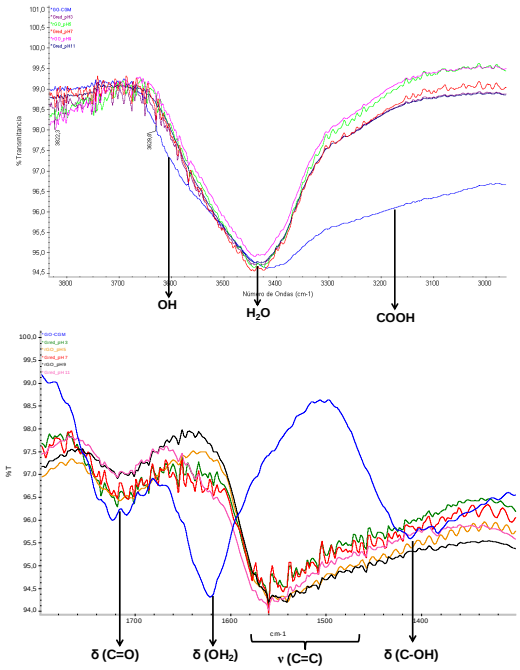

Figure 34. Zoom-in of the 3800-3000cm^{-1} (*top)* and 1800-1300cm^{-1} (*bottom*) regions.

4.1.2.4. X-Ray Diffraction Powder (XRD)

Figure 35 shows the XRD patterns of the starting GO and the rGO samples as obtained at variable pH. Whilst pristine graphite shows the expected interlayer separation of 3.35 nm (2θ = 26.5º) corresponding to the (100) plane, this is dramatically increased upon oxidation to produce a basal spacing of 7.9 nm (2θ = 11.22º) in GO, as result of the intercalation of water molecules between the hydrophilic graphene oxide sheets. This sharp peak disappears as result of the hydrotermal treatment, and a weak broad band is observed at *ca.* 3.7 nm (2θ = 23.8º), thus confirming partial restoration of the graphitic structure in the rGO samples. These samples exhibit a slightly higher basal spacing than that obtained for layered graphite likely due to the presence of residual oxygen functionalities as indicated by the TG and FT-IR studies (*vide supra*). No obvious differences can be observed for the different pH values, they exhibit equivalent patterns with no apparent broadening of the peaks thus suggesting that a similar interlayer distance are achieved for all of them.[15]

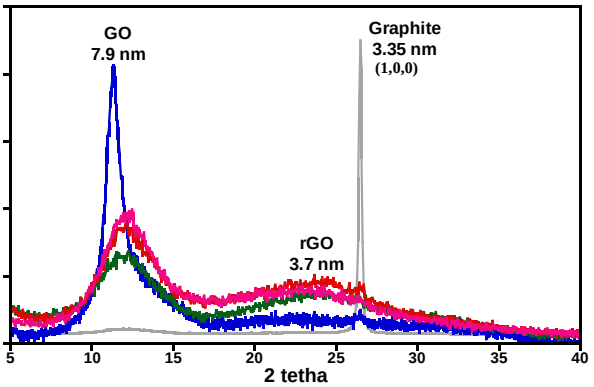

Figure 35. XRD diffraction powder of graphite (grey), GO (blue), rGO pH3 (green), rGO pH7 (red) and rGO pH11 (pink). The materials obtained at pH = 5 and 9 exhibit equivalent PXRD patterns with no significant peak broadening.

4.1.2.5. High Resolution Electron Microscopy (HR-TEM)

HR-TEM images were acquired from dropping freshly prepared dispersions of the as-prepared reduced samples in ethanol on a carbon-coated copper grid. These images have been used to determine the effects triggered by the pH of the medium on the size and morphology of the resulting reduced graphite oxide samples. To provide a clear idea of the size of the starting material, HR-TEM images of the GO used as precursor in our experiments is shown in **Figure 36**. In turn, **Figure 37** is representative of the rGO size at the different pHs. Comparison of both figures clearly show how the reducing hydrothermal treatment provokes a reduction of the size of the starting GO layers –whose size originally corresponds to tens of micrometers– into smaller rGO sheets –with sizes varying between 1 and 10 μm–. **Figure 37** clearly illustrates how the size of the resulting rGO layers is strongly affected by the pH of the reaction medium, with smaller sizes as the pH becomes more acidic. At highly acidic conditions (pH = 3) it is easy to find broken sheets of typically 1 μm (**Figure 37a**), while under basic conditions the resulting sheets reach sizes of tens of micrometers **(Figure 37e**). On the other hand, **Figure 38** displays clear changes in the morphology of the rGO samples as a function of the pH. In fact, besides the rGO sheets observed in **Figure 37**, other graphitic forms as multi-walled nanotubes (**Figure 38b-d)**, nanoonions or fullerenes (**Figure 38a)** were found and their formation can be probably associated to the decomposition of the carbon layers

occurring at pH = 7 and below. It has been extensively described that 2D systems are difficult to synthesize as they tend to scroll up giving quasi-0D onions or 1D-tubes in order to decrease the peripheral dangling bonds, thus decreasing the total energy of

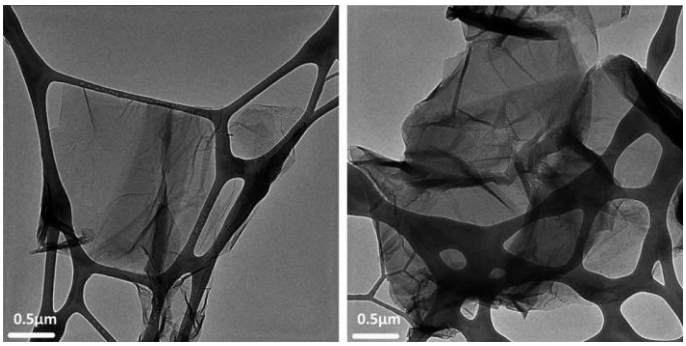

Figure 36. HR-TEM images of the starting GO material

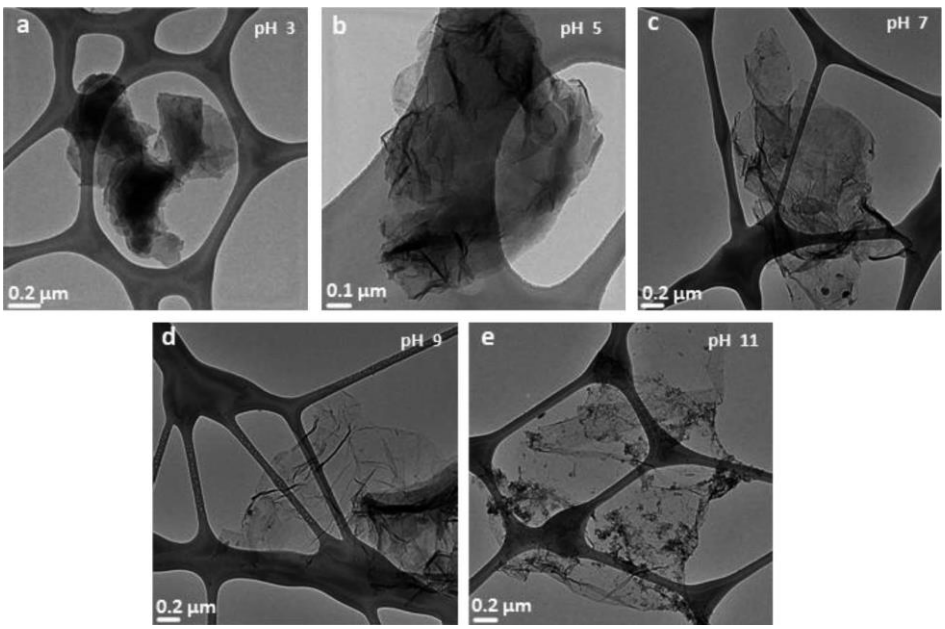

Figure 37. HR-TEM images for the rGO obtained at pH = 3, 5, 7, 9 and 11 illustrating the evolution of the size of the carbon layers as a function of the pH.

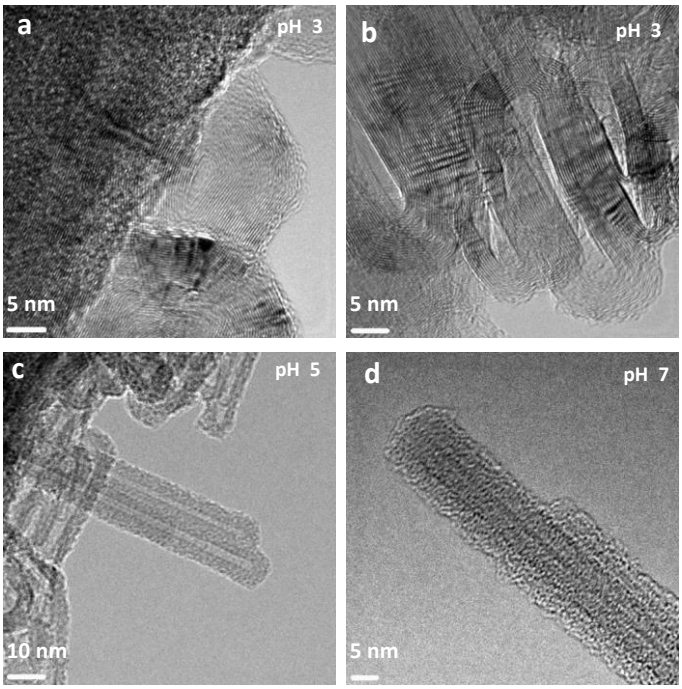

Figure 38. HR-TEM images showing the formation of nanoforms at the lower pH values (pH 3, 5 and 7) as result of the decomposition of the carbon layers.

the system.[16] As rGO sheets become smaller, the effective periphery area becomes higher, thus increasing the tendency of the G sheets to scroll up forming those closed nanoforms. As it is shown in **Figure 38**, it is easy to find closed structures at pH = 3, 5 and 7. Still, it is quite interesting to notice that at the lower pH the nanoforms observed are smaller, varing between very short multiwall-nanotubes (around 25 nm of length at pH = 3 (**Figure 38b**)) and longer ones (tens of nanometers of length at pH = 5 and 7 (**Figure 38c & d**). One also observes that as the pH increases the tendency of the sheets to agglomerate is lower. The reason for such observation may reside in the fact that as the pH becomes more basic, an increase on the negative charge of the sheets is generated, thus producing a repulsion between the individual layers preventing the agglomeration of the sheets.[9] This enables to observe an hexagonal difraction pattern for sheets obtained at pH = 9 and 11 (**Figure 39**), further confirming that the sp^2 bonding network has been almost restored and suggesting a better crystalinity for the samples obtained at greater pHs.

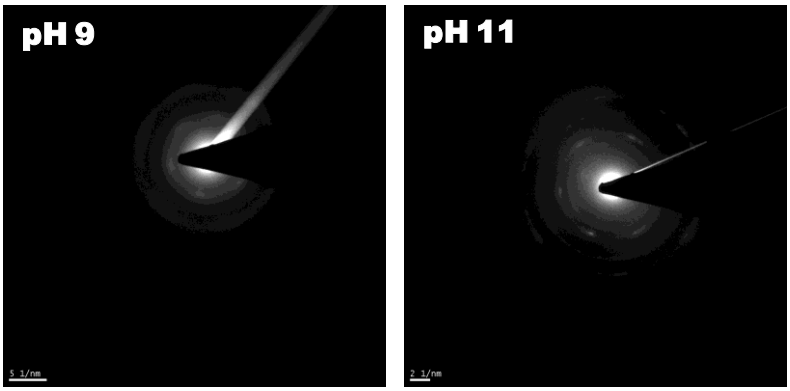

Figure 39. Hexagonal difraction pattern of graphene sheets obtained at pH9 and pH 11, extracted from Figure 37d & e.

4.1.2.6. X-Ray Photoelectron Spectroscopy (XPS)

The surface composition of GO and the different reduced samples was further studied by C1s XPS spectrum (**Figure 40**). On one hand, it is clearly observed a high level of oxidation for GO showing four main peaks: 284.8 eV (C-C sp^2), 286.2 eV (C-O), 287.8 eV (C=O) and 289.0 eV (C(O)O).[17] Those peaks, which correspond to oxygenated moieties, have an effective area much higher than the non-oxygenated signal placed at 284.8 eV, confirming the high oxidation level achieved for the employed GO. Besides, with the hydrothermal treatment the C-C sp^2 content tend to become more important, while the oxygenated peaks decrease considerably, and a new peak corresponding to C-N bond (285.9 eV) can be appreciated.[7] It is possible to compare the relative intensity of C-C sp^2 bonds with those corresponding to defects (C-O) (**Figure 40**), confirming that as the pH increases the number of defects is considerably lower. As it is summarized in **Figure 40**, the ratio I_{C-C}/I_{C-O} increases from 0.118 in the case of GO, to 1.41 for rGO at pH = 11, being 0.78 at pH = 3, 0.94 at pH = 5, 0.98 at pH = 7 and 1.14 at pH = 9. This tendency seems to confirm that, besides affecting the morphology of the produced rGO samples, the pH also affects the efficiency of the reduction process by providing better results under more basic conditions.[9,10].

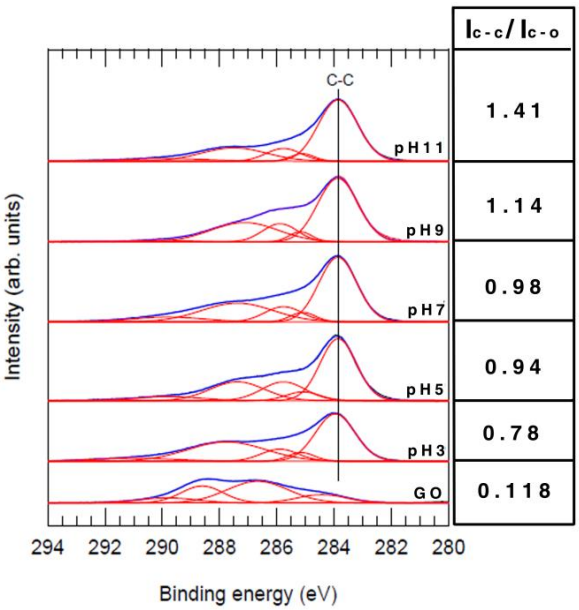

Figure 40. C1s XPS spectra for GO, and rGO obtained at pH3, pH5, pH7, pH9 and pH11. The relative intensity of the C-C/C-O ratio is summarized on the right panel.

4.1.2.7. Transport measurements

The electrical conductivity of the samples has been tested as it can provide direct information on the quality of graphene, being perhaps the best indicator to know to which extent the reduction from GO to rGO has taken place. For this matter, the electrical conductivities at room temperature of compressed-powder samples of GO and rGO obtained at the different pHs have been measured (**Figure 41**). GO is an insulator due to the lack of π-conjugation across the system. Upon reduction, the samples acquired a semiconducting behavior with conductivities in the range 10 – 100 S/m). This result clearly indicates the restoration of the sp^2 electronic structure. It is important to stress that these measurements strongly depend on the compression pressure, and therefore it is not straightforward to obtain an absolute value of powder conductivity which could be compared with other values reported in the literature. Moreover, this fact makes impossible to obtain an accurate comparison between the quality of the different rGO samples, and it can just be pointed out that similar conductivities are achieved.[7]

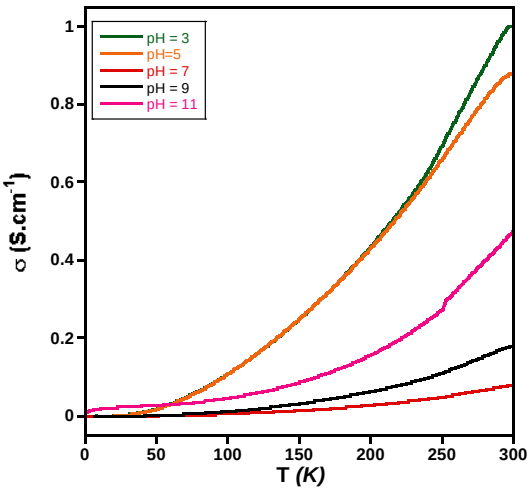

	GO	rGO pH3	rGO pH5	rGO pH7	rGO pH9	rGO pH11
Electrical Conductivity (S/m)	X	100	87	7.8	17	50

Figure 41. Measured Electrical Conductivity for GO and rGO obtained at the different pHs as a function of temperature.

4.1.2.7. Raman Spectroscopy

This technique is a practical method for characterizing the graphitic-like species and, in this case, particularly useful to study the size of the graphitic domains formed as result of the reductive treatment.

Figure 42 shows the first order Raman spectra for GO and rGO samples, showing the typical G (1580 cm^{-1}) and D (1340 cm^{-1}) bands of graphitic species. It is worth mentioning that the G band is associated with E_{2g} vibrational modes of the aromatic domains, whilst the D band arises from the breathing modes of the graphitic domains. Given that the activation of this latter band requires the presence of defects, it gives an estimation of the sp^3 carbons present in the lattice. In fact, it tends to disappear in defect-free graphitic materials.[18] Even though I_G/I_D ratio has been traditionally used to compare the structural order between amorphous and graphitic systems,[19] Paredes *et al.* recently demonstrated that the I_G/I_D ratio can be

only employed to estimate the average size of C sp^2 domains.[20] In the table inserted in

Figure 42 the I_G/I_D ratio for GO and rGO extracted from the integration of the G and D bands at the different pHs is summarized. The I_G/I_D ratio found for GO is lower than that found in any of the reduced samples, in good agreement with the high oxygen content present in this sample as described above. The I_G/I_D ratio in the rGO samples tends to increase as the pH decreases. This trend seems to indicate that, despite the presence of defects is less abundant under more basic conditions, as confirmed by our XPS studies (*vide supra*), the average size of these graphitic domains is lower for the rGO samples obtained at higher pH values. Moreover, it is possible to observe the 2D band (2700 cm^{-1}), which gives information about the number of layers of the sample. In our case, no clear differences can be observed in the 2D region of the different samples. Instead, it appears as a very broad band indicating the presence of defects[21] and suggesting the presence of aggregates of some layers in the final product.[22]

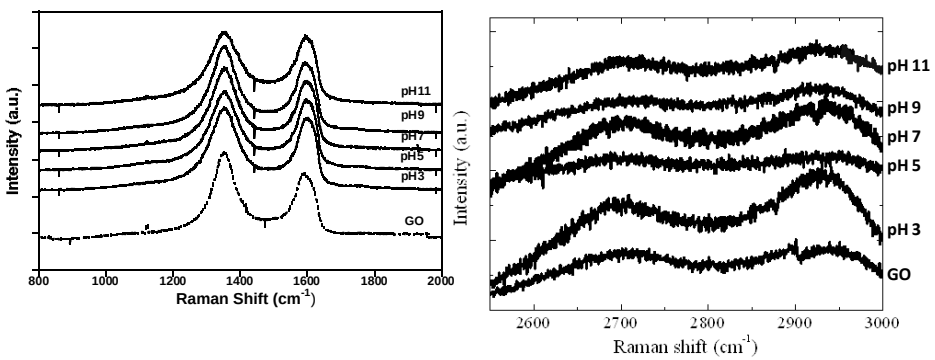

Sample	GO	pH=3	pH=5	pH=7	pH=9	pH=11
I_G/I_D	0.07673	0.29788	0.27792	0.20268	0.23416	0.13898

Figure 42. μ-Raman spectra of GO and reduced samples obtained at the different pH values showing the G and D bands (*left*), and the 2D band (*right*). In the bottom part of the figure, a table containing the calculated I_G/I_D ratio extracted from the integration of the G and D bands is shown.

4.1.3. Conclusions

We have shown how the hydrothermal reduction of graphene oxide is very sensitive to the pH used in the reduction step. This has been confirmed with the use of complementary physical techniques that provide a clear picture of the morphology and internal structure of the reduced species. Our HR-TEM images clearly show how acidic conditions lead to a higher amount of defects in the resulting rGO samples, with smaller sizes of the sheets, and a pronounced tendency of these sheets to aggregate and scroll up giving rise to other graphitic nanoforms like nanoonions, multi-walled nanotubes or fullerenes. The internal structure of the rGO platelets has been additionally studied with XPS and μ-Raman spectroscopy, confirming that the reduction under more basic conditions promotes a decrease in the number of defects present in the resulting rGO and bigger graphitic domains.

In our opinion, this study provides a better understanding of how the morphology and structural properties of rGO are affected by the pH of the reaction medium and will be of help for the development of novel graphene-like hybrid composites under hydrothermal conditions.

4.1.4. Experimental

4.1.4.1 General synthesis remarks.

Graphite powder was purchased from Fisher Scientific (G/0900/60). The samples were filtered employing a vacuum filter funnel of pore size number 3, over cellulose nitrate membrane filters (0.8μm pore size). Temperature conditions were controlled employing a programmable Memmert oven (Paraffin oven UNE PA).

4.1.4.2 Synthesis of GO.

GO was obtained by the Hummers method.[8] In a typical experiment, to a flask containing 6.5 g of graphite and 3.3 g of $NaNO_3$ at 0 ºC, 150 mL of H_2SO_4 65 % were carefully added. Once the ice bath was removed, 19.6 g of $KMnO_4$ were added rising up the temperature to 50 ºC and maintaining it with continuous stirring

for further 30 minutes, after which, 300 mL of water were added slowly so the temperature increases to 90 ºC. After 20 minutes of vigorous stirring, 600 mL of water were added. Finally, 50 mL of H_2O_2 were added, and the slurry centrifuged and filtered under vacuum achieving GO as a brown solid.

4.1.4.3. Synthesis of rGO.

rGO was obtained by placing a 0.7 $mg.mL^{-1}$ aqueous solution of GO in a Teflon-lined autoclave. The pH was adjusted employing either HCl 2% or NaOH 2M to 3, 5, 7, 9 and 11 pH values. The resulting solutions were treated under hydrothermal conditions by applying a gradient in which the temperature was raised to 180 ºC in 40 min, maintained at 180 ºC for 6 h and leaving it to room temperature for 40 min. The resulting rGO appeared at the bottom of the autoclave in the form of a black solid; it was centrifuged and thoroughly washed with water. Finally, it was filtered over cellulose nitrate membrane filters (0.8μm pore size) and oven dried at a 100ºC.

4.1.4.4. Physical Characterization.

IR spectrum was taken using FT-IR Nicolet 5700 spectrometer in the 4000-400 cm^{-1} frequency range, using powdered samples diluted in KBr pellets.

HR-TEM images were obtained using a TECNAI G2 F20 microscope. Field Emission Gun (FEG)200 kV.

Thermogravimetric analysis was carried out with a Mettler Toledo TGA/SDTA 851 apparatus in the 25-800 ^oC temperature range under 30 $mL.mol^{-1}$ of nitrogen flow and at 10 $K.min^{-1}$ scan rate.

X-ray powder profile (XRD) was collected using a Siemens D-500 X-ray diffractometer (Cu-Kα radiation, λα = 1.54184 Å). Sample was grounded and mounted on a flat sample plate. Profile was collected as step scans in the $5^o < 2\theta < 70^o$ range with a spot size of 0.02º.

X-ray photoelectron spectroscopy (XPS) measurements were performed in an ultra-high vacuum system ESCALAB210 (base pressure $1.0x10^{-10}$ mbar) from Thermo VG Scientific. Photoelectrons were excited by using the Mg-Kα line (1253.6 eV). All spectra have been referred to the Fermi level.

D.C. conductivity measurements were performed with the four contacts method for two pressed pellets of each sample with similar results in both pellets. The contacts between the platinum wires (25 mm diameter) and the samples were done using graphite paste. The samples were measured with dc intensity currents of 1-100 μA in a Quantum Design PPMS-9 equipment, giving reproducible and very similar results in all cases.

μ-Raman measurements at room temperature were performed in backscattering using a Jobin – Yvon T64000 triple spectrometer equipped with a nitrogen cooled charge coupled device detector (CCD). The 514.5 nm line of an Ar laser was used for excitation.

4.2. Anthracene as a precursor of Graphite-like materials

4.2.1. Introduction

In the previous section of this chapter, we have shown how G can be obtained by the HT reduction of GO. This procedure is one of a series of top-down methods that have been already described for the synthesis of G. Amongst these top-down methodologies we can also find important procedures such as micromechanical exfoliation of graphite or the unzipping of CNT. But, although the reduction of GO offers good yields, it lacks in the quality needed for some applications. Besides, the micromechanical exfoliation of graphite and the unzipping of CNTs do not offer the scalability necessary for real applications.

For practical applications, probably the bottom-up approaches are more promising, as these methods allow a fine control on the dimensionality of the resulting carbon nanoforms. In this direction, chemical vapor deposition (CVD)[23] or the organic synthesis from small aromatic hydrocarbons,[24] are worth-mentioning. CVD is probably the most promising technique nowadays, but it requires high temperatures and high pressures which translates into a very expensive and complicated process, and normally leads to variable yields.[25] In turn, the organic synthesis from small aromatic hydrocarbons is very appealing as it would permit the synthesis of tailor-made G. In turn, the synthetic pathways are not always easy and the yields are low.[26] Probably, a key step for the development of new strategies to synthesize good quality G in good yield requires the study of appropriated precursors. In this direction, the use of polyaromatic hydrocarbons (PAHs) has attracted much attention, and it can be found in the literature some examples in which different PAHs have been employed for the growing of G over a variety of substrates.[26b,27] This procedure generally implies first, the sublimation of the precursors over a substrate, and in a second step a cyclodehydrogentation catalyzed by the metallic substrate. Still, the search for new precursors which would lead to the formation of G without the aid of a catalyst is highly desirable as it would open the window to the use of novel non-metallic substrates and it would lower the production costs. In this context, Talyzin and coworkers reported the formation of low-dimensional oligomers from reaction of coronene molecules instead of the

formation of large graphitic flakes.[28] Interestingly, they have recently reported how the synthesis of G can successfully be accomplished when the coronene molecules are confined inside a nanometric scaffold.[29a]

Inspired by this work, we have targeted the anthracene molecule as a suitable PAH for the production of G (**Figure 43**). Due to its low melting (218 ºC) and boiling point (340 ºC), it can be considered a very cheap precursor for the formation of graphite by the successive fusion of anthracene rings. The low melting point compared to that of coronene (438 ºC) suggested us that the kinetic energy for the fusion of the molecules should be lower. Hence, the formation of graphite from these small aromatic precursors should be favored over other possible PAHs with greater fusion temperature, which, for example, in the case of coronene just permitted the synthesis of big oligomers, but not of graphite. Moreover, as it can be sublimed at low temperature, an open possibility towards both, its deposition over different surfaces or its confinement into appropriated host systems can be envisioned.[29] This deposition/confinement, followed by the adequate fusion conditions probably would lead to the formation of single G layers of superior physical quality and electronic conductivity than that enabled by the top-down chemical reduction of graphite. With all this in mind, first we will explore the formation of graphite from sublimation of anthracene by a simple heat treatment without the aid of a catalyst (point 4.2.2, page 117). Next, we will explore how this reaction can be controlled to produce single G layers by confining these molecules in nanometric 3D and 2D frameworks. On one hand MCM-41 having a mesoporous structure has been employed (point 4.2.3, page 126). Their nanometric channels have been used to direct the synthesis of ultrathin G nanoforms (GNFs) by inserting anthracene molecules in them prior to applying a similar thermal procedure to that described at point 4.2.2 of this Chapter. On the other hand, a lamellar compound (TaS_2) has been chosen to drive the synthesis of 2D graphene layers by the insertion of anthracene molecules between the TaS_2 sheets (point 4.2.4, page 140).

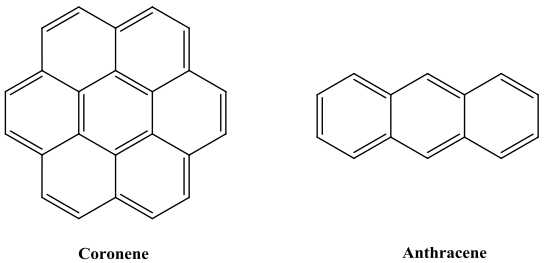

Figure 43. Molecular structure of coronene and anthracene.

4.2.2. Bulk synthesis of graphite from anthracene

First we will show how graphite can be obtained directly from anthracene by a simple thermal treatment. The as-made graphite has been thoroughly characterized and compared with pristine graphite to illustrate the differences introduced between both materials.

4.2.2.1 Results and discussion

4.2.2.1.1. Synthesis

Graphite was obtained by fusion of anthracene rings following a two-step procedure (**Scheme 8**). In a first step, anthracene was loaded inside a quartz tube and sealed under vacuum. The system was then heated following the temperature gradient summarized at **Figure 44**. The gradient was selected on the basis of the melting point of anthracene (218 ºC). During this first process, anthracene rings start to fuse giving rise to oligomers in an analogous way to what it has been previously described for other similar systems, so **G1** is obtained.[28] As the system becomes larger its melting point as well as its decomposition temperature increases; this justifies the use of a temperature gradient. In a second stage, an annealing under nitrogen atmosphere was performed. This treatment favors a cyclodehydrogenation giving rise to the formation of C-C bonds resulting in the creation of graphite (**G2**).[27] A first prove of the formation of graphite is observed at first glance by the color evolution. As shown in **Figure 45**, anthracene is a white powder, while G1 is brown and G2 becomes black. This evolution towards the color black indicates that an extended conjugation is present in the final sample.[30]

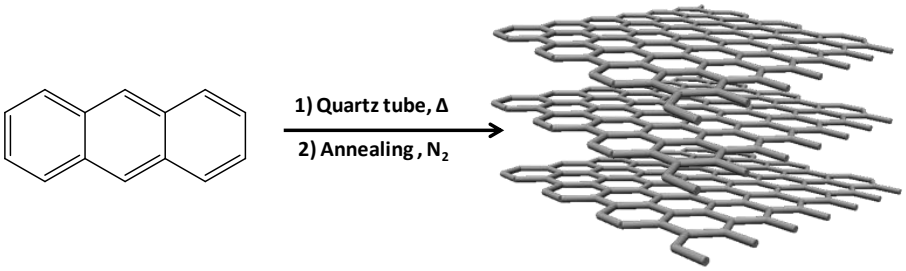

Scheme 8. Schematic representation of the synthesis pathway followed for the formation of graphite.

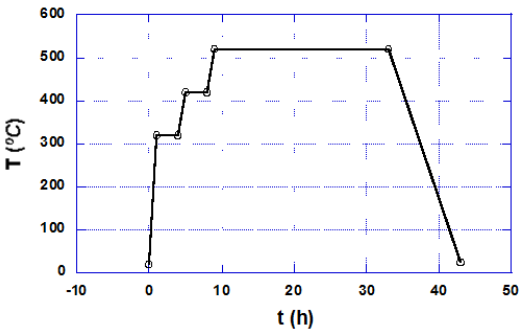

20ºC → 320ºC	t=60min
320ºC	t=3h
320ºC → 420ºC	t=60min
420ºC	t=3h
420ºC → 520ºC	t=60min
520ºC	t=24h
520ºC → 25ºC	t=10h

Figure 44. Temperature gradient followed during step 1.

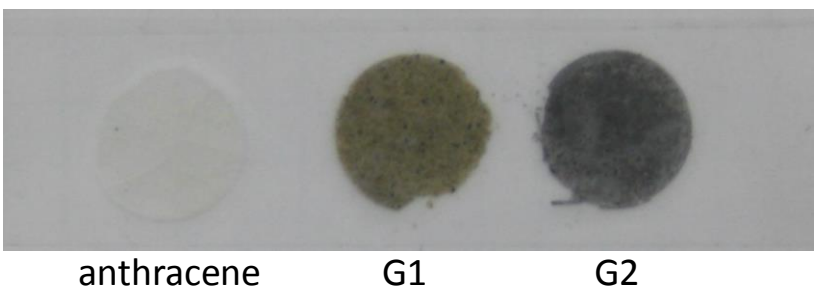

Figure 45. Color evolution from anthracene to G2. The picture has been taken over samples diluted in KBr

4.2.2.1.2. FT-IR

This technique clearly shows an evolution towards graphite from anthracene. In **Figure 46**, the FT-IR of anthracene, G1, G2 is shown. On one hand, anthracene and G1 have a very similar spectrum, as occurred with the employment of coronene.[28] In both cases, a peak centered at 3047 cm^{-1} corresponding to the stretching of aromatic C-H can be observed, along with a wide number of signals in the range 1300-1600 cm^{-1} (annular backbone) and in the range 950-1250cm^{-1} (breading modes of the in-plane aromatic C-H vibrations). Finally, two very intense signals can be observed at 736 cm^{-1} and 883 cm^{-1} which can be assigned to the breading modes of the out-of-plane aromatic C-H vibrations. Although this observation seems to discard the occurrence of important changes during step 1, our HR-TEM studies confirm the presence of important morphological differences between the starting material and G1 (*vide infra*). The observation of anthracene in the FT-IR of G1 is probably due to the presence of small traces of anthracene that remains within G1 (as shown by X-ray diffraction powder and thermogravimetric analysis, *vide infra*). Since anthracene is much more active under IR irradiation it dominates the spectra, and prevents the observation of new peaks. Alike G1, G2 presents a very different FT-IR spectrum. As shown in **Figure 46**, the signals which were assigned to anthracene almost disappear upon annealing, and just the intense peaks which corresponded with the out-of-plane aromatic C-H vibrations can be observed; that should mean that some C-H may be present preferentially at the sheets rims. In addition, new peaks which can be assigned to the formation of graphitic-like structures can be observed at *ca.* 1550cm^{-1} (ν(C=C)) and at *ca.* 1130 cm^{-1} (δ(C=C)).[31] This confirms that during the annealing the dehydrogenation takes place giving rise to a highly conjugated system, which can be associated with the formation of a graphitic structure.

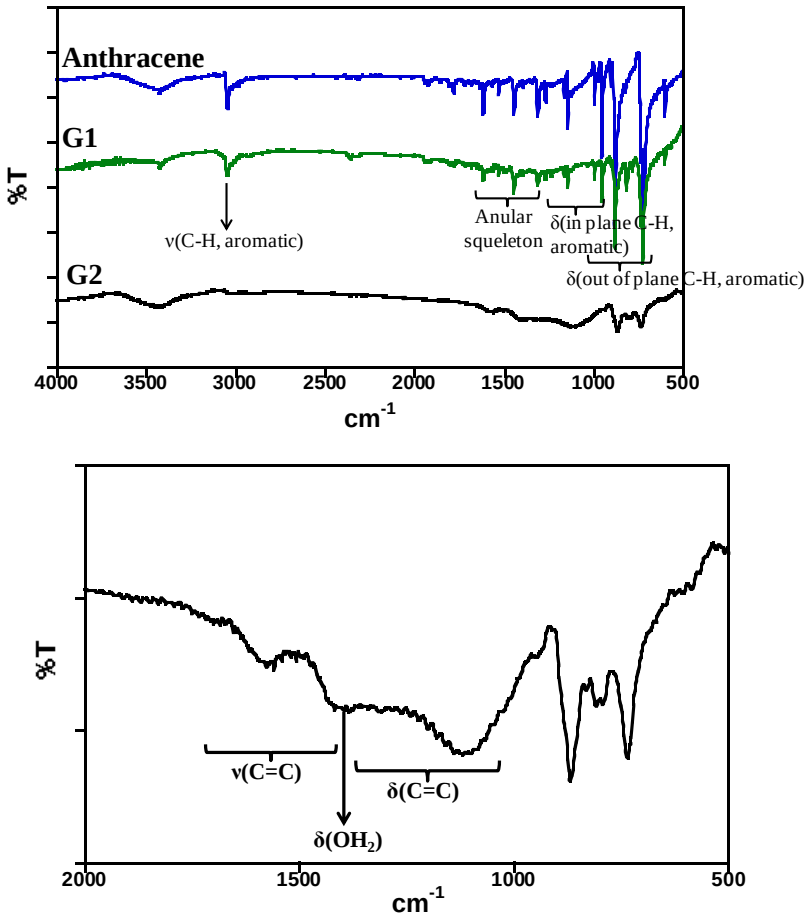

Figure 46. FT-IR of anthracene (blue), G1 (green) and G2 (black). In the bottom image a zoom in to the 500-2000 cm^{-1} region for G2 is shown.

4.2.2.1.3. X-Ray Diffraction powder (XRD)

Figure 47, shows the XRD of graphite, anthracene, G1 and G2. For G1, the crystallinity is much lower than that observed for the untreated material, and some features associated to anthracene still observed. This observation suggests that the formation of a new material by heating the anthracene PAHs in the sealed tube is not complete and a fraction of the started material remains unreacted. Upon annealing, XRD of G2 shows a clear evolution to a more well defined structure with a clear peak centered at $2\theta = 25.8^{o}$ (3.45 Å) that is comparable to the interlayer space of graphite ($2\theta = 26.5^{o}$; 3.36 Å). This also indicates that the fusion of anthracene rings

is taking place and that the final thermal treatment drives the packing on the graphene layers formed in-situ to produce bulk graphite. Notice that in the absence of a template the π-π interactions between anthracene molecules drives a 3D packing giving rise to a multi-lamellar arrangement once the fusion has taken place.[32] This issue will be addressed by the confinement of the anthracene molecules in a nanometric host as a previous step to the fusion of the small anthracene molecules (vide infra). This confinement will diminish the inter-anthracene interactions favouring the alignment which will conduce to the synthesis of graphitic nanoforms (GNFs) of finite width.

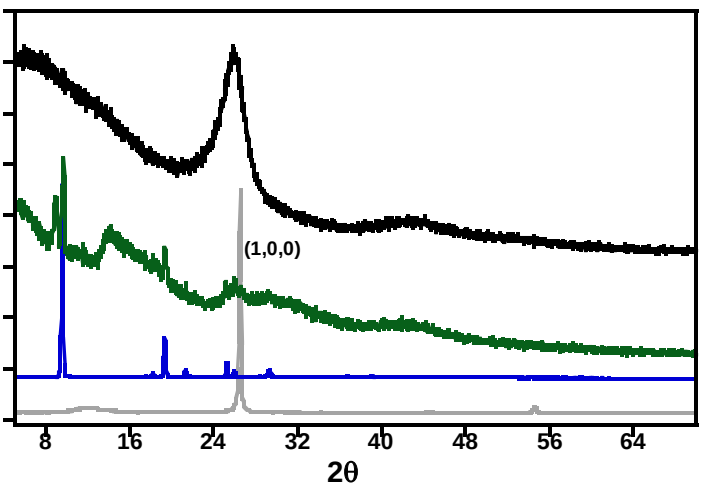

Figure 47. XRD of graphite (gray), anthracene (blue), G1 (green) and G2 (black)

4.2.2.1.4. Thermogravimetric analysis

The graphitization was further explored in terms of increased thermal stability. **Figure 48** shows the thermogravimetric analysis of anthracene, G1 and G2, and commercially available graphite. As shown, anthracene decomposes at very low temperature (230 ºC). In contrast, for G1, the pyrolysis of the 95% of the sample occurs at 655ºC. Notice that, a first weigh loss (5%) which should be associated to non-reacted anthracene can be seen at 230ºC. This observation is consistent with the FT-IR and the XRD (*vide supra*). Regarding G2, its thermal stability is very similar to that observed for G1 (630ºC), although no starting anthracene is observed and the pyrolysis happens more abruptly, thus indicating a more homogeneous system. The slight reduction of thermal stability in G2 when compared to pristine graphite (741 ºC) is likely due to the presence of defects in the carbon layers intrinsic to the experimental procedure. This has been confirmed by μ-Raman spectroscopy (*vide infra*).

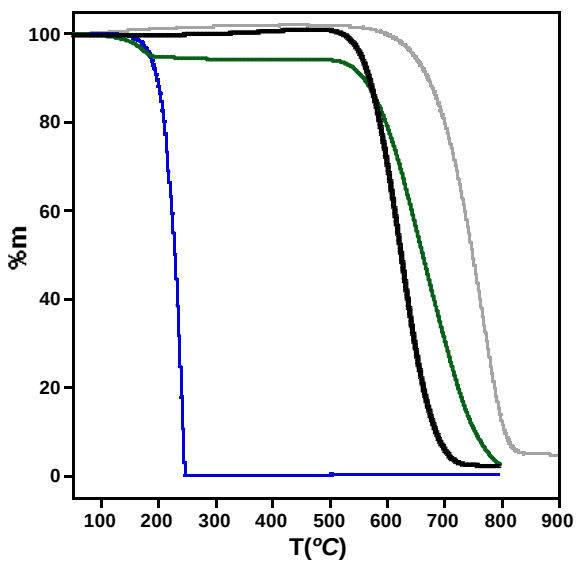

Figure 48. Thermogravimetric analysis of under ambient graphite (gray), anthracene (blue), G1 (green) and G2 (black).

4.2.2.1.5. Raman spectroscopy.

μ-Raman spectroscopy is a useful technique to identify graphitic-like species. **Figure 49** shows the first order Raman spectra of anthracene (blue), G1 (green), G2 (black) and commercially available graphite (grey). At first sight, the spectrum of anthracene is completely different from those of G1 and G2. Alike the FT-IR of G1, which is dominated by the remaining fraction of non-reacted anthracene molecules, its Raman spectra does not display any vibration modes from the starting material. Both, G1 and G2 display the G (*ca.* 1580 cm^{-1}) and D bands (*ca.* 1340cm^{-1}) intrinsic to graphitic-like structures. The G band can be associated with E_{2g} vibrational modes being characteristic of highly conjugated sp^2 systems, while the D band appears as a consequence of the reduction of the sp^2 domains and it is activated by the presence of defects tending to diminish in defect-free graphitic materials.[18] In our case, G1 present a number of peaks that correspond with the splitting of the D band (1264 cm^{-1}, 1355 cm^{-1} and 1439 cm^{-1}) and can be associated with the presence of big oligomers that we cannot identify.[33] For G2 a more well-defined D-band is observed, although, its notably broadness compared to the D band of graphite indicates the presence of some defects that may arise from the synthesis procedure. Moreover, the observed G band appears blue-shifted with respect graphite (1595 cm^{-1} vs 1580 cm^{-1}) which also is indicative of the presence of some defects in the lattice (**Figure 49b**).[34] Still, after the annealing a clearly evolution to a less defective graphite is deduced since the bands shown by G1 also appears at higher frequencies than for G2 (1610 cm^{-1} vs 1595 cm^{-1}). Moreover, the same I_G/I_D ratio is calculated for both, G1 and G2, so no clue about the size of the graphitic domains can be extracted. Finally, a broad 2D band also blue shifted with respect to the 2D band of graphite (2830 cm^{-1} vs 2700 cm^{-1}) is observed in G2, suggesting the aggregation of some graphene layers (< 10 layers) in the final product.[35]

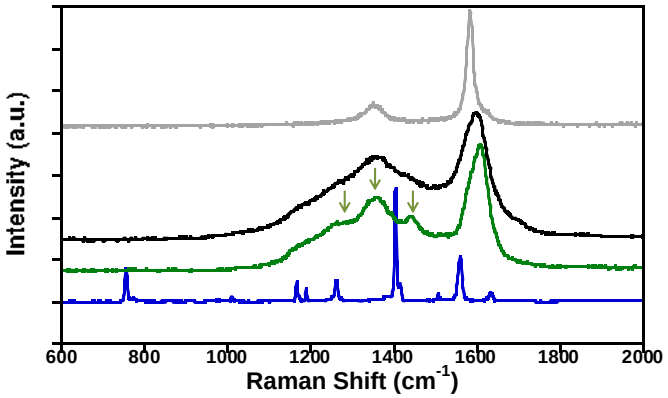

(a)

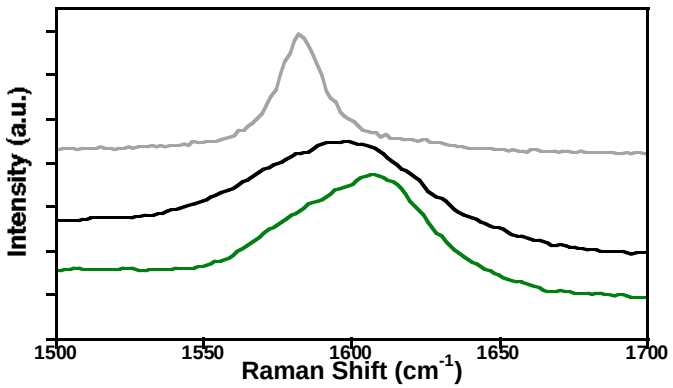

(b)

Figure 49. (a) Raman of anthracene (blue), G1 (green), G2 (black) and graphite (grey). In G1, the splitting of the D band is marked with green arrows. (b) Zoom-in to the G band of graphite, G1, G2 in which a clear blue-shift is observed from G1 to graphite.

4.2.2.1.6. HR-TEM

HR-TEM images were taken from dropping freshly prepared dispersions of G1 and G2 in NMP over a carbon-coated copper grid. The acquired images give insights into the morphology of the prepared products (**Figure 50** and **Figure 51**). G1 (**Figure 50**) can be described as a very defective layer in which a great amount of holes are present. Upon annealing (**Figure 51**), G1 evolves to more well-defined layers which morphology is comparable to that shown by graphite as it was expected by FT-IR and XRD (vide supra). This is in good agreement with the formation of low-dimensional oligomers from the fusion of anthracene in the early stages of the

thermal treatment, which then start to associate to produce an incomplete graphene layer. This process is accelerated in G2 by thermal annealing. Thus, the formation of carbon layers is completed and a packing in three-dimensions to produce bulk graphite is observed. Unfortunately, the obtained layers appear to be very aggregated making impossible the visualization of a single graphene layer and its correspondent hexagonal diffraction pattern by Selected Area Electron Diffraction (SAED). It is worth remaining that without the use of a template, strong π-π interactions between the molecules of anthracene are present which ineluctably leads to a 3-D packing.

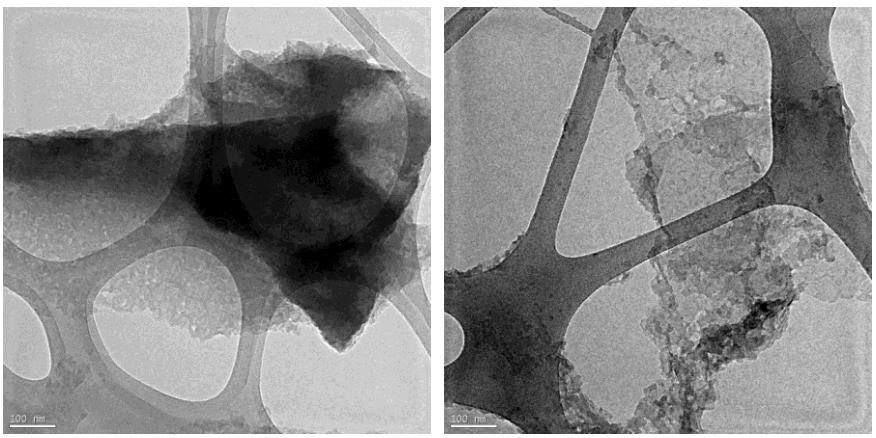

Figure 50. HR-TEM images of G1

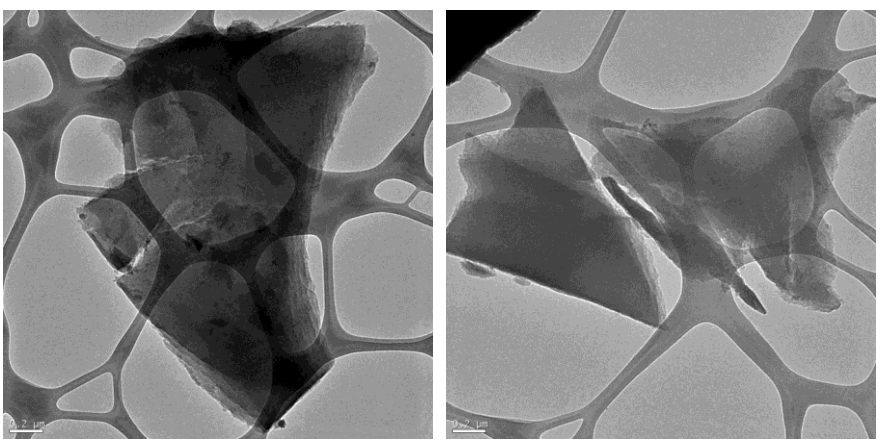

Figure 51. HR-TEM images of G2

4.2.2.2. Conclusions

Graphite has been obtained from anthracene by a simple two step procedure. The methodology implies a first step in which the fusion of anthracene rings to form oligomers take place under vacuum at high temperature. In a second step, an annealing, which promotes cyclodehydrogenation is performed under inert atmosphere. Alike the fusion of coronene molecules, the use of anthracene permits the synthesis of graphite. This should be associated with the low melting point of anthracene compared to coronene, which may cause a reduction of the kinetic energy of the fusion of the molecules. Moreover, anthracene is a very cheap molecule, therefore a very attractive PAH molecule for the synthesis of graphene. As we have seen, this procedure does not allow obtaining single graphene flakes. To reach this goal a template capable of confining the anthracene molecules needs to be used. This route of synthesis will be developed in the next section.

4.2.2.3. Experimental.

4.2.2.3.1. General synthesis remarks

Graphite powder was purchased from Fisher Scientific (G/0900/60). The temperature conditions were obtained by employing a tubular furnace (Gallur). The quartz tubes employed had a dimensions of 25 cm lenth and 1,5 cm of diameter.

4.2.2.3.2. Synthesis of Graphite (G2)

Step 1. 2 g of anthracene were loaded inside a queartz ampoule, and sealed under vaccum. Afterwards, the quartz ampoule was place inside a furnace and the temperature raised to 520 ºC following the temperature gradient indicated in **Figure 44**. After the heat treatment a dark-brown solid appeared at the quartz tube walls (G1).

Step 2. G1 was placed inside a furnace purged with nitrogen. The temperature was set at 450ºC and maintained during 4h under nitrogen atmosphere so G2 was obtained as a black solid.

4.2.2.3.3. Physical characterization

IR spectrum was taken using FT-IR Nicolet 5700 spectrometer in the 4000-400cm^{-1} frequency range, using powdered samples diluted in KBr pellets.

HR-TEM images were obtained using a TECNAI G2 F20 microscope. Field Emission Gun (FEG)200 kV.

Thermogravimetric analysis was carried out with a Mettler Toledo TGA/SDTA 851 apparatus in the 25-800^{o}C temperature range under air atmosphere.

X-ray powder profile (XRD) was collected using a Siemens D-500 X-ray diffractometer (Cu-Kα radiation, λα = 1.54184 Å). Sample was grounded and mounted on a flat sample plate. Profile was collected as step scans in the 5º < 2θ < 70º range with a spot size of 0.02º.

μ-Raman measurements at room temperature were performed with a dispersive Jobin-Yvon LabRam HR 800 microscope, working with an excitation line of 532 nm. The scattered light was detected with a thermoelectric cooled (-70 ºC) charge coupled device detector (CCD). It also has an Olympus BXFM optic microscope. All the measurements were carried out directly over the sample. In the performed experiments, the power employed over the samples was of the order of 0.3 mW, and the exposition time 60 seconds.

4.2.3. Synthesis of Ultrathin Graphene Nanoforms Induced by the Fusion of anthracene rings inside the channels of MCM-41

To date, it has been reported the synthesis of graphene nanoribbons (GNRs) by employing CNTs as templates,[29a,36,37] but, as far as we know, no attempts concerning other possible nanometric hosts have been done. In this regard, MCM-41 is a promising possibility. MCM-41 is a popular mesoporous material which, although composed by an amorphous silica wall, it has a long range ordered mesoporous framework with uniform mesopores ranging between 2 and 10 nm depending on the surfactant employed for their synthesis. [38] MCM-41 has commonly been employed as catalyst, as support for drug delivery or as absorbent amongst others. Moreover, it has been employed to encapsulate different nanoparticles and single molecule magnets, [39] and it has already been used for growing carbon nanowire arrays.[40] Still, to the best of our knowledge it has not yet been employed to direct the synthesis of graphene nanoforms (GNFs) from small PAHs. Due to its uniform mesoporosity and its tolerance to high temperatures (> 800 ºC),[41] we considered it a suitable host for the growth of GNFs by thermal-driven fusion of anthracene molecules confined in a nanometric space. In this regard, the use of anthracene instead of other larger PAHs such as coronene, is also more suitable as larger PAHs have larger hydrophobicity which hinders its introduction inside the pores of MCM-41.[42]

4.2.3.1. Results and discussion

4.2.3.1.1. Synthesis of graphitic nanoforms

GNFs were synthesized by following a three-step procedure (**Scheme 9**). First, MCM-41 was used as nanoscaffold and its pores where loaded with anthracene (A) molecules dissolved in dichloromethane by impregnation (MCM41@A).[43] Dichloromethane was chosen as solvent for the impregnation given its increased hydrophilicity when compared to other organic solvents. The hydrophilicity is a key step to fruitfully fill the pores due to the high hydrophobicity of the anthracene molecules. Once anthracene was introduced, the resulting MCM41@A was loaded inside a quartz tube and sealed under vacuum. The tube was then subjected to a

thermal treatment similar to that described in section 4.2.2. In this thermal step, the anthracene molecules fused giving rise to bigger oligomers (MCM41@G1). Finally, the system was annealed under inert conditions so MCM41@GNFs was obtained. Etching with a diluted solution of fluorhydric acid (HF) will permit to observe the GNFs formed within the pores.

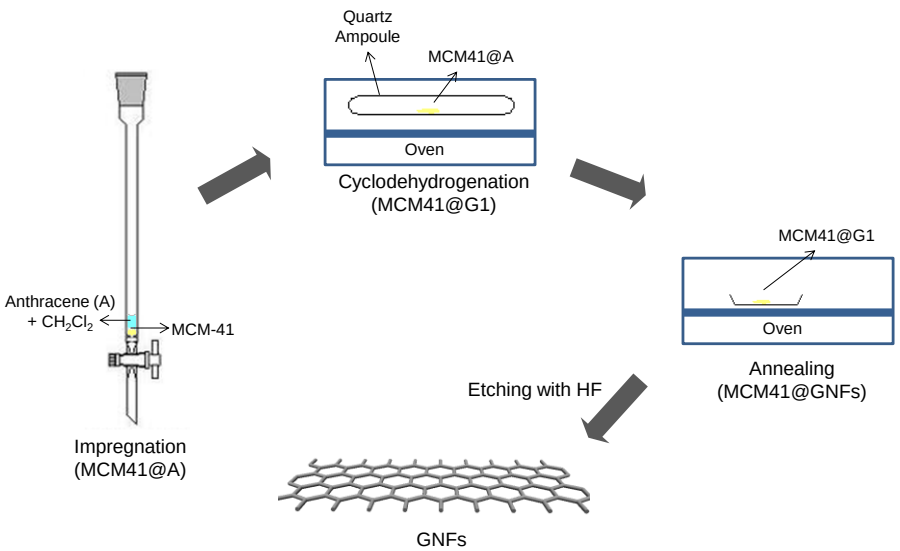

Scheme 9. Representation of the steps followed to synthesize GNFs.

4.2.3.1.2. X-Ray Diffraction powder (XRD)

All the composites have been characterized by powder X-ray diffraction (XRD). First XRD was performed over the calcined MCM-41 before its impregnation with anthracene. As shown in **Figure 53**, in the low angle scattering regime ($2\theta < 10^{o}$) MCM-41 shows a strong diffraction peak which is associated to the (100) reflection of the hexagonal cell. From this intense reflection at d = 34.3 Å the pore center distance can be calculated to a_o = 40Å, according to the hexagonal unit cell relation ($a_o = 2\ d_{100} / \sqrt{3}$).[43]. Moreover, two other weak reflections peaks are observed, which can be indexed to (110) and (210) reflections. This observation represents a proof of the existence of a highly ordered hexagonal pore system.

After impregnation treatment, XRD was again performed. In this case, no differences were obtained in the low angle regions meaning that after the impregnation the hexagonal disposition of the channels was maintained. It is worth-reminding that although the difference in intensities of the (100) reflection has been extensively used as an indicative of the filling of the pores, this is just valid when highly scattering materials are introduced (for example metals). Therefore, for anthracene it was not expected. In contrast, after the thermal treatment, the (100) reflection becomes broader and the other two lower their intensity. Moreover, the (100) peak is shifted to higher 2Θ value. The change in the relative peak intensity and the lattice contraction usually occurs when the substituted MCM-41 is subjected to elevated temperatures, and suggests the presence of high amounts of loaded materials inside the MCM-41 pores.[44] Besides, when analyzing the high angle region, no order is observed for MCM41@A. This last observation discards the presence of anthracene agglomerates either inside or outside the pores, thus indicating that the anthracene loading is adequate to proceed with the next reaction step. Interestingly, in the long angle region, for annealed material (MCM41@GNFs) a peak centered at $2\Theta = 11.7^{o}$ (d = 7.6 Å) appears. This spectrum, which is very similar to that shown by graphite oxide, has also been observed for GNRs,[45] thus suggesting that after the thermal treatment the formation of GNFs has been successful.

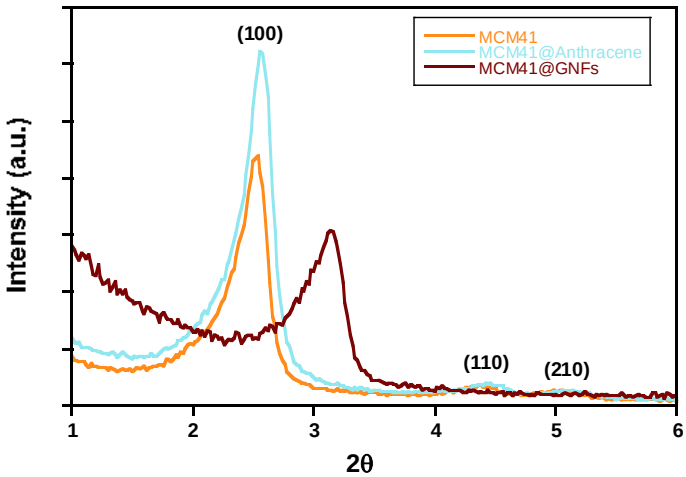

Figure 52. XRD of MCM-41 showing the low angle scattering regime (2θ < 10º) of calcined MCM-41 (orange), MCM41@A (light blue) and MCM41@GNFs (brown).

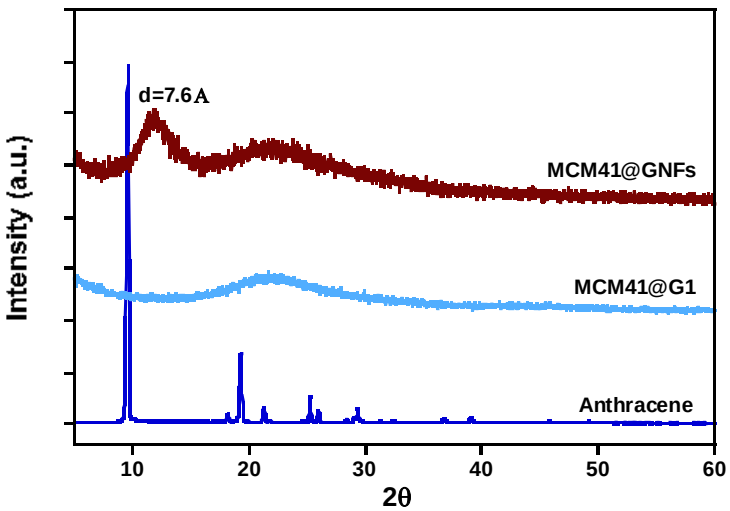

Figure 53. XRD showing the high angle regions of anthracene (blue) and MCM41@A (light blue), and MCM41@GNFs (brown)

4.2.3.1.3. Adsorption Experiments

Nitrogen adsorption/desorption experiments were used to confirm the porosity of the samples and to demonstrate the filling of the pores after the impregnation with anthracene molecules. **Figure 54** shows the nitrogen adsorption/desorption isotherm of calcined MCM-41 and MCM41@A measured at 77 K. Calcined MCM-41 behaves as a mesoporous material during the process, showing a type IV isotherm behavior according to IUPAC classification. A linear increase in nitrogen adsorption occurs at low pressures (0.05 – 0.25, relative pressures) due to monolayer adsorption prior to the step in which nitrogen uptakes inside the mesopores. From this linear region the specific surface area was determined using BET equation being 943 m^2 g^{-1}**,** and it is well correlated with other experimental values reported in the literature.[46.] Then, a steep gas uptake is observed due to the condensation of nitrogen molecules inside the mesopores. This sharp curvature along with the absence of a hysteresis loop suggests the presence of a narrow pore size distribution in the calcined MCM-41. The desorption isotherm is almost identical meaning that the adsorption/desorption process is reversible, and therefore the pores are accessible. In the case of MCM41@A the amount of physisorbed nitrogen decreases considerably and it is accompanied with a shift of the inflection point of the step to a smaller value of relative pressure. Both effects can be attributed to the inclusion of anthracene molecules inside the pores of MCM-41, and are related to a smaller specific BET surface area (943 m^2 g^{-1} vs 98 m^2 g^{-1}). The pore size calculated by using a "Barrett, Joyner and Halenda" (BJH) model on the adsorption branch of the isotherm is around 5.9 nm for MCM41@A. Finally, in MCM41@A a hysteresis loop is observed. This behavior is typical of filled mesoporous, and is due to the presence of different pathways of adsorption and desorption that are generated by the existence of the loaded material.

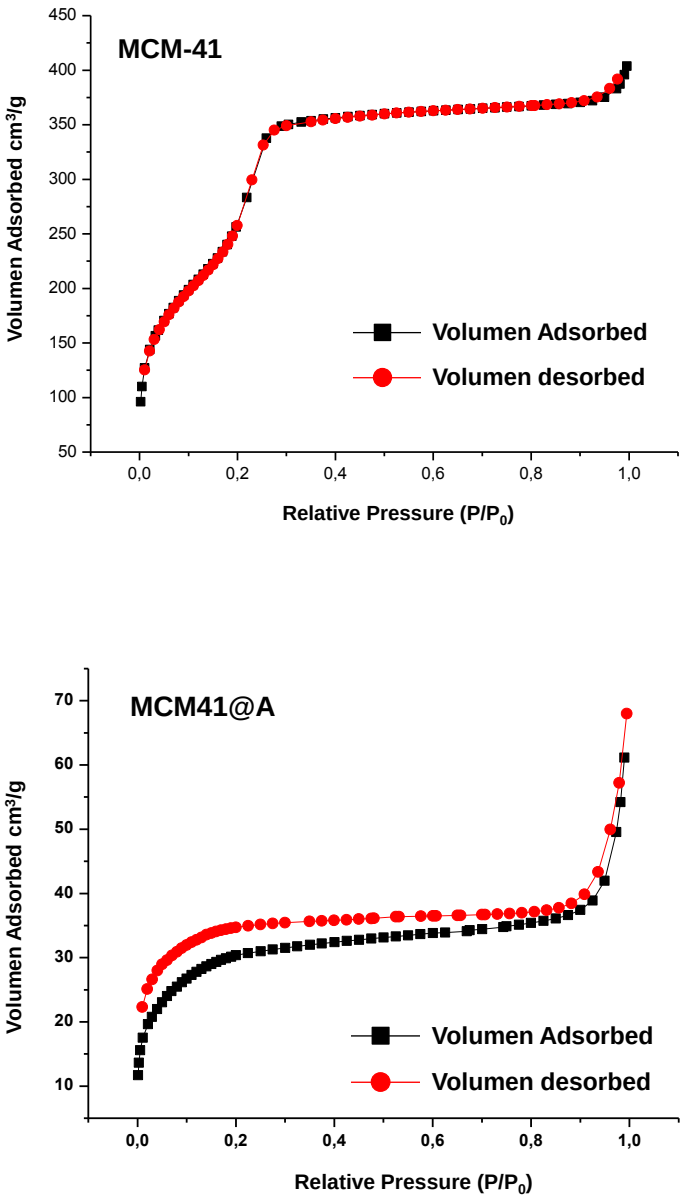

Figure 54. Nitrogen adsorption/desorption isotherms of calcined MCM-41 (*top*) and MCM41@A (*bottom*)

4.2.3.1.4. Scanning Electron Microscopy (SEM)

Scanning electron microscopy (SEM) was employed to give general structural information of the samples before and after the impregnation with anthracene molecules (**Figure 55**). The similarity between both samples and the absence of big agglomerated in the case of MCM41@A further suggest the absence of anthracene molecules blocking the pores, so the adsorption behavior described should be associated to the presence of anthracene molecules inside the MCM-41 pores.

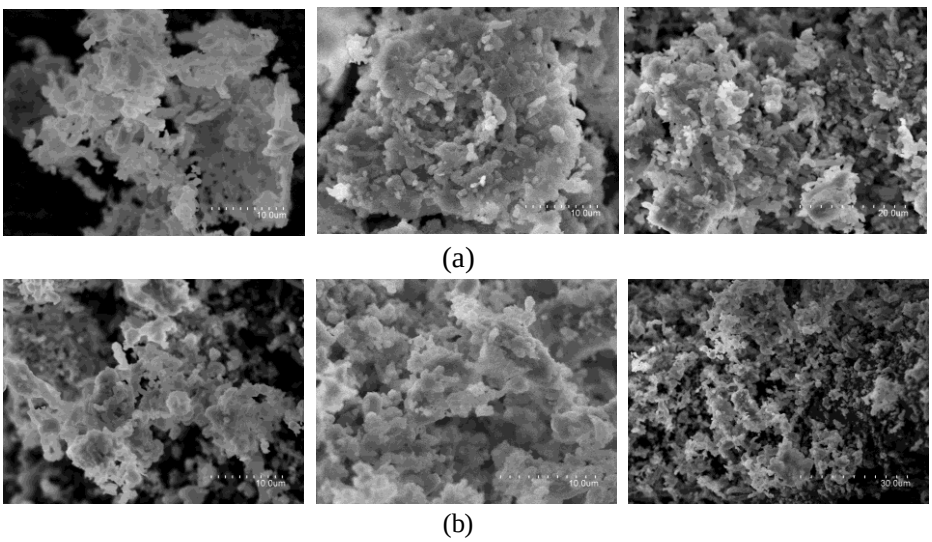

Figure 55. SEM micrographs of (a) MCM-41 and (b) MCM41@A.

4.2.3.1.5. Thermogravimetric Analysis

The relative quantity of carbonaceous material loaded inside the pores can be estimated by thermogravimetric analysis (TGA). As shown in **Figure 56** calcined MCM-41 suffers a very gradual release of mass (2 %) upon heating the sample to 900 ºC under ambient conditions. Due to the great thermal stability of the mesoporous material in all the temperature range, any change in the TGA could be correctly assigned to the loaded carbon material. When the MCM-41 is loaded with anthracene molecules (light blue line) a gradual mass release is observed at around

300 ºC. Hence, the weight loss assigned to anthracene is *ca.* 2 % of the total mass of the sample. This small amount is due to the important influence that the mass of the mesoporous has with respect the loaded carbon material. Interestingly, after the heat treatment the thermal stability is increased up to 600 ºC where again a weight loss of *ca.* 2 % is observed. This increased thermal stability must be assigned to the presence of graphitic-like species that have formed during the process. No clear differences in the thermal behavior are shown in the system before and after the annealing probably because, as it would be suggested by Raman spectroscopy (*vide infra*), the stability of the GNFs is more dependent on the confinement effects rather than to the formed specie itself. Probably, if we were able to perform a TGA of the samples after removing the silica scaffold we would be able to observe differences in the thermal behavior. Unfortunately, this is not possible as we are limited by the mass obtained after removing the nanomold.

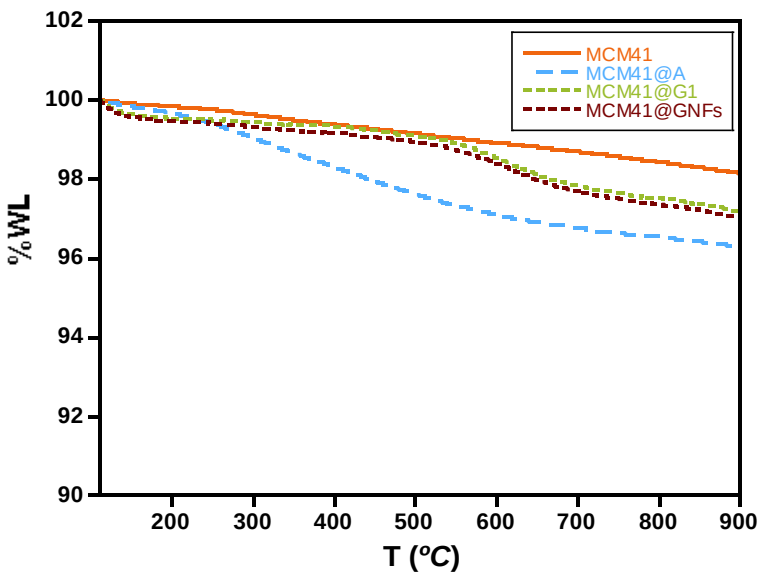

Figure 56. Thermogravimetry under ambient conditions of MCM-41 (orange, solid line), MCM41@A (light blue, dashed line), MCM41@G1 (light green, dotted line) and MCM41@GNFs (brown, sotted line).

4.2.3.1.6. Raman spectroscopy.

The Raman spectra of MCM41@GNFs (**Figure 57**) shows the typical G and D bands of graphitic-like species, meaning that our procedure has resulted in the formation of graphitic-like structures. Although no clear differences can be observed between the Raman spectra of MCM41@G1 and MCM41@GNFs, the comparison with the Raman spectra obtained in the case of the unconfined system (G1, point 4.2.2.1.6, pag. 124) gives important information. On one hand, the better definition of both, the G and D bands in MCM41@GNFs points out to a less sp^3 content. On the other hand, although we have previously explained that the position of the G band can give information about the defect content, for GNRs it has been demonstrated that the G band appears up-shifted by ca. 5 cm^{-1} with respect the bulk material. This may be attributed to confinement effects.[47] In our case, the G band of the confined system appears up-shifted by 8 cm^{-1} with respect to G1 (1605 cm-1 vs 1597cm-1), suggesting the presence of GNFs of finite size. In addition, the higher I_G/I_D ratio (see table at **Figure 57**) –which gives an estimation of the size of the graphitic domains– suggests that the confinement gives rise to GNFs with larger sp^2 domains. At this point is worth-noting that although in graphene an annealing always entails an increase in the I_G/I_D, for GNRs this premise does not work and normally the I_G/I_D remains the same as occur in our samples (I_G/I_D ratio of 1.63 for MCM41@G1 and of 1.56 for MCM41@GNFs). This behavior indicates that the basal plane defects in GNRs contribute less than the defects at the ribbon edges in activating the D band, and suggests that we have succeeded in our attempt of synthesizing confined GNFs within the pores of MCM-41. Interestingly, when the silica scaffold is etched off with HF the solid residue suffer some structural changes according to Raman spectroscopy (**Figure 57**). On one hand, both bands red shift about 10 cm-1 with respect the confined system which points to a more defective material. Moreover, the I_G/I_D decreases considerably to 1.35. Both, the band shifts and the decrease of the I_G/I_D ratio points to a high defective material with reduced sp2 domains, having a structure comparable to G1. This results suggest that the stability of the GNFs after removing the silica scaffold is greatly diminished, as it will be confirmed by HR-TEM analysis (vide infra).

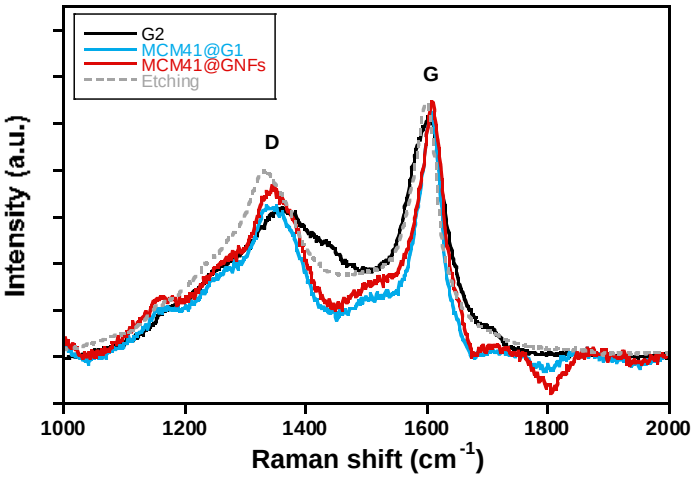

	G (cm^{-1})	D (cm^{-1})	I_G/I_D
G1	1597	1360	1.3
MCM41@G1	1605	1346	1.63
MCM41@GNFs	1605	1346	1.56
GNFs (Etching)	1600	1335	1.35

Figure 57. µRaman spectra of G1 (black), MCM41@G1 (light blue), MCM41@GNFs (red) and the result of the etching with concentrated HF (grey, dotted line). At the bottom a table in which the data extracted from the spectra is summarized has been included.

4.2.3.2. Etching with HF

In an attempt of isolating the material formed within the pores, an etching with fluorhydric acid (HF) was performed. HF is known to dissolve the silica scaffold of the mesoporous, and it may not affect the carbon materials formed within the pores. With this aim, MCM41@GNFs was treated with a few milliliters of concentrated HF, so immediately a black residue appeared. Unfortunately, the observation of GNFs by HR-TEM was not successful (Figure 58), probably because after removing the scaffold the carbon inside the pores tends to aggregate and break into small pieces preventing the observation of single GNFs, as previously suggested by Raman spectroscopy.

In order to stabilize the nanoforms generated inside the pores, a partial

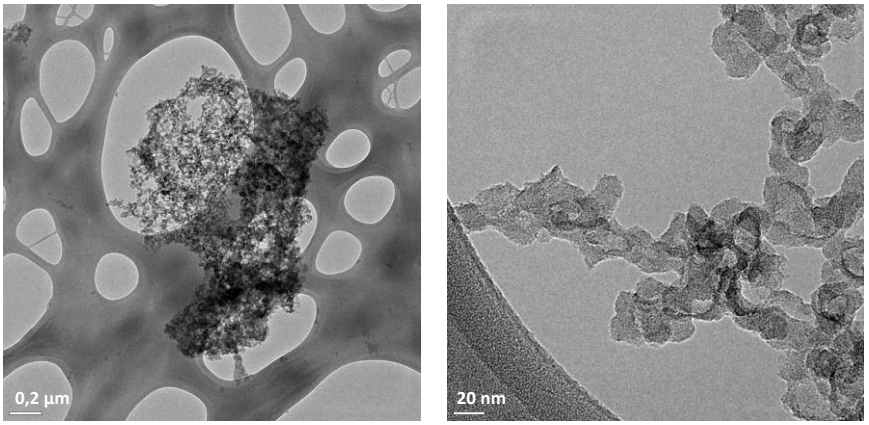

Figure 58. HR-TEM images MCM41@GNFs after the etching with concentrated HF.

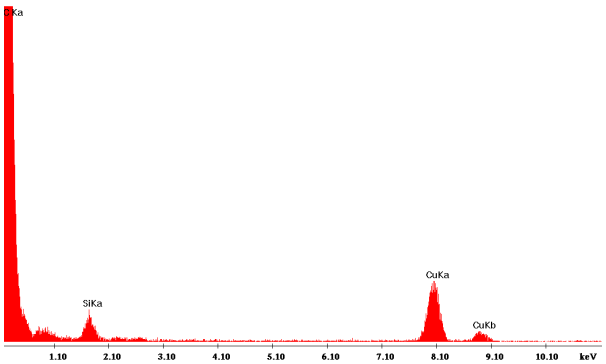

Figure 59. Microanalysis obtained from the sample MCM41@GNFs treated with diluted HF.

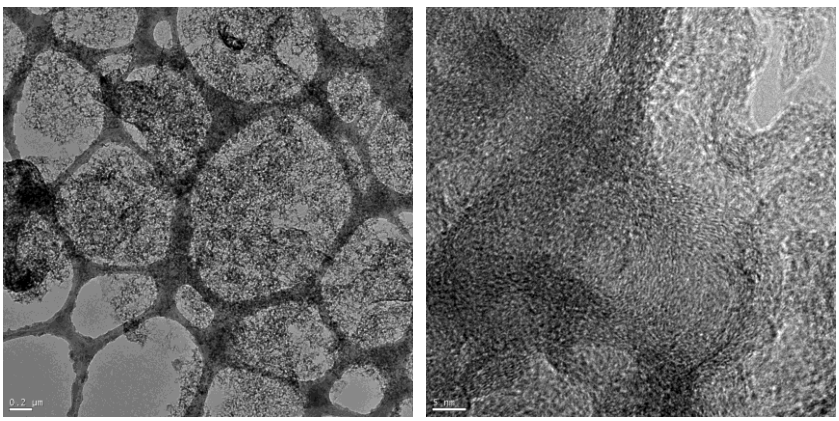

Figure 60. HR-TEM images of MCM41@G1 after the etching with diluted HF.

etching of the mesoporous was carried out. With this aim, a much diluted HF solution was employed. In the resulting material both, carbon and silicon were found by microanalysis (**Figure 59**), supporting a partial etching of the MCM-41 scaffold. Before the annealing and after the etching with diluted HF, HR-TEM images of MCM41@G1 showed just an amorphous material (**Figure 60**). Interestingly, after the annealing a considerably increase of the graphitization was achieved (**Figure 61**) and it was possible to observe carbon nanoforms upon with an amorphous matrix that should be attributed to the residual silica. The isolated GNFs showed an interlayer space of ca. 0.37 nm, which matches perfectly that displayed by pristine graphite (*ca.* 0.35 nm). Very interestingly, the graphitic species observed did not exceed the 4-5 nm in width in good agreement with the size of the pores employed in the synthesis of the material. This suggests that the confinement inside the mesoporous induces the graphitization of the material.

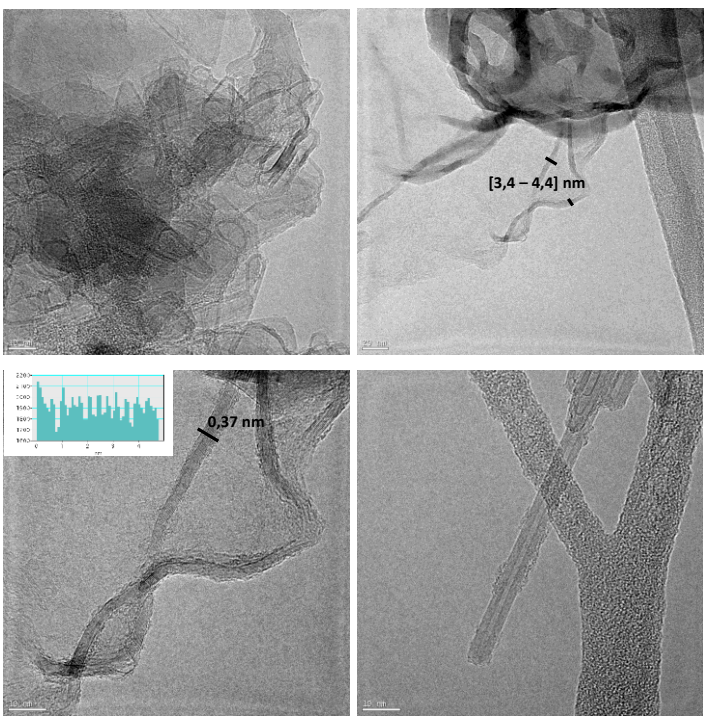

Figure 61. HR-TEM images of MCM41@GNFs after the etching with diluted HF. The images clearly show an increased graphitization, with the appearance of nanoforms of 4-5 nm in width.

4.2.3.3. Conclusions

GNFs have been grown by confinement inside the pores of a mesoporous MCM-41. The confinement of the molecular PAHs inside a nanometric host minimizes the π-π interactions between the aromatic core of the anthracene molecules, thus forbidding a 3D packing. Besides, this confinement favors a 1D alignment of the anthracene molecules that promotes the formation of GNFs of finite width rather than bulk graphite. The procedure consisted in three simple steps. In a first step, anthracene molecules were introduced inside the pores by a simple impregnation methodology. SEM microscopy, XRD and adsorption experiments demonstrated that the anthacene molecules were effectively introduced inside the pores, and no extra material –which could have led to undesired reactions– was left outside the pores. Afterwards, the MCM41@A was introduced inside a quartz ampoule and sealed under vacuum. The ampoule was subjected to a thermal treatment, followed by an annealing under nitrogen atmosphere in a similar way to what has been described for the synthesis of bulk graphite. The convenient filling of the pores with anthracene molecules was demonstrated by SEM microscopy, adsorption/desorption isotherms and XRD. After the thermal treatment TGA, XRD and μ-Raman suggested the successful formation of GNFs within the pores. Finally, after dissolving partially the silica scaffold with diluted HF we have been able to observe by HR-TEM a clear graphitization of the sample, along with the appearance of GNFs whose width does not exceed the pore size of the MCM-41. Therefore, our results confirm that the confinement of anthracene molecules inside a nanometric host induces a graphitization. This is not possible to achieve in the unconfined material (section 4.2.2), and serves to direct the synthesis of nanometric graphitic species. It should be pointed out that so far it has just been described the synthesis of GNRs by confinement inside CNTs,[29a,36,37] but no work regarding other possible hosts have been reported. Therefore, we have shown for the first time a possible alternative. The use of MCM-41 to direct the synthesis of GNFs, has some advantages with respect the use of CNTs. Typically, when CNTs are employed as host, the correspondent PAHs are put together with the CNTs and heated in a sealed tube, therefore it is possible to find big oligomers both outside and inside the CNT that should be carefully removed. In our procedure as the PAH can be inserted

before the thermal treatment, no material is obtained outside the pores. In addition, a vast quantity of MCM-type materials having different pore characteristics are known, so it could be possible to play with the pore diameter in order to obtain GNFs of the desired size. Finally, as we can selectively remove the silica scaffold by etching in HF it should be possible to isolate the GNFs by choosing the adequate pore size in which the GNFs obtained are sufficiently stable.

Future work will involve the employment of chemical-modified anthracene molecules having peripheral substituents in order to improve the packing in the solid state through inter-molecular interactions, thus favoring the efficiency of the fusion upon thermal heating. In addition, we aim to employ porous scaffolds having a larger pore size in order to study the effects that the pore size may have in the GNFs achieved.

4.2.3.4. Experimental.

4.2.3.4.1. General synthesis remarks

The temperature conditions were obtained by employing a tubular furnace (Gallur). The dimensions of the quartz ampoule were 7 cm of length, having a diameter of 0.5 cm.

4.2.3.4.2. Synthesis of graphene nanoforms (GNFs)

Step 1. *Introduction of anthracene molecules inside the pores of MCM-41 (MCM41@A)*

Anthracene molecules were introduced inside the pores of the MCM-41 following an impregnation methodology. 200 mg of MCM-41 (pre-calcinated at 700 ºC during 10 h) were introduced inside a closed silica column. Afterwards, 70 mg of anthracene dissolved in 10 mL of dichloromethane were introduced inside the column, and the column was kept closed for 30 minutes. Finally, by applying pressure the dichloromethane containing the non-introduced anthracene was quickly evacuated, followed by washing the sample with one additional milliliter of dichloromethane. Finally, MCM41-A was dried at 110 ºC during 2 hours.

Step 2. *Synthesis of GNFs*

Step 1. 150 mg of MCM41@A were loaded inside a quartz ampoule and sealed under vacuum. Afterwards, the quartz ampoule was place inside a furnace and the temperature raised to 520 ºC following the temperature gradient indicated in **Figure 62** (MCM41@G1).

Step 2. 100 mg MCM41@G1 were placed inside a furnace purged with nitrogen. The temperature was set at 400ºC and maintained during 4h under nitrogen atmosphere so MCM41@GNFs was obtained

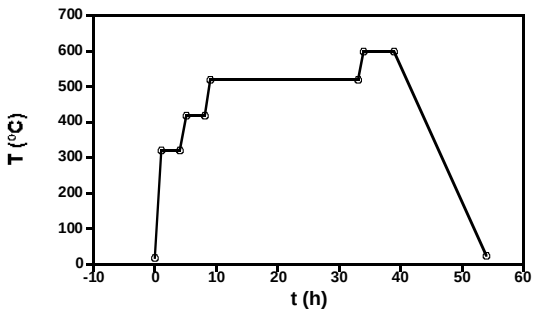

25 ºC → 320 ºC	60 min
320 ºC	3 h
320 ºC → 420 ºC	60 min
420 ºC	3 h
420 ºC → 520 ºC	60 min
520 ºC	24 h
520 ºC → 600 ºC	60 min
600 ºC	5 h
600 ºC → 25 ºC	15 h

Figure 62. Temperature gradient followed for the synthesis of MCM41@G1.

Etching with HF. To achieve a partial etching of the silica scaffold, a diluted solution of HF (0.1 mL HF in 1 mL of water) was employed directly over the sample. The black residue formed was washed thoroughly with water.

4.2.3.4.3. Physical characterization.

FT-IR spectrum was taken using a FT-IR Nicolet 5700 spectrometer in the 4000-400 cm^{-1} frequency range, using powdered samples diluted in KBr pellets.

HR-TEM images were obtained using a TECNAI G2 F20 microscope. Field Emission Gun (FEG)200 kV.

Thermogravimetric analysis was carried out with a Mettler Toledo TGA/SDTA 851 apparatus in the 25-800^{o}C temperature range under 30mL mol^{-1} of nitrogen flow and at 10K min^{-1} scan rate.

X-ray powder profile (XRD) was collected using a Siemens D-500 X-ray diffractometer (Cu-Kα radiation, λα = 1.54184 Å). Sample was grounded and

mounted on a flat sample plate. Profile was collected as step scans in the $5^{o} < 2\theta < 70^{o}$ range with a spot size of 0.02^{o}.

Scanning electron microscopy (SEM) was performed with an Hitachi S-4800 microscope, having a resolution of 1.4 nm at 1kV.

Surface area, pore size and volume values were calculated from nitrogen adsorption-desorption isotherms (-196°C) recorded on a Micromeritics ASAP-2020 automated analyser. Samples were degassed for 12 hours at 110ºC and 10^{-6} Torr prior to analysis. Surface areas were estimated according to the BET model, and pore size dimensions were calculated by using the BJH model.

μ-Raman measurements at room temperature were performed with a dispersive Jobin-Yvon LabRam HR 800 microscope, working with an excitation line of 532 nm. The scattered light was detected with a thermoelectric cooled (-70 ºC) charge coupled device detector (CCD). It also has an Olympus BXFM optic microscope. All the measurements were carried out directly over the sample. In the performed experiments, the power employed over the samples was of the order of 0.3 mW, and the exposition time 60 seconds.

4.2.4. Synthesis of graphene by confinement of anthracene in between TaS_2 layers.

Amongst the vast quantity of layered inorganic systems available we have chosen Tantalum disulphide (TaS_2) as the lamellar host. TaS_2 belongs to the general family of metal dichalcogenide compounds (MX_2: M = Ti, Mo, Nb, Ta; X = S, Se, Te). This family of inorganic compounds was extensively studied since the observation of superconductivity in TaS_2 in the early seventies.[48] From a structural point of view, TaS_2 is composed by layers of TaS_2 interacting by weak van der Waals forces. Thus, it is possible to intercalate between them other systems or even exfoliate them into individual sheets.

Owing to these features, TaS_2 appears to be a promising host to growth graphene by following a thermal procedure similar to that described at point 4.2.2. On one hand, it possesses a lamellar structure in which a vast variety of systems has been introduced.[49] On the other hand, TaS_2 is obtained at very high temperatures and possess a great thermal stability (m.p. 3000 ºC), which turns it into a perfect host to carry out thermal processes without affecting their structure. In addition, the resulting hybrid may show interesting properties as it could combine for the first time the conducting properties of graphene with the superconductivity offered by TaS_2.

4.2.4.1. Results and discussion

4.2.4.1.1. Synthesis of TaS_2@G

TaS_2@G was obtained in a single step by placing Tantalum, sulphur and anthracene inside a quartz ampoule sealed under vacuum. The ampoule was then heated at 900 ºC so the anthracene molecules fused giving rise to graphene, while forming TaS_2. The result was a composite made up of TaS_2 and G (TaS_2@G). The stoichiometry of both components (TaS_2 and anthracene) was settled on basis of the dimensions of both TaS_2 and graphene which were selected to be 1 eq to 1 eq. Besides, the selected temperature is considerably higher when compared to that followed for the previous systems (point 4.2.2 and point 4.2.3). This temperature

was necessary in order to obtain TaS_2 of high crystallinity and, as it will be shown, it will not have any negative effect on the resulting G sheets.

4.2.4.1.2. X-ray diffraction powder (XRD)

X-ray diffraction powder gives signs of some important changes in the crystal structure of the obtained hybrid with respect to pure TaS_2. As shown in **Figure 63**, the hybrid TaS_2@G shows evidences about the successful synthesis of TaS_2 by the appearance of characteristics peaks of the phase 2H of TaS_2 (marked with an asterisk in **Figure 63**). In addition, the absence of the characteristic bands of anthracene and graphite demonstrates that, first, anthracene is no more present in the samples so it should have reacted, and second, the as-made graphene should be well isolated as otherwise the typical peak of graphite should have appeared. Finally, some minor signals (marked with an arrow in **Figure 63**) are also observed, along with the disappearance of some features of isolated TaS_2. Although these peaks have not been assigned they suggest the presence of new features that have appeared during the thermal process and may be assigned to the hybrid. Hence, XRD demonstrates the presence of TaS_2 in the hybrid sample but with some new features that must be characteristic of TaS_2@G.

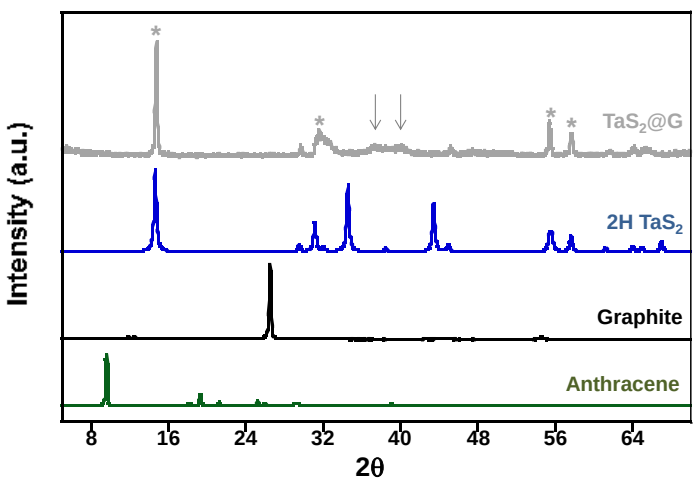

Figure 63. XRD of anthracene (green), graphite (black), TaS2 (blue) and the hybrid TaS2@G (grey). In the hybrid the characteristic bands of TaS2 have been marked with an asterisk and those new bands typical of the hybrid have been marked with an arrow.

4.2.4.1.3. Thermogravimetric analysis (TGA)

Thermogravimetric analysis was carried out under nitrogen atmosphere to avoid the formation Tantalum Oxide. Although a TGA measurement under air conditions would have served for quantifying the percentage of carbon in the sample, it was not possible in the present case due to this oxidation process. **Figure 64** shows the TGA of pristine graphite and TaS_2@G. As shown, under inert conditions graphite does not suffer any weight loss meaning that it does not possess defects. In the case of TaS_2@G just a 10% of the mass sample is lost upon heating, thus meaning that the defect content, although present, must be low.

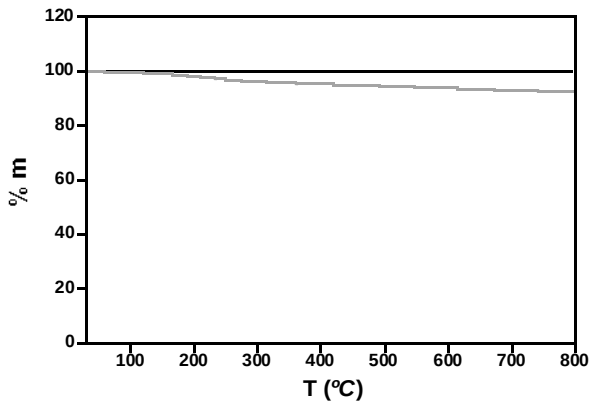

Figure 64. Thermogravimetric analysis under nitrogen atmosphere of graphite (black) and the hybrid TaS_2@G (grey).

4.2.4.1.4. Raman Spectroscopy

As it is shown in **Figure 65**, both, the G and D bands characteristic of graphitic species are present in the spectra. This means that the synthesis of graphene from anthracene has been successful, although some defects are present in the lattice as it was previously suggested by TGA. Those defects may come from the synthesis procedure. Importantly, it must be mentioned that the low I_G/ I_D ratio calculated (being 0.6) –which gives information about the size of the graphitic domains- suggests that our sample is composed by very small sp^2 domains. In addition, in **Figure 65** it is possible to observe the Raman modes of TaS_2, which appear in the low frequency region, thus demonstrating again then presence of both TaS_2 and graphene, in the hybrid sample.

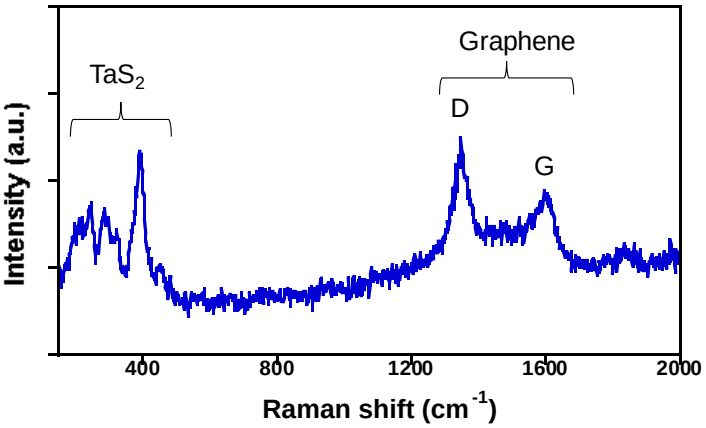

Figure 65. Raman spectra of TaS_2@G.

4.2.4.1.5. Morphology Analysis

SEM images show a very homogeneous lamellar morphology. As shown in **Figure 66**, the hybrid TaS_2@G is composed by micrometer size platelets, which may correspond to the hybrid. Although SEM does not permit to distinguish easily between graphene and TaS_2 sheets, it was possible to observe hexagonal platelets corresponding to isolated TaS_2 crystals (**Figure 66b**).

As SEM cannot permit to resolve the thickness of individual sheets, HR-TEM was employed to identify both G and TaS_2 in the hybrid sample. **Figure 67** (*top*) shows the HR-TEM images of TaS_2@G prepared by dropping freshly exfoliated TaS_2@G in methanol over a carbon grid. As shown, the sample consists of micrometer size layers that resembles those found in the literature for graphene.[3, 50] In addition, a close look into the high resolution regimen (**Figure 67c**) permitted the observation of the hexagonal atomic distribution typical of TaS_2. Finally, selected area electron diffraction (SAED) pattern of the hybrid sample was performed (**Figure 68**). As shown, two concentric rings which have been attributed to graphene and to TaS_2 respectively were observed. First, a well-defined hexagonal pattern (in red) which can be assigned to the (100) plane of TaS_2, can be seen in the first ring. In the second ring the hexagonal pattern is not so well defined probably because the crystallinity of graphene is considerably lower when compared to that of

TaS_2. Still, it is possible to assign it to the (100) planes of graphene having a distance of 0.22 nm (well correlated with that extracted from XRPD of graphite, 0.219 nm).

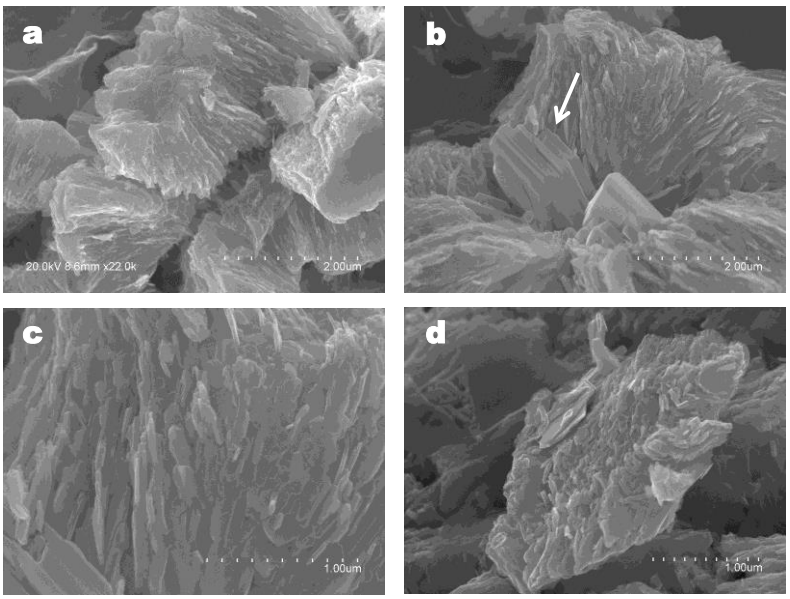

Figure 66. SEM imagines of the hybrid TaS2@G. In (b) an arrow points to the presence of isolated TaS_2 crystals.

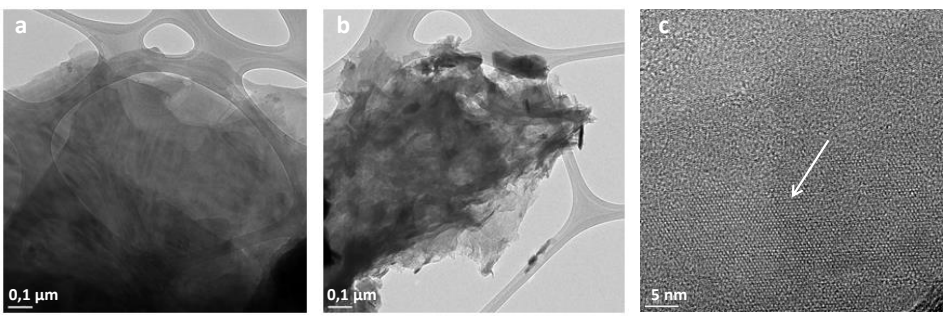

Figure 67. HR-TEM images of TaS_2@G (*top*), a) and b) shown two general images of the hybrid while c) corresponds with a high resolution image where the hexagonal pattern of TaS_2 is observed.

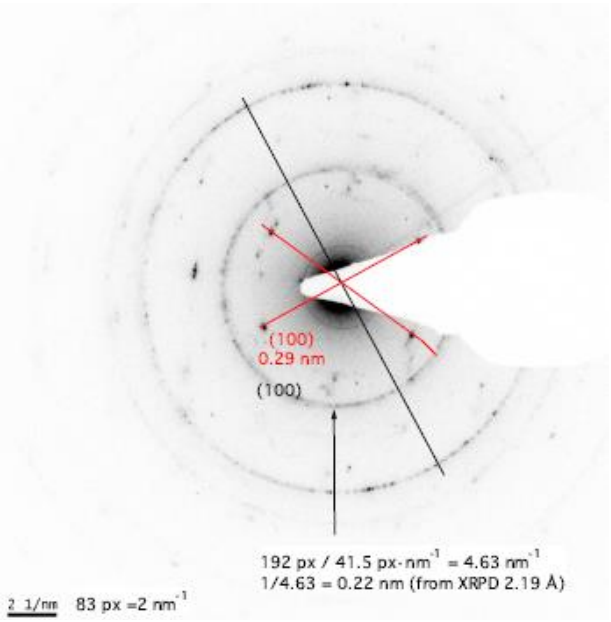

Figure 68. SAED pattern corresponding to **Figure 67**.

4.2.4.2. Conclusions

When anthracene molecules are introduced inside a quartz ampoule along with tantalum and sulphur, and the mixture is subjected to the thermal procedure required for the synthesis of lamellar TaS_2, a hybrid made up of TaS_2 and graphene is obtained. The presence of both components has been demonstrated by XRD, Raman and by the SAED pattern. Although, it has not been possible to observe single graphene flakes, SEM images suggest a kind of lamellar arrangement, in which it is very likely that graphene sheets has been embedded in between layers of TaS_2.

Future work will involve the study of the electronic and superconducting properties of the hybrid. In addition, we are going to try to obtain a more controlled system by employing as starting material TaS_2, and trying to introduce anthracene molecules in between the TaS_2 layers prior to the formation of graphene.

4.2.4.3. Experimental

4.2.4.3.1. General synthesis remarks

The temperature conditions were obtained by employing a tubular furnace (Gallur). The dimensions of the quartz tube were 30 cm of length, having a diameter of 1.5 cm.

4.2.4.3.2. Synthesis of TaS_2@G

4 mmol of Tantalum (0.72 g) and 8 mmol of sulphur (0.26 g) were carefully mixed with 0.52 mmol of anthracene (92 mg). Then they were placed inside a quartz ampoule which was sealed under vacuum. The quartz ampoule was heated at 900ºC during 9 days. Finally TaS_2@G appeared as a black homogeneous solid inside the quartz tube and analyzed without any further treatment.

4.2.4.3.3. Physical characterization.

HR-TEM images were obtained using a TECNAI G2 F20 microscope. Field Emission Gun (FEG)200 kV.

Thermogravimetric analysis was carried out with a Mettler Toledo TGA/SDTA 851 apparatus in the 25-800^{o}C temperature range under 30mL mol^{-1} of nitrogen flow and at 10K min^{-1} scan rate.

X-ray diffraction powder profile (XRD) was collected using a Siemens D-500 X-ray diffractometer (Cu-Kα radiation, λα = 1.54184 Å). Sample was grounded and mounted on a flat sample plate. Profile was collected as step scans in the $5^{o} < 2\theta < 70^{o}$ range with a spot size of 0.02º.

Scanning electron microscopy (SEM) was performed with an Hitachi S-4800 microscope, having a resolution of 1.4 nm at 1kV.

μ-Raman measurements were performed with a dispersive Jobin-Yvon LabRam HR 800 microscope, working with an excitation line of 532 nm. The scattered light was detected with a thermoelectric cooled (-70 ºC) charge coupled device detector (CCD). All the measurements were carried out directly over the sample. In the performed experiments, the power employed over the samples was of the order of 0.3 mW, and the exposition time 60 seconds.

4.3. References.

[1] K.S. Novoselov, A.K. Geim, S.V. Morozov, D. Jiang, Y. Zhang, S.V. Dubonos, I.V. Grigorieva, A. A. Firsov, *Science*, **2004**, *306*, 666.

[2] S. Park, R.S. Ruoff, *Nature Nanotech.*, **2009**, *4*, 217.

[3] D.R. Dreyer, S. Park, C.W. Bielawski, R. S. Ruoff, *Chem. Soc. Rev.*, **2010**, *39*, 228; Y. Hernandez, V. Nicolosi, M. Lotya, F.M. Blighe, Z. Sun, S. De, I. T. McGovern, B. Holland, M. Byrne, Y. K. Gun'ko, J. J. Boland, P. Niraj, G. Duesberg, S. Krishnamurthy, R. Goodhue, J. Hutchison, V. Scardaci, A. C. Ferrari, J. N. Coleman, *Nat. Nanotech.*, **2008**, *3*, 563.

[4] K.A. Mkhoyan, A. W. Contryman, J. Silcox, D.A. Stewart, G. Eda, C. Mattevi, S. Miller, M. Chhowalla, *Nano Lett.*, **2009**, *9*, 1058.

[5] R.L.D. Whitby, A. Korobeinyk, V. M. Gun'ko, R. Busquets, A.B. Cundy, K. Lászlo, J. Skubiszewska-Zieba, R. Leboda, E. Tombacz, I.Y. Toth, K. Kovacs, S.V. Mikhalovsky, *Chem. Commun.*, **2011**, *47*, 9645.

[6] W.S. Hummers, R.E. Offeman, *J. Am. Chem. Soc.*, **1958**, *80*, 1339.

[7] S. Stankovich, D. A. Dikin, R. D. Piner, K. A. Kohlhaas, A. Kleinhammes, Y. Jia, Y. Wu, S. T. Nguyen, R. S. Ruoff, *Carbon*, **2007,** *45*, 1558.

[8] a) H.-J. Shin, Ki Kang Kim, A. Benayad, S.-M. Yoon, Hyeon Ki Park, I.-S. Jung, Mei Hua Jin, H.-K.Jeong, Jong Min Kim, J.-Y. Choi, Young Hee Lee., *Adv. Funct. Mater,* **2009**, *19*, 1987. b) I. K. Moon, J. Lee, H. Lee, *Chem. Commun.*, **2011**, *47*, 9681.

[9] Y. Zhou, Q. Bao, L. A. L. Tang, Y. Zhong, K. P. Loh, *Chem. Mater.*, **2009**, *21*, 2950.

[10] X. Fan, W. Peng, Y. Li, X. Li, S. Wang, G. Zhang, F. Zhang, *Adv. Mater.*, **2008**, *20*, 4490.

[11] J. Shen, B. Yan, M. Shi, H. Ma, N. Li, M. Ye, *J. Mater. Chem.*, **2011**, *21*, 3415; H. Song, L. Zhang, C. He, Y. Qu, Y. Tian, Y. Lv, *J. Mater. Chem.*, **2011**, *21*, 5972.

[12] A) H. Li, G. Zhu, Z.-H. Liu, Z. Yang, Z. Wang, *Carbon*, **2010**, *48*, 4391; K. Chang, W. Chen, *Chem. Commun.*, **2011**, *47*, 4252.

[13] J. I. Peredes, S. Villar-rodil, A. Martinez-Alonso, J. M. D. Tascon, *Langmuir*, **2008**, *24*, 10560.

[14] C. D. Zangmeister, *Chem.Mater.*, **2010**, *22*, 5625.

[15] D. Long, W. Li, L. Ling, J. Miyawaki, I. Mochida, S.-H. Yoon, *Langmuir*, **2010**, *26*, 16096.

[16] a) A. Chuvilin, U. Kaiser, E. Bichoutskaia, N.A. Besley, A. N. Khlobystov, *Nat Chem.*, 2010, **2**, 450; J.-W. Seo, Y.-W. Jun, S.-W. Park, H. Nah, T. Moon, B. Park, J.-G. Kim, Y. J. Kim, J. Cheon, *Angew. Chem. Int. Ed.*, **2007**, *46*, 8828. b) A. Yella,

E. Mugnaioli, M. Panthöfer, U. Kolb, W. Tremel, *Angew. Chem. Int. Ed.*, **2010**, *49*, 3301.

[17] S. Stankovich, R. D. Piner, X. Chen, N. Wu, S. T. Nguyen, R. S. Ruoff, *J. Mater. Chem.*, **2006**, *16*, 155.

[18] G. Eda, M. Chhowalla, *Adv. Mater.*, **2010**, *22*, 1.

[19] J.-L. Chen, X.-P. Yan, *J. Mater. Chem.*, **2010**, *20*, 4328.

[20] J. I. Paredes, S. Villar-Rodil, P. Solís-Fernández, A. Martínez-Alonso, J. M. D. Tascón, *Langmuir*, **2009**, *25*, 5957.

[21] J. M. Englert, C. Dotzer, G. Yang, M. Schmid, C. Papp, J. M. Gottfried, H.-P. Steinrück, E. Spiecker, F. Hauke, A. Hirsch, *Nature Chem.*, **2011**, *3*, 279.

[22] S. P. Economopoulos, G. Rotas, Y. Miyata, H. Shinohara, N. Tagmatarchis, *ACS Nano*, **2010**, *4*, 7499.

[23] D. Wei, Y. Liu, *Adv. Mater.*, **2010**, *22*, 3225-3241.

[24] L. Zhi, K. Müllen, *J. Mater. Chem.*, **2008**, *18*, 1472.

[25] D.A.C. Brownson, C.E. Banks, *Phys. Chem. Chem. Phys.*, **2012**, *14*, 8264.

[26] a) X. Yang, X. Dou, A. Rouhanipour, L. Zhi, H.J. Räder, K. Müllen, *J. Am. Chem. Soc.*, **2008**, *130*, 4216. b) J. Cai, P. Ruffieux, R. Jaafar, M. Bieri, T. Braun, S. Blankenburg, M. Muoth, A.P. Seitsonen, M. Saleh, X. Feng, K. Müllen, R. Fasel, *Nature*, **2010**, *466*, 470.

[27] M. Treier, C.A. Pignedoli, T. Laino, R. Rieger, K. Müllen, D. Passerone, R. Fasel, *Nat. Chem.*, **2011**, *3*, 61.

[28] A.V. Talyzin, S.M. Luzan, K. Leifer, S. Akhtar, J. Fetzer, F. Cataldo, Y.O. Tsybin, C.W. Tai, A. Dzwilewski, E. Moons, *J. Phys. Chem. C*, **2011**, *115*, 13207.

[29] a) A.V. Talyzin, I.V. Anoshkin, A.V. Krasheninnikov, R.M. Nieminen, A.G. Nasibulin, H. Jiang, E.I. Kauppinen, *Nano Lett.*, **2011**, *11*, 4352. b) J. Sun, H. Liu, D. G. Evans, W. Yang, X. Duan, Chem. Commun., **2012**, *48*, 8126.

[30] Y. Xhou, Q. Bao, L.A.L. Tang, Y. Zhong, K.P. Loh, *Chem. Mater.*, **2009**, *21*, 2950.

[31] C. Bosch-Navarro, E. Coronado, C. Marti-Gastaldo, J.F. Sánchez-Royo, M. Gomez-Gomez, *Nanoscale*, **2012**, *4*, 3977.

[32] M. Fujihara, Y. Myata, R. Kitaura, Y. Nishimura, C. Camacho, S. Irle, Y. Iizumi, T. Okazaki, H. Shinohara, *J. Phys. Chem C*, **2012**, *116*, 15141.

[33] C. Castiglioni, C. Mapelli, F. Negri, G. Zerbi, *J. Chem. Phys.* **2001**, *114*, 963.

[34] K.N. Kudin, B. Ozbas, H.C. Schniepp, R.K. Prud'homme, I.A. Aksay, R.Car, *Nano Lett.*, **2008**, *8*, 36.

[35] A.C. Ferrari, J. C. Meyer, V. Scardaci, C. Casiraghi, M. Lazzeri, F. Mauri, S. Piscanec, D. Jiang, K.S. Novoselov, S. Roth, A.K. Geim, *PRL*, **2006**, *97*, 187401.

[36] M. Fujihara, Y. Myata, R. Kitaura, Y. Nishimura, C. Camacho, S. Irle, Y. Iizumi, T.

Okazaki, H. Shinohara, *J. Phys. Chem C*, **2012**, *116*, 15141.

[37] T.W. Chamberlain, J. Biskupek, G. A. Rance, A. Chuvilin, T.J. Alexander, E. Bichoutskaia, U. Kaiser, A.N. Khlobystov, *ACS Nano*, **2012**, *6*, 3943.

[38] J. Rouquerol, D. Avnir, C.W. Fairbridge, D.H. Everett, J.H. Haynes, N. Pernicone, J.D.F. Ramsay, K.S.W. Sing, K.K. Unger, *Pure & Appl. Chem.*, **1994**, *66*, 1739.

[39] M. Clemente-Leon, E. Coronado, A. Forment-Aliaga, P. Amorós, J. Ramírez-Castellanos, J.M. González-Calbet, *J. Mater. Chem.* **2003**, *13*, 3089.

[40] a) B. Tian, S. Che, Z. Liu, X. Liu, W. Fan, T. Tatsumi, O. Terasaki, D. Zhao, *Chem. Commun.*, **2003**, 21, 2726. b) M. Inagaki, H. Orikasa, T. Morishita, *RSC Adv.*, **2011**, *1*, 1620. c) F. de Clippel, A. Harkiolakis, T. Vosch, X. Ke, L. Gielbeler, S. Oswald, K. Houthoofd, J. Jammaer, G. Van Tendeloo, J.A. Martens, P.A. Jacobs, G.V. Baron, B.F. Sels, J.F.M. Denayer, *Microporous and Mesoporous Materials*, **2011**, *144*, 120.

[41] D. Das, C.-M. Tsai, S. Cheng, *Chem. Commun.*, **1999**, 129, 473.

[42] M. Ogawa, H. Shirai, K. Kuroda, C. Kato, *Clays and Clay Minerals*, **1992**, *40*, 485.

[43] C. Charnay, S. Begu, C. Tourne-Peteilh, L. Nicole, D.A. Lerner, J.M. Devoisselle, *European Journal of pharmaceutics and biopharmaceutics*, **2004**, *57*, 533.

[44] a) J. Yu, Z.ñ feng, L. Xu, M. Li, Q. Xin, Z. Liu, C. Li, *Chem. Mater.*, **2001**, *13*, 994. b) T. Abdel-Fattah, *Fullerenes, nanotubes and carbon nanostructures*, **2006**, *14*, 585. c) G.D. Mihai, V. Meynen, M. Mertens, N. Bilba, P. Cool, E.F. Vansant, *J. Mater. Sci.*, **2010**, *45*, 5786.

[45] D.V. Kosynkin, A.L. Higginbotham, A. Sinitskii, J.R. Lomeda, A. Dimiev, B. Katherine Price, J.M. Tour, *Nature*, **2009**, *458*, 872.

[46] C.P. Jaroniec, M. Kruk, M. Jaroniec, *J. Phys. Chem. B*, **1998**, *102*, 5503

[47] D.V. Kosynkin, A.L. Higginbotham, A. Sinitskii, J.r. Lomeda, A. Dimiev, B.K. Price, J.M. Tour, *Nature*, **2009**, *458*, 872.

[48] F.R. Gamble, F. DiSalvo, R. Klemm, T. Geballe, *Science*, **1970**, *168*, 568.

[49] a) E. Coronado, C. Martí-Gastaldo, E. Navarro-Moratalla, E. Burzuri, A. Camon, F. Luis, *Adv. Mater.*, **2011**, *23*, 5021. b) E. Coronado, C. Martí-Gastaldo, E. Navarro-Moratalla, A. Ribera, S.J. Blundell, P.J. Baker, *Nat. Chem.*, **2010**, *2*, 1031.

[50] C.N.R. Rao, K. Biswas, K.S. Subrahmanyam, A. Govindaraj, *J. Mater. Chem.*, **2009**, *19*, 2457

5 Chemical Functionalization of Graphene[*,†]

Chemical derivatization of graphene is undoubtedly the most direct way to overcome important issues such as its solubilization in common solvents, or the modification of its intrinsic physical properties by introduction of suitable organic functions or combination with discrete or extended moieties. This chapter will be divided in two parts. In the first one, a new strategy to chemically modify graphene with amino groups and further functionalize them with gold nanoparticles will be described. This kind on graphene-based composites can be employed in a variety of fields such as catalysis, Li-ion batteries, fuel cells, supercapacitors, sensors, photovoltaic devices and so on. Alike the vast majority of chemical routes available, our approach introduces an additional degree of control over the level of coverage of Au NPs by controlling the degree of functionalization. The second section reports the functionalization of graphene with paramagnetic moieties through the Bingel-Hirsch cyclopropanation reaction. In this case, a hybrid which combines conductivity and magnetism will be described. We will show how the conduction mechanism varies as a function of the density of radicals grafted to the carbon layers. Moreover, we will show how the presence of paramagnetic moieties influences de magnetoresistive behavior of the system by the appearance of a low field magnetoresistance (LFMR) effect. Finally, the derivatization of G with diamagnetic ethylmalonate molecules, following an analogous route, will permit us to discard the chemical derivatization as the responsible for the observed differences in the MR response that must be rather ascribed to the grafting of the organic spin carriers.

[*] C. Bosch-Navarro, E. Coronado, C. Marti-Gastaldo, *Carbon*, **2013**, *54*, 201.

[†] C. Bosch-Navarro, F. Busolo, E. Coronado, Y. Duan, C. Marti-Gastaldo, H. Prima-García, *J. Mater. Chem. C.*, Submitted

5.1. Controllable coverage of chemically modified graphene sheets with gold nanoparticles by thermal treatment of graphite oxide with N,N-Dimethylformamide

5.1.1. Introduction

The high surface area and extraordinary electronic properties that either GO or chemically modified graphene (CMG) possess performs them as very interesting matrix for the deposition of metal nanoparticles (NPs) which would be of interest in biomedicine, surface-enhanced Raman scattering, energy storage, electrochemical sensing or catalysis.[1] In this context, many examples in which metal NPs such as Au, Ag, Pd, Pt, Ni or Cu appeared decorating G sheets with different purposes have been described in previous works, although, to the best of our knowledge, the level of coverage achieved through these routes is poorly controlled.[1b, 2]

As it has been widely described in this Thesis, a vast amount of different routes to synthesize G are currently available (see Chapter 2). Amongst these methodologies, the thermal reduction of GO, either under high-pressure (Chapter 4, point 4.1, page 100) or in open-air conditions, provides a simple and reliable method.[3] A possible solvent we can use for this purpose is the N,N-dimethylformamide (DMF), which has high polarity and boiling point (153ºC). Furthermore, DMF can play an active chemical role in several processes.[4] In particular, the decomposition of DMF at high temperatures and further reaction with carboxylic acids and epoxy groups present in the reaction medium can produce amides or amines in the final product. This fact is particularly interesting as DMF has been typically employed as innocent solvent for the functionalization of CNTs or G.[5]

Here we demonstrate that the reduction of GO can be carried out under thermal conditions in DMF in an open-air system. Favored by the high content of oxygen functionalities present in GO, this thermal reaction not only promotes reduction but also introduces nitrogen functionalities across the graphene-like lattice from their reaction with the dimethylamine molecules generated from the decomposition of the solvent. In addition, we will show how by varying the reaction conditions (reaction temperature and reaction time) the nitrogen content along the

layers can be controlled. Next, we have taken advantage of the chemical affinity between nitrogen and gold nanoparticles (Au NPs) to produce CMG-Au NPs composites with control over the coverage of the NPs on the graphene-like layers in relation to the degree of functionalization achieved.

5.1.2. Results and discussion

5.1.2.1. Synthesis

In a first step, GO was prepared from graphite powder according to the Hummers procedure.[6] Next, GO was suspended in DMF and heated under open-air conditions at temperatures between 85-120º C and periods of time varying from 1 to 5 days (CMG f(T,t)). In this thermal process, reduction takes places by deoxygenation of GO in a similar way to that described for other high boiling point organic solvents such as NMP or DMSO.[3c] In the last step, the affinity between these functional groups and gold was used to direct the attachment of Au NPs from solution to CMG f(T, t) via weak covalent bond by adding a solution of freshly prepared NPs in toluene to a dispersion of the former in anhydrous DMF.[7]

5.1.2.2. Evidence on the functionalization with amino groups

5.1.2.2.1. FT-IR

A comparison between the FT-IR spectra of the starting GO and the products resulting from its reaction with DMF provided a clear indication of chemical transformation (**Figure 69**). In fact, as result of the thermal reduction, the disappearance of the GO characteristic vibration modes attributed to oxygen moieties (1730 cm^{-1}, 1620 cm^{-1}) is accompanied by a broadening of the vibration modes related to the aromatic structure (1550 cm^{-1}, 1130 cm^{-1}), thus indicating a partial recovery of the graphene-like structure of the layers. Moreover, in the reduced samples, new bands associated to the appearance of C-N groups can be observed at 1400 cm^{-1}, and the lack of a sharp an intense band around 1670 cm^{-1} discards the presence of absorbed DMF, thus confirming the functionalization. Unfortunately, this technique does not allow establishing a quantitative correlation between this transformation and the different temperature and reaction times.

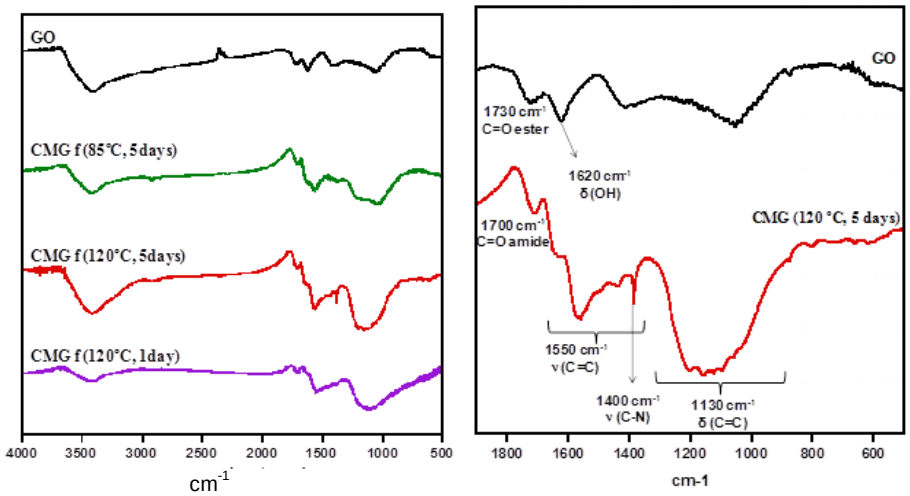

Figure 69. FT-IR spectra of GO (black), CMG f(85 ºC, 5days) (green), CMG f(120 ºC, 5 days) (red), and CMG f(120 ºC, 1 day) (purple) (*left*). Zoom-in to the area 1850-500 cm^{-1} showing the characteristic bands of GO and the CMG f(T, t), in order to simplify the figure just GO (black) and CMG f(120 ºC, 5 days) (red) are shown (*right).*

5.1.2.2.2. Elementary Analysis and Thermogravimetry

According to the elemental analysis performed on GO and CMG f(T, t) (**Table 4)**, **Figure 70** displays the variation on the O/C and N/C ratios with the reaction time, varying between 1 and 5 days and temperature, ranging from 85 to 120º C. **Figure 70a** shows the variation of the N/C content in the samples as a function of the temperature for a fixed reaction time. N/C increases continuously from nearly 0, for the starting GO, to 0.06 for both, 85 and 100º C, up to a maximum value of 0.08 for the reaction performed during 5 days at 120º C. The introduction of N-functionalities is in good agreement with a drastic reduction of the overall oxygen content across the layers therefore supporting the reduction of GO by thermal deoxygenation in DMF. The role played by the reaction time on the functionalization progress was studied by continuously stirring a suspension of as-prepared GO in DMF at 120º C during 1, 3 and 5 days. **Figure 70b** shows a positive correlation of the overall N content with time, with a direct relationship between the reaction time

Table 4. Elementary analysis of GO and CMG f(T, t) samples.

Sample	%wt C	%wt O	%wt N	%wt H	ratio O/C	ratio N/C
GO	49.62	52.44	0.12	2.70	1.06	0.002
CMG f(85ºC,5 days)	68.85	24.85	4.01	2.20	0.36	0.058
CMG f(100ºC,5 days)	69.83	23.44	4.12	2.61	0.34	0.059
CMG f(120ºC,5 days)	64.51	27.89	5.13	2.47	0.43	0.080
CMG f(120ºC,3 days)	69.19	23.67	4.64	2.50	0.34	0.067
CMG f(120ºC,1 day)	68.26	25.18	3.56	3.00	0.37	0.052

and the functionalization efficiency. In addition, according to what has been previously reported by Feringa et al.,[8] the degree of functionalization can be estimated on basis to the nitrogen content. The maximum degree of functionalization is obtained for CMG f(120ºC, 5 days) (being 1 nitrogen atom per 22 carbon atoms), and the lowest one for CMG f(85ºC, 5 days) and (CMG f(120ºC, 1 day), being 1 nitrogen per 27 carbon atoms and 1 nitrogen per 32 carbon atoms, respectively.

This chemical change also introduces important differences in the thermal decomposition of the reduced samples with respect to GO (**Figure 71**), whilst the pyrolysis of GO undergoes through two processes centered around 200 and 500ºC, corresponding to the decomposition of oxygen functionalities and the graphitic layers, respectively, CMG f(T, t) exhibit increased thermal stability upon heating in air, with a less severe mass removal at temperatures below 500 ºC likely due to a partial restoration of the graphitic structure.[9] Besides, the O/C ratio follows the opposite trend to that observed for the N/C ratio, being greater for the CMG samples treated at higher temperature and during longer periods of time (**Figure 70**). This increase is most likely due to the introduction of oxygen-containing functional groups decorating the surface of graphene, rather than to an improved deoxygenation.[3a] Still, the notably decrease of the O/C ratio for the CMG f(T,t) samples when compared to GO demonstrates that the reduction process has taken place during the thermal treatment.

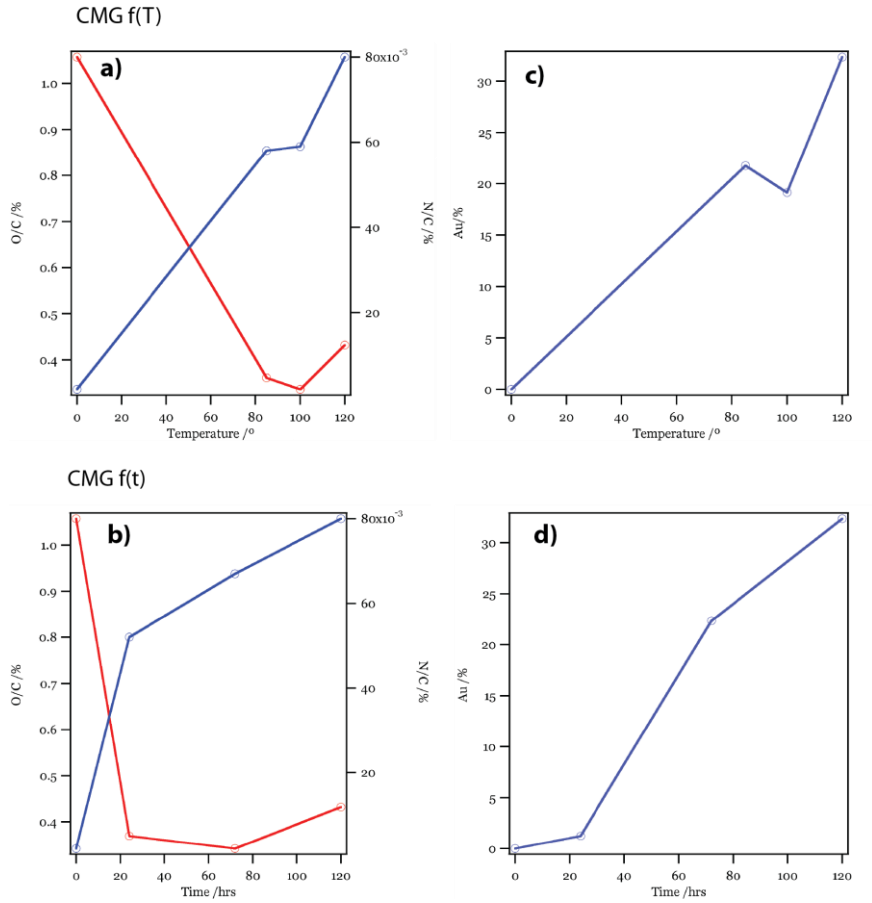

Figure 70. Variation of the O/C and N/C % ratios for CMG (a and b) and the Au content as extracted from thermal analysis (c and d) in the CMG-Au NPs composites studied as a function of the temperature (*top*) and the reaction time (*bottom*).

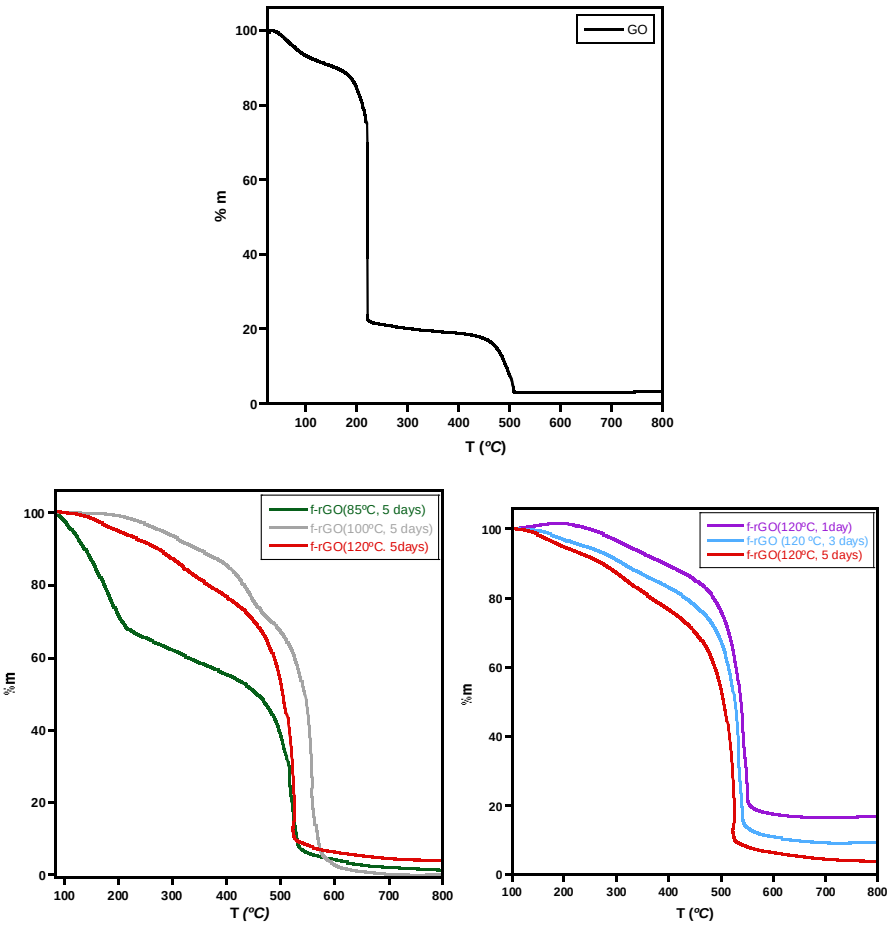

Figure 71. Thermal decomposition under O_2 atmosphere of: GO (black, solid line) (*left*); CMG f(85 ºC, 5 days) (green, solid line), CMG f(100 ºC, 5 days) (grey, solid line), CMG f(120ºC, 5 days) (red, solid line), CMG f(120 ºC, 3 days) (blue, solid line), CMG f(120 ºC, 1 days) (purple, solid line), (*middle and right*).

5.1.2.2.3. Functionalization mechanism

At this point it is worth commenting on the mechanism that must be responsible for introduction of nitrogenated groups across the carbon layers (see **Figure 72**). On the basis of recent reports, the reaction of amines with the carboxylic groups or epoxides covering the surface of the GO sheets lead to their amination by formation of amides and/or 1,2-aminoalcohols, respectively.[10] In our case, the reacting amine must be released from the thermal decomposition of DMF. This process is catalyzed under acid conditions like those generated from the dispersion

of the as-prepared GO in water (pH = 5.4) and generates dimethylamine molecules that are likely to interact with the GO sheets present in the reacting mixture.[10a] Since both, temperature and reaction time, will control the gradual decomposition and subsequent release of dimethylamine, they can be used to control the efficiency of the subsequent functionalization of the surface of GO to generate N-functionalities across the graphene layers, thus introducing a degree of control over the functionalization extent.

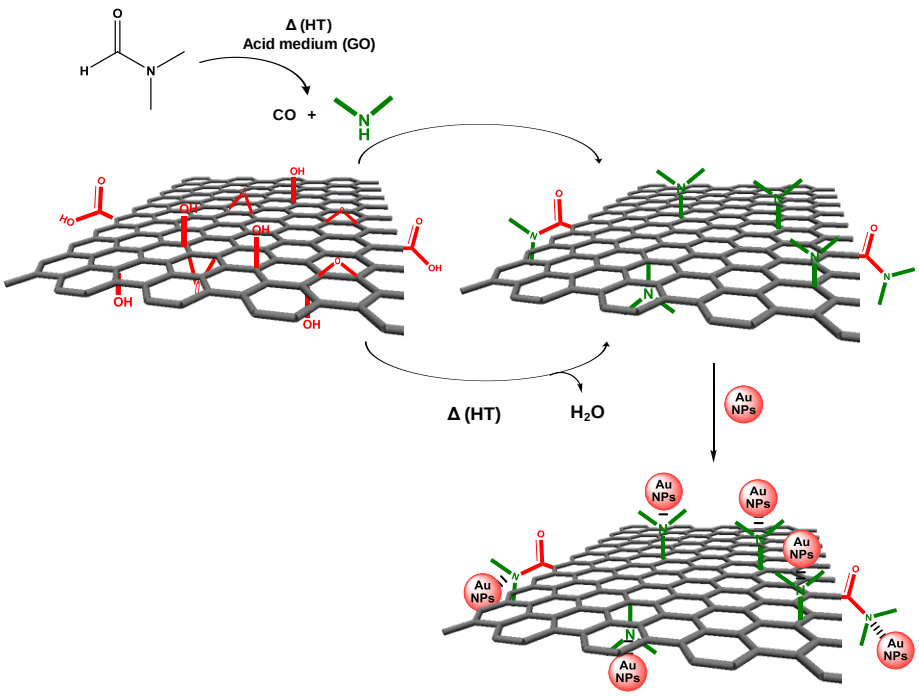

Figure 72. A schematic illustration of the functionalization/reduction process to obtain CMG f(T, t) and CMG f(T,t)@Au

5.1.2.3. Anchoring of Gold Nanoparticles

5.1.2.3.1. Thermogravimetry

As a first clue of success, the comparative thermogravimetric analysis of the samples, before and after grafting, permitted a rough estimation of the amount of metal loaded in each case (**Figure 71** and **Figure 73**). A direct correlation between the Au loading and the density of N-functionalities across the layers is observed. Hence, **Figure 70c and d** shows how the Au% follows the same trend already plotted for the degree of functionalization in CMG f(T, t), with higher loadings for longer reaction times and higher temperatures (

Table 5). It is worth mentioning that the little increase in the mass weight observed for some samples below 200ºC (around 1-2%) might come from the apparatus and it is connected to a flotation effect derived from the Archimedes' principle. When the chamber containing the sample is heated, this produces an increase in the density of the gas inside the chamber which, according to this principle, results in an increase of the mass. Once the pressure inside the chamber is stabilized this effect ceases. It is worth noting that the effect becomes more pronounced when low mass samples are being measured, just like in our case.

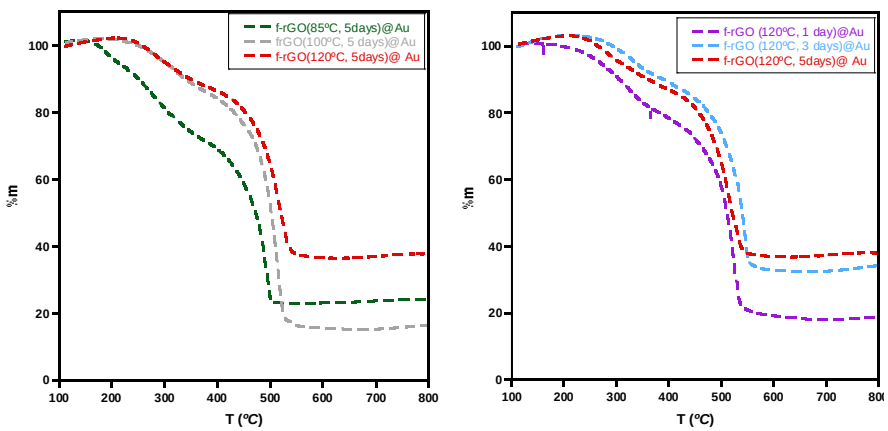

Figure 73. Thermal decomposition under O_2 atmosphere of CMG f(85 ºC, 5 days)@Au (green, dotted line), CMG f(100 ºC, 5 days)@Au (grey, dotted line), CMG f(120 ºC, 5 days)@Au (red, dotted line), and CMG f(85 ºC, 5 days)@Au (purple, dotted line), CMG f(100 ºC, 5 days)@Au (blue, dotted line), CMG f(120 ºC, 5 days) (red, dotted line) (*top*).

Table 5. Table showing the residual mass for the different samples and the % Au extracted from the thermogravimetric analysis.

Sample	% m	%m (Au)
CMG f(85 ºC, 5 days)	2.08	21.77
CMG f(85 ºC, 5 days)@Au	23.85	
CMG f(100 ºC, 5 days)	0	19.3
CMG f(100 ºC, 5 days)@Au	19.3	
CMG f(120 ºC, 5 days)	4.17	32.34
CMG f(120 ºC, 5 days)@Au	36.51	
CMG f(120 ºC, 3 days)	9.12	22.35
CMG f(120 ºC, 3 days)@Au	31.47	
CMG f(120 ºC, 1 day)	16.78	1.24
CMG f(120 ºC, 1 day)@Au	18.02	

5.1.2.3.2. X-Ray Photoelectron Spectroscopy

Further insights on the chemical nature of the CMG f(T, t) samples before and after the Au NPs grafting were extracted from XPS. **Figure 74b** and **Figure 75c** summarizes the binding energy (BE) values as extracted from high-resolution spectra. The evolution of the C1s signal between GO and the samples reacted with DMF (**Figure 74**) clearly confirms the reduction of the former after the functionalization process. In fact, **Figure 74 a & b** shows how for the conditions yielding a maximum degree of functionalization - 120ºC, 5 days - the disappearance of the C sp^3 signal (285.6 eV) is accompanied by a drastic increase of the C sp^2 content (285 eV).[10, 11] Besides reduction, this chemical treatment also provokes the appearance of a N1s signal for the CMG f(T, t) samples, which can be adjusted to two contributions at ca. 400.2 and 402.4 eV associated to the presence of N-C and N-O bonds, respectively **(Figure 75**). Finally, upon addition of Au NPs, the appearance of a new contribution at lower BE (~399.2 eV) associated to the presence of N-Au bonds (**Figure 75a**),[12] gives unfailing evidences of the chemical attachment of the NPs to the CMG layers as result of their functionalization.

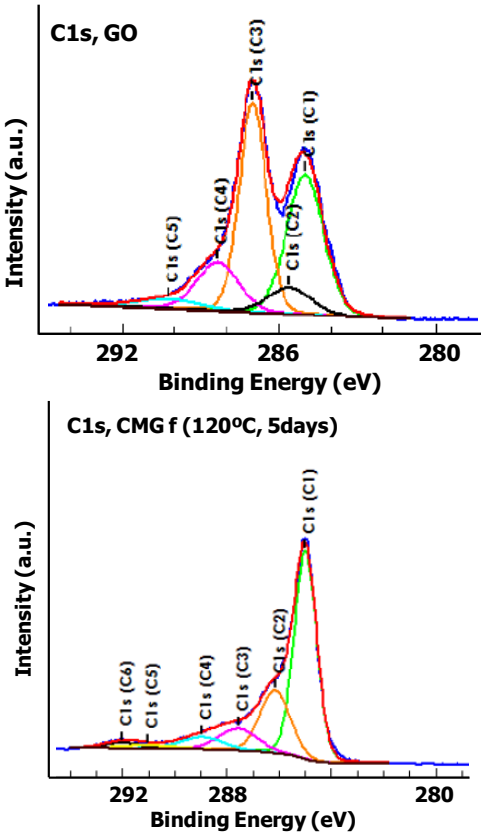

(a)

	C1 **285eV(sp^2 graphitic C)**	C2 **285.6eV(sp^3) 286eV(C-N) 286.5eV(C-O)**	C3 **288eV (C=O) 288.2eV (N-C=O)**	C4 **288.3eV(C=O)**	C5 **291eV ππ*shake up satellite**	C6 **290eV (CO3)**
GO	34.5%	4.2%	38.8	14%	x	3.9
CMG(85ºC,5d)	58.4%	27.4%	8%	5.5%	0.6%	x
CMG(120ºC,5d)	55.7%	22.6%	10.6%	6.5%	2.2%	2.5%
CMG(120ºC, 1d)	48%	31.8%	11.8%	6.8%	2.1%	x

(b)

Figure 74. (a) C1s XPS spectra of GO and CMG f(120ºC, 5 days), the rest of CMG f (T,t) samples showed equivalent spectra and have not been included to simplify the figure; (b) Table showing the Binding Energies extracted from C1s spectrums for the different CMG f(T, t) samples and the percentage of each type of carbon. All the spectra show the experimental data plotted in blue, while the fitting appears in different colors.

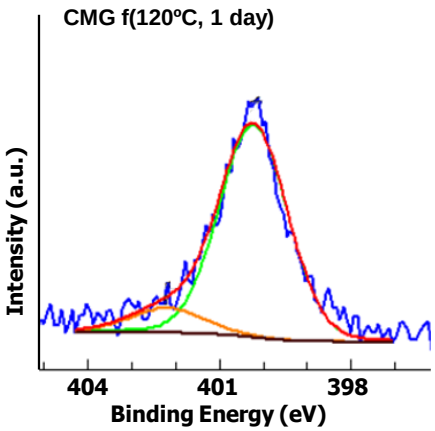

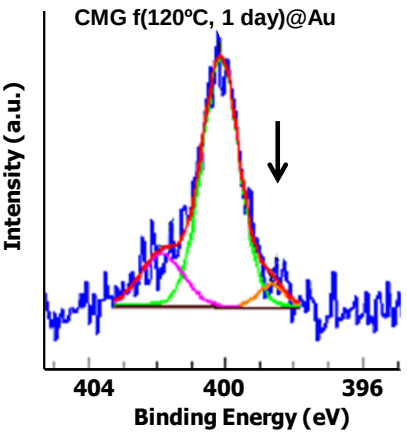

(a)

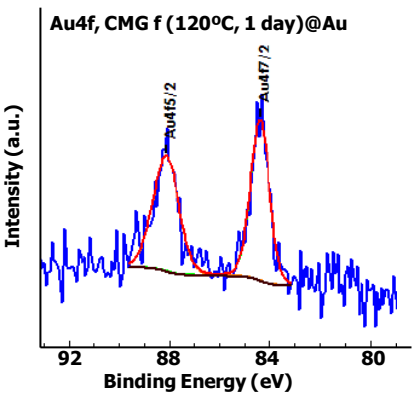

(b)

	N1s 398.8 eV (N-Au) 400.2 eV (N-C) 401.8 eV (N-O)	$Au4f_{7/2}$ 84.4 eV (Au^0) 86 eV (Au_2O_3)
CMG (85ºC,5 days)	400.2 eV / 65.8% 401 eV / 34.2 %	X
CMG (120ºC,5 days)	398.3 eV / 9.3% 400.2 eV / 81.2% 401.8 eV / 9.5 %	X
CMG (120ºC,1 day)	400.22 eV / 88.8% 402.2 eV / 11.2%	X
CMG (85ºC,5 days)@Au	399.2 eV / 15.1% 400.26 eV / 64.5% 402.04 eV / 30.4%	84.4 eV / 81.8% (Au^0) 86.0 / 18.2% (Au_2O_3)
CMG (120ºC,5 days)@Au	399.2 eV / 22.3% 400.38 eV / 50.8% 402.43 eV / 26.9%	84.45 eV / 95.2% (Au^0) 86.0 eV / 4.8% (Au_2O_3)
CMG (120ºC,1 day)@Au	398.67 eV / 8.6% 400.14 eV / 75.8% 401.85 eV / 1806%	84.42 eV / 100% (Au^0)

(c)

Figure 75. (a) N1s XPS spectra of CMG (120ºC, 1 day) and (c) CMG(120ºC, 1 day)@Au. The blue line represents the experimental data and the colored lines correspond to the deconvolution of the peaks. An arrow indicates the contribution associated to the presence of N-Au bonds in CMG f(120ºC, 1day)@Au. (b)) $Au4f_{7/2}$ XPS spectra of CMG f(120ºC, 1 day)@Au. In both cases, the rest of CMG f(T, t) and CMG f(T,t)@Au samples showed very similar N1s and $Au4f_{7/2}$ spectra so they have not been included to simplify the figure. (c) Table showing the Binding Energies extracted from N1s and Au4f XPS spectrums for the different CMG f(T, t) and CMG f(T, t)@Au samples.

5.1.2.3.3. HR-TEM

Finally, HR-TEM images of the CMG f (T, t)@Au NPs composites where acquired. **Figure 76** confirms the absence of Au NPs in the surface of GO, thus demonstrating that the NPs are unable to bind chemically unmodified GO. In turn,

Figure **77 a, b, and c**, corresponding to the grafting of Au NPs to GO reacted with DMF at 85, 100 and 120 ºC during 5 days, clearly show the presence of Au NPs as black dots with sizes of *ca.* 5 nm grafted across the CMG surface. The presence of Au was additionally confirmed with EDAX metal analysis as performed *in-situ* (Figure 78 **d**). In addition, the level of coverage seems to be directly connected to the temperature of the CMG chemical treatment, thus supporting that the N-functionalities act as "anchor points" for the binding of the NPs. This same tendency is also observed for the reaction time. Hence,

Figure **77 c, d and e**, corresponding to the grafting of Au NPs to GO reacted with DMF at 120º C during 1, 3 and 5 days, show again an enhanced coverage level for the CMG samples reacted during longer periods of time. It is worthwhile mentioning that the presence of graphene-like layers in the composites was confirmed by selected area electron diffraction (SAED), which exhibit the expected hexagonal pattern diffraction associated to the in-plane symmetry intrinsic to graphene (Figure 78). This result discards damages in the in-plane structure of the material during the chemical treatment.

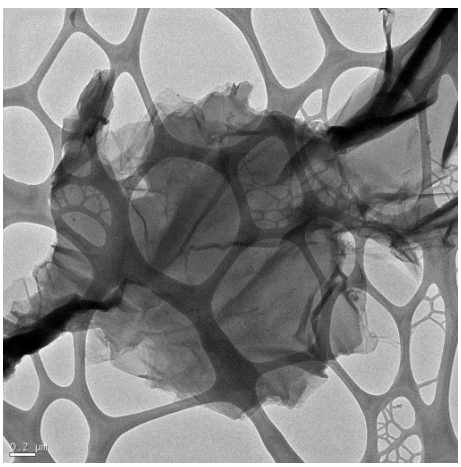

Figure 76. HR-TEM images of GO after the addition of Au NPs showing no gold deposition

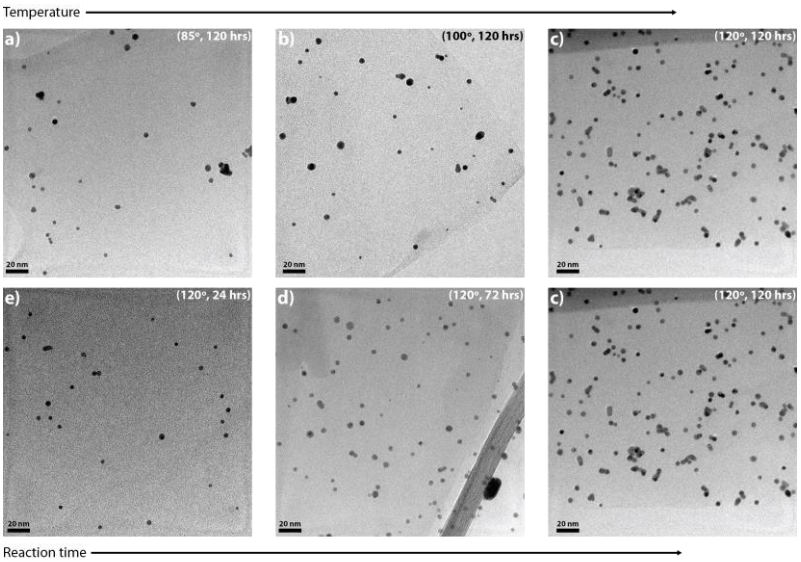

Figure 77. HRTEM images of CMG f(T,t) after gold deposition showing how the surface coverage can be modulated with temperature (top) and reaction time (bottom). Specific experimental conditions for each sample are indicated in the top-right corner. Au NPs appear as black dots decorating the surface of the functionalized samples.

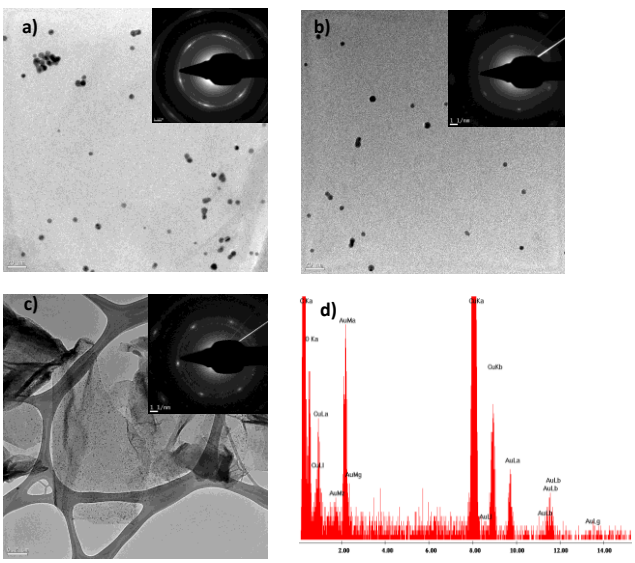

Figure 78. Additional HR-TEM and Fast Fourier transform of a) CMG f (85ºC, 5days), b) sample CMG f (120ºC, 1day) and c) sample CMG f (120 ºC, 5 days) showing the hexagonal diffraction pattern typical of graphitic forms. For CMG f (120 ºC, 5 days)@Au the EDX spectrum showing the presence of gold in the sample is depicted in (d) (copper signal is associated to the supporting grid).

5.1.3. Conclusions

We have described a straightforward method for the reduction and functionalization of GO to obtain CMG through thermal treatment in DMF. The synthesized CMG f(t, T) samples can be decorated with Au NPs by their chemical interaction with the N-functionalities, which have been introduced across the graphene layers during the chemical treatment. Despite the grafting of metal NPs on chemically synthesized graphene has been already described, the methodologies reported do not permit controlling the grafting density. In turn, thanks to the direct relationship between the temperature and the reaction time and the efficiency of the thermal functionalization affecting the CMG layers, our route exploits these chemical variables to control the level of coverage upon deposition of the Au NPs. It is worthwhile mentioning that our results indicate that the functionalization takes place even at relatively low temperatures (*ca.* 85ºC), whereas DMF is generally used as innocent solvent in the chemical functionalization of GO for many purposes.

This simple and low cost procedure provides an attractive alternative for the fabrication of other 2D nanocomposites with a wider range of metal NPs and enhanced control on their loading across the graphene-like layers which will might be of great help to finely tune their physical properties.

5.1.4. Experimental

5.1.4.1. General synthesis remarks

Graphite powder was purchased from Fisher Scientific. It was dispersed in DMF and sonicated by using a Brandsonic 5510 MT operating at 135 W. Centrifugation was performed at 10 ºC employing a Eppendorf Centrifugation System working at 12000 rpm during 10 minutes. The samples were filtered employing a vacuum filter funnel of pore size number 3 and nylon membrane filters (Ø 0.2 μm pore).

5.1.4..2. Synthesis of Au NPs.

In a extraction funnel a solution of $NaAuCl/H_2O$ (0.186 g/14.9 mL) was mixed with a solution of Tetraoctylammoniumbromid/Toluene (1.214 g/41 mL), and

left without disruption during 1 hour. After 1 hour, an aqueous solution of sodium borohydride (0.063 g in 15.9 mL) was dropwised to the organic layer, and the mixture stirred at room temperature overnight. Finally, the mixture was extracted first with H_2SO_4 0.1 M, followed by a basic extraction with NaOH 0.1 M and a last one with H_2O. The organic layer was dried over anhydrous sodium sulphate, and filtered off to obtain a red solution of AU NPs (30mM).

5.1.4.3. Synthesis of GO

The same procedure as that described at Chapter 4 (point 4.1.4.2., page 113) has been followed.

5.1.4.4. Synthesis of CMG f(T,t)

Firstly, 50 mg of GO were exfoliated in dry DMF (100 mL) by applying ultrasounds to a freshly prepared dispersion during 30 minutes. Next, the sample was heated at T (85 ºC, 100 ºC, 120 ºC) during t (1 day, 3 days, 5 days). Once the reaction time was over, the sample was left to stand at room temperature and centrifuged with continuous washing cycles, first with THF and next with methanol. Finally, CMG f(T, t) was isolated as a black solid by filtering under vacuum through a nylon membrane filter and dried overnight at 100 ºC.

5.1.4.5. Synthesis of CMG f(T,t)@Au

2 mg of CMG f(T, t) were dispersed in 10mL of anhydrous DMF. Then, 0.5 mL of Au NPs in toluene were added and the mixture stirred at room temperature during 30 minutes and left to stand at room temperature overnight. Next, the hybrid material was cleaned by centrifugation washing it repeatedly with toluene in order to get rid of the excess of Au NPs not attached to the graphene sheets. Finally, CMG f(T, t)@Au was isolated by filtration under vacuum over a nylon membrane filter.

5.1.4.6. Physical Characterization

Infrared Spectroscopy (FT-IR) was taken using FT-IR Nicolet 5700 spectrometer in the 4000-400 cm^{-1} frequency range, using powdered samples diluted in KBr pellets.

Thermogravimetric analysis was carried out with a Mettler Toledo TGA/SDTA 851 apparatus in the 25-800 Cº temperature range under a 30 $mL.mol^{-1}$ air flow and a 10 ºC min^{-1} scan rate.

High Resolution Transmission Microscopy (HR-TEM) images was performed employing a TECNAI G2 F20 microscope, Field Emission Gun (FEG)200 kV.

Electron spectroscopy for chemical Analysis (ESCA) and X-ray photoelectron spectroscopy (XPS), were performed using a Thermo Scientific K-Alpha ESCA instrument equipped with aluminium Kα1,2 monochromatized radiation at 1486.6 eV X-ray source. The non-conductive nature of the samples made necessary to use an electron flood gun to minimize surface charging. Neutralization of the surface charge was performed by using a low energy flood gun (electrons in the range 0 to 14 eV) and a low Argon ions gun. The XPS measurements were carried out using monochromatic Al-Kα radiation (h=1486.6 eV). Photoelectrons were collected from a take-off angle of 90° relative to the sample surface. The measurement was done in a Constant Analyser Energy mode (CAE) with a 100 eV pass energy for survey spectra and 20 eV pass energy for high resolution spectra. Charge referencing was done by setting the lower binding energy C 1s photo peak at 285.0 eV C1s hydrocarbon peak. Surface elemental composition was determined using the standard Scofield photoemission cross sections.

μ-Raman measurements at room temperature were performed with a dispersive Jobin-Yvon LabRam HR 800 microscope, working with an excitation line of 532 nm. The scattered light was detected with a thermoelectric cooled (-70 ºC) charge coupled device detector (CCD). It also has an Olympus BXFM optic microscope. All the measurements were carried out directly over the sample. In the performed experiments, the power employed over the samples was of the order of 0.3mW, and the exposition time 60 seconds.

5.2 Covalent grafting of organic radicals to graphene. Magnetoresistance properties.

5.2.1. Introduction

Graphene (G) is currently subject of wide interest due to its unique physical properties (see Chapter 2). Among these, its extraordinary electronic properties like its ability to be used as a zero-gap semiconductor with ballistic electron transport, have attracted important attention. Still, pristine chemically unmodified graphene does not possess a band gap therefore limiting its implementation into fully operational transistor devices for which big resistivity changes are required.[13] Hence, to gain control over the electronic properties of G appears to be one of the main challenges for the future development of G-based electronics. In this context, the chemical synthesis of G from bulk graphite has demonstrated to be a versatile approach as the introduction of hydroxyl, epoxy and carboxylate groups, whose concentration and relative ratio mainly depends on the oxidation method followed, introduces structural defects across the aromatic sp^2 structure of the G layers thereby disrupting its electronic properties and introducing a band-gap which, according to theoretical calculations, can range from a few tenths to 4 eV.[14] Besides this direct chemical modification, the grafting of electronically active organic molecules appears as an feasible alternative. In fact, the direct attachment of chemically-functionalized electron donor or acceptor molecules to carbon nanotubes has been already exploited to modify their electronic properties via charge-transfer.[15] By following an equivalent approach, the chemical doping of G, either covalently or non-covalently, can be considered a potential pathway to chemically engineer its electronic structure, as it would lead to a band-gap originated from the interaction of the grafted dopants and the carbon layers.[16] Moreover, G can play an important role in the development of new applications that involve chemical doping. In this context, it is worth outlining some recent studies approaching the magnetoresistance (MR) of G that provide valuable information about its electron transport properties and, more important, highlight its potential to be implemented as electrode in organic magnetoelectronic devices.[17-18]This interest is further supported by a number of recent reports that describe the appearance of MR by combination of G with different magnetic components,[19] or the presence of intrinsic MR in ultrathin

unmodified G stacks.[18] These electronic features, alongside with its favorable two-dimensional geometry, confirm graphene as an outstanding component for the fabrication of multi-layered electronic or magnetic devices. However, to the best of our knowledge, a study describing how the chemical doping of G with electronically active organic functionalities can modify its MR response is still missing.

To date, most of the works exploring the functionalization of G through the formation of covalent bonds stem from the derivatization of the previously prepared GO, as despite their electronic properties are rather inferior to those exhibited by unmodified G, the presence of oxygen-rich groups across the carbon layers makes it chemically more reactive. However, the liquid phase exfoliation of graphite is an appealing alternative to obtain high-quality G, which can be next covalently functionalized in order to produce hybrid materials with superior electronic capabilities. Unfortunately, the absence of defects confers this G significant inertness that hampers further chemical functionalization. Hence, the number of articles describing the covalent functionalization of G obtained from the liquid-phase exfoliation of graphite is very limited.[20, 21]

Amongst the chemical procedures that have been traditionally used for the functionalization of carbon-based materials, the Bingel-Hirsch (B-H) cyclopropanation appears as an attractive synthetic approach to functionalize G as it is a one-pot reaction that takes place at room temperature.[22] Still, the chemical modification of G under B-H conditions have only proved to be successful with tetrathiafulvalene (TTF) molecules.[23] In this work, Tagmatarchis and co-workers required the aid of microwaves radiation to favor the reaction. Although this strategy has proven advantageous in the functionalization of CNTs or fullerenes,[24, 25, 26] it can also provoke over-functionalization[25] or give rise to non-desired side-products from competitive reactions.[27]

Here we describe the covalent grafting of 4,4'-[(1,3-dioxo-1,3-propanediyl)bis(oxy)]bis[2,2,6,6-tetramethyl-1-piperidinyloxy] (**1-TEMPO**) organic radicals to G with the Bingel-Hirsch reaction (**Figure 79**). G layers have been produced by liquid-phase exfoliation of commercial graphite in o-dichlorobenzene (oDCB) or benzylamine with the aid of ultrasounds. In contrast with previous works,

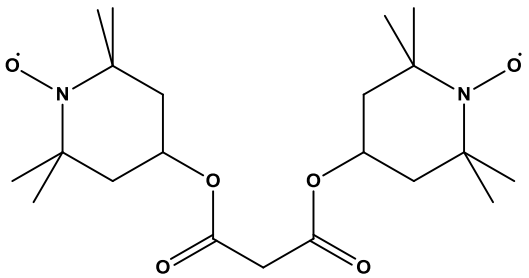

1

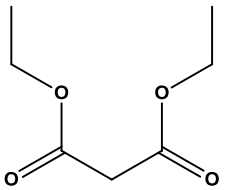

2

Figure 79. Molecular structure of 4,4'-[(1,3-dioxo-1,3-propanediyl)bis(oxy)]bis[2,2,6,6-tetramethyl-1-piperidinyloxy] (**1**) and its non-magnetic counterpart, diethylmalonate (**2**).

we have discarded the use of microwave radiation, as a low functionalization degree will favour the study of the electronic and magnetic properties of the resulting layers by keeping almost unaltered the electronic properties of pristine graphene. The use of different solvents enables modifying the efficiency of the reaction therefore modulating the density of radicals grafted.[23] This variable degree of functionalization has permitted studying the effect of the radical concentration over the G sheets on its electronic transport with electrical conductivity and MR measurements. Finally, G has been covalently grafted with ethylmalonate (**2**) molecules, which can be considered non-magnetic analogues of the radicals,[23] to check if the presence of the paramagnetic radicals is at the origin for the observed MR changes.

5.2.2. Results and discussion

5.2.2.1. Functionalization of graphene with organic radicals

5.2.2.1.1. Synthesis

As illustrated in **Figure 80**, the functionalization of graphene with organic radicals was carried out with a two-step procedure. In a first stage, G was directly obtained from graphite by using a simple exfoliation method previously described by Tour and co-workers.[28] We used either oDCB or benzylamine as solvent because (i) they have proven to be effective for the exfoliation of graphite from single to few layers of G by simple sonication,[28] and (ii) they have been previously used to

functionalize CNTs under Bingel-Hirsch conditions.[23, 29] In a second stage, the TEMPO biradical (**1**) was covalently grafted to the G surface via Bingel-Hirsch reaction at room temperature.[30] Here, the use of two different solvents permits modifying the degree of functionalization. Whilst the use of oDCB leads to very low functionalization (**1-G**), the use of belzylamine enables accessing higher density of grafted radicals (**1-G+**). This can be justified on basis to the electro-donating properties of both solvents. The superior electron-donating character of benzylamine over oDCB may play an important role in the exfoliation step probably because of the appearance of charge-transfer complexes between G and benzylamine, thus favouring the B-H reaction and subsequent grafting of **1**.[23]

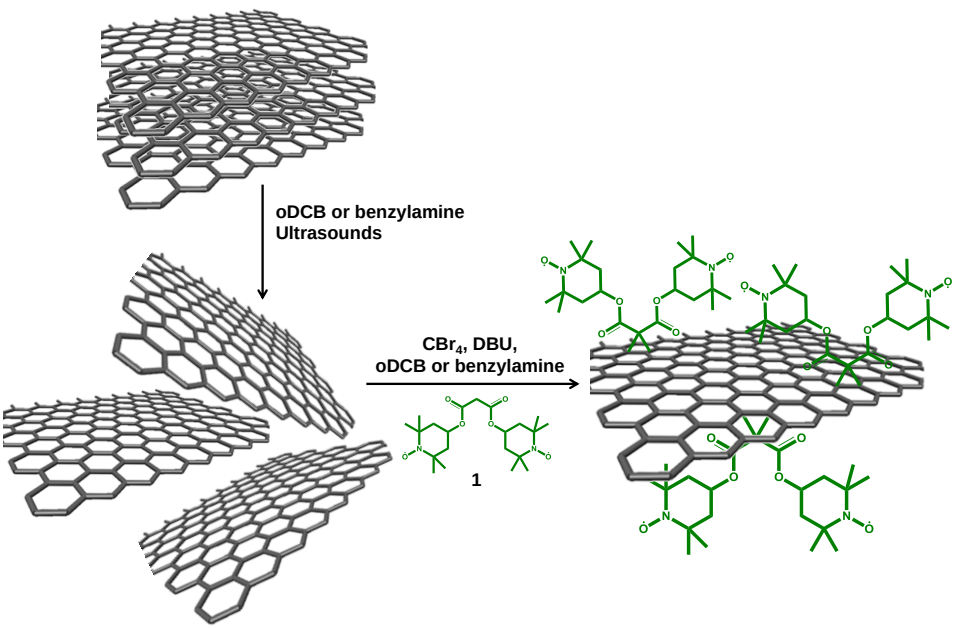

Figure 80. Chemical procedure for the synthesis of **1-G** and **1-G+**.

5.2.2.1.2. HR-TEM

The morphology of exfoliated G and after the functionalization with TEMPO radicals was studied by HR-TEM microscopy (**Figure 81**). In both cases, aggregates of few micrometric low-contrast G layers showing superposed hexagonal diffraction patterns typical of G sheets could be observed, thus demonstrating that the exfoliation and chemical derivatization have not affected the internal structure of G. Unfortunately the observation of a single G layer was not possible given that in high boiling point solvents like oDCB or benzylamine, G sheets tend to aggregate.[21,31]

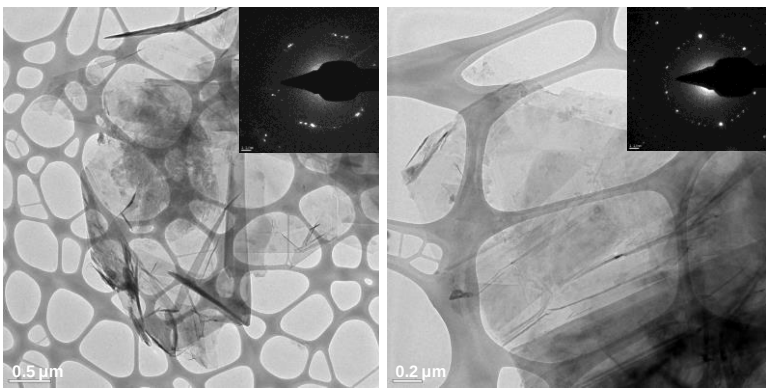

(a)

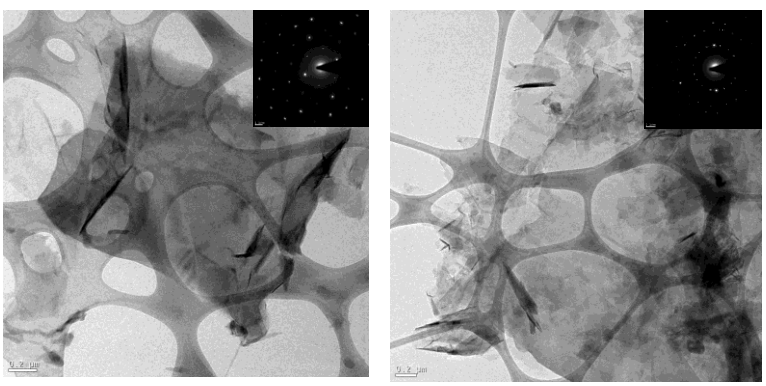

(b)

Figure 81. HR-TEM images of (a) exfoliated graphene in oDCB (*left*) and **1-G** dispersed in ethanol (*right*), and (b) exfoliated graphene in benzylamine (*left*) and **1-G+** dispersed in ethanol (*right*). Insets display the Selected Area Electron Diffraction (SAED) collected for each sample that show the superposition of hexagonal diffraction patterns indicative of the presence of few-layers graphene.

5.2.2.1.3. Thermogravimetric Analysis

The first evidence supporting successful covalent functionalization of the G sheets with organic radicals is provided by the thermogravimetric analysis under nitrogen atmosphere. As shown in **Figure 82** pristine graphite remains stable in all the temperature range studied whilst **1-G** and **1-G+** show a weight loss of ca. 2.5% and 7% respectively at around 300 ºC, which can be exclusively associated to the grafted radicals. These values correspond to approximately 1 TEMPO biradical per ca. 1300 carbon atoms for **1-G**, whilst the use of benzylamine permits increasing the degree of functionalization up to 1:450 atoms in **1-G+**, therefore confirming the compatibility of the B-H reaction with mild conditions. These values are consistent with the increase in the nitrogen and oxygen contents extracted from the CHN analysis of unmodified graphite, **1-G** and **1-G+**, respectively (**Table 6**). Nevertheless, these functionalization values remain considerably below those obtained for the covalent grafting of G with TTF assisted by microwaves (*ca.* 20%).[23] It is worth reminding that we discarded the use of microwaves because they are known to favor the chemical decomposition of the radical.[27] Anyway, to restrict to low degrees of functionalization can be advantageous in the present case, as the resulting covalently grafted G layers will preserve electronic structures and conducting properties of unmodified G. Hence, this doped material will be suited for the study of the influence of the grafting on its electronic properties.

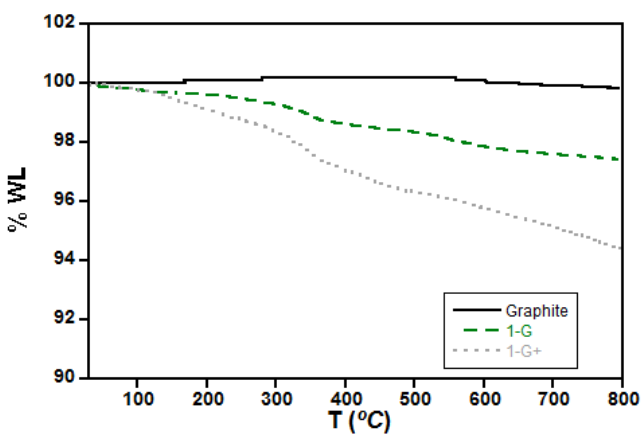

Figure 82. Thermal decomposition under inert conditions of Graphite (black solid line), **1-G** (green dashed line) and **1-G+** (grey dotted line).

Table 6. CHN analysis performed over pristine graphite, **1-G** and **1-G+**.

	%C	%O	%N
Graphite	97.57	0.05	0.03
1-G	96.17	3.21	0.35
1-G+	93.78	5.64	0.58

5.2.2.1.5. Raman spectroscopy

Raman spectroscopy was also used to provide overall structural information of the functionalized samples and further support the functionalization of the G layers. The Raman spectra of pristine graphite, **1-G** and **1-G+** are represented in **Figure 83**. In general, the Raman spectra of graphitic-like structures are composed by a G band (~1580 cm^{-1}) associated to graphitic domains, and a D band (1340 cm^{-1}). The intensity of the latter is proportional to the presence of defects or sp^2 disruptions in the layers. Thereby an increase in the I_D/I_G ratio can be used as an indicative of a larger amount of defects.[32] As shown in **Figure 83**, the Raman spectra of graphite is characterized by having a strong G band, accompanied by a weak D band, which is indicative of a small amount of defects at the sheet rims. **1-G** and **1-G+** display very similar Raman spectra, confirming that the sp^2 conjugation is hardly disrupted in both cases. The small increase in the I_D/I_G ratio upon grafting of the radicals, 0.27 for **1-G** and **1-G+** (*cf.* 0.14 for unmodified graphite), supports that the functionalization takes place with almost negligible introduction of defects across the layers and minimum disruption of their aromatic structure. The presence of the 2D (2710 cm^{-1}) and 2G' (3240 cm^{-1}) bands in all the samples further confirms the high quality of the functionalized samples and supports the low degree of functionalization.

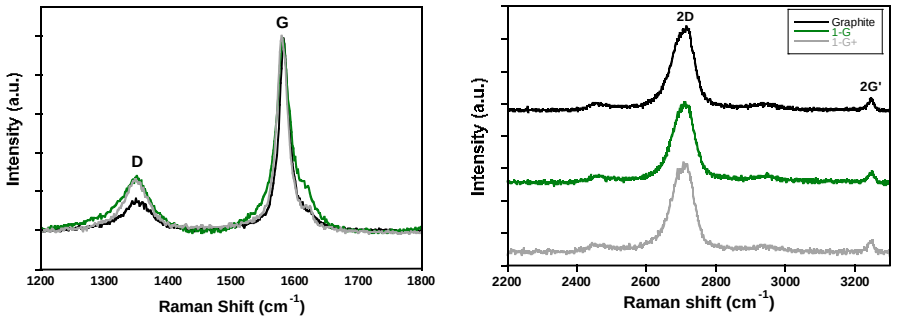

Figure 83. (*left*) First order Raman Spectra of graphite (black), **1-G** (green) and **1-G+** (grey). For the sake of clarity the spectra have been normalized with respect to the intensity of the G band of graphite. (*right*) Second order Raman of graphite (black), **1-G** (green) and **1-G+** (grey).

5.2.2.1.6. X-Ray Photoelectron Spectroscopy (XPS)

XPS was next used to confirm the presence of nitroxide groups in the functionalized samples intrinsic to the introduction of biradical molecules across the G layers. **Figure 84** and **Figure 85** represent the XPS measurements of pristine graphite, **1-G** and **1-G+**. A low content of oxygen moieties (1.5%) likely associated to atmospheric oxygen absorbed by the sample can be extracted from the spectra of graphite. As result of the B-H reaction with **1**, the oxygen content in the solids is increased up to 3.3 and 4.8% for **1-G** and **1-G+**, respectively, alongside with the introduction of some of nitrogen functionalities. The analysis of C1s high resolution XPS spectra for the solids (**Figure 84**) show the appearance of an intense narrow peak centered at a binding energy (BE) of 284.6 eV, that confirms a high sp^2 carbon content. This is accompanied by the π-π^* shake-up satellite peak characteristic of carbon aromatic structures, which, despite being present in all the samples, exhibits the highest intensity for pristine graphite, thus confirming a higher defect content for the functionalized samples. Study of the N1s XPS spectra confirms the presence of radicals across the G lattice. As illustrated in **Figure 85**, whilst this region is silent for graphite, the N1s signals in **1-G** and **1-G+** can be deconvoluted into two contributions, one at lower BEs (400.2 eV) corresponding to C-N bonds, and a second one at higher BEs (401.3 eV) which can be assigned to N-O bonds (**Table 7**).[33]

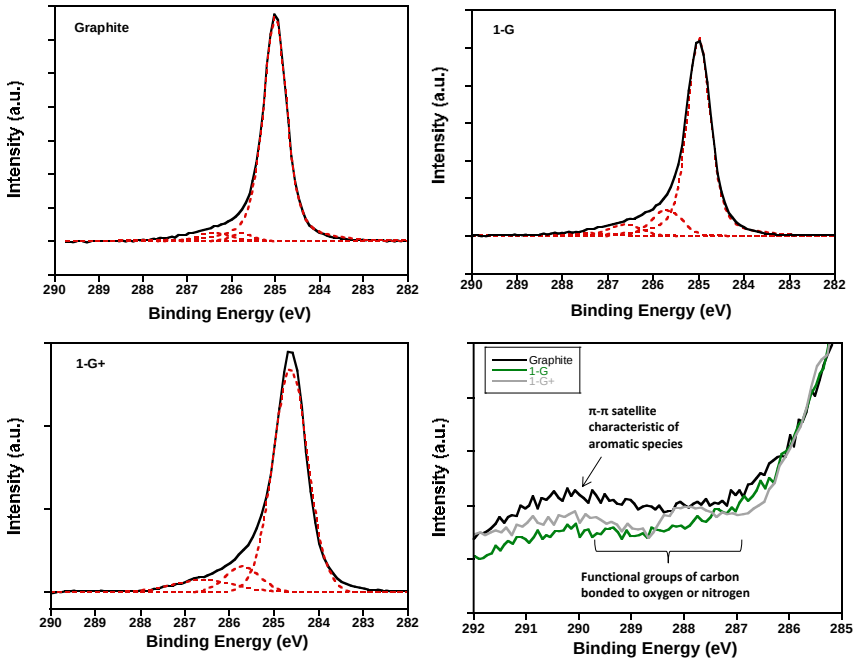

Figure 84. C1s high resolution XPS spectra of Graphite, **1-G** and **1-G+** (the black-solid line is the experimental while the fitting appears represented by a red-dotted line). Moreover, a zoom-into the π-π* shake up satellite peak is shown for Graphite (black), **1-G** (green) and **1-G+** (grey).

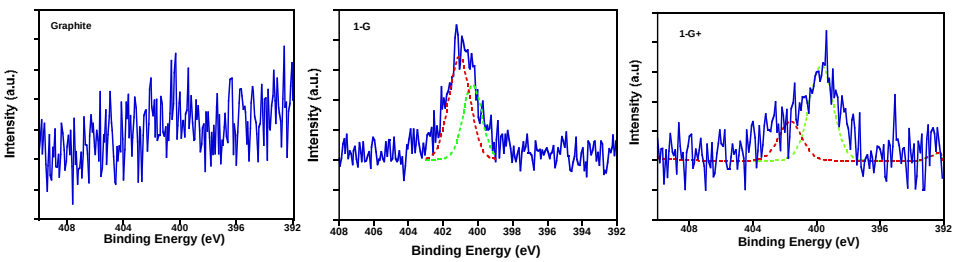

Figure 85.N1s high resolution XPS spectra of Graphite, **1-G** and **1-G+** (the experimental signal appears in blue, while the fitting appears in green (C-N) and red (N-O)).

Table 7. Binding Energies (BE) extracted from N1s XPS spectrum.

Sample	***N1s (B.E.)***	
	C-N	N-O
Graphite	X	X
1-G	400.3 eV	401.1 eV
1-G+	399.7 eV	401.6 eV

5.2.2.1.7. Electron Paramagnetic Resonance (EPR)

The covalent attachment of the TEMPO molecules to the G sheets by B-H reaction was also confirmed with X-band EPR spectroscopy as collected from powdered samples at room temperature. As reported in the literature,[34] the spectrum of unmodified G displays a very weak EPR signal characterized by a single Lorentzian (**Figure 86, *left***). For the sake of clarity this background signal was subtracted from the spectra discussed below. **Figure 86** shows the EPR spectrum of the TEMPO biradical (**1**) in frozen toluene (red) and **1-G** (green), **1-G+** (grey) and the mechanical mixture of **1** and graphite (black, dashed line) at room temperature. Notwithstanding the poor signal-to-noise ratio, the EPR spectra of **1-G** and **1-G+** confirm the presence of paramagnetic moieties. Hence, between 3350-3400 G they display the general features observed for **1** in frozen toluene, thus proving the presence of the radicals in the solids. In particular, the EPR of **1-G** exhibits a rigid-limit powder pattern that resembles that reported for immobilized nitroxides on a rigid matrix.[35] As for **1-G+**, it displays the same overall spectrum than **1-G** although the higher concentration of organic radicals across the G layers is likely to be responsible for the poorer resolution of the hyperfine structure of the grafted radicals due to intermolecular interactions. It is worth mentioning that these signals are remarkably different from the spectrum collected for the mechanical mixture of **1** and graphite. As reported elsewhere, in the case of drop casting or mechanical mixture, the hyperfine structure is lost due to the strong intermolecular interactions, typical of a concentrated spin system, resulting in a single broad line.[35] This indicates that the radicals are well insulated in **1-G** and **1-G+** as result of the covalent grafting, thereby excluding a hypothetic cluster formation or any other spurious physisorption.

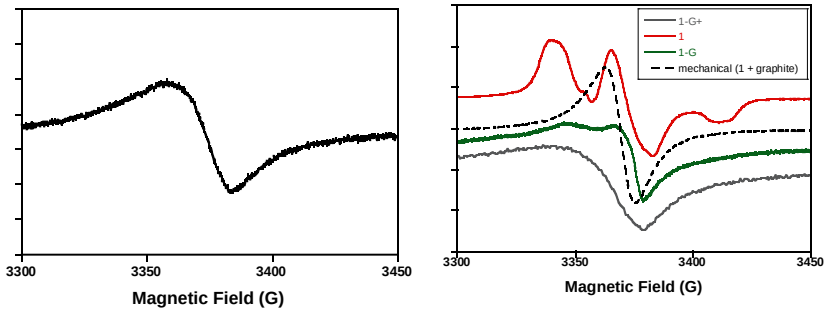

Figure 86. (*left*) EPR spectra at 300 K of unmodified graphene. (*right*) Powder EPR spectra of **1-G** (green) and **1-G+** (grey) at 300K.Comparison with the spectra of the radical **1** in frozen toluene (red), and of a mechanical mixture of **1** and graphite at 300K (black).

5.2.2.2. Electrical conductivity and magnetoresistance

The electrical conductivity of a pellet of the compressed sample was calculated with the plot of the slope of the I-V curves in the ohmic region at very low voltages (**Figure 87**). For a better understanding of the real origin of the changes in the electronic properties of **1-G** and **1-G+** we also studied the grafting of ethylmalonate molecules to G (**2-G**) by following equivalent B-H reaction conditions.[21] The incorporation of these non-magnetic analogues of the biradical permits understanding whether the observed electronic changes derive from the paramagnetic nature of the radicals or they are instead associated to the chemical functionalization and subsequent re-hybridation of a number of carbon atoms in the G layers. We have also measured pellets made up from exfoliated G in oDCB and the mechanical mixture of graphite with the radical **1** to record the response of bare pristine G layers and rule out mere physisorption of the radicals, respectively.

All samples exhibit conductivities between (1-30) $S \cdot cm^{-1}$ (see **Figure 87** for more details) in good agreement with the values reported in the literature for graphene sheets. [36] Unfortunately, these experimental values are strongly dependent on the density of the pellets controlled by the compression step therefore preventing further comparison.[37] Exfoliated G displays the highest conductivity of the series with 30 $S \cdot cm^{-1}$. As expected for the chemical derivatization and subsequent introduction of sp^3 defects throughout the carbon layers, this σ value decreases down to 24 and 29 $S \cdot cm^{-1}$ for **1-G** and **2-G**, respectively; down to a minimum of 0.93 $S \cdot cm^{-1}$ for **1-G+** as result of the higher degree of functionalization. **Figure 88** displays the temperature dependence of the conductivity for **1-G** and **1-G+**. Whilst

1-G shows the typical metallic behaviour already described for pristine G,[30] **1-G+** exhibits semiconducting behaviour. As suggested above, this drastic decrease in conductivity and the change from metallic to semiconductor behaviour appears as a consequence of the higher grafting density.

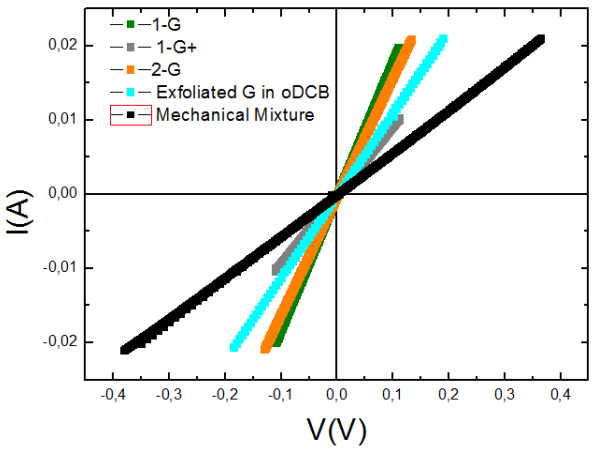

Sample	Conductivity [S cm^{-1}]	Surface [cm^2]
1-G+	0.93	$1.77\ 10^{-3}$
1-G	24.00	$1.87\ 10^{-5}$
2-G	31.00	$1.53\ 10^{-5}$
Exfoliated G in oDCB	29.19	$8.75\ 10^{-5}$
Mechanical mixture of G and 1	28.22	$1.25\ 10^{-4}$

Figure 87. I-V conductivity versus temperature of **1-G** (green), **1-G+** (grey), **2-G** (orange), exfoliated graphene in oDCB (light blue) and the mechanical mixture of graphite with **1** (black). In the bottom part, a table summarize the conductivity values calculated from inverse of the slope of the I-V curves for the different samples in the ohmic region at very low voltages.

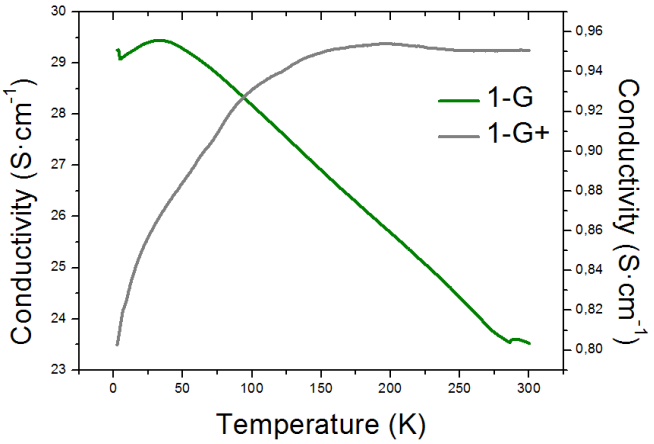

Figure 88. σ(T) plot showing the metallic and a semiconducting behaviour of **1-G** (green) and **1-G+** (grey), respectively.

Figure 89 displays the field dependence of the MR of exfoliated G and functionalized **1-G**, **1-G+** and **2-G**. All of them show a non-saturating positive MR effect in the presence of an external magnetic field with MR values oscillating between 3.6-5 %, thus suggesting that the MR response observed in the functionalized samples can be ascribed to the presence of G layers. As represented in the right panel of **Figure 89**, at 2 K all the samples exhibit a weak anti-localization effect, that is a sharp decrease in the resistance at field zero, which is typical of G monolayers and is due to the transport carriers through phase-coherent disordered G.[38] It is worth outlining that this effect persists even though our measurements involve stacks of G instead of a single monolayer. The MR of the exfoliated G is around 5% at 2K. This value is remarkably lower than that reported in the literature.[38] Liao and co-workers found highly anisotropic MR values ranging from 0.66 to 100% for single-layers of G as a function of the direction of the external magnetic field. Alike, our measurements have been collected from pressed pellets, where the random orientation of the layers does not allow for any preferential symmetry directions. Instead, granular systems formed by ferromagnetic nanoparticles embedded in an isolated or conductive matrix give a MR % ratio consistent with our results.[39]

The MR changes introduced by the chemical functionalization by comparison of exfoliated G with **1-G**, **1-G+** and **2-G** are very low. Next, comparison

between the MR%(H) curves of the chemically functionalized samples permits extracting the effect of the grafting of paramagnetic/diamagnetic units across the G layers. The introduction of TEMPO radicals provokes the appearance of a low field MR effect (LFMR) with a hysteretic behavior and two symmetric peaks, at 4500 G and 10000 G, for **1-G** and **1-G+** respectively. This is not the case for the introduction of diamagnetic ethylmalonate units in **2-G** or exfoliated G (**Figure 90**). This distinctive feature, which has been already reported for granular assemblies, can be then ascribed to the presence of the magnetic radicals.[39, 40] In fact, as shown in **Figure 91**, the extent of the LFMR effect is proportional to the density of the radical's grafting, with **1-G+** displaying a larger LFMR effect that persists at higher temperatures (8K) than **1-G** (2K). Above these temperatures the LFMR effect vanishes for both samples (**Figure 92**). Besides, the intensity of this effect is also dependent on the intensity of the magnetic field applied externally as the maximum values of LFMR are recorded at 10000 and 4500G for **1-G+** and **1-G**, respectively. We believe that this characteristic dependence with the magnetic field might be associated with the spin-dependent transport between the magnetic radicals.

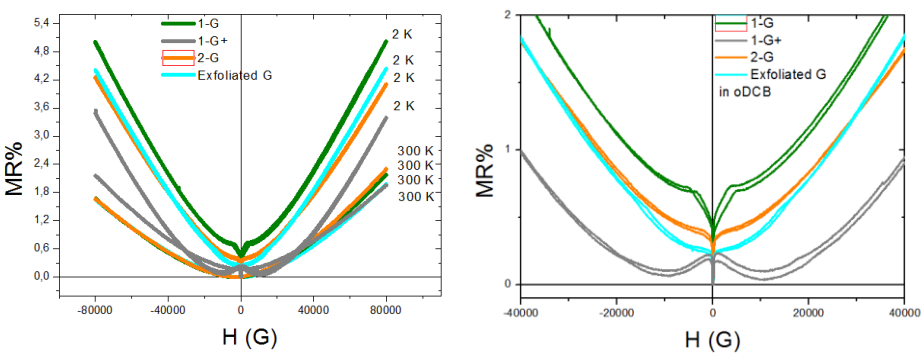

Figure 89. MR versus magnetic field at 300 K and 2 K for **1-G** (green), **1-G+**, (grey) **2-G** (orange) and the exfoliated G in oDCB (blue) (*left*). At the *right*, a zoom-in into the low field area for the low T measurements shows an anti-localization effect for the four samples.

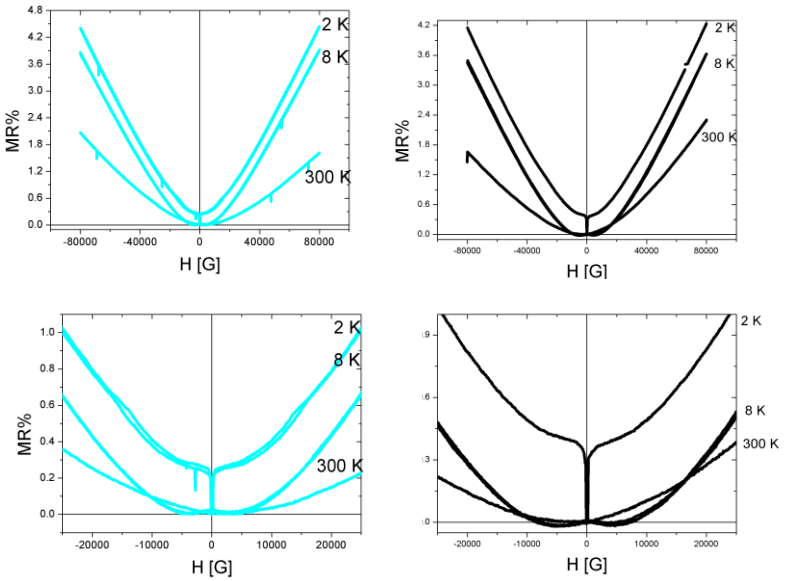

Figure 90. MR versus magnetic field at different temperature of G-exfoliated in oDCB (*left*), **2-G** (*right*). The bottom panel shows a zoom-in of the low field area for lower and higher temperature with the appearance of an anti-localization effect at 2 K. The LFMR effect present in **1-G** and **1-G+** is not observed for any of them.

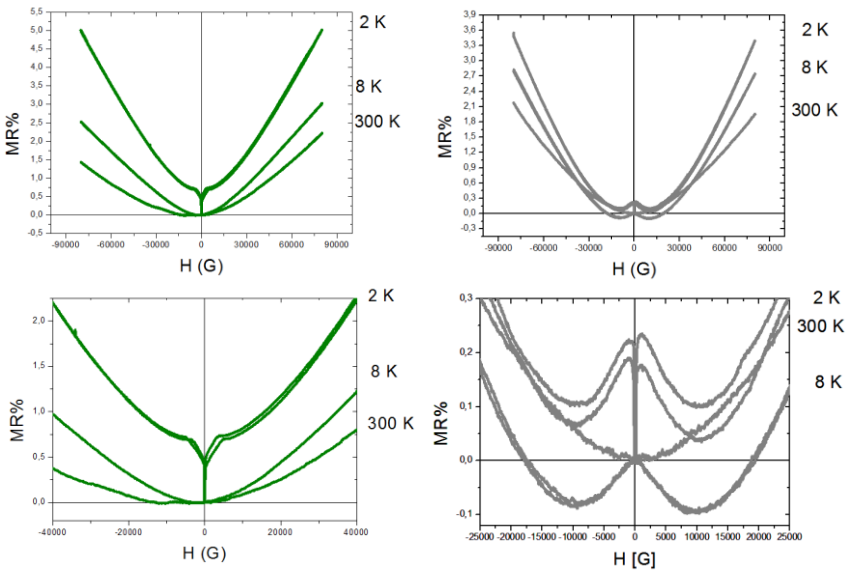

Figure 91. MR%(H) of **1-G** (*left*) and **1-G+** (*right*) as collected between 2-300 K. The bottom panel shows a zoom-in of the low field area for low-T measurement with the appearance of an anti-localization effect at 2 K and the LFMR effect present until 8 K that vanishes at higher temperatures.

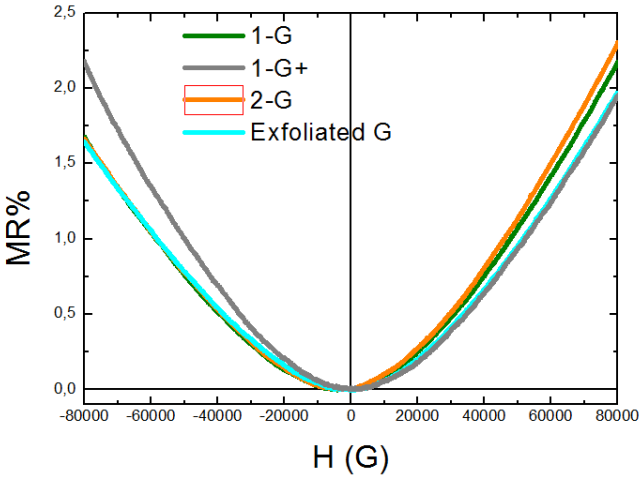

Figure 92. MR versus magnetic field at 300K of **1-G** (green), **1-G+** (grey), **2-G** (orange) and exfoliated G in oDCB (blue). The three samples at 300 K show no differences between them at the low magnetic field part.

5.2.3. Conclusions

We have reported the liquid phase exfoliation of graphite in oDCB or benzylamine to *in-situ* produce G layers that can be further functionalized with paramagnetic TEMPO radicals by using the Bingel-Hirsch cyclopropanation reaction to isolate **1-G** and **1-G+**, respectively. Derivatization of graphene proceeds at room temperature, and for the first time, without the aid of energetic microwaves radiation. The use of different solvents enables accessing variable density of the radicals' grafting throughout the carbon layers, which oscillate between 1 biradical per 1300 and 450 carbon atoms for **1-G** and **1-G+**, respectively. TGA, μ-Raman, XPS and EPR measurements confirm the covalent grafting of the organic moieties besides ruling out their spurious physisorption to the carbon layers.

Our transport measurements indicate that the electronic properties of G layers are clearly affected by the degree of functionalization introduced. Hence, its conductivity changes from metallic to semiconducting as the density of grafted radicals increases from **1-G** to **1-G+** as result of a stronger disruption of the original aromatic sp^2 structure. MR%(H) measurements confirm that the functionalized samples share the general features ascribed to G monolayers but with the distinctive appearance of a LFMR effect at low temperatures whose intensity is proportional to

the density of radicals covering the G surface. To further establish whether this change might be introduced by the re-hybridation of carbon atoms associated to chemical derivatization we have also studied the MR response of G grafted with diamagnetic ethylmalonate molecules. Our results confirm that the LFMR effect is intrinsic to the grafting of paramagnetic moieties rather than to the functionalization.

5.2.4. Experimental

5.2.4.1. General synthesis remarks

Graphite powder was purchased from Fisher Scientific. 4-hydroxy-TEMPO, triethylamine, malonyl chloride, Diethyl Malonate, 1,8-diazabicycloundec-7-ene (DBU), tetrabromomethane (CBr_4) and the solvents were purchased from Aldrich and used as supplied. Exfoliation of G was accomplished using a horn sonicator Brandson Sonifier 450 working at a Dutty cycle at 40% and with an output control of 2 during 30 minutes. Centrifugation was performed at 10 °C using an Eppendorf Centrifugation System working at 500 rpm for 30 minutes. PTFE membrane filters where purchased from ALBET labscience (diameter ø 47 mm, pore size 0.45µm).

5.2.4.2. Synthesis of TEMPO Biradical (1).

1 was synthesized as reported elsewhere.[41] In a typical experiment 800 mg of 4-hydroxy-TEMPO (4.64 mmol, 2 eq) and 746 µL of triethylamine (5.1 mmol, 2.2 eq) were dissolved in 20 mL of dry dichloromethane. Next, 226 µL of malonyl chloride (2.32 mmol, 1 eq) were dissolved in 10 mL of dry dichloromethane and added drop by drop over 20 minutes whilst keeping the reaction mixture at 0 ºC for 1 h. The solution was mechanically stirred overnight, washed with saturated $NaHCO_3$ and dried with anhydrous Na_2SO4. The solvent was removed under vacuum and the mixture was purified by flash chromatography using acetonitrile/dichloromethane (1/3) as eluent so **1** was isolated as a reddish solid (775 mg, 81 %). FT-IR: 1745 cm^{-1} ν (C=O), 1464 cm^{-1} ν (N-O). MS (EI) calc. for $C_{21}H_{36}N_2O_6^{\cdot}$ 412.52, found 412.26 g mol^{-1}.

5.2.4.3. Synthesis of 1-G

In a first stage, single to few layers of G were exfoliated from graphite by mechanically stirring a mixture of 30 mg of graphite powder and 50 mL of ortho-dichlorobenzene (oDCB) for1 hour. Next the mixture was sonicated with a horn sonicator Brandson Sonifier 450 during 30 minutes and finally centrifuged for 30 min at 500 rpm to separate the supernatant solution from the non-exfoliated material. In a second stage, the exfoliated G in oDCB [40 ml] was combined with 76.8 mg [0.174 mmol, 1 eq] of **1**, 47 mg of CBr_4 [0.143 mmol, 0.8 eq] and 48 μL [0.32 mmol, 1.8 eq] of DBU. The mixture was mechanically stirred overnight at room temperature according to the Bingel-Hirsch reaction conditions.[22b] **1-G** was isolated as a black glittering powder by filtering the mixture over PTFE filters, and washing it thoroughly with oDCB, water and ether.

5.2.4.4. Synthesis 1-G+

It was obtained following the same procedure described for **1-G** but employing benzylamine as solvent.

5.2.4.5. Synthesis 2-G

It was obtained following the same procedure described for **1-G** but employing 26.4 μL of diethylmalonate [0.174 mmol, 1eq] (**2**) instead of **1**.

5.2.4.6. Physical characterization

Thermogravimetric analysis were carried out with a Mettler Toledo TGA/SDTA 851 apparatus in the 25-800 Cº temperature range under a 30 $mL.mol^{-1}$ nitrogen flow and a 10 K min^{-1} scan rate.

EPR was performed with an X-Band EPR spectrometer model Bruker ELEXYS E580. The EPR spectrometer operates in the range 4 -300 K, and magnetic fields in the range 0 – 2 T.

Electron spectroscopy for chemical Analysis (ESCA) and X-ray photoelectron spectroscopy (XPS), were performed using a Thermo Scientific K-Alpha ESCA instrument equipped with an aluminium Kα1,2 monochromatized radiation working at 1486.6 eV. Photoelectrons were collected from a take-off angle

of 90° relative to the sample surface. The measurement was done in a Constant Analyser Energy mode (CAE) with a 100 eV pass energy for survey spectra and 20 eV pass energy for high resolution spectra. Charge referencing was done by setting the lower binding energy C1s photo peak at 285.0 eV C1s hydrocarbon peak. Surface elemental composition was determined using the standard Scofield photoemission cross sections.

μ-Raman measurements at room temperature were performed with a dispersive Jobin-Yvon LabRam HR 800 microscope, working with an excitation line of 532 nm. The scattered light was detected with a thermoelectric cooled (-70 ºC) charge coupled device detector (CCD). It is also equipped with an Olympus BXFM optic microscope. All the measurements were carried out directly over the sample. In the experiments, the power employed over the samples was of the order of 0.3mW, and the exposition time 60 seconds.

High Resolution Transmission Microscopy (HR-TEM) images were acquired with a TECNAI G2 F20 microscope equipped with a Field Emission Gun (FEG) operating at 200 kV.

The electrical conductivity (σ) and magnetoresistance (MR) measurements were measured by using a standard four-probe contacts method with Pt wire in a physical properties measurement system (PPMS-9) by Quantum Design. Powders were pressed into pellets for resistivity and MR measurements. Electrical contacts were made with highly conducting silver and the surface of the samples oscillated between $8.75 \cdot 10^{-5}$ and $1.77 \cdot 10^{-3}$ cm^2 as illustrated in **Figure 87**.

5.2. References

[1] a) J. Lu, I. Do, L.T. Drzal, R.M. Worden, I. Lee, *ACS Nano*, **2008**, *2*, 1825. b) C. Xu, X. Wang, J. Zhu, *J. Phys. Chem. C* **2008**, *112*, 19841. c) Y.C. Si, E.T Samulski, *Chem. Mater.* **2008**, *20*, 6792.

[2] a) G.Goncalves, P.A.A.P Marques, C.M. Granadeiro, H.I.S. Nogueira, M.K. Singh, J. Grácio, *Chem. Mater.* **2009,** *21*, 4796. b) Z. Xiong, L.L. Zhang, J. Ma, X.S. Zhao, *Chem. Commun.* **2010**, *46*, 6099. c) M. Quintana, K. Spyrou, M. Grzelczak, W.R. Browne, P. Rudolf, M. Prato, *ACS Nano* **2010**, *4*, 3527. d) M. Quintana, A. Montellano, A.E. del Rio Castillo, G.van Tendeloo, C. Bittencourt, M. Prato, *Chem. Commun.*, **2011**, *47*, 9330.

[3] a) S. Dubin, S. Gilje, K. Wang, V.C. Tung, K. Cha, A.S.Hall, *ACS Nano*, **2010,** *4*, 3845. b) Y. Zhou, Q. Bao, L.A.L. Tang, Y. Zhong, K.P. Loh, *Chem. Mater.*, **2009**, *21*, 2950. c) V.H. Pham, T.V.Cuong, S.H. Hur, E. Oh, E.J. Kim, E.W. Shin, J. S. Chung, *J. Mater. Chem.* **2011**, *21*, 3371. d) C. Bosch-Navarro, E. Coronado, C. Marti-Gastaldo, J.F. Sanchez-Royo, M. Gomez-Gomez, *Nanoscale*, **2012**, *4*, 3977. e) Y. Zhu, M.D. Stoller, W. Cai, A. Velamakanni, R.D. Piner, D. Chen, R.S. Ruoff, *ACS Nano*, **2010**, *4*, 1227.

[4] J. Muzart, *Tetrahedron*, **2009**, *65*, 8313.

[5] a) V. Georgakilas, A.B. Bourlinos, R. Zboril, T.A. Steriotis, P. Dallas, A.K. Stubos, C. Trapalis, *Chem. Commun.*, **2010**, *46*, 1766. b) V. Georgakilas, K. Kordatos, M. Prato, D.M. Guldi, M. Holzinger, A. Hirsch, *J. Am. Chem. Soc.*, **2002**, *124*, 760.

[6] W.S. Hummers, R.E. Offeman, *J. Am. Chem. Soc.*, **1958**, *80*, 1339.

[7] T. Sainsbuty, T. Ikuno, D. Okawa, D. Pacile, J.M.J. Frechet, A. Zettl, *J. Phys. Chem. C*, **2007**, *111*, 12992.

[8] X. Zhang, L. Hou, A. Cnossen, A.C. Coleman, O. Ivashenko, P. Rudolf, B.J. van Wees, W.R. Browne, B.L. Feringa, *Chem. Eur. J.*, **2011**, *17*, 8957.

[9] S. Stankovich, D.A. Dikin, R.D. Piner, K.A. Kohlhaas, A. Kleinhammes, Y. Jia, Y. Wu, S.T. Nguyen,R.S. Ruoff, *Carbon*, **2007**, *45*, 1558.

[10] a) O.C.Compton, D.A. Dikin, K.W. Putz, L.C. Brinson, S.T. Nguyen, *Adv. Mater.*, **2010**, *22*, 892. b) A.B. Bourlinos, D. Gournis, D. Petridis, T. Szabó, A. Szeri, I. Dékány, *Langmuir*, **2003**, *19*, 6050. c) K. Ai, Y. Liu, L. Lu, X. Cheng, L. Huo, *J. Mater. Chem.*, **2011**, *21*, 3365.

[11] J.I. Paredes, S. Villar-Rodil, P. Solís-Fernández, A. Martínez-Alonso, J.M.D. Tascón, *Langmuir*, **2009,** *25*, 5957.

[12] A. Devia, H.A. Castillo, V.J. Benavides, Y.C. Arango, J.H. Quintero, *Materials Characterization*, **2008,** *59*, 105.

[13] H. Zhang, E. Bekyarova, J.-W. Huang, Z. Zhao, W. Bao, F. Wang, R.C. Haddon, C.N. Lau, *Nano Lett.*, **2011**, *11*, 4047.

[14] J.-A. Yan, L. Xian, M.Y. Chou, *Phys. Rev. Lett.*, **2009**, *103*, 086802.

[15] M.A. Herranz, N. Martin, S. Campidelli, M. Prato, G. Brehm, D.M. Guldi, *Angew. Chem. Int. Ed.*, **2006**, *45*, 4478.

[16] a) D.C. Elias, R.R. Nair, T.M. G. Mohiuddin, S.V. Morozov, P. Blake, M.P. Halsall, A.C. Ferrari, D.W. Boukhvalov, M.I. Katsnelson, A.K. Geim, K.S. Novoselov, *Science*, **2009**, *323*, 610. b) S.H. Cheng, K. Zou, F. Okino, H.R. Gutierrez, A. Gupta, N. Shen, P.C. Eklund, J.O. Sofo, J. Zhu, *Phys. Rev. B*, **2010**, *81*, 205435. c) Y.-H. Zhang, K.-G. Zhou, K.-F. Xie, J. Zeng, H.-L. Zhang, Y. Peng, *Nanotech.*, **2010**, *21*, 065201. d) C.-C. Teng, C.-C. M. Ma, C.-H. Lu, S.-Y. Yang, S.-H. Lee, M.-C. Hsiao, M.-Y. Yen, K.-C. Chiou, T.-M. Lee, *Carbon*, **2011**, *49*, 5107.

[17] a) V.M. Karpan, G. Giovanneti, P.A. Khomyakov, M. Talanana, A.A. Starikov, M. Zwierzycki, J. van der Brink, G. Brocks, P.J. Kelly, *Phys. Rev. Lett.*, **2007**, *99*, 176602. b) A. Candini, S. Klyatskaya, M. Ruben, W. Wernsdorfer, and M. Affronte, *Nano Lett*, **2011**, *11*, 2634.

[18] Z-M. Liao, H-C. Wu, S. Kumar, G.S. duesberg, Y-B. Zhou, G.L.W. Cross, I.V. Shvets, D-P. Yu, *Adv. Mater.*, **2012**, *24*, 1862.

[19] J. Zhu, Z. Luo, S. Wu, N. Haldolaarachchige, D.P. Young, S. Wei, Z. Guo, *J. Mater. Chem.*, **2012**, *22*, 835.

[20] a) M. Quintana, K. Spyrou, M. Grzelczak, W. R. Browne, P. Rudolf, M. Prato, *ACS Nano*, **2010**, *4*, 3527. b) J. R. Lomeda, C. D. Doyle, D. V. Kosynkin, W.-F. Hwang, J. M. Tour, *J. Am. Chem. Soc.*, **2008**, *130*, 16201. c) V. Georgakilas, A. B. Bourlinos, R. Zboril, T. A. Stereotis, P. Dallas, A. K. Stubos, C. Trapalis, *Chem. Commun.*, **2010**, *46*, 1766. d) X. Zhang, L. Hou, A. Cnossen, A. C. Coleman, O. Ivashenko, P. Rudolf, B. J. van Wees, W. R. Browne, B. L. Feringa, *Chem. Eur. J.*, **2011**, *17*, 8957.

[21] S. P. Economopoulos, G. Rotas, Y. Miyata, H. Shinohara, N. Tagmatarchis, *ACS Nano*, **2010**, *4*, 7499.

[22] a) F. Diederich, C. thilgen, *Science*, **1997**, *271*, 317. b) K. S. Coleman, S. R. Bailey, S. Fogden, M. L. H. Green, *J. Am. Chem. Soc.*, **2003**, *125*, 8722. c) C. F. Richardson, D. I. Schuster, S. R. Wilson, *Org. Lett.*, **2000**, *2*, 1011.

[23] S. P. Economopoulos, G. Rotas, Y. Miyata, H. Shinohara, N. Tagmatarchis, *ACS Nano*, **2010**, *4*, 7499.

[24] a) S. P. Economopoulos, G. Pagona, M. Yudasaka, S. Iijima, N. Tagmatarchis, *J. Mater. Chem.*, **2009**, *19*, 7326. b) F. G. Brunetti, M. A. Herrero, J. M. Muñoz, A. Diaz-Ortiz, J. Alfonsi, M. Meneghetti, M Prato, E. Vazquez, *J. Am. Chem. Soc.*, **2008**, *130* 8094. c) Y. Wang, Z. Iqbal, S. Mitra, *Carbon*, **2005**, *43*, 1015.

[25] E. Vazquez, M. Prato, *ACS Nano*, **2009**, *3*, 3819.

[26] a) F. Diederich, C. Thilgen, Science, 1996, 271, 317. b) J. R. Pinzon, T. Zuo, L. Echegoyen, *Chem. Eur. J.*, **2010**, *16*, 4864. c) D. Tasis, N. Tagmatarchis, A. Bianco, M. Prato, *Chem. Rev.*, **2006**, *106*, 1105.

[27] a) P. Lidström, J. Tierney, B. Whatey, J. Westman, *Tetrahedron*, **2001**, *57*, 9225. b) R. T. McBurney, F. Portela-Cubillo, J. C. Walton, *RSC Adv.*, **2012**, *2*, 1624.

[28] C.E. Hamilton, J.R. Lomeda, Z. Sun, J.M. Tour, *Nano Lett.*, **2009**, *9* (10), 3460.

[29] a) M. Quintana, K. Spyrou, M. Grzelczak, W. R. Browne, P. Rudolf, M. Prato, *ACS Nano*, **2010**, *4*, 3527. b) J.R. Lomeda, C.D. Doyle, D.V. Kosynkin, W.-F. Hwang, J.M. Tour, *J. Am. Chem. Soc.*, **2008**, *130*, 16201. c) V. Georgakilas, A.B. Bourlinos, R. Zboril, T.A. Stereotis, P. Dallas, A.K. Stubos, C. Trapalis, *Chem. Commun.*, **2010**, *46*, 1766. d) X. Zhang, L. Hou, A. Cnossen, A.C. Coleman, O. Ivashenko, P. Rudolf, B.J. van Wees, W.R. Browne, B.L. Feringa, *Chem. Eur. J.*, **2011**, *17*, 8957.

[30] a) X. Camps, A. Hirsch, *J. Chem. Soc. Perkin Trans*, **1997**, *1*, 1595; b) C. Bingel, *Chem. Ber.*, **1993**, *126*, 1957.

[31] U. Khan, A. O'Neil, M. Lotya, S. De, J. N. Coleman, *Small*, **2010**, *6*, 864

[32] J.I. Paredes, S. Villar-Rodil, P. Solís-Fernández, A. Martínez-Alonso, J.M.D. Tascón, *Langmuir*, **2009**, *25*, 5957.

[33] Y. Deng, Y. Li, J. Dai, M. Lang, X. Huang, *Journal of Polymer Science Part A: Polymer Chemistry*, **2011**, *49*, 1582-1590.

[34] L. Ciric, A. Sienkiewicz, B. Nafradi, M. Mionic, A. Magrez, L. Forrò, *Phys. Status Solidi B*, **2009**, *246*, 2558.

[35] a) F. Busolo, L. Franco, L. Armelao, M. Maggini, *Langmuir*, **2010**, *26*, 1889. b) S. Ruthstein, R. Artzi, D. Goldfarb, R. Naaman, *Phys. Chem. Chem. Phys.*, **2005**, *7*, 524. c) L. Gorini, F. M. Piras, A. Caneschi, A. Magnani, S. Menichetti, D. Gatteschi, M. Mannini, L. Sorace, *Langmuir*, **2007**, *22*, 2389. d) C. Corvaja, F. Conti, L. Franco, M. Maggini, *C. R. Chimie*, **2006**, *9*, 909. e) D. Q. Fan, J. P. He, W. Tang, J.T. Xu, Y. L. Yang, *Eur. Polymer. J.*, **2007**, *42*, 26. f) I. Ratera, J. Veciana, *Chem. Soc. Rev.*, **2012**, *41*, 303.

[36] Z-S. Wu, W. Ren,* L. Gao, J. Zhao, Z. Chen, B. Liu, D. Tang, B. Yu,C. Jiang, H-M. Cheng, *ACS Nano*, **2009**, 2, 411.

[37] S. Stankovich, D.A. Dikin, R.D. Piner, K.A. Kohlhaas, A. Kleinhammes, Y. Jia, Y. Wu, S.T. Nguyen, R.S. Ruoff, *Carbon*, **2007**, 45, 1558.

[38] Z-M. Liao, H-C. Wu, S. Kumar, G.S. Duesberg, Y-B. Zhou, G.L.W. Cross, I. V. Shvets, D-P. Yu, *Adv. Mater.*, **2012**, 24, 1862.

[30] K.I. Bolotin, K.J. Sikes, J. Hone, H.L. Stormer, P. Kim, *Phys. Rev. Letter.*, **2008**, 101, 096802.

[39] a) J. Dugay, R.P. Tan, A. Meffre, T. Blon, L.M. Lacroix, J. Carrey, P.F. Fazzini, S. Lachaize, B. Chaudret, M. Respaud, *Nano Lett.*, **2011**, *11*, 5128. b) J. Varada, W.A. Ortiz, J.A. de Oliveira, B. Vodungbo, Y.L. Zheng, D. Demaille, M. Marangolo, D.H. Mosca, *J. Appl. Phys.*, **2007**, *101*, 014318.

[40] Z. Guo, S. Park, T. Hahn, *Appl. Phys. Lett.*, **2007**, *90*, 053111.

[41] V.P. Gubskaya, L.S. Berezhnaya, A.T. Gubaidullin, I.I. Faingold, R.A. Kotelnikova, N.P. Konavalova, V.I. Morozov, I.A. Litvinov, I.A. Nuretdinov, *Org. Biomol. Chem.*, **2007**, *5*, 976.

Spanish Summary

"Nanocompuestos Híbridos Multifuncionales basados en Nanotubos de Carbono y Grafeno Modificado Químicamente"

A continuación resumiremos los puntos más relevantes tratados en cada uno de los capítulos del presente texto. En primer lugar, vamos a describir en qué consiste la estructura de la Tesis. Seguidamente, introduciremos en los dos primeros capítulos los aspectos más relevantes de los nanotubos de carbono (CNT) (**Capítulo 1**) y del grafeno (G) (**Capítulo 2**). Finalmente, para cada capítulo de resultados haremos una breve introducción, a la que le seguirá la exposición de los resultados más relevantes extraídos, así como las correspondientes conclusiones, y las perspectivas de trabajo futuro más inmediatas que se deriven de los mismos.

La presente Tesis trata sobre la química y el estudio de nuevos sistemas híbridos multifuncionales basados en CNT y G. En primer lugar se ha incluido una breve descripción histórica de ambos sistemas desde el descubrimiento de los fullerenos (**prefacio**). Posteriormente, en los **Capítulo 1** y **2** se ha realizado una introducción detallada sobre los aspectos más relevantes de la síntesis, propiedades y aplicaciones de los CNT (**Capítulo 1**) y el G (**Capítulo 2**).

Los resultados se han dividido en tres capítulos:

Capítulo 3, está relacionado en el desarrollo de materiales híbridos basados en CNT, y a su vez se divide en dos partes. En la primera parte, se estudia la deposición de moléculas imán (SMM) de Mn_4 sobre CNTs de pared múltiple. La disposición de SMM en la superficie de los CNTs, así como las propiedades eléctricas de los CNTs puede tener importantes implicaciones dentro del campo del magnetismo molecular. En nuestra aproximación, utilizaremos interacciones electrostáticas entre las moléculas magnéticas y los CNTs, las cuales contribuirán a la preservación de la estructura de las moléculas imán, y mostraremos cómo sus propiedades magnéticas se ven afectadas por su interacción con los CNTs. En la segunda parte, vamos a desarrollar un híbrido entre una molécula de un óxido metálico (polioxometalato; POM) fotoactivo y CNTs. A diferencia de en el caso anterior, el POM ha sido convenientemente modificado con unidades de pireno capaces de interaccionar con las paredes de CNT sin necesidad de que éstas sean modificadas. La deposición de moléculas fotoactivas sobre CNT puede tener implicaciones en el campo de la fotovoltaica, así como en otros dispositivos electrónicos. Además, seremos capaces de describir el sistema molécular a nivel atómico a través de la utilización de técnicas de microscopía electrónica.

El **Capítulo 4** se centra en la síntesis química de G. Este capítulo también ha sido dividido en dos partes. En la primera parte, el G se obtendrá a partir de óxido de grafito (GO) a través de un tratamiento hidrotermal (HT). Concretamente, nuestro trabajo tratará de describir la importancia del pH en el proceso de reducción hidrotermal del GO, mediante la descripción exhaustiva tanto de las características, como de las morfologías obtenidas a los distintos pHs. En la segunda parte, se llevará a cabo una aproximación de tipo "bottom-up" para la obtención de grafito. Para ello, se utilizarán moléculas de antraceno como material de partida, las cuales, a través de un tratamiento térmico se fusionarán dando lugar a grafito. Además, se introducirán ideas de cómo el confinamiento nanométrico puede dar lugar a la formación de grafeno siguiendo un protocolo similar basado en la fusión de moléculas de antraceno en el interior de cavidades de tamaño nanométrico.

Finalmente, el **Capítulo 5** trata de la funcionalización de G a través de enlaces covalentes. En una primera parte, se describirá un procedimiento general para la síntesis de G químicamente modificado (CMG) mediante la aplicación de un simple tratamiento térmico de funcionalización/reducción de GO en DMF. El CMG obtenido será posteriormente decorado con nanopartículas de oro (Au NPs). Nuestro método introduce un grado de control sobre la cantidad de Au NPs depositadas sobre el CMG, y podría tener relevancia para varias aplicaciones tales como sensores, almacenamiento de energía o catálisis. En una segunda parte, usaremos la reacción de Bingel-Hirsch (B-H) para llevar a cabo una funcionalización controlada de las láminas de G con radicales paramagnéticos. Es interesante notar que estos radicales influyen en la respuesta de magnetoresistencia del híbrido por la aparición, a bajas temperaturas, de un efecto de magnetoresistencia a bajo campo (LFMR).

Capítulo 1: Introducción a los nanotubos de carbono

En este capítulo se hace una descripción detallada de los nanotubos de carbono. El capítulo incluye:

- Tipos de CNTs
- Síntesis de CNTs
- Purificación de CNTs.
- Funcionalización de CNTs.
- Propiedades de CNTs.

A continuación vamos a resumir brevemente los aspectos relevantes de este capítulo para los capítulos de resultados.

Los CNT son el resultado de enrollar una lámina de grafito formando un tubo. Existen dos tipos básicos de CNT, los nanotubos de pared simple (SWNT) y los nanotubos de pared múltiple (MWNT). Los SWNT están compuestos por una única lámina grafítica, mientras que los MWNT son el resultado de enrollar varias láminas grafíticas de forma concéntrica. Los SWNT presentan propiedades electrónicas mucho más atractivas que los MWNT, ya que pueden ser metálicos o semiconductores, mientras que los MWNT son siempre metálicos. Ahora bien, la principal ventaja de los MWNT es su robustez. Cuando se lleva a cabo la funcionalización de las paredes, en los MWNT ésta tiene lugar sobre la capa más externa lo que hace que se afecte de forma mínima a las propiedades electrónicas de los nanotubos. En el caso de los SWNT, la funcionalización covalente afecta directamente a las propiedades físicas debido a la introducción de defectos.

Además de las propiedades eléctricas, los CNTs poseen extraordinarias propiedades mecánicas, así como ópticas y una gran superficie lo que los hacen adecuados para aplicaciones que abarcan desde la electrónica molecular, hasta la energía fotovoltaica o los sensores.

Atendiendo a la morfología de los CNTs, se pueden llevar a cabo distintos tipos de funcionalización: (a) funcionalización no covalente mediante interacción de tipo π-π, (b) funcionalización covalente de las paredes del nanotubos y (c) llenado de la cavidad interna del nanotubos. Dado que en el **Capítulo 3** se van a utilizar tanto

interacciones covalentes como no covalentes, a continuación, vamos a dar una breve descripción de las mismas:

a) Funcionalización no covalente

Este tipo de interacción es muy atractiva ya que permite el anclaje de diferentes sistemas sin afectar a las propiedades electrónicas de los nanotubos. La funcionalización no covalente se basa en interacciones de tipo π-π o en fuerzas de van der Waals y, además de para la introducción de funcionalidad adicional a los CNTs, se ha utilizado mucho para facilitar la solubilización de los mismos.

Existe infinidad de ejemplos de funcionalización no covalente, entre los que se incluye la utilización de polímeros, así como de ADN. En lo que atañe a esta Tesis, cabe enfatizar otro tipo de sistemas de carácter aromático capaces de unirse de forma no covalente fuertemente a las paredes de los nanotubos. Entre estos sistemas destacan los grupos pireno. Este tipo de grupos se han utilizado, por ejemplo, para unir no covalentemente fullerenos, "quantum dots" o moléculas imán a las paredes de nanotubos de carbono (**Figura 1**).

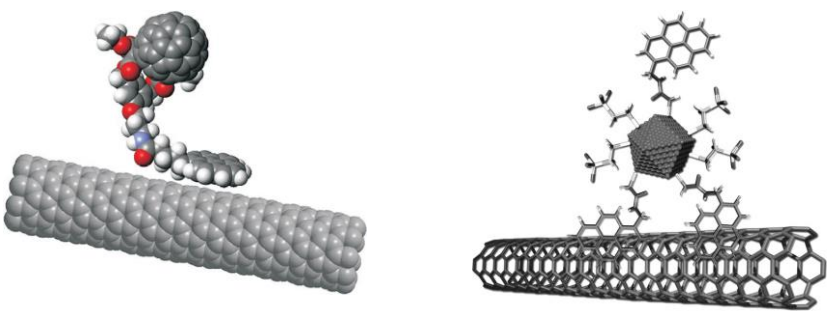

(a) (b)

Figura 1. Representación de la interacción π-π en el híbrido SWNT@fullereno-pireno extraído de la referencia [1] (a), y en el híbrido SWNT@CdTe QD extraído de la referencia [2] (b).

b) Funcionalización covalente

La introducción de enlaces covalentes deriva en la alteración de la estructura sp^2 de los nanotubos, lo que produce una alteración de las propiedades electrónicas. En cualquier caso, los sistemas anclados pueden introducir nuevas funcionalidades, así como incrementar la solubilidad de los CNTs, lo que abre muchas puertas a nuevas a diferentes aplicaciones. El método de funcionalización covalente más simple se deriva del proceso de purificación en medio ácido. El tratamiento de los nanotubos en medio HNO_3/H_2SO_4, además de servir para la eliminación de los catalizadores metálicos utilizados en la síntesis de los CNTs, produce una oxidación parcial de las paredes. Los grupos carboxilato, epoxi e hidroxi introducidos pueden servir como grupos aniónicos de anclaje para producir una posterior interacción de tipo electrostático, así como para la introducción de otro tipo de enlace (por ejemplo, formación de amidas) y, además, sirven para incrementar la solubilidad de los nanotubos.

Además de la funcionalización en medio ácido, se han descrito distintas reacciones químicas para la funcionalización de CNTs. Entre ellas destaca la reacción de Prato, que tiene lugar entre un aminoácido, un aldehído y la pared de los nanotubos, y la reacción de Bingel-Hirsch que tiene lugar entre un bromo malonato y la pared de los nanotubos en presencia de una base (**Figura 2**). Esta última reacción será utilizada en el **Capítulo 5** para crear un híbrido entre el grafeno y radicales orgánicos.

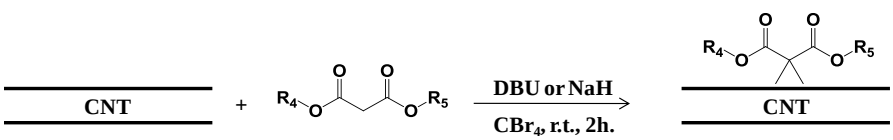

Figura 2. Bingel reaction conditions for the in situ formation of a bromomalonate derivative.

Capítulo 2: Introducción al grafeno

En este capítulo se hace una descripción detallada del grafeno. El capítulo incluye:

- Clasificación y propiedades de G
- Síntesis de G
- Funcionalización del G y aplicaciones

A continuación vamos a resumir brevemente los aspectos relevantes de este capítulo para los capítulos de resultados.

Grafeno hace referencia a una única lámina de grafito, y por tanto se puede definir como una monocapa bidimensional de átomos de carbono con hibridación de tipo sp^2 dispuestos de forma hexagonal. Aunque la definición de G no admite una clasificación más amplia, debido a que determinados derivados de G (óxido de grafito (GO), nanocintas de grafeno (GNRs)) se utilizan apenas sin distinción, cabe hacer un breve inciso sobre ellos. El GO es el resultado de oxidar el grafito con ácidos fuertes, lo que introduce una serie de grupos oxigenados sobre las láminas aumentando así el espacio interlaminar y permitiendo su exfoliación en láminas individuales. A diferencia del G, el GO es aislante debido a la gran cantidad de defectos que posee. Para recuperar la estructura grafítica, y con ello las propiedades del G, es necesario un paso posterior de reducción, pero, dado que es imposible reestablecer la estructura de tipo sp^2 en su totalidad, siempre se observará un comportamiento semiconductor, por lo que al grafeno resultante de la reducción del GO se le suele llamar óxido de grafeno reducido (rGO). Por su parte los GNR serían el resultado de cortar de forma infinita una lámina de G en una de las direcciones del espacio, de modo que obtendríamos una lámina larga de grafeno pero de ancho nanométrico. Como resultado del confinamiento, los GNRs pueden poseer distintas geometrías (“zig-zag” o “arm-chair”) y por tanto pueden ser metálicos o semiconductores.

En relación con la síntesis del grafeno y debido a la relevancia que tendrán en los capítulos posteriores, vamos a centrarnos en dos métodos químicos de obtención: (a) la exfoliación de grafito en fase líquida y (b) la síntesis a partir del GO.

a) Exfoliación de grafito en fase líquida

Se ha descrito que determinados disolventes son capaces de exfoliar el grafito en láminas de grafeno individuales o en agregados de unas pocas láminas (**Figura 3**). Esto sólo es posible si el coste energético es muy bajo, por lo que sólo se produce cuando la interacción G-disolvente es muy similar a la interacción G-G. Entre los disolventes posibles destacan: NMP (N-Metilpirrolidona), oDCB (orto-diclorobenceno) o DMF (N,N-Dimetilformamida), aunque también es posible la utilización de disolventes de menor punto de ebullición como puede ser el EtOH (etanol), siempre y cuando se realice un proceso de intercambio de disolvente. [3]

El método de exfoliación de grafito en fase líquida da lugar a láminas de una gran calidad estructural, pero con rendimientos relativamente bajos (menor al 1 wt%) lo que dificulta su implementación en aplicaciones reales y hace necesaria la búsqueda de métodos que permitan una producción de G a mayor escala.

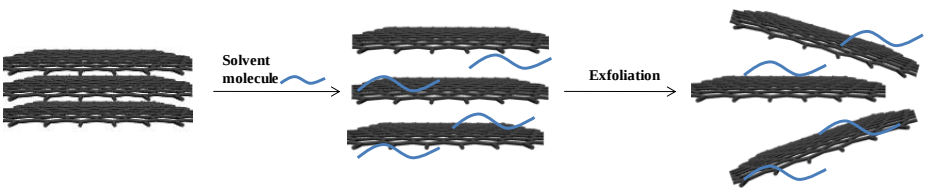

Figura 3. Representación del proceso de exfoliación de grafito en fase líquida para dar lugar a grafeno.

b) Síntesis a partir de óxido grafito.

Como hemos dicho antes, una forma de obtener grafeno o rGO es a partir de la reducción de GO. El GO se obtiene en grandes cantidades a partir de la oxidación de grafito en medio ácido (HNO_3/H_2SO_4),[4] y posteriormente se debe reducir para recuperar la estructura sp^2 y de ese modo reestablecer en la medida de lo posible las propiedades electrónicas (**Figura 4**). En la bibliografía se han descrito diferentes métodos de reducción. El más conocido es la utilización de hidracina como agente de reducción, aunque también es posible usar otros reductores tales como el $NaBH_4$ o el ácido ascórbico. [5] En cualquier caso, dada la toxicidad de la hidracina así como su incompatibilidad con la presencia de otras sustancias o grupos funcionales, se han desarrollado otras alternativas menos nocivas y/o agresivas. Entre ellas cabe destacar

la utilización de agua en condiciones hidrotermales como medio reductor (**Capítulo 4**), [6] o la "flash reduction" que consiste en la utilización de un "flash" de xenón directamente sobre la muestra. [7] En este caso, el grafeno (rGO) se obtiene en grandes cantidades, pero sus propiedades electrónicas se ven relativamente mermadas debido a la presencia de defectos, incluso después de la reducción.

Por último decir que, debido a las similitudes entre los CNTs y el G, las mismas aproximaciones que se han descrito para funcionalizar los CNTs se pueden utilizar para el G. Así pues, tanto la reacción de Prato, como la Bingel-Hirsch, o la utilización de pirenos y otros compuestos arómaticos para la producción de interacciones de tipo π-π han sido utilizadas de forma análoga a lo descrito para CNTs.

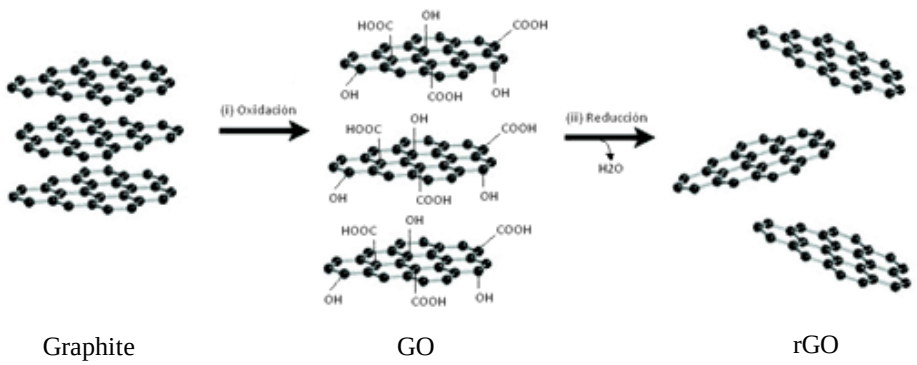

Figura 4. Representación de la síntesis química y reducción de GO.

Capítulo 3: Materiales híbridos basados en nanotubos de carbono

PARTE 1: *Anclaje Electrostático de Moléculas Imán Mn_4 en Nanotubos de Pared Múltiple Modificados Químicamente*

Introducción

En este trabajo se describe el anclaje de moléculas imán (SMM) a MWNTs. Los SMMs son sistemas discretos formados por clústers magnéticos, en los cuales los iones metálicos están conectados a través de ligandos de tipo oxo. Algunos de estos sistemas se comportan como imanes duros a baja temperatura, mostrando, además, fenómenos cuánticos interesantes. Estas características los convierten en atractivos candidatos para el desarrollo de sistemas para la Spintrónica Molecular, el Magnetismo Molecular o la Computación Cuántica.[89,].[10] Con este fin, es necesario depositar las moléculas imán sobre sustratos adecuados o conectarlos a electrodos. Los CNTs se han postulado como excelentes sustratos, ya que sus propiedades electrónicas son sensibles a cualquier cambio químico del entorno.[11, 12]

Nosotros nos hemos centrado en dos rutas químicas que permiten la interacción electrostática entre los SMMs (cargados positivamente) y los MWNT (modificados químicamente con cargas negativas). Como SMM hemos seleccionado $[Mn_4(O_2CCH_3)_2(pdmH)_6]^{4+}$ (Mn_4) (pdmH=deprotonated pyridine-2,6-dimethanol)[13] debido a su estabilidad estructural.[14] En este caso, utilizaremos MWNTs ya que son mucho más robustos que los de pared simple, lo que nos permitirá llevar a cabo la modificación de las paredes sin afectar a sus propiedades físicas.

Resultados y Conclusiones

La interacción electrostática ha sido seleccionada como método de anclaje ya que, por un lado, favorece una interacción fuerte entre ambos componentes y, por otro lado, previene la modificación estructural de la molécula imán, lo que evita por tanto la alteración de sus propiedades físicas. Para llevar a cabo el anclaje se han seguido dos rutas diferentes (**Figura 5**). Por un lado, un proceso consistente en dos etapas: primero se introducen grupos carboxílicos sobre las paredes del nanotubos

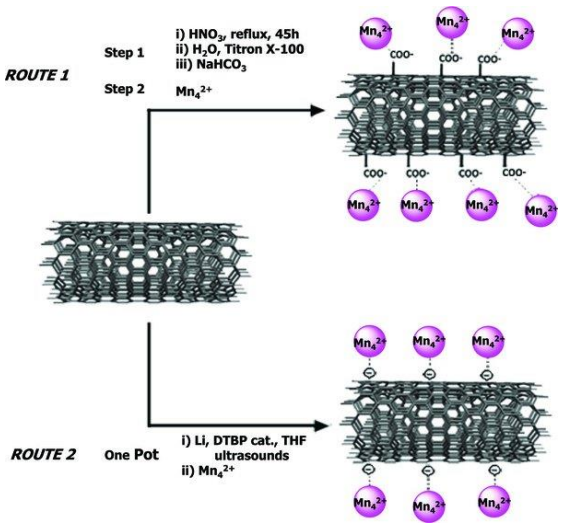

Figura 5. Rutas químicas seguidas para anclar electrostáticamente los SMM catiónicos sobre los MWNTs funcionalizados con cargas negativas.

(cargas negativas) y, posteriormente, se añade el complejo de Mn_4 que se une directamente a los grupos carboxilato. El segundo proceso consiste en un único paso en el que el Mn_4 se combina con MWNT aniónicos generados *in-situ* por su reducción con litio. El uso de dos rutas diferentes se puede justificar en base a los efectos que se generan en los CNTs por el proceso de funcionalización. Así, mientras que la ruta 1 da lugar a híbridos poco conductores ya que los grupos carboxílicos actúan como defectos, la ruta 2 da lugar a un incremento en la conductividad del híbrido, si lo comparamos con los MWNT puros, ya que la introducción de cargas negativas en este caso implica un dopaje de tipo n.

La caracterización física de ambos híbridos se ha llevado a cabo a través de varias técnicas complementarias tales como FT-IR o termogravimetría (TG), así como por microscopía electrónica de alta resolución (HR-TEM) y espectroscopía de rayos-X de energía dispersada (EDS) (**Figura 6**). Todas estas técnicas apuntan a que los híbridos se han formado, y demuestran que la cantidad de SMM adherido a las paredes de los MWNT es mayor para el híbrido **2** que para el **1**, lo que permitió la identificación de Mn mediante la técnica de STEM-XEDS (**Figura 7**). Por otro lado, el estudio de XPS realizado demuestra la integridad del Mn_4 tras su interacción con los nanotubos.

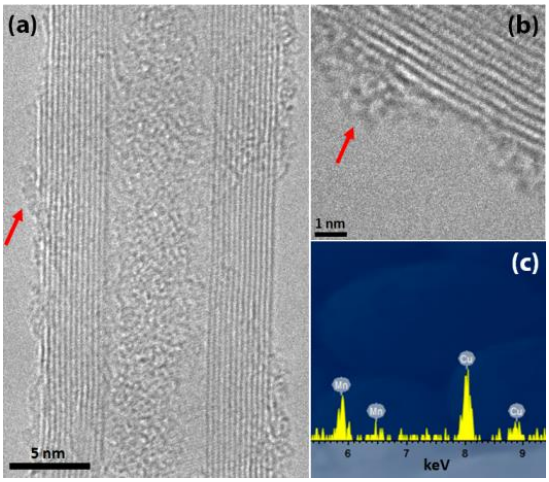

Figura 6. (a, b) Imágenes de HR-TEM del híbrido resultante de la ruta 1 en las que se indica con una flecha la presencia de Mn_4 SMM. c) Espectro de EDS correspondiente a la imagen (a) que confirma la presencia de Mn en el híbrido.

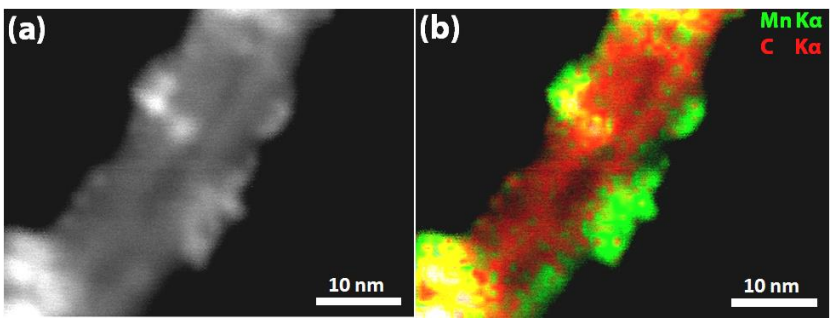

Figura 7. a) Imagen HAADF-STEM con contraste Z del híbrido 2. b) Mapping elemental obtenido a través de STEM-XEDS de la imágen (a) que muestra la perfecta concordancia entre la distribución de Mn y los puntos brillantes presentes en el nanotubo. Debido a la menor concentración de Mn en el caso del híbrido 1, la adquisición de este tipo de imágenes no fue posible.

Por último, las propiedades magnéticas de ambos híbridos han sido medidas. Aunque los MWNT de por si muestran una débil respuesta ferromagnética proveniente de las partículas magnéticas usadas en su síntesis, la adición de Mn_4 SMM provoca un aumento de la señal con valores de saturación a 2.17 y 5.43 $emu.g^{-1}$ a 5 T, para **1** y **2**, respectivamente (**Figura 8**, *izq.*). La mayor señal observada para el híbrido **2** apunta a un mayor grado de funcionalización en éste, tal y como ya había sido anticipado por XPS y HR-TEM. El aumento de la magnetización a bajo

campo es menos pronunciada en el caso de los híbridos que en el caso del Mn_4 puro, lo que parece indicar que el compuesto polinuclear posee una estructura electrónica diferente al interaccionar con los MWNTs. También han sido realizadas medidas ac magnéticas. Para el híbrido **1** no se ha podido observar señal fuera de fase en todo el intervalo estudiado, lo que se debe atribuir a la poca cantidad de SMM en este híbrido. Por su parte, el híbrido **2** muestra un incremento exponencial de la señal en fase (χ') acompañado por una respuesta positiva en la componente imaginaria por debajo de 5 K (**Figura 8**, *derecha*). Aunque no es posible observar la presencia de un máximo en la señal χ'', la posición de la señal de susceptibilidad magnética parece depender de la frecuencia, tal y como cabría esperar para una relajación lenta del spin. Estas características sugieren la presencia de estados superparamagnéticos, y respaldan la presencia de Mn_4 en el híbrido. Aun así, existen claras diferencias entre el híbrido y el Mn_4 puro a bajas temperaturas. La temperatura de bloqueo del Mn_4 puro aparece a menor temperatura, *ca.* 3.5 K, y presenta una mayor dependencia con la frecuencia tanto de la señal en fase como de la señal fuera de fase. Es muy probable que estas diferencias se deban a pequeños cambios estructurales en el compuesto magnético una vez unido a los nanotubos como consecuencia de una distorsión química o una pérdida de simetría.

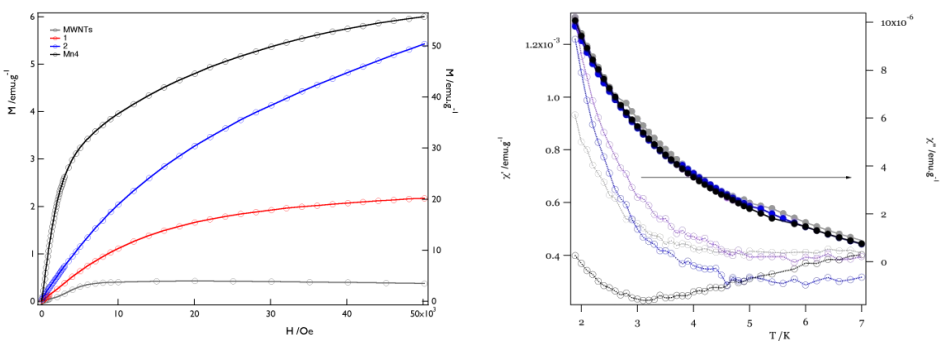

Figura 8. (*Izq.*) Magnetización en función del campo para MWNTs (gris), Mn4 (negro), 1 (rojo) y 2 (azul). (*Derecha*) ac susceptibilidad del híbrido 2 en el rango de 1 (negro), 10 (gris), 110 (azul) y 333 Hz (violeta). La susceptibilidad en fase está representada por símbolos llenos, mientras que la susceptibilidad fuera de fase está representada por símbolos vacíos.

PARTE 2: Híbrido entre Polioxometalato y Nanotubos de Pared Simple a través de Interacciones Supramoleculares

Introducción

En este trabajo se describe la interacción de tipo π-π entre un polioxometalato (POM) modificado con grupos pireno y las paredes de un nanotubo de pared simple (SWNT). Los POM son clústers polinucleares de óxidos metálicos. Estas moléculas inorgánicas poseen una gran versatilidad química y estructural, de manera que existen infinidad de POMs distintos que se pueden utilizar para diversas aplicaciones tales como catálisis o ciencia de materiales.[15] Debido a su versatilidad, los POMs se han utilizado ampliamente para la obtención de híbridos orgánicos-inorgánicos, lo que incluye algunos ejemplos con CNTs.[16] En general, en los ejemplos que se conocen de híbridos POM-CNT la interacción entre ellos se basa en una simple quemisorción, pero a día de hoy no se conocen muchos ejemplos en los que se hayan explorado detalladamente otros tipos de interacciones.

En este apartado, nosotros hemos modificado en colaboración con el grupo de Anna Proust un POM con unidades de pireno ({(TBA)6(P2W17O61{O(Si-Ph-ethylpyrene))2} = POM(pyr)) capaz de interaccionar con las paredes de los nanotubos vía π-π (**Figura 9**). Las interacciones de tipo π-π nos permitirán llevar a cabo el anclaje sin afectar las propiedades del nanotubos por lo que en este caso se utilizarán nanotubos de pared simple (SWNT) por poseer propiedades electrónicas mejor definidas que los MWNT. El objetivo final de este trabajo es el estudio de las propiedades fotofísicas del sistema híbrido.

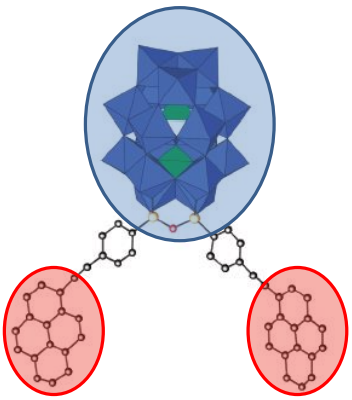

Figura 9. Representación el POM(pyr) utilizado para la síntesis del híbrido. La parte fotofísica (POM) está representada con un círculo azul, mientras que los grupos de anclaje (unidades de pireno) se indican con un círculo rojo.

Resultados y Conclusiones

Las interacciones de tipo π-π permiten anclar el POM sin afectar directamente a las propiedades de los SWNTs. Por su parte, los SWNT han sido seleccionados ya que poseen características analíticas y espectroscópicas que los hacen más fáciles de estudiar, además sus propiedades de transporte los hacen más adecuados para estudios de transferencia de carga. A pesar de que las interacciones de tipo π-π dan lugar a una unión muy débil entre ambos componentes, el anclaje de una molécula electroactiva a través de este tipo de interacción puede producir una transferencia de carga fotoinducida de manera que las propiedades físicas de los SWNTs se vean afectadas.

El anclaje entre el POM y el SWNT se ha estudiado en primer lugar a través de TG y Raman. Además, el estudio de XPS realizado demuestra la integridad del POM una vez anclado a los nanotubos de carbono. Por último, a través del estudio de HR-TEM y EDS podemos confirmar la presencia del POM sobre las paredes del nanotubo. Es interesante notar que en este sistema la utilización de técnicas de microscopía electrónica de alta resolución ha permitido visualizar la estructura del clúster metálico sobre el SWNT (**Figura 10**).

En la actualidad las medidas fotofísicas las están llevando a cabo en el grupo del Professor D. Guldi.

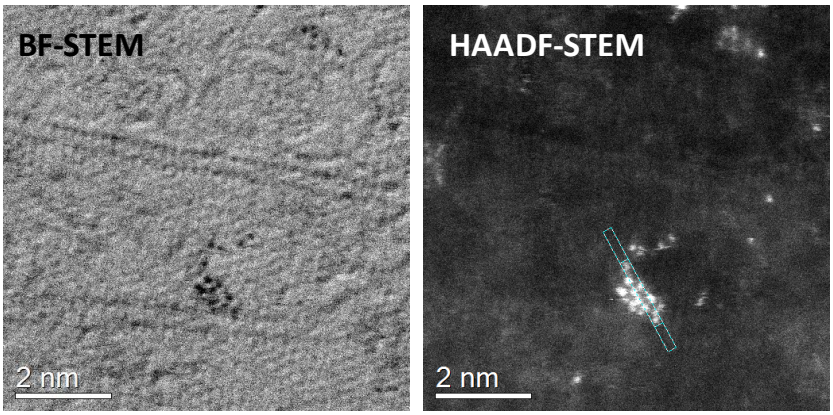

Figura 10. Imágenes BF-STEM y HAADF-STEM que muestran la presencia de POMs (puntos brillantes) de 1,4-1,9 nm sobre las paredes del nanotubo.

Capítulo 4: Síntesis Química de Grafeno

PARTE 1: Influencia del pH en la Síntesis de Óxido de Grafito Reducido bajo Condiciones Hidrotermales

Introducción

Uno de los métodos más simples y menos nocivos para la reducción de GO es la reducción en condiciones hidrotermales (HT). Este método, además se ha utilizado para obtener de forma rápida y sencilla compuestos híbridos de rGO con nanopartículas de óxidos metálicos[17], o compuestos laminares.[18] Dado la versatilidad del citado proceso de reducción es muy importante entender los factores que pueden afectar al producto final. En este apartado, hacemos nuestra aportación a esta causa mediante el estudio detallado del efecto que tiene el pH sobre el rGO obtenido a través del método HT. Para ello fijaremos el pH en el intervalo 3-11 y mostraremos como, en función del pH, se obtienen diferentes nanoformas con diferentes morfologías; además, demostraremos que el grado de reducción está afectado por el pH (**Figura 11**).

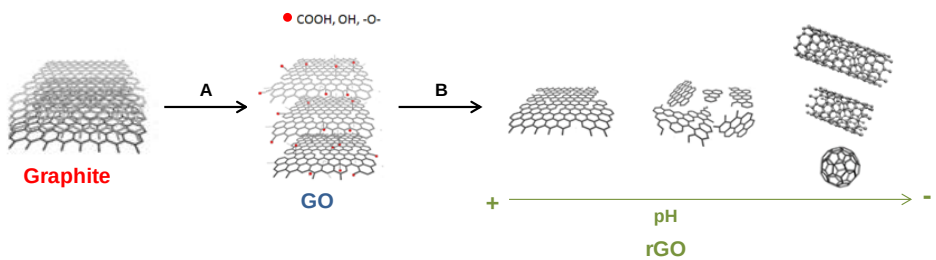

Figura 11. Representación de los procesos que ocurren durante el experimento. A) Oxidación de grafito para obtener GO. B) Reducción hidrotermal a 180 ºC a diferentes pH en el intervalo 3-11. En función del pH, se observan cambios importantes en la morfología y tamaño de las nanoformas de carbono obtenidas.

Resultados y Conclusiones

GO se obtuvo a través del método de Hummers.[4] Posteriormente, el GO dispersado en agua se puso en el interior de un autoclave de Teflón y el pH se ajustó a 3, 5, 7, 9 y 11. Tras el tratamiento hidrotermal, las distintas muestras se analizaron por una variedad de técnicas complementarias.

En primer lugar, el estudio termogravimétrico, el FT-IR y el estudio de difracción de rayos-X muestran que la reducción ha tenido lugar en todo el rango de pHs. Posteriormente se llevó a cabo el estudio de XPS, Raman y HR-TEM. El XPS muestra como a medida que se utilizan pHs más altos, el número de defectos disminuye (**Figura 12**). Por su parte, la espectroscopía Raman demuestra que a mayor pH el tamaño de los dominios es menor (**Figura 13**). Esto nos permite concluir que, a mayor pH, se obtienen láminas de rGO que poseen un menor número de defectos, pero con un tamaño de dominios sp^2 más pequeño. Por su parte, el HR-TEM nos permitió realizar un estudio morfológico de las láminas obtenidas. Por un lado, las imágenes de HR-TEM corroboran los resultados de Raman. Por otra parte, esta técnica muestra que al disminuir el pH la tendencia de las láminas a aglomerarse es menor y la predisposición a enrollarse dando lugar a otras nanoformas grafíticas, como pueden ser nanocebollas o nantubos, es mayor. Es muy interesante ver como a medida que el pH disminuye las nanoformas encontradas son de menor tamaño lo que guarda relación con el tamaño de las láminas encontradas (**Figura 14** y **Figura 15**). Una posible explicación a estas nanoformas encontradas a bajos pH puede ser que los compuestos bidimensionales no son estables ya que tienden a enrollarse con el fin de disminuir el número de enlaces de los extremos, disminuyendo así la energía total del sistema.[19] Esta tendencia es mayor cuanto menor es el tamaño de las láminas ya que en este caso, la relación entre los enlaces de los extremos y la superficie de las láminas es mayor.

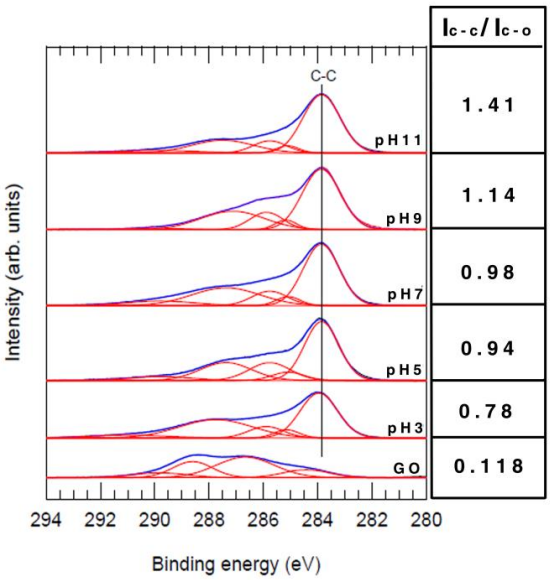

Figura 12. Espectro XPS de C1s de GO y de las muestras rGO obtenidas a los distintos pH. En la tabla adjunta, se muestra como el ratio C-C/C-O aumenta a medida que aumentamos el pH de la reacción lo que apunta a un menor número de defectos para los rGO obtenidos a mayor pH.

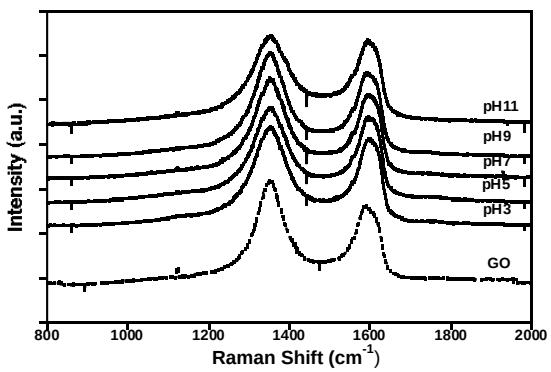

Sample	GO	pH=3	pH=5	pH=7	pH=9	pH=11
I_G/I_D	0.07673	0.29788	0.27792	0.20268	0.23416	0.13898

Figura 13. Espectro Raman en el que se murestra la banda G y D del GO y de las muestras rGO obtenidas a distintos pHs. En la tabla adjunta se resume el ratio I_G/I_D extraído del espectro. Tal y como muestra este ratio tiende a disminuir a media que aumenta el pH lo que sugiera la presencia de dominios sp^2 de menor tamaño en las muestras obtenidas a pH más elevados.

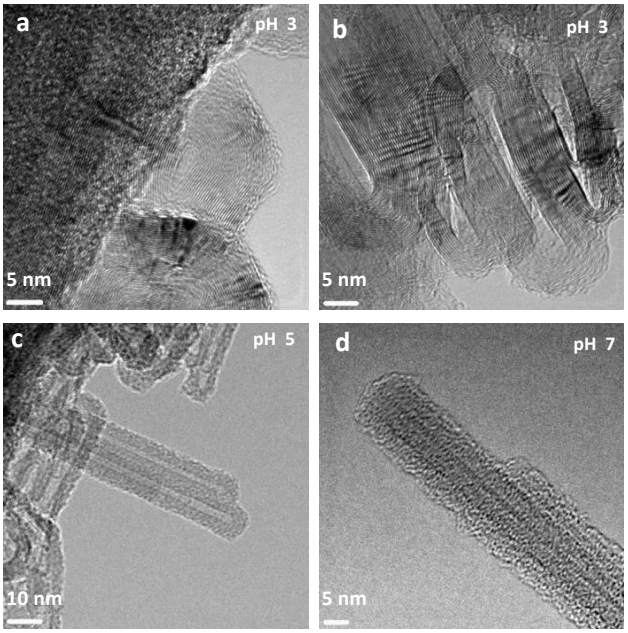

Figura 14. Imágenes de HR-TEM mostrando la formación de nanoformas de carbono a pHs 3, 5 y 7.

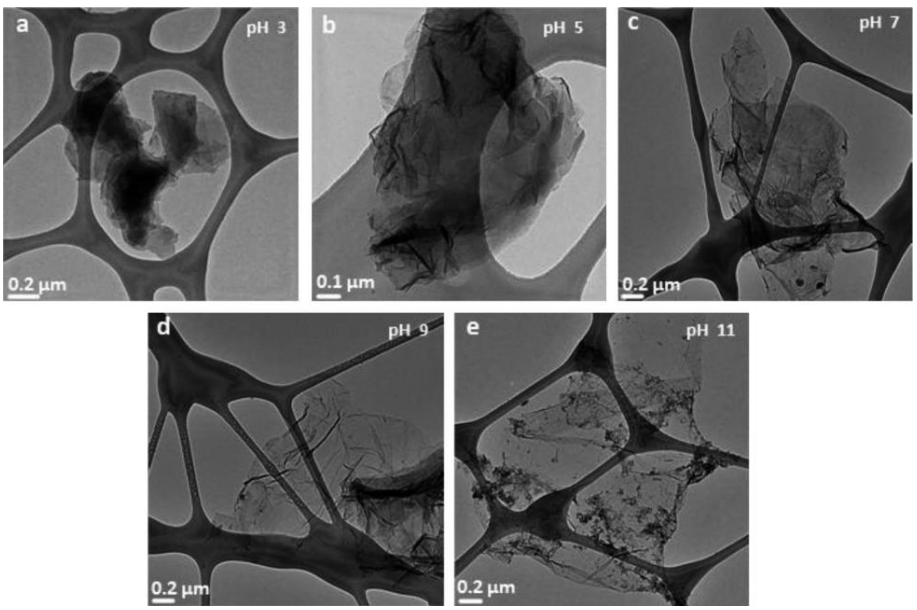

Figura 15. Imágenes de HR-TEM del rGO obtenido a pH = 3, 5, 7, 9, 11, en las que se muestra la evolución en el tamaño de las láminas en función del pH.

<u>PARTE 2:</u> Antraceno como Precursor de Materiales tipo Grafito

Introducción

Otra forma de obtener grafeno es a partir de los métodos "ascendentes" o "bottom-up". Estos métodos se basan en la fusión de moléculas de hidrocarburos de pequeño tamaño para dar lugar a compuestos aromáticos de mayor tamaño que acaban convirtiéndose en grafeno. Este procedimiento es muy interesante ya que permite diseñar la forma y tamaño del G resultante. El problema con el que se enfrenta este procedimiento es el bajo rendimiento.[20] Para intentar mejorarlo posiblemente sea interesante el estudio de nuevos precursores. En esta dirección, el estudio de hidrocarburos aromáticos (PAHs) es muy prometedor y, de hecho, existen varios ejemplos en los que se ha conseguido crecer sobre sustratos metálicos láminas de G a partir de PAHs.[21] En general, estos procesos necesitan de catalizadores metálicos para promover la fusión de los PAHs. Sería muy interesante encontrar PAHs adecuados que fueran capaces de dar lugar a G sin necesidad de estos catalizadores. En este sentido, Talyzin y colaboradores han demostrado la formación de oligomeros de baja dimensionalidad a partir de la fusión del coroneno.[22] Además, en un trabajo posterior, demostraron como la síntesis de grafeno se puede conseguir al confinar las moléculas de coroneno en el interior de CNTs como paso previo a su posterior fusión.[23]

Nosotros, inspirados por el trabajo de Talyzin hemos considerado la molécula de antraceno como un precursor adecuado y barato para la obtención de grafeno debido a su bajo punto de fusión (218 ºC) y ebullición (340 ºC) (**Figura 16**). A continuación vamos a mostrar cómo, en primer lugar, a partir de antraceno somos capaces de obtener grafito a través de un simple tratamiento térmico. En segundo lugar, siguiendo condiciones de fusión similares, utilizaremos por un lado el material mesoporoso MCM-41 y, por otro, el compuesto laminar TaS_2 para confinar las moléculas de antraceno e intentar así obtener grafeno confinado en estos materiales inorgánicos.

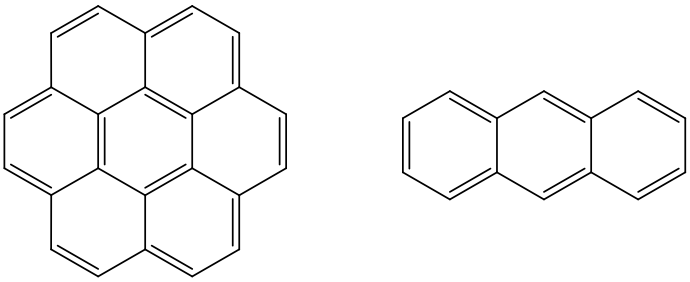

Fijura 16. Estructura molecular del coroneno y el antraceno.

Resultados y Conclusiones

Síntesis de Grafito a partir de Antraceno

En esta primera parte mostramos como el grafito se puede obtener a partir de antraceno en dos simples etapas. Primero, se pone el antraceno en un tubo de cuarzo sellado a vacío y calentamos con una rampa térmica hasta 520 ºC. Luego, llevamos a cabo un recocido en atmosfera inerte de modo que obtenemos grafito.

Tanto el análisis termogravimétrico (TGA), como el FT-IR, como la difracción de rayos-X (XRD) muestran como, tras los sucesivos tratamientos térmicos, se tiende a una estructura cada vez más grafítica. De hecho, el XRD muestra un espacio interlaminar comparable al del grafito puro (**Figura 17 a**), y la TG muestra un incremento considerable de la estabilidad térmica con valores parecidos al del grafito tras el recocido térmico (**Figura 17 b**). Además, las imágenes de HR-TEM tomadas antes y después del recocido muestran una tendencia clara hacia láminas de tipo grafito, lo que además se confirma por la aparición de las bandas típicas de compuestos grafíticos en el espectro Raman (**Figura 17 c**).

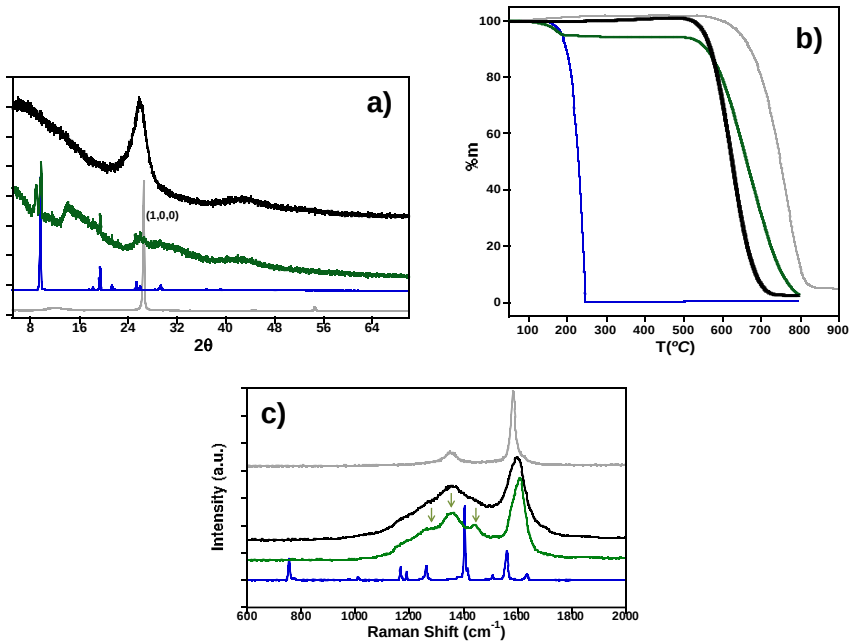

Figura 17. a) XRD, b) TGA y c) Espectro Raman del grafito (gris), del antraceno (azul), del producto resultante de la fusión (verde) y del producto resultante del recocido térmico (negro).

Síntesis de nanoformas de grafeno ultraestrechas inducidas por fusión de moléculas de antraceno confinado en el interior de los poros de una MCM-41

En este caso, como paso previo a la fusión, las moléculas de antraceno se han introducido en el interior de los poros de una sílice porosa MCM-41 siguiendo un método de impregnación. El llenado ha sido demostrado a través de XRD, isotermas de absorción y microscopía SEM. Posteriormente, la evolución a estructuras grafíticas tras el proceso de fusión y recocido se ha seguido por Raman, XRD y TGA. Por último, tras disolver parcialmente el mesoporoso usando una disolución diluida de HF, se ha podido observar por HR-TEM una clara grafitización de la muestra, así como la aparición de nanoformas de carbono cuyo tamaño concuerda con el tamaño de los poros de la MCM-41 (**Figura 18**). Por lo tanto, podemos concluir que el confinamiento de las moléculas de antraceno en el interior de un sistema nanométrico como paso previo a su fusión induce una grafitización que no había sido posible observar en el sistema sin confinar.

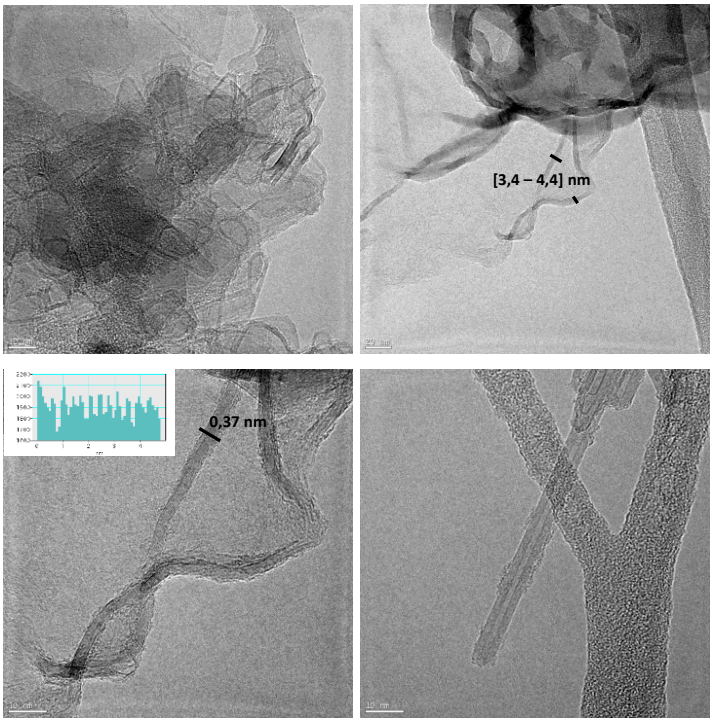

Figura 18. Imágenes de HR-TEM de las nanoformas de carbono observadas tras disolver parcialmente el mesoporoso con HF diluido. Las imágenes muestran una clara grafitización, y la aparición de nanoformas cuyo tamaño no excede los 4-5 nm en ancho.

Síntesis de grafeno por confinamiento de moléculas de antraceno entre láminas de TaS_2.

Aquí, siguiendo el procedimiento de fusión descrito en los apartados anteriores, hemos conseguido crecer un híbrido grafeno-TaS_2. La presencia de ambos componentes se ha determinado a través de XRD, Raman y SAED (**Figura 19**). Además, aunque no se han podido determinar láminas individuales, el SEM sugiere un cierto ordenamiento laminar (**Figura 20**). Dado las propiedades superconductoras del TaS_2, en la actualidad estamos intentando estudiar las propiedades electrónicas y superconductoras del híbrido. Además, en un futuro pretendemos obtener un sistema más ordenado mediante el intercalado de antraceno entre láminas de TaS_2 como paso previo a la fusión.

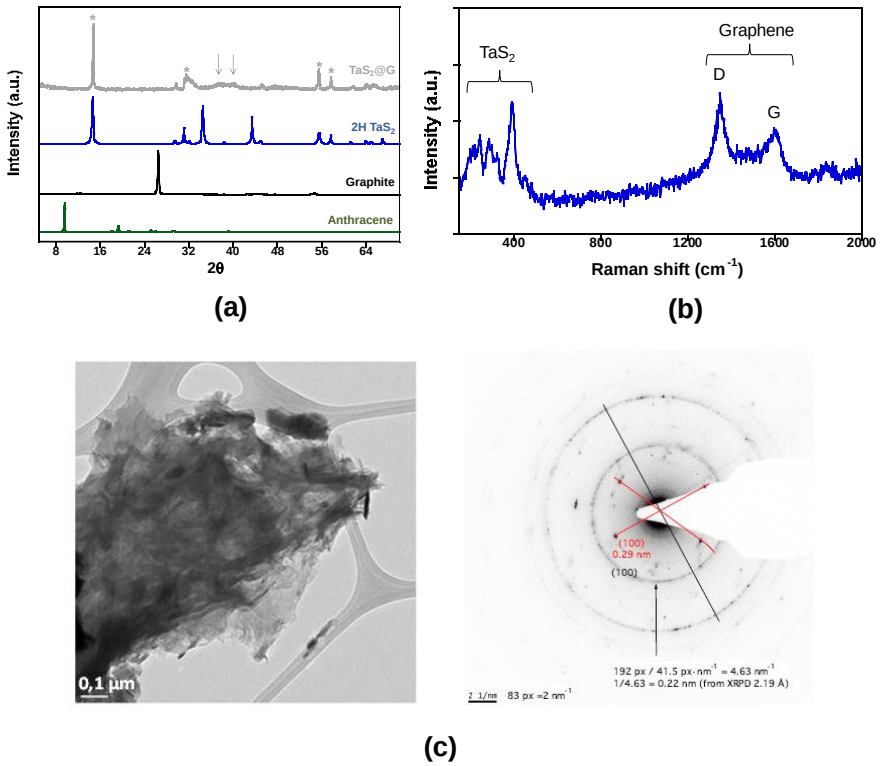

Figura 19. a) XRD del antraceno (verde), del grafito (negro), del TaS_2 (azul) y del híbrido TaS_2@G (gris). b) Espectro Raman del TaS_2@G que muestra la presencia de TaS_2 y G en el híbrido. c) Imagen de HR-TEM y su correspondiente SAED. En el SAED se ven dos anillos concentricos que se pueden asociar al plano (100) del grafeno (negro) y al plano (100) del TaS_2 (rojo).

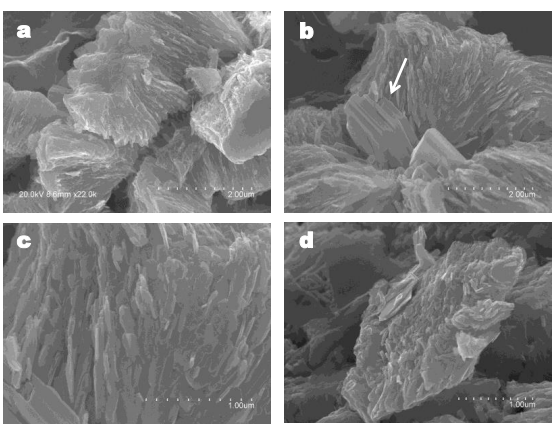

Figura 20. Imágenes SEM del híbrido TaS_2@G. En la figura (b) la presencia de cristales de TaS_2 aislados se indica con una flecha.

Capítulo 5: Funcionalización Química de Grafeno

PARTE 1: Deposición Controlada de Láminas Grafeno Químicamente Modificado con Nanopartículas de Oro a través del Tratamiento Térmico del Óxido de Grafito con N,N-Dimetilformamida

Introducción

La deposición de nanopartículas (NPs) sobre láminas de grafeno puede tener interés en una infinidad de aplicaciones, tales como, catálisis, sensores, almacenamiento de energía, biomedicina, etc. En la literatura se puede encontrar un gran número de artículos describiendo la síntesis de compuestos entre G y NPs, pero, que nosotros sepamos, ninguno de estos trabajos incluye un procedimiento que permita adquirir un nivel de control sobre la cantidad de NPs depositadas.[24]

En este trabajo, describimos un proceso simple de funcionalización de grafeno que nos permite controlar el grado de funcionalización. El método consiste en someter al GO a un tratamiento térmico de reducción/funcionalización en DMF para obtener grafeno modificado químicamente (CMG). Al calentar el GO en DMF, además de promover la reducción del GO, se introduce una serie de grupos funcionales nitrogenados en forma de aminas y amidas. Mostraremos como, variando las condiciones de reacción (tiempo y temperatura), somos capaces de variar el contenido de nitrógeno en el CMG resultante. Estos grupos nitrogenados pueden ser empleados en un paso posterior como puntos de anclaje para NPs de Au, de modo que, al controlar el grado de funcionalización seremos capaces de variar la cantidad de NPs de Au sobre el G.

Resultados y Conclusiones

La síntesis consiste en someter al GO a un proceso térmico en DMF, de modo que se reduce y se introducen una serie de grupos nitrogenados. El grado de funcionalización puede variarse fácilmente con la temperatura (T) y el tiempo (t), de modo que llevamos a cabo una serie de experimentos manteniendo el tiempo en 5 días de reacción y variando T entre 85-120 ºC (CMG(T, 5d)); y otra serie de experimentos manteniendo T en 120 ºC y variando t entre 1-5 días (CMG(120 ºC,

t)). Sobre este CMG se le añadirán NPs Au disueltas en tolueno que se unirán a través de un enlace covalente débil a los grupos nitrogenados introducidos.

En base a los resultados que a continuación resumiremos, se puede proponer el siguiente mecanismo de reacción (**Figura 21**): por un lado, es bien conocido que el tratamiento térmico de GO conduce a una reducción del mismo. Por otro lado, la DMF tiende a descomponerse en dimetilamina a alta temperatura. Tal proceso de descomposición está catalizado en medio ácido, por lo que se vería favorecido en presencia de GO (el pH de la disolución de GO es 5.4). Estas aminas generadas serían capaces de reaccionar, de forma similar a las descritas en previos trabajos, con los grupos oxigenados presentes en GO para dar aminas, amidas o 1,2-aminoalcoholes.[25] Debido a que tanto T como t influyen en la descomposición gradual de la DMF, ambos factores se pueden utilizar para controlar la generación de dimetilamina y, por tanto, para controlar el grado de funcionalización del G. Como la cantidad de NPs Au que se anclan a las láminas es proporcional a número de grupos funcionales, este procedimiento permite controlar la deposición de NPs de Au sobre las láminas de G.

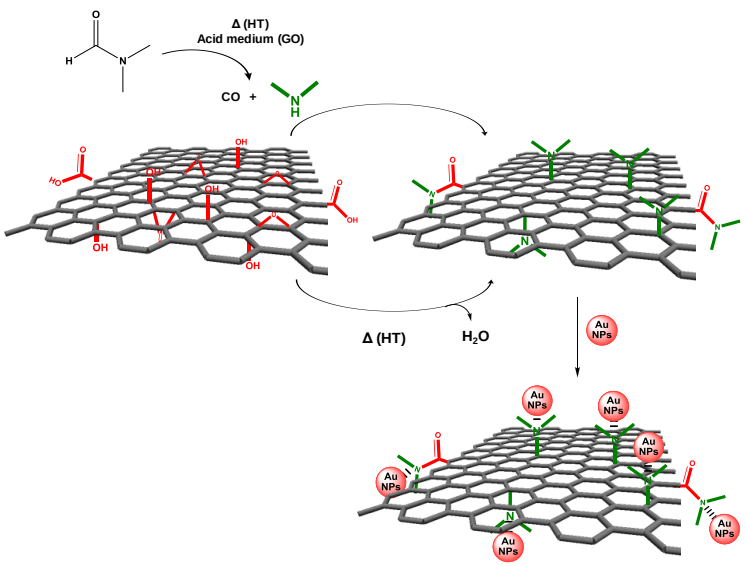

Figura 21. Representación de los posibles procesos que tienen lugar durante la funcionalización/reducción de GO para obtener CMG y su posterior interacción con nanopartículas de oro.

Tanto la reducción como la presencia de grupos nitrogenados han sido confirmadas por FT-IR y análisis elemental. Además, a través del análisis térmico de todas las muestras (antes y después del tratamiento térmico en DMF, y antes y después de añadir el oro), se ha demostrado que el grado de funcionalización es mayor cuanto mayor es el tiempo y la temperatura de reacción (**Figura 22**). A través del XPS se ha podido confirmar la presencia de enlaces N-Au (**Figura 23**). Finalmente, mediante HR-TEM se muestra claramente como a medida que aumentamos la temperatura (o el tiempo de reacción) aumenta la deposición de NPs de Au sobre la superficie de G (**Figura 24**).

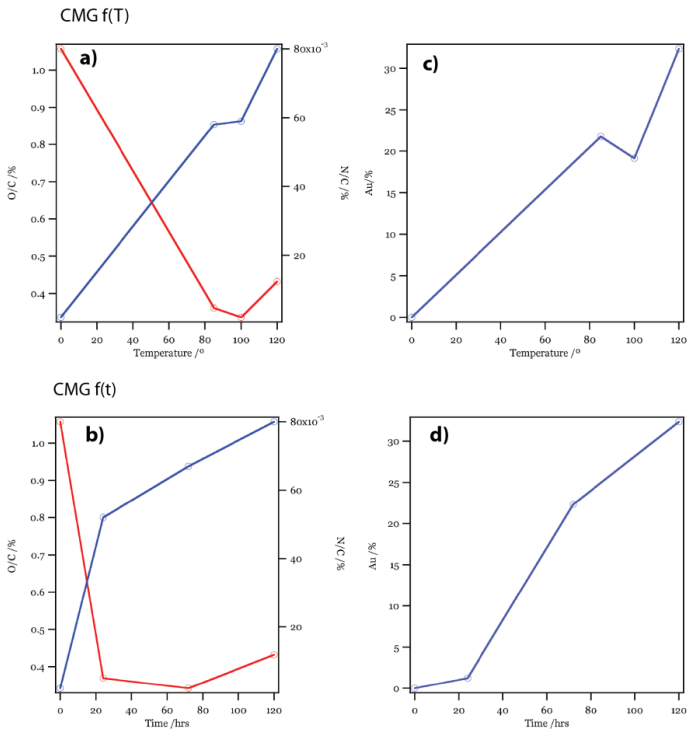

Figura 22. Variación en la relación entre el % de O/C y el % de N/C (a y b) y del contenido de oro (c y d) extraído del análisis térmico. En la parte superior de la imagen se muestran estas relaciones en función de la temperatura, mientras que en la parte inferior se muestra en función del tiempo de reacción.

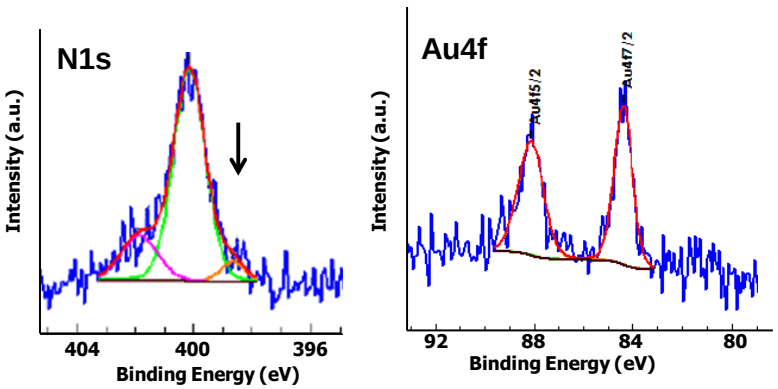

Figura 23. Espectro XPS de nitrógeno (N1s) y de oro (Au4f) para la muestra CMG@Au obtenida a 120ºC y 1 día. En el N1s, una flecha indica la energía correspondiente al enlace N-Au.

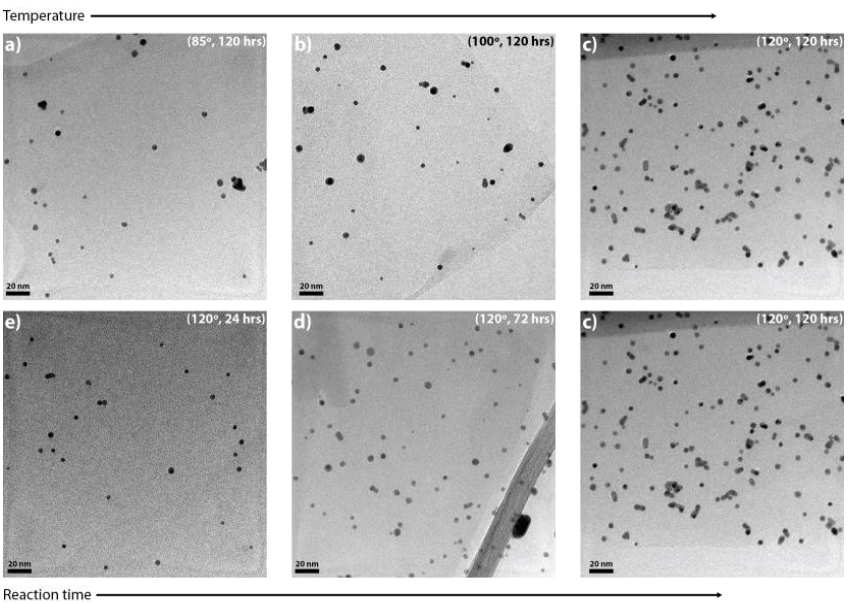

Figura 24. Imágenes de HR-TEM de las muestras CMG f(T, t) tras la deposición de NPs Au que muestran como variando la T (arriba) y el t (abajo) se puede controlar la deposición superficial con NPs Au.

PARTE 2: Anclaje Covalente de Radicales Orgánicos al Grafeno e influencia de este anclaje sobre la Magnetoresistencia del Material Híbrido.

Introducción

La modificación de las láminas de G con moléculas activas dadoras o aceptoras es un mecanismo adecuado para poder variar las propiedades electrónicas del G. Esto es muy importante de cara al desarrollo de futuros dispositivos electrónicos basados en grafeno. De modo que el dopaje del G vía enlaces covalentes o no-covalentes podría considerarse como un medio potencial para controlar químicamente sus propiedades, lo que podría dar lugar a nuevas aplicaciones. En este sentido, recientemente se está prestando bastante atención a las propiedades de magnetoresistencia (MR) del grafeno, así como a la de determinados compuestos derivados de él, [26], [27] lo que da pie a pensar en el potencial del G como componente fundamental para la fabricación de dispositivos electrónicos o magnéticos de carácter laminar. En cualquier caso, todavía no se ha estudiado cómo el dopaje del G con radicales orgánicos puede afectar la MR del mismo.

Por otro lado, en lo que concierne a la reactividad del G, dada la poca reactividad que posee, la mayoría de las reacciones químicas se han llevado a cabo a partir de GO. Como ya hemos comentado con anterioridad, el método de exfoliación en fase líquida de grafito es mucho más atractivo si queremos preservar al máximo las propiedades del G. Sin embargo, este método, al dar lugar a láminas mucho más perfectas que el GO, también da lugar a láminas menos reactivas, lo que ha hecho que a día de hoy el número de artículos que describen la funcionalización de G exfoliado a partir de este procedimiento sea muy limitado. [28, 29] Concretamente la reacción de Bingel-Hirsch (B-H) ha sido utilizada únicamente para la funcionalización del G con moléculas de tetratiafulvaleno, para lo cual ha sido necesaria la utilización de microondas como fuente de energía adicional. [30] Los microondas favorecen las reacciones químicas sobre G, pero también pueden dar lugar a una sobre-funcionalización, a reacciones paralelas o la descomposición de los reactivos.[31, 32, 33, 34]

Nosotros en este trabajo vamos a mostrar cómo es posible funcionalizar las láminas de grafeno con radicales orgánicos, a través de la reacción de B-H y sin la utilización de microondas. El grafeno se obtendrá a través del método de exfoliación

en fase líquida, y mostraremos cómo es posible variar el grado de funcionalización simplemente cambiando el disolvente empleado para la exfoliación. Además, llevaremos a cabo un estudio de MR de los productos obtenidos.

Resultados y Conclusiones

La funcionalización de las láminas de G con radicales orgánicos se ha conseguido a través de un proceso en dos etapas (**Figura 25**). Primero el G se ha obtenido por exfoliación en fase líquida usando o-diclorobenceno (oDCB) o bencilamina como disolventes. En una etapa posterior el radical orgánico (**1**) se ha enlazado covalentemente al G mediante la realización de la reacción B-H a temperatura ambiente. El uso de dos disolventes se justifica en base al grado de funcionalización obtenido. Mientras que cuando usamos oDCB se llega a un nivel de funcionalización muy bajo (**1-G**), el uso de bencilamina resulta en un mayor grado de funcionalización (**1-G+**). Esto probablemente se deba a que el mayor carácter electro-dador de la bencilamina comparada con el oDCB juegue un papel muy importante debido a la aparición de complejos de transferencia de carga entre en G y la bencilamina lo que favorece la reacción.

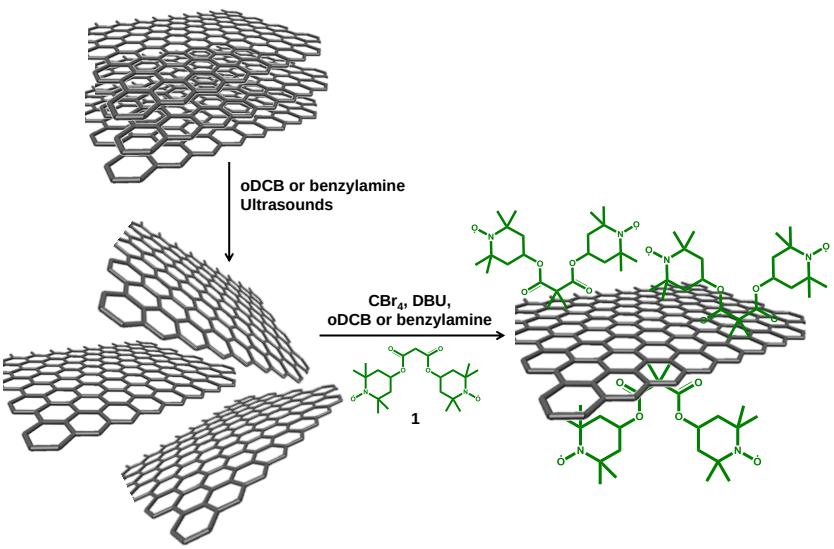

Figura 25. Procedimiento químico seguido para la obtención de **1-G** y **1-G+.**

El grado de funcionalización es de 1 biradical por cada 1300 átomos de carbono para **1-G** y de 1 biradical por cada 450 átomos de carbono para **1-G+**, en base a los resultados de termogravimetría (**Figura 26 a**). La presencia de enlaces covalentes resultantes de la reacción de B-H se estableció primero mediante espectroscopia Raman que muestra un incremento en la intensidad de la banda D (**Figura 26 b**), y por XPS que muestra la presencia de enlaces C-N y N-O en las muestras funcionalizadas (**Figura 26 c**). Finalmente, fue confirmado ineludiblemente a través de Resonancia Paramagnética Electrónica (EPR) la cual descarta una posible fisisorción del radical sobre el grafeno (**Figura 26 d**).

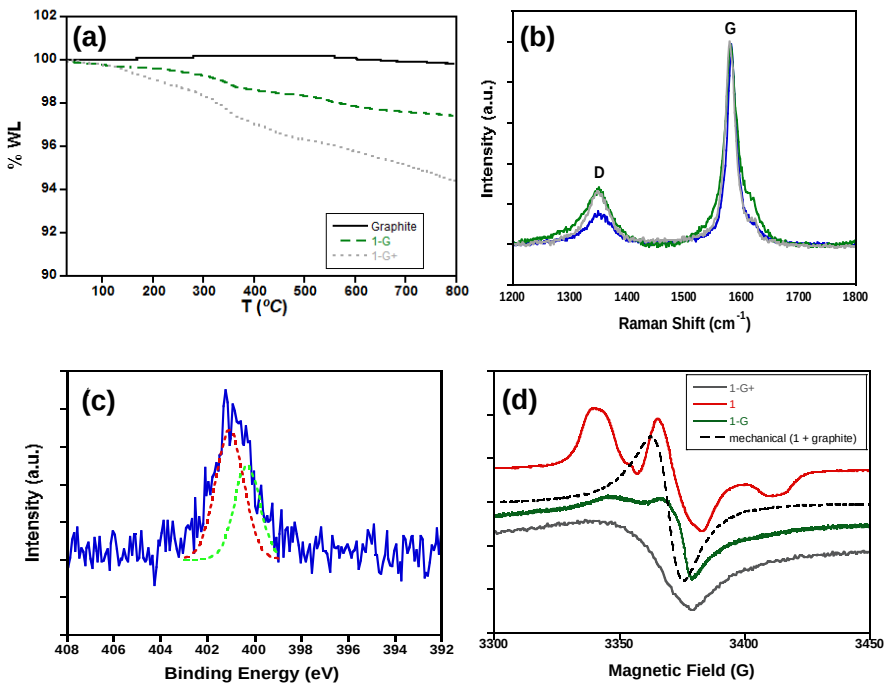

Figura 26. a) TGA bajo atomósfera inerte y b) Espectro Raman del grafito (negro), **1-G** (verde) y **1-G+** (gris). c) Espectro de XPS de N1s para **1-G** (la línea azul es el experimental, mientras que la verde se corresponde con los enlaces de tipo C-N y la roja con los enlaces de tipo N-O). d) Espectro de EPR de **1-G** (verde),**1-G+** (gris) y una mezcla mecánica del radical con grafito (negro) a 300 K. En rojo se muestra el espectro de EPR del radical en tolueno congelado.

Finalmente se llevaron a cabo medidas de transporte sobre las muestras. Para ello se utilizaron como blanco grafeno exfoliado en oDCB y G funcionalizado con moléculas de etilmalonato (**2-G**; que son los análogos no magnéticos de los radicales empleados) siguiendo el procedimiento descrito para la obtención de **1-G**. Para empezar, el mecanismo de conducción cambia con el grado de funcionalización (**Figura 27**, *izq.*), de modo que **1-G** muestra un comportamiento metálico mientras que **1-G+** muestra un comportamiento de tipo semiconductor, tal y como cabía esperar. Las medidas de MR en función del campo confirman que las muestran funcionalizadas con radicales poseen un comportamiento similar a monocapas de G, pero además muestran a bajas temperaturas un fenómeno de MR a bajo campo (LFMR), el cual es proporcional a la densidad de radicales. Dado que este fenómeno sólo es observable en las muestras funcionalizadas con radicales orgánicos, podemos confirmar que el LFMR es intrínseco a la presencia de especies paramagnéticas y no a la simple funcionalización (**Figura 27**, *derecha*).

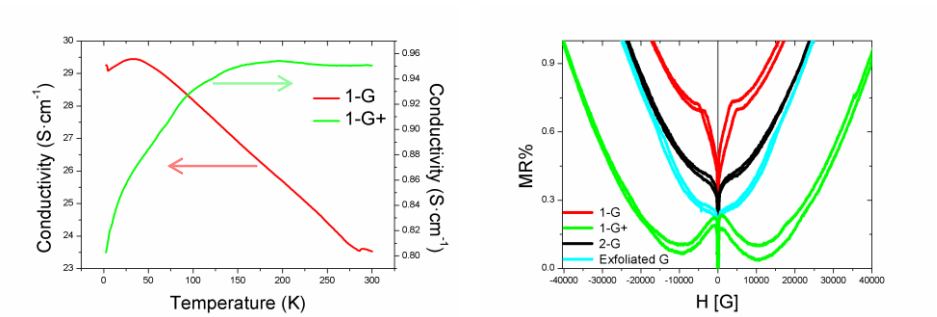

Figura 27. (izq.) Curvas de conductividad frente a la temperatura mostrando el comportamiento metálico y semiconductor de 1-G (rojo) y 1-G+ (verde), respectivamente. (derecha) Curva de MR frente al campo a 2 K mostrando la aparición del LFMR para 1-G (rojo) y 1-G+ (verde), así como su ausencia en 2-G (negro) y el grafeno exfoliado en oDCB (azul)

Referencias

[1] D.M. Guldi, E. Menna, M. Maggini, M. Marcaccio, S. Paolucci, F. Paolucci, S. Campidelli, M. Prato, G.M. Aminur Rahman, S. Schergna, *Chem. Eur. J.*, **2006**, *12*, 3975.

[2] C. Schulz-Drost, V. Sgobba, C. Gerhards, S. Leubner, R.M. Krick Calderon, A. Ruland, D.M. Guldi, D.M., *Angew. Int. Ed.*, **2010**, *49*, 6425.

[3] X. Zhang, A.C. Coleman, N. Katsonis, W.R. Browne, B.J. van Wees, B.L. Feringa, *Chem. Commun.*, **2010**,*45*, 7539.

[4] W.S. Hummers, R.E. Offeman, *J. Am. Chem. Soc.*, **1958**, *80*, 1339.

[5] a) S. Stankovich, D.A. Dikin, R.D. Piner, K.A. Kohlhaas, A. Kleinhammes, Y. Jia, Y. Wu, S.T. Nguyen, R.S. Ruoff, *Carbon*, **2007**, *45*, 1558. b) H.-J. Shin, K.K. Kim, A. Benayad, S.-M. Yoon, H.K. Park, I.-S. Jung, M.H. Jin; H-K. Jeong, J.M. Kim, J.-Y. Choi, Y.H. Lee., *Adv. Funct. Mater.*, **2009**, 19, 1987.

[6] Y. Zhou, Q. Bao, L.A.L. Tang, Y. Zhong, K.P. Loh, *Chem. Mater.*, **2009**, *21*, 2950.

[7] L.J.Core, R. Cruz-Silva, J. Huang., *J. Am. Chem. Soc.*, **2009**, *131*, 11027.

[8] a) R. Sessoli, D. Gatteschi, A. Caneschi, M. A. Novak, *Nature* **1993**, *365*, 141; b) D. Gatteschi, R. Sessoli. *Angew. Chem. Int. Ed.* **2003**, *42*, 268.

[9] a) N.Ishikawa, M. Sugita, T. Ishikawa, S. Koshihara, Y. J. Kaizu, *J. Am. Chem. Soc.* **2003**, *125*, 8694; b) M. A. Aldamen, J. M. Clemente-León, E. Coronado, C. Martí-Gastaldo, A. Gaita-Ariño, *J. Am. Chem. Soc.* **2008**, *130*, 8874.

[10] a) E. Coronado, J. Camarero, *J. Mat. Chem.* **2009**, *19*, 1678; b) M. N. Leuenberger, D. Loss Nature **2001**, *410*, 789.

[11] L. Bogani, W. Wernsdorfer, *Nature Mater*., **2008**, *7*, 179.

[12] a) P. G. Collins, K. Bradley, M. Ishigami, A. Zettl, *Science* **2000**, *287*, 1801; b) S. Sanvito, A. R. Rocha, *J. Comput. Theor. NanoSci.* **2006**, *3*, 624; c) B. L. Allen, P. D. Kichambare, A. Star, *Adv. Mater.* **2007**, *19*, 1439.

[13] J. Yoo, E. K. Brechin, A. Yamaguchi, M. Nakano, J. C. Huffman, A. L. Maniero, L.-C. Brunel, K. Awaga, H. Ishimoto, G. Christou, D. N. Hendrickson, *Inorg. Chem.* **2000**, *39*, 3615.

[14] H. Miyasaka, K. Nakata, K. Sugiura, M. Yamashita, R. Clerac, *Angew. Chem. Ed.* **2004**, *43*, 707.

[15] a) M. Clemente-Leon, E. Coronado, C. Martí-Gastaldo, F.M. Romero, *Chem. Soc. Rev.*, **2011**, *40*, 473. b) S. Cardona-Serra, J.M. Clemente-Juan, E. Coronado, A. Gaita-Ariño, A. Camon, M. Evangeliste, F. Luis, M.J. Martinez-Perez, J. Sese, *J. Am. Chem. Soc.*, **2012**, *134*, 14982. c) D.-L. Long, E. Burkholder, L. Cronin, *Chem. Soc. Rev.*, **2007**, *36*, 105.

[16] D. Pan, J. Chen, W. Tao, L. Nie, S. Yao, *Langmuir*, **2006**, *22*, 5872.

[17] J. Shen, B. Yan, M. Shi, H. Ma, N. Li, M. Ye, *J. Mater. Chem.*, **2011**, *21*, 3415; H. Song, L. Zhang, C. He, Y. Qu, Y. Tian, Y. Lv, *J. Mater. Chem.*, **2011**, *21*, 5972.

[18] A) H. Li, G. Zhu, Z.-H. Liu, Z. Yang, Z. Wang, *Carbon*, **2010**, *48*, 4391; K. Chang, W. Chen, *Chem. Commun.*, **2011**, *47*, 4252.

[19] a) A. Chuvilin, U. Kaiser, E. Bichoutskaia, N.A. Besley, A. N. Khlobystov, *Nat Chem.*, 2010, **2**, 450; J.-W. Seo, Y.-W. Jun, S.-W. Park, H. Nah, T. Moon, B. Park, J.-G. Kim, Y. J. Kim, J. Cheon, *Angew. Chem. Int. Ed.*, **2007**, *46*, 8828. b) A. Yella, E. Mugnaioli, M. Panthöfer, U. Kolb, W. Tremel, *Angew. Chem. Int. Ed.*, **2010**, *49*, 3301.

[20] a) X. Yang, X. Dou, A. Rouhanipour, L. Zhi, H.J. Räder, K. Müllen, *J. Am. Chem. Soc.*, **2008**, *130*, 4216. b) J. Cai, P. Ruffieux, R. Jaafar, M. Bieri, T. Braun, S. Blankenburg, M. Muoth, A.P. Seitsonen, M. Saleh, X. Feng, K. Müllen, R. Fasel, *Nature*, **2010**, *466*, 470.

[21] M. Treier, C.A. Pignedoli, T. Laino, R. Rieger, K. Müllen, D. Passerone, R. Fasel, *Nat. Chem.*, **2011**, *3*, 61.

[22] A.V. Talyzin, S.M. Luzan, K. Leifer, S. Akhtar, J. Fetzer, F. Cataldo, Y.O. Tsybin, C.W. Tai, A. Dzwilewski, E. Moons, *J. Phys. Chem. C*, **2011**, *115*, 13207.

[23] A.V. Talyzin, I.V. Anoshkin, A.V. Krasheninnikov, R.M. Nieminen, A.G. Nasibulin, H. Jiang, E.I. Kauppinen, *Nano Lett.*, **2011**, *11*, 4352.

[24] a) G.Goncalves, P.A.A.P Marques, C.M. Granadeiro, H.I.S. Nogueira, M.K. Singh, J. Grácio, *Chem. Mater.* **2009,** *21*, 4796. b) Z. Xiong, L.L. Zhang, J. Ma, X.S. Zhao, *Chem. Commun.* **2010**, *46*, 6099. c) M. Quintana, K. Spyrou, M. Grzelczak, W.R. Browne, P. Rudolf, M. Prato, *ACS Nano* **2010**, *4*, 3527. d) M. Quintana, A. Montellano, A.E. del Rio Castillo, G.van Tendeloo, C. Bittencourt, M. Prato, *Chem. Commun.*, **2011**, *47*, 9330.

[25] a) O.C.Compton, D.A. Dikin, K.W. Putz, L.C. Brinson, S.T. Nguyen, *Adv. Mater.*, **2010**, *22*, 892. b) A.B. Bourlinos, D. Gournis, D. Petridis, T. Szabó, A. Szeri, I. Dékány, *Langmuir*, **2003**, *19*, 6050. c) K. Ai, Y. Liu, L. Lu, X. Cheng, L. Huo, *J. Mater. Chem.*, **2011**, *21*, 3365.

[26] Z-M. Liao, H-C. Wu, S. Kumar, G.S. duesberg, Y-B. Zhou, G.L.W. Cross, I.V. Shvets, D-P. Yu, *Adv. Mater.*, **2012**, *24*, 1862.

[27] J. Zhu, Z. Luo, S. Wu, N. Haldolaarachchige, D.P. Young, S. Wei, Z. Guo, *J. Mater. Chem.*, **2012**, *22*, 835.

[28] a) M. Quintana, K. Spyrou, M. Grzelczak, W. R. Browne, P. Rudolf, M. Prato, *ACS Nano*, **2010**, *4*, 3527. b) J. R. Lomeda, C. D. Doyle, D. V. Kosynkin, W.-F. Hwang, J. M. Tour, *J. Am. Chem. Soc.*, **2008**, *130*, 16201. c) V. Georgakilas, A. B. Bourlinos, R. Zboril, T. A. Stereotis, P. Dallas, A. K. Stubos, C. Trapalis, *Chem. Commun.*, **2010**, *46*, 1766. d) X. Zhang, L. Hou, A. Cnossen, A. C. Coleman, O. Ivashenko, P. Rudolf, B. J. van Wees, W. R. Browne, B. L. Feringa, *Chem. Eur. J.*, **2011**, *17*, 8957.

[29] S. P. Economopoulos, G. Rotas, Y. Miyata, H. Shinohara, N. Tagmatarchis, *ACS Nano*, **2010**, *4*, 7499.

[30] S. P. Economopoulos, G. Rotas, Y. Miyata, H. Shinohara, N. Tagmatarchis, *ACS Nano*, **2010**, *4*, 7499.

[31] a) S. P. Economopoulos, G. Pagona, M. Yudasaka, S. Iijima, N. Tagmatarchis, *J. Mater. Chem.*, **2009**, *19*, 7326. b) F. G. Brunetti, M. A. Herrero, J. M. Muñoz, A. Diaz-Ortiz, J. Alfonsi, M. Meneghetti, M Prato, E. Vazquez, *J. Am. Chem. Soc.*, **2008**, *130* 8094. c) Y. Wang, Z. Iqbal, S. Mitra, *Carbon*, **2005**, *43*, 1015.

[32] E. Vazquez, M. Prato, *ACS Nano*, **2009**, *3*, 3819.

[33] a) F. Diederich, C. Thilgen, Science, 1996, 271, 317. b) J. R. Pinzon, T. Zuo, L. Echegoyen, *Chem. Eur. J.*, **2010**, *16*, 4864. c) D. Tasis, N. Tagmatarchis, A. Bianco, M. Prato, *Chem. Rev.*, **2006**, *106*, 1105.

[34] a) P. Lidström, J. Tierney, B. Whatey, J. Westman, *Tetrahedron*, **2001**, *57*, 9225. b) R. T. McBurney, F. Portela-Cubillo, J. C. Walton, *RSC Adv.*, **2012**, *2*, 1624.

ANEX

Experimental Techniques

A.1. Transmission Electron Microscopy (TEM)

Transmission Electron Microscopy (TEM) is a technique is which a beam of electrons interacts with an ultrathin object owing to an image that is formed due to the electrons that are able to break through the observed specimen. The image is magnified and focused onto an imaging device (i.e. fluorescent screen, photographic film or CCD camera).

In light microscopes the resolution is limited by the numerical aperture of the system (*NA*) and the wavelength (λ) of the photons that are being used.

$$d = \frac{\lambda}{2\,n\,sin\alpha} \approx \frac{\lambda}{2\,N\,A}$$

In an optical microscope the smallest λ that can be employed is of the range of ultraviolet light (400 nm), meaning that the smallest objects that can be observed are those that are separated not less than 400 nm. In order to increase resolution, one can try to find a source with lower λ, in this direction, x-ray (λ ~ 0.15 nm) is probably the best choice, but they have the main drawback of being absorbed by the glass lens and that they could not be diverted by magnetic lens. TEM solve those problems by employing an electron beam as the desired electromagnetic source taking advantage of the wave nature that the electrons acquire by applying a potential difference (as theorized by Louis-Victor de Broglie). The wavelength of the electrons is found by equating the de Broglie equation to the kinetic energy of an electron, and a applying a correction to account relativistic effects that must be taken in consideration as in TEM the electrons acquire a velocity close to that of light (*c*).

$$\lambda_e \approx \frac{h}{\sqrt{2\,m_0\,E\left(1+\frac{E}{2\,m_0\,c^2}\right)}}$$

h = Plank constant.

m_0 = rest mass of the electron.

E = Energy of the accelerated electron.

So, for example, if the electrons are subjected to a field of 100.000 volts, they would act as a wave of 0.0037 nm, thus being possible the development of microscopes capable to reach the atomic level since in inorganic solids the atoms are separated of the order of 0.2 nm. However, some other aspects related to the microscope set-up lead to a resolution loss.

The main components of al electron microscope are (**Figure A.1.1.**):

- *Vacuum system* (~ 10^{-4}- 10^{-9} *Pa*, depending on the applied voltage), that avoids the interaction of the electrons with the gas particles and allows the generation of a voltage difference between the cathode and the ground without generating an arc.
- *Specimen stage*, which are designed to hold standard TEM grids (3.05 mm diameter ring, and a thickness and mesh size ranging from a few to a 100 μm). The sample is placed in the inner part of the grid. The grids, typically, are made of copper, molybdenum, gold or platinum. The specimen stage also includes airlocks to insert it into the vacuum.
- *Electron gun* that creates the beam of electrons that would interact with the sample to generate a magnified image.
- *Electron lens*, are used to focus the electron beam. They are typically magnetic, as classical lens does not work with electrons.
- *Fluorescent screen or photographic film*, that is placed behind the target object to record the enlarged image.
- *Computer* used to display the generated image.

So, first of all the electron gun generates the electron beam. With this purpose either a tungsten filament or a lanthanum hexaboride source may be employed. By connecting this gun to a high voltage source (~ 100-300 kV) it would start emitting electrons into the vacuum. Once generated, the upper lenses of the microscope serve for tuning the electron probe to the desired size for its further interaction with the sample.

Manipulation of the electrons is carried out by considering two physical aspects. On one hand, the interaction of the electrons with a magnetic field will cause the electron to move following the right hand rule, which implies that the

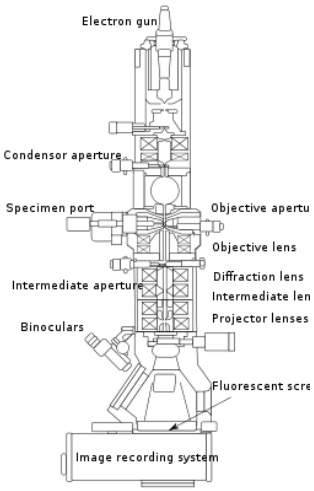

Figure A.1.1. Arrangement of optical components in a TEM microscope.

electron beam could be manipulated by electromagnets. On the other hand, electrostatic fields can cause the electrons to be deflected through a constant angle. Coupling of two deflections in opposite directions with a small gap allows for the formation of a shift in the beam path. The combination of these two effects upon with the visualization system provides the required beam control.

The lenses are a very important part of the TEM as they allow the convergence of the beam, thus permitting changing the magnification of the image by simple modifying the amount of current that flows through the coil. Classically, a TEM consist in three stages of lensing, (i) the condenser lenses which are responsible of the initial formation of the beam after the emission of the electrons, (ii) the objective lenses which focuses the electron beam into the sample, and (iii) the projector lenses which expands the beam onto the imagine device.

Finally, the imagine device can be either a phosphorus screen for direct observation of the image, or it may have a screen coupled CCD to record the image.

Notice that, for imaging with a TEM the samples should be ultrathin to allow the electron beam to pass through it. TEM can increase the size of an object by a million times.

The vast majority of HR-TEM images taken a long the present Thesis have been done using a TECNAI G2 F20 microscope, Field Emission Gun (FEG)200 kV.

A.2. Infra-red Spectroscopy (FT-IR)

Infra-red spectroscopy (FT-IR) is a common technique employed to indentify organic or inorganic compounds by analysis of their constituents bonds. FT-IR takes advantage of the fact that each chemical bond in a molecule vibrates at different energy depending on its nature, so by means of energy they can be identify.

Although the IR radiation covers from 10 to 14000 cm^{-1}, it can be divided in three parts: (i) the far-IR (400-10 cm^{-1}), which is near the microwave region and promotes rotational vibrations; (ii) the mid-IR (4000-400 cm^{-1}) in which the fundamental vibrations take place, it is the employed region for molecule identification; and (iii) the near-IR (14000-4000 cm^{-1}) which excites overtones or harmonic vibrations.

The frequency of the absorbed energy is given by the Hook law:

$$\nu = \frac{1}{2\pi c}\sqrt{f\,\frac{m_A + m_B}{m_A \,.\, m_B}}$$

in which c is the speed of light, f is a strength bond constant and m_A and m_B are the mass of the bonded atoms. So, lighter atoms and stronger bonds lead to higher absorption energies.

The normal modes of vibration (F) are given by a simple rule depending on the number of atoms (N): $F = 3N - 6$

Normally, IR spectra are recorded as absorbance or transmittance as a function of frequency, and either solid, liquid or gaseous samples can be measured.

In this thesis, IR spectrums were taken using FT-IR Nicolet 5700 spectrometer in the 4000-400cm^{-1} frequency range, using powdered samples diluted in KBr pellets.

A.3. Raman Spectroscopy

Both, IR spectroscopy and Raman spectroscopy, are common spectroscopic techniques employed to detect vibrational states, which main difference relies in the way in which light interacts with matter. While in IR spectroscopy, IR energy covering a range of frequencies is directed onto the sample, and just those frequencies matching that of the gap between two different vibrational states it is absorbed, in Raman spectroscopy a single frequency is employed, and it is the scattered radiation, one vibrational unit of energy different from the incident beam, what is detected, therefore, no requiring a frequency match. What happens in Raman is that the interaction with light distorts the cloud of electrons and promotes the formation of a non-stable "virtual state" so the photon is rapidly re-radiated. Normally, if only cloud distortion is involved in scattering, the scattered photons will suffer very small changes in frequency and elastic scattering would occur. This process is known as Rayleigh scattering. The cases in which the process is inelastic and the energy of the incident photon is different from that of the scattered photon by one vibrational unit are known as Raman scattering. It is a very week process, as only one in every 10^6-10^8 scattered photons does it in an inelastic way.

Figure A.3.1 shows the basic processes for one vibration. At room temperature almost all the photons are in the lowest energy vibrational level. Rayleigh scattering will be the most intense as almost all of the scattered photons follow that procedure. Raman scattering may occur following two different processes. On one hand, if part of the energy is absorbed by the molecule, the photon would be promoted from the lowest vibrational level (*m*) to an excited vibrational state (*n*), leading to what is known as Stokes scattering. On the other hand, it is also possible that, due to thermal energy, some molecules were initially in the excited state (*n*) so they would be able to scatter to the ground state (*m*), thus transferring energy to the scattered photon in a process call anti-Stokes. The relative intensity of those processes would depend on the population of *m* and *n*, what can be worked out from Boltzmann equation, however, at room temperature the number of molecules that shall be in the excited state would be markedly lower, and therefore the intensity

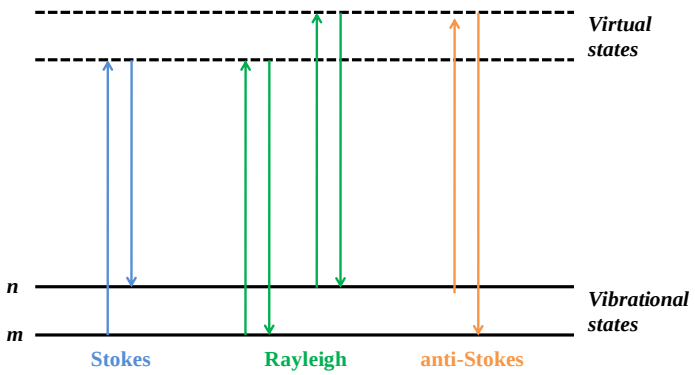

Figure A.3.1. Diagram of the Rayleigh and Raman scattering processes.

of Stokes scattering would be notably higher than anti-stokes scattering. Usually, Raman scattering is recorded only in the low energy side to give Stokes scattering.

The main components of μ-Raman set-up are (**Figure A.3.2.**):

- *A light source*, typically a visible laser (*i.e.* Nd:YAG laser) with a wavelength of 532 nm and a power of 200mW.
- *Mirrors* to guide the light to a notchfilter.
- *Notchfilter* which possess a dielectric coating capable of reflecting the light of only a particular wavelength, therefore, it acts as a mirror for this particular wavelength and reflects the light to a microscope objective.
- *Microscope objective*, which focus the light onto the sample.
- *Fiber* that guides the light to the spectrometer.
- *Spectrometer* which possess a detector.
- *Computer program* that analyze the collected data.

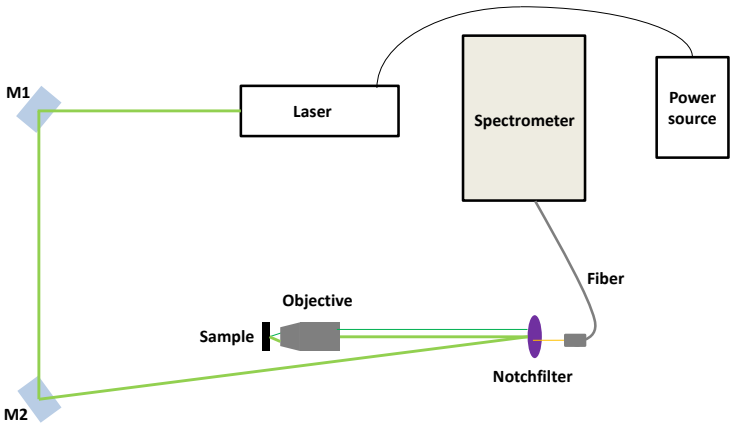

Figure A.3.2. Representation of a typical µ-Raman set-up.

So, first the light from the laser is guide to the notchfilter by two mirrors. Then, the notchfilter cut off the laser line and reflects the light of only a particular wavelength towards a 40x microscope objective. The objective focuses the light onto the sample. The scattered light is collected by the objective and hits the notchfilter at the same position as the incident beam if the setup is calibrated correctly. The notchfilter then cuts off the laser light and only the inelastically scattered part hits the fiber behind the notchfilter. The fiber guides the light into the spectrometer. The spectrometer consists of a fixed grating and a detector. The grating disperses the light onto the detector. Due to this process the spectral distribution of the light is converted into a spatial distribution and can be recorded by the detector. The data analysis is done by a computer program.

The vast majority of µ-Raman spectra carried out over the present Thesis were performed by using a dispersive Jobin-Yvon LabRam HR 800 microscope, working with an excitation line of 532 nm. The scattered light was detected with a thermoelectric cooled (-70 ºC) charge coupled device detector (CCD). It also has an Olympus BXFM optic microscope. All the measurements were carried out directly over the sample. In the performed experiments, the power employed over the samples was of the order of 0.3mW, and the exposition time 60 seconds.

A.4. X-ray photoelectron spectroscopy (XPS)

XPS is a semi-quantitative non-destructive spectroscopic technique that measures the elemental composition and electronic states of the elements that exist within a material. Typically, a sample is irradiated with a source of X-rays, so the energy of the incident photon is transferred to a bound electron. If the energy of the photon is greater than the binding energy (BE) of the electron, and the electron has enough energy to overcome the work function of the solid, it can leave the solid and been measured.

A typical XPS spectrum is represented by the number of electrons detected versus the BE of those electrons. Each element possess characteristic XPS peaks at characteristic BE that serve to identify the elements present on the surface of the analysed materials. These characteristic peaks correspond to the electron configuration of the electrons within the atoms (1s, 2s, 2p,…). As the number of detected electrons in each peak is related to the amount of element within the area irradiated, the surface composition can be quantified.

The basic components of a XPS set up are (**Figure A.5.1**):

- *Source of X-rays*
- *Ultra-high vacuum (UHV) chamber*, in which the sample will be introduced.
- *Electron focusing system* composed of lens that conduce the photoelectrons to the spectrometer
- *Spectrometer* which possess an analyser capable of selecting the energy of the photoelectrons
- *Electron detector*
- *Computer program* that analyse the collected data

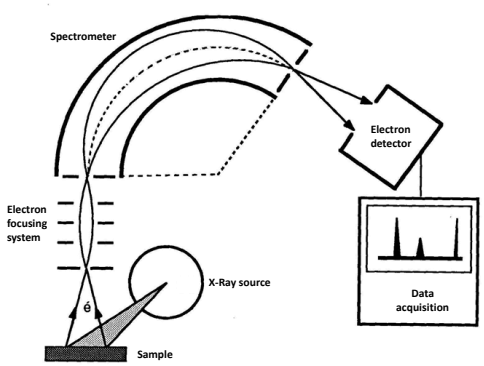

Figure A.4.1. Respresentation of the typical components of an XPS set-up.

So, in a typical experiment, the sample is fitted inside a UHV chamber and irradiated with the X-ray source which produces photons capable of de-bound electrons for the surface of sample (top 1-10 nm of the sample). Those photoelectrons pass through the electron focusing system and arrive to the spectrometer, in which a hemispherical capacitor –composed by two metallic hemispheres– defines the path energy of the electrons and measures the kinetic energy of the photoelectron. This kinetic energy is finally detected in the detector and transduced by a computer programme.

The vast majority of XPS measurements done in the present Thesis have been done by using a Thermo Scientific K-Alpha ESCA instrument equipped with aluminium $K\alpha_{1,2}$ monochromatized radiation at 1486.6 eV X-ray source. In non-conductive samples it was necessary to use an electron flood gun to minimize surface charging. Neutralization of the surface charge was performed by using a low energy flood gun (electrons in the range 0 to 14 eV) and a low Argon ions gun. The XPS measurements were carried out using monochromatic Al-K radiation (h=1486.6 eV). Photoelectrons were collected from a take-off angle of 90° relative to the sample surface. The measurement was done in a Constant Analyser Energy mode (CAE) with a 100 eV pass energy for survey spectra and 20 eV pass energy for high resolution spectra. Charge referencing was done by setting the lower BE C 1s photo peak at 285.0 eV C1s hydrocarbon peak. Surface elemental composition was determined using the standard Scofield photoemission cross sections.

Curriculum Vitae

Curriculum Vitae

Personal Information

Name	Concha Bosch Navarro
Address	Marqués de Zenete 16-13 Valencia (Spain)
Telephone	+34 686238994
E-mail	concepcion.bosch@uv.es
Nationality	Spain
Date of birth	11/03/1984

Work Experience

July 2012 – Present	Research technician – Institute for Molecular Science (ICMol), University of Valencia
July 2008 – July 2012	PhD student (FPU fellowship from the Spanish Ministry of Education), ICMol, University of Valencia
Jan. 2008 – July 2008	Collaboration grant– ICMol, University of Valencia
Sept. 2007 – Dec. 2007	Research initiation scholarship (granted by CSIC) Institute of Chemistry Technology (ITQ), CSIC, Polytechnic University of Valencia

Synthesis of new fluorinated templates for the synthesis of zeolites with applications in catalysis

Education and Training

Jan. 2008- Present	phD in Nanoscience and Nanotechnology ICMol, University of Valencia

Development of multifunctional hybrid materials based on carbon nanotubes and graphene oriented towards molecular magnetism and/or molecular electronics.

2007 – 2009	Master in Nanoscience and Nanotechnology – University of Valencia
2006- 2007 (9 months)	Erasmus stay at Imperial College of London (London) Nine moths project based in the development of polyphosphazenes for gene delivery
2002 – 2007	Chemistry degree – University of Valencia

Journal Publications

C. Bosch-Navarro, F. Busolo, E. Coronado, Y. Duan, C. Marti-Gastaldo, H. Prima-Garcia, "Influence of the covalent grafting of organic radicals to graphene on its magnetoresistance", *J. Mater. Chem. C* **2013** (*submitted*).

C. Bosch-Navarro, E. Coronado, C. Martí-Gastaldo, "Controllable coverage of chemically modified graphene sheets with gold nanoparticles by thermal treatment of graphite oxide with N,N-dimethylformamide", *Carbon* **2013**, *54*, 201.

C. Bosch-Navarro, E. Coronado, C. Martí-Gastaldo, B. Rodríguez-González, L.M. Liz-Marzán, "Electrostatic anchoring of Mn4 single molecules magnets onto chemically modified multiwalled carbon nanotubes", *Adv. Funct. Mater.* **2012**, *22*, 979.

C. Bosch-Navarro, E. Coronado, C. Martí-Gastaldo, J.F. Sánchez-Royo, M. Gómez Gómez, "Influence of the pH on the synthesis of reduced graphene oxide under hydrothermal conditions", Nano*scale* **2012**, *4*, 3977.

J.G. Martínez, T.F. Otero, C. Bosch-Navarro, E. Coronado, C. Martí-Gastaldo, H. Prima-García, "Graphene electrochemical responses sense surroundings", *Electrochimica acta* **2012**, *81*, 49.

	A. Alberola, C. Bosch-Navarro, E. Coronado, J.R. Galán-Mascarós, P. Gaviña, S. Tatay, "Synthesis of brominated tetrathiafulvalenes via phosphite-mediated cross-coupling", *Synthetic Metals* **2010**, *160*, 1797.
Conference contributions	
October 2012	"5th European School on Molecular Nanoscience (ESMOLNA2012)", Cuenca (Spain), Oral Communication.
September 2012	"40 International Conference on Coordination Chemistry (ICCC40)", Valencia (Spain), Poster.
September 2011	"European Conference on Molecular Electronics (ECME2011)", Barcelona (Spain), Poster.
August 2011	"International Nanoscience Student Conference (INASCON2011)", Fuglsocentret (Denmark), Oral Communication.
September 2010	"Trends in Nanotechnology (TNT2010)", Braga (Portugal), Poster.
April 2010	"Fundamentals of Molecular Electronic Assemblies (FUNMOLS)", Muggendorf (Germany), Poster.
September 2009	"European Conference on Molecular Electronics (ECME2009)", Copenhagen (Denmark), Poster.
Febrary 2009	"I Symposium Consolider", Miraflores de la Sierra (Madrid, Spain), Oral Communication.
October 2008	"I European School on Molecular Nanoscience (ESMOLNA2008)", Gandia (Valencia, Spain), Oral Communication.